

Modelling and simulation of adaptation and degradation in anisotropic biological tissues

von der Fakultät Maschinenbau
der Technischen Universität Dortmund
zur Erlangung des akademischen Grades

Doktor-Ingenieur (Dr.-Ing.)

genehmigte Dissertation

von

Tobias Waffenschmidt

aus Freudenberg

| | |
|-----------------------------|---|
| Referent: | Prof. Dr.-Ing. A. Menzel |
| Korreferenten: | Prof. Dr.-Ing. E. Kuhl Prof. Dr.-Ing. E. Tekkaya |
| Tag der Einreichung: | 08.07.2013 |
| Tag der mündlichen Prüfung: | 13.12.2013 |

*We absolutely must leave room for doubt
or there is no progress and there is no learning.
There is no learning without having to pose a question.
And a question requires doubt.*

Richard P. Feynman (1918–1988)
The Pleasure of Finding Things Out

Acknowledgements

The work presented in this thesis was carried out between 2008–2013 during my time as a research assistant at the Institute of Mechanics of the Faculty of Mechanical Engineering of TU Dortmund University. I would like to take this opportunity to thank the people who have supported me during this work and those who were especially important to me during that time.

First of all, I would like to express my sincere gratitude to my advisor Professor Andreas Menzel. I got to know him during his time at the University of Siegen and I followed him after completing my studies there to the TU Dortmund University. His strong support and guidance regarding both academic research and teaching, his encouraging and motivating character, his creative suggestions and ideas and his confidence in my work have contributed significantly to the success of this thesis.

Furthermore, I would like to thank Professor Ellen Kuhl for kindly accepting to be the co-referee of this thesis and Professor Erman Tekkaya for his kind willingness to serve as the third referee. I very much appreciate their sincere interest in my work. I also want to thank Juniorprofessor Björn Kiefer for accepting the chairmanship of the examination committee. And I would like to express my gratitude to Professor Peter Betsch, who first introduced me to the subject of Computational Mechanics during my studies in Siegen.

Next, I would like to thank all my colleagues at the Institute of Mechanics. I very much appreciated the pleasant and friendly working atmosphere, the intercultural spirit and the many stimulating professional and non-professional discussions and activities. The cordial and friendly atmosphere will always be associated with positive memories. I would especially like to thank Kerstin Walter, who at any time has two or three open ears for any (non-)professional organisation-management-life issues and Tina McDonagh for her outstanding assistance in proof-reading various manuscripts. Special thanks also go to my room-mate Thorsten Bartel for simply being the best room-mate I can imagine, as well as to Björn Kiefer and Ralf Denzer, who prevented me from running into mechanical dead ends on several occasions. I shall not forget my former colleagues Jayabal “brown friend” Kaliappan and especially Vadim “Kollege” Palnau who evolved to real friends during our time together at the institute. In a real sense, to “enjoy work”, was made possible by you.

I would also like to thank my colleague and co-author César Polindara, with whom I had the opportunity to work together for six months. The collaborative work together with him undoubtedly enriched the material presented in this dissertation.

In addition, I thank the “Group of Structural Mechanics and Material Modelling” at the University of Zaragoza for their warm welcome during my two-month stay in 2009. My sincere thanks, in particular, go to Victor Alastrué who I already got to know in Siegen.

Furthermore, I am deeply indebted to my good friend Stefan Uhlar. As the advisor of my first student thesis, he was the one who introduced me to the world of “Computational Mechanics”. I would like to thank him for the many activities and exhilarating mechanics-discussions back in the days in Siegen and later on in Dortmund. I also thank Adrian Vetter and Alexander Neef, for our more than two-decades-lasting close friendship, and special thanks also go to Achim Wehrmann and my handballteam for many stimulating non-mechanical hours in the gym.

Most of all, however, I would like to express my most grateful thanks to my family, in particular my parents and my sister Biene, and especially to Hannah. Without their everlasting support, their patience, understanding and love this work would not have been possible.

Dortmund, December 2013

Tobias Waffenschmidt

Zusammenfassung

Die vorliegende Arbeit befasst sich mit der konstitutiven Beschreibung von Adaptions- und Schädigungsvorgängen für die Simulation des Materialverhaltens anisotroper biologischer Gewebe auf Grundlage der Kontinuumsmechanik finiter Deformationen. Die konstitutiven Modelle basieren auf elastischen und inelastischen physikalischen Phänomenen, welche auf der Mikroebene des jeweiligen Materials in Erscheinung treten und das makroskopische Materialverhalten maßgeblich beeinflussen. Im Hinblick auf die Modellierung *weicher* biologischer Gewebe werden zunächst die mechanischen Eigenschaften eines anisotropen nichtlinear elastischen Kontinuums unter Eigenspannungen untersucht. Desweiteren wird eine gradienten-erweiterte Schädigungsformulierung für das kontinuierliche Versagen von Kollagenfasern entwickelt und ein Modell für die Anisotropie-Entwicklung unter mechanischer Belastung präsentiert. Im Hinblick auf Adaptionsvorgänge in *harten* biologischen Geweben, wie zum Beispiel Knochen, wird ein Energie-getriebenes anisotropes Wachstumsmodell vorgeschlagen. Die konstitutiven Modelle werden mit Hilfe homogener Deformationsfälle validiert und ihre Leistungsfähigkeit durch eine Reihe verschiedener Finite-Elemente-Simulationen hervorgehoben.

Abstract

This thesis deals with the constitutive modelling of adaptation and degradation processes for the simulation of the material behaviour of anisotropic biological tissues. The modelling is based on the framework of finite deformation continuum mechanics. The constitutive models proposed are motivated by elastic and inelastic physical mechanisms originating from the micro-mechanical structure of the material. With regard to the modelling of *soft* biological tissues, e.g. arteries, the range of topics covers the investigation of energetic properties of an anisotropic residually stressed non-linear elastic continuum, a gradient-enhanced continuum damage model for the progressive failure of collagen fibres and a remodelling formulation for the deformation-driven evolution of anisotropy. With regard to adaptation processes in *hard* biological tissues, e.g. bone, a growth model for the energy-driven evolution of density is proposed. The constitutive models are discussed with respect to their numerical implementation. The modelling capabilities of the constitutive formulations are validated by homogeneous deformation cases and illustratively underlined by a variety of different finite element simulations.

Publications

The following peer-reviewed journal articles were published or submitted during the progress of this thesis and essentially contribute to this thesis. The original articles are partially modified wherever it is considered meaningful, for instance, to indicate interconnections, to specify details and avoid unnecessary repetitions. The articles listed below are ordered according to their appearance in the thesis.

Chapter 2: [282] Waffenschmidt, T., Menzel, A., 2014. *Extremal states of energy of a double-layered thick-walled tube – application to residually stressed arteries*. Journal of the Mechanical Behavior of Biomedical Materials 29, 635–654.

Chapter 3: [284] Waffenschmidt, T., Polindara, C., Menzel, A., Blanco, S., 2014. *A gradient-enhanced large-deformation continuum damage model for fibre-reinforced materials*. Computer Methods in Applied Mechanics and Engineering 268, 801–842.

Chapter 4: [208] Menzel, A., Waffenschmidt, T., 2009. *A microsphere-based remodelling formulation for anisotropic biological tissues*. Philosophical Transactions of the Royal Society A 367, 3499–3523.

[210] Menzel, A., Waffenschmidt, T., Alastrué, V., 2010. *An anisotropic micro-sphere approach applied to the modelling of soft biological tissues*, in: Kreiss, G., Lötstedt, P., Målqvist, A., Neytcheva, M. (Eds.), Numerical Mathematics and Advanced Applications, Springer. pp. 637–644.

Chapter 5: [283] Waffenschmidt, T., Menzel, A., Kuhl, E., 2012. *Anisotropic density growth of bone – a computational micro-sphere approach*. International Journal of Solids and Structures 49, 1928–1946.

[281] Waffenschmidt, T., Menzel, A., 2012. *Application of an anisotropic growth and remodelling formulation to computational structural design*. Mechanics Research Communications 42, 77–86.

The articles were prepared in collaboration with one or more co-authors. The author of this thesis contributed essential aspects with regard to the outline of the theory ([282], [284], [210], [283], [281]), carried out the numerical implementation and simulations completely ([282], [208], [210], [283], [281]) and partially ([284]), and contributed essential parts to the preparation of all of the papers listed above.

Contents

| | |
|--|-----------|
| Notation | xi |
| 1 Introduction | 1 |
| 1.1 Motivation and state of the art | 1 |
| 1.1.1 Mechanical properties of soft biological tissues | 1 |
| 1.1.2 Damage effects in soft biological tissues | 4 |
| 1.1.3 Remodelling effects in soft biological tissues | 7 |
| 1.1.4 Growth effects in hard biological tissues | 13 |
| 1.2 Scope and outline | 17 |
| 2 Extremal states of energy of a double-layered thick-walled tube | 21 |
| 2.1 Finite anisotropic hyperelasticity | 22 |
| 2.1.1 Basic kinematics | 22 |
| 2.1.2 Decoupled volumetric-isochoric stress response | 23 |
| 2.2 Basic equations of a thick-walled tube | 24 |
| 2.2.1 Kinematics | 24 |
| 2.2.2 Residual stresses | 27 |
| 2.2.3 Total potential energy | 28 |
| 2.2.4 Euler-Lagrange equations | 30 |
| 2.3 Analysis of a double-layered thick-walled tube | 32 |
| 2.3.1 Constitutive model | 33 |
| 2.3.2 Material, structural and geometrical parameters | 35 |
| 2.3.3 Loading parameters | 36 |
| 2.3.4 Algorithmic treatment | 37 |
| 2.3.5 Results | 38 |
| 3 A gradient-enhanced continuum model for the simulation of damage | 61 |
| 3.1 Gradient enhancement of a continuum damage formulation | 63 |
| 3.1.1 General gradient-enhanced format of the free energy function | 63 |
| 3.1.2 Total potential energy | 64 |
| 3.1.3 Variational form | 65 |
| 3.1.4 Strong form – Euler-Lagrange equations | 66 |
| 3.2 Constitutive relations | 67 |
| 3.2.1 Hyperelastic part of the free energy function | 67 |

| | | |
|----------|--|------------|
| 3.2.2 | Gradient-enhanced part of the free energy function | 69 |
| 3.2.3 | Gradient-enhanced damage model – continuous formulation | 71 |
| 3.2.4 | Gradient-enhanced damage model – algorithmic setting | 74 |
| 3.3 | Finite element discretisation | 78 |
| 3.3.1 | Discretisation | 78 |
| 3.3.2 | Linearisation | 81 |
| 3.3.3 | Local tangent moduli | 83 |
| 3.4 | Numerical examples | 85 |
| 3.4.1 | Test 1 – homogeneous uniaxial tension | 85 |
| 3.4.2 | Test 2 – isotropic plate with a hole | 88 |
| 3.4.3 | Test 3 – anisotropic plate with a hole | 93 |
| 3.4.4 | Anisotropic artery-like tube | 96 |
| 4 | A microsphere model for the simulation of remodelling effects | 105 |
| 4.1 | Basic micro-kinematics and balance equations | 106 |
| 4.2 | Non-affine hyperelastic microsphere model | 106 |
| 4.3 | Microsphere-based remodelling formulations | 109 |
| 4.3.1 | Remodelling for transversely isotropic material behaviour | 110 |
| 4.3.2 | Remodelling for orthotropic material behaviour | 113 |
| 4.4 | Implementation | 116 |
| 4.5 | Numerical examples | 116 |
| 4.5.1 | Specification of the strain energy | 116 |
| 4.5.2 | Transversely isotropic remodelling | 121 |
| 4.5.3 | Orthotropic remodelling | 127 |
| 5 | A microsphere model for the simulation of growth effects | 141 |
| 5.1 | Basic micro-kinematics and balance equations | 142 |
| 5.2 | One-dimensional growth | 142 |
| 5.2.1 | Constitutive equations | 143 |
| 5.2.2 | Implementation | 143 |
| 5.2.3 | Numerical example | 147 |
| 5.3 | Anisotropic growth – a microsphere approach | 150 |
| 5.3.1 | Extension to a three-dimensional formulation | 150 |
| 5.3.2 | Implementation | 151 |
| 5.3.3 | Numerical example | 153 |
| 5.4 | Numerical example – application to bones | 156 |
| 5.4.1 | Subject-specific problem – proximal tibia | 156 |
| 5.4.2 | Three-dimensional density prediction | 164 |
| 5.4.3 | Potential limitations | 166 |
| 5.5 | Numerical example – application to computational structural design | 167 |
| 5.5.1 | Cantilever | 168 |
| 5.5.2 | Crank | 170 |

| | | |
|----------|--|------------|
| 5.5.3 | Stool | 172 |
| 5.5.4 | Coathanger | 172 |
| 5.5.5 | Evolution of anisotropy | 175 |
| 6 | Concluding remarks | 177 |
| A | Thin-walled cylindrical tube – membrane approximation | 183 |
| B | Comparison of continuum and microsphere-based neo-Hooke models | 187 |
| B.1 | Decoupled continuum neo-Hooke model | 187 |
| B.2 | Decoupled microsphere-model | 188 |
| B.2.1 | Volumetric contribution | 189 |
| B.2.2 | Isochoric neo-Hooke-type contribution | 189 |
| B.3 | Closed form expressions of surface integrals | 194 |
| C | Visualisation of anisotropy | 195 |
| C.1 | Stereographic pole projection | 195 |
| C.2 | Orientation distribution functions related to higher-order moments | 195 |
| D | Implementation of element-formulations via Abaqus subroutine UEL | 199 |
| D.1 | Vector-matrix-format based on Voigt notation | 199 |
| D.2 | UEL-implementation in Abaqus | 202 |
| D.3 | UEL-interface in Abaqus | 203 |
| D.4 | Approximation of Jacobians on element-level | 204 |
| D.5 | Postprocessing for the UEL-subroutine in Abaqus | 206 |
| E | Implementation of constitutive models via Abaqus subroutine UMAT | 209 |
| E.1 | Consistent tangent moduli based on Jaumann stress rates | 209 |
| E.2 | UMAT-implementation in Abaqus | 210 |
| E.3 | UMAT-interface in Abaqus | 211 |
| E.4 | Approximation of consistent tangent moduli | 211 |
| F | Arc-length methods | 213 |
| F.1 | Basic equations | 213 |
| F.2 | Application within general user-elements via Abaqus subroutine UEL | 216 |
| G | Deformation-dependent loads | 219 |
| G.1 | Variational form | 219 |
| G.2 | Discretisation | 220 |
| G.3 | Linearisation | 220 |
| G.4 | Implementation via Abaqus subroutine UEL | 221 |
| | Bibliography | 223 |

Notation

Even though the notation used in this thesis becomes obvious from its context, we briefly summarise some essential relations below for the sake of the reader's convenience.

Tensors Referring to the three-dimensional Euclidean space represented by the set of Cartesian basis vectors $\{\mathbf{e}_i\}$ with $i = 1, 2, 3$, we express tensors of first, second and fourth order in terms of their coefficients $(\bullet)_i$ according to the summation convention as

$$\begin{aligned}\mathbf{a} &= a_i \mathbf{e}_i, \\ \mathbf{A} &= A_{ij} \mathbf{e}_i \otimes \mathbf{e}_j, \\ \mathbf{A} &= A_{ijkl} \mathbf{e}_i \otimes \mathbf{e}_j \otimes \mathbf{e}_k \otimes \mathbf{e}_l.\end{aligned}$$

We use non-bold italic letters for scalars, bold-face italic letters for vectors as well as second-order tensors and bold-face sans-serif letters for fourth-order tensors.

Inner tensor products Different inner products of tensors are represented by dots where the number of dots characterises the number of contractions, so that

$$\begin{aligned}\mathbf{a} \cdot \mathbf{b} &= a_i b_i, \\ \mathbf{A} \cdot \mathbf{b} &= A_{ij} b_j \mathbf{e}_i, \\ \mathbf{A} \cdot \mathbf{B} &= A_{ij} B_{jk} \mathbf{e}_i \otimes \mathbf{e}_k, \\ \mathbf{A} : \mathbf{B} &= A_{ij} B_{ij}, \\ \mathbf{A} : \mathbf{B} &= A_{ijkl} B_{kl} \mathbf{e}_i \otimes \mathbf{e}_j.\end{aligned}$$

The special case of an n -fold contraction of two n th-order tensors results in a scalar.

Outer tensor products Different outer or rather dyadic product of tensors, represented by the classic symbol \otimes as well as the non-standard symbols $\overline{\otimes}$ and $\underline{\otimes}$, are defined by

$$\begin{aligned}\mathbf{a} \otimes \mathbf{b} &= a_i b_j \mathbf{e}_i \otimes \mathbf{e}_j, \\ \mathbf{A} \otimes \mathbf{B} &= A_{ij} B_{kl} \mathbf{e}_i \otimes \mathbf{e}_j \otimes \mathbf{e}_k \otimes \mathbf{e}_l, \\ \mathbf{A} \overline{\otimes} \mathbf{B} &= A_{ik} B_{jl} \mathbf{e}_i \otimes \mathbf{e}_j \otimes \mathbf{e}_k \otimes \mathbf{e}_l, \\ \mathbf{A} \underline{\otimes} \mathbf{B} &= A_{il} B_{jk} \mathbf{e}_i \otimes \mathbf{e}_j \otimes \mathbf{e}_k \otimes \mathbf{e}_l.\end{aligned}$$

The dyadic product of two vectors results in a second-order tensor, whereas the standard and non-standard dyadic products of two second-order tensors result in fourth-order tensors.

Identity tensors The second-order identity tensor \mathbf{I} as well as the symmetric, volumetric and deviatoric fourth-order identity tensors \mathbf{l}_{sym} , \mathbf{l}_{vol} and \mathbf{l}_{dev} , respectively, are defined in terms of the Kronecker delta symbol $\delta_{ij} = \mathbf{e}_i \cdot \mathbf{e}_j$ as

$$\begin{aligned}\mathbf{I} &= \delta_{ij} \mathbf{e}_i \otimes \mathbf{e}_j, \\ \mathbf{l}_{\text{sym}} &= \frac{1}{2} [\mathbf{I} \overline{\otimes} \mathbf{I} + \mathbf{I} \underline{\otimes} \mathbf{I}], \\ \mathbf{l}_{\text{vol}} &= \frac{1}{3} \mathbf{I} \otimes \mathbf{I}, \\ \mathbf{l}_{\text{dev}} &= \mathbf{l}_{\text{sym}} - \mathbf{l}_{\text{vol}},\end{aligned}$$

where $\delta_{ij} = 1$ for $i = j$ and $\delta_{ij} = 0$ for $i \neq j$.

Operators The partial derivative of a (tensorial) quantity (\bullet) with respect to some (tensorial) quantity (\circ) is defined as $\partial_{(\circ)}(\bullet) := \partial(\bullet)/\partial(\circ)$. Accordingly, the total differential can be expressed as $d_{(\circ)}(\bullet) = \partial_{(\circ)}(\bullet) d(\circ)$ and the variation equally reads $\delta_{(\circ)}(\bullet) = \partial_{(\circ)}(\bullet) \delta(\circ)$. The (spatial) gradient of a vector field $\mathbf{a}(\mathbf{x})$ is represented in terms of the Nabla operator ∇ as

$$\nabla_{\mathbf{x}} \mathbf{a} = \frac{\partial a_i}{\partial x_j} \mathbf{e}_i \otimes \mathbf{e}_j$$

with respect to the spatial position vector \mathbf{x} defined in Euclidian space. The divergence of a vector field $\mathbf{a}(\mathbf{x})$ and a tensor field $\mathbf{A}(\mathbf{x})$ are both represented as

$$\nabla_{\mathbf{x}} \cdot \mathbf{a} = \frac{\partial a_i}{\partial x_i} \quad \text{and} \quad \nabla_{\mathbf{x}} \cdot \mathbf{A} = \frac{\partial A_{ij}}{\partial x_j} \mathbf{e}_i,$$

and enable the Laplace operator to be introduced as $\Delta_{\mathbf{x}}(\bullet) = \nabla_{\mathbf{x}} \cdot [\nabla_{\mathbf{x}}(\bullet)]$. Finally, the cofactor is defined as

$$\text{cof}(\mathbf{A}) = \partial_{\mathbf{A}} \det(\mathbf{A}) = \det(\mathbf{A}) \mathbf{A}^{-\text{t}}$$

with the abbreviation $\mathbf{A}^{-\text{t}} = [\mathbf{A}^{-1}]^{\text{t}}$ where \mathbf{A}^{t} and \mathbf{A}^{-1} represent the transpose and the inverse of the second-order tensor \mathbf{A} , respectively.

1 Introduction

1.1 Motivation and state of the art

The goal of this thesis is the constitutive modelling of adaptation and degradation processes for the simulation of the material behaviour of anisotropic soft and hard biological tissues. The modelling is based on the framework of finite deformation continuum mechanics. The constitutive models proposed are motivated by (in)elastic physical mechanisms originating from the micro-mechanical structure of the material. With regard to the modelling of *soft* biological tissues, e.g. arteries, the range of topics covers the investigation of energetic properties of an anisotropic residually stressed non-linear elastic continuum, a gradient-enhanced continuum damage model for the progressive failure of collagen fibres and a remodelling formulation for the deformation-driven evolution of anisotropy. With regard to the modelling of *hard* biological tissues, e.g. bone, a growth model for the energy-driven evolution of density is established. The constitutive models are discussed with respect to their numerical implementation. The modelling capabilities of the constitutive formulations are validated by homogeneous deformation cases and illustratively underlined by a variety of different finite element simulations.

1.1.1 Mechanical properties of soft biological tissues

The investigation of the mechanical behaviour of soft biological tissues has gained much attention during the last decades; see e.g. Humphrey [144] for a general overview. Various biological tissues and structures are designed to optimally support external loading often resulting in complex microstructures of these materials. The design of, for instance, blood vessels is characterised by a residually stressed fibre-reinforced layer-wise orthotropic composite with highly nonlinear elastic response. The particular structure of blood vessels is typically governed by their different circulatory tasks to accommodate functional demands and stresses and may significantly vary by location. Generally, we distinguish *arteries*, associated with high pressures, and *veins*, associated with low pressures. Even though both types of blood vessel consist of three main layers, arteries generally have smaller lumina and thicker walls than veins. The artery's three layers

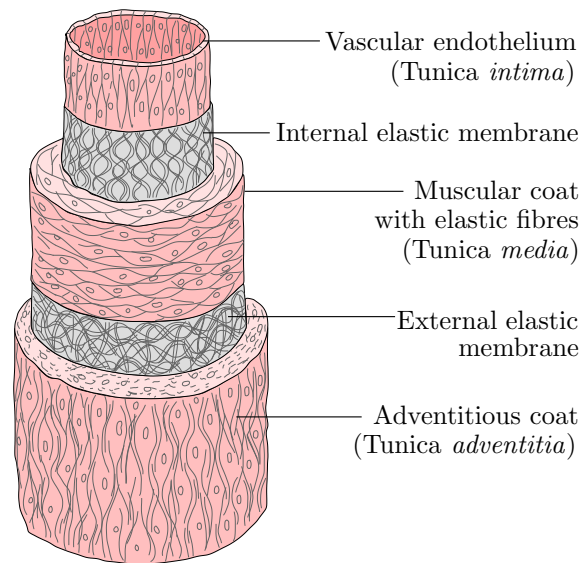


Figure 1.1: Structure of a healthy arterial wall consisting of three main layers, i.e. intima, media and adventitia. Modified from Faller et al. [95].

are better defined and the dominant middle muscular layer is more pronounced. A schematic sketch of an artery is provided in Figure 1.1; see Faller et al. [95] for a more detailed characterisation of arteries. The innermost layer, i.e. the so-called *intima*, consists of a single layer of longitudinally arranged flat endothelial cells applied to a thin connective tissue layer. The intima allows an exchange of substances, fluids and gases and is directly subjected to the shear force of blood flow through the vessel. For healthy arteries the intima, however, is very thin and its contribution to the solid mechanical properties of the arterial wall is negligible. The middle layer, i.e. the so-called *media*, contains nearly concentric flat spirals of smooth muscle cells and interwoven elastic tissue fibres which are almost circumferentially oriented. This structure gives the media great strength and resistibility in circumferential and longitudinal direction. From the mechanical point of view, the media is the most significant layer in a healthy artery. Dilating and constricting the diameter of the artery ensures a continuous blood flow and counteracts the expansion of the vessel wall caused by blood pressure. The outermost layer, i.e. the so-called *adventitia*, embeds the vessel in its surrounding and mainly consists of connective tissue. The interwoven collagen fibers are arranged longitudinally in helical structures reinforcing the wall. They counteract external forces such as longitudinal stretching and significantly contribute to the stability and strength of the arterial wall. At low pressure, the adventitia is much more compliant than the media. However, at higher pressure levels the collagen fibers reach their straightened lengths and prevent the artery from overstretching and rupturing. Moreover, arterial walls have an elastic, fenestrated membrane between intima and media and a second but thinner elastic membrane between media and adventitia. Figure 1.2 shows two representative

micrographs of a thoracic aorta, i.e. the media (a) and the adventitia (b); the figures are taken from the work by Schriefel et al. [255]. The fibres reinforcing the arterial wall, as well as residual stresses present in the blood vessel, strongly influence its overall behaviour and performance. Turn-over and remodelling processes of the collagenous fibres occurring in the respective layers—either resulting from natural growth phenomena or from artificially induced changes in loading condition such as stent deployment—support the optimisation of the multi-layered composite structure of arteries for the particular loading conditions present in the artery. As a result of the complex interaction between residual stresses and nonlinear anisotropic material properties, arteries may optimally sustain different blood pressure or blood flow within the vessel. In addition to reducing or rather homogenising the distributions of the respective stress components, the optimal design of the artery reduces the change in its axial direction under the action of blood flow to a minimum.

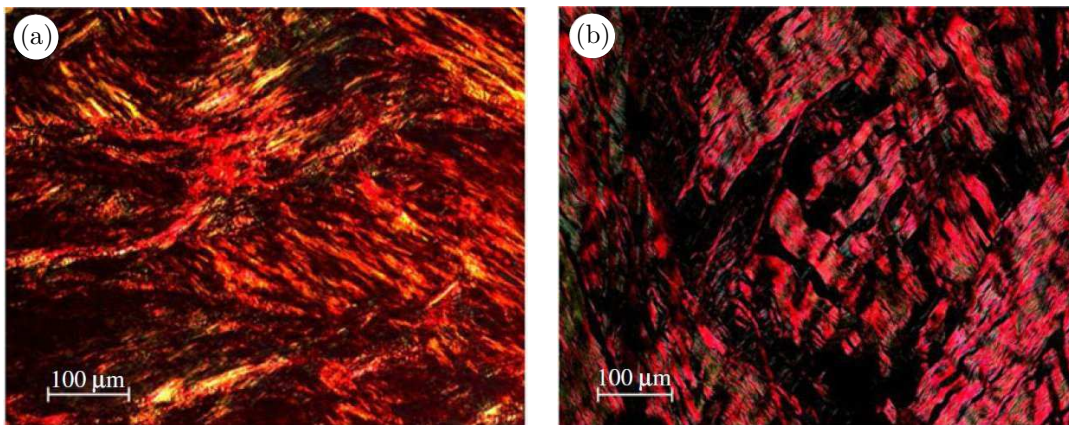


Figure 1.2: Polarised light micrographs of the media (a) and the adventitia (b) of a thoracic aorta wall. The images show two distinct collagen fibre families oriented in the θ - z -plane of the arterial wall. Reprinted from Schriefel et al. [255], with kind permission from Royal Society Publishing.

Several advanced constitutive models for the simulation of the mechanical response of arteries have been proposed in the literature and have successfully been applied to realistic patient-specific case studies; see, for instance, the works by Rissland et al. [251], Holzapfel and Ogden [138], Balzani et al. [23] and Creane et al. [77].

In order to test basic capabilities of the respective constitutive models with respect to the simulation of arteries, it is common to analyse an idealised test case, i.e. the combined inflation, bending, and axial extension of a thick-walled cylindrical tube; see the article by Holzapfel et al. [135]. The bending and extension modes are typically related to residual stress states within the arterial wall—which may change in time due to, for instance, ageing effects as discussed in Cardamone et al. [57]— whereas the inflation refers to loading induced by blood pressure. Alternative approaches for the inclusion of residual stress states in arteries are discussed in, for instance, Olsson et al. [228] and Hoger [131].

The problem in connection with the inflation of a tube is commonly studied by means of hyperelastic forms together with the underlying equilibrium conditions, respectively the Euler-Lagrange equations; see, for instance, Gent and Rivlin [108], the monographs by Green and Adkins [113] as well as Ogden [225], and the series of papers by Haughton and Ogden [124, 126, 127]. This allows the investigation of the distribution of stresses under particular loading levels, fibre angles and residual stress states within the multi-layered thick-walled tube; see the contributions by Pipkin and Rivlin [239] and Spencer et al. [266], wherein inextensibility of the fibres is assumed. From the mechanical point of view, the fibres reinforce the arterial wall whereas the residual stresses decrease, e.g., the circumferential stresses within the wall. However, it generally remains unclear which stimulus yields a particular fibre orientation or realignment under changing loading conditions.

Moreover, we shall generally account for the interaction of the fibre reorientation with the states of residual stresses; see the work by Alford et al. [14], wherein the response of an artery in the context of varying properties of the underlying constituents has been investigated. Different modelling concepts have been suggested in the literature to simulate the alignment of fibres, commonly denoted as turnover or remodelling. Particular remodelling formulations are proposed by, for instance, Driessen et al. [89], where a kinematics-based fibre alignment was suggested, or Humphrey and Rajagopal [145], wherein a mixture-theory-based remodelling approach was established. Coaxial states of stresses and strains render the strain energy to take an extremal state, see Sgarra and Vianello [258], which has motivated alternative remodelling formulations for biological tissues with one fibre family, see e.g. Menzel [197], and two families of fibres, see Menzel [199]. For an overview on different growth and remodelling approaches the reader is referred to the articles by Ambrosi et al. [16] and Menzel and Kuhl [202] and the introductory Sections 1.1.3 and 1.1.4.

1.1.2 Damage effects in soft biological tissues

The understanding and physical description of damage and failure effects in materials presents a major challenge in various engineering-related disciplines. Failure processes in ductile steels, for instance, are characterised by a complex interaction of plastic deformation and damage effects. These phenomena originate from the motion and accumulation of dislocations which interact and result in micro-cracks and micro-voids and finally lead to a necking-like reduction of effective area and possibly to ultimate failure of the material. Damage processes in concrete are typically initiated at the interface between stiff grains and the ambient cement matrix, result in a coalescence and propagation of micro-cracks and finally lead to a global stiffness loss accompanied by localised degradation patterns. To give a particular example with regard to the present work, damage processes in anisotropic soft biological tissues are closely related to the progressive failure of fibres embedded in the ambient bulk or matrix material. An exemplary qualitative simulation result based on the constitutive model subsequently proposed in this con-

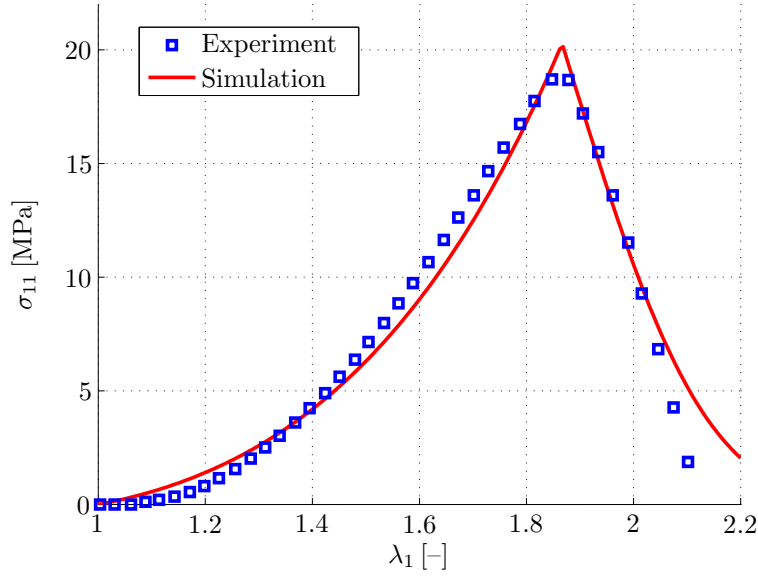


Figure 1.3: Qualitative simulation based on the constitutive model proposed in Section 3.2 and experimental stress-stretch data of a fascia tissue specimen under uniaxial isochoric tension, cf. Martins et al. [196]. Material parameters are chosen as $\mu_e = 0.01$ [kPa], $\kappa_e = 499.0$ [kPa], $k_1 = 0.55$ [kPa], $k_2 = 0.01$, $\kappa_d = 3.5$ [kPa], $\eta_d = 0.6$ [kPa $^{-1}$].

tribution, together with experimental stress-stretch data from Martins et al. [196], is provided in Figure 1.3. The results refer to the mechanical response of a fascia tissue specimen under uniaxial isochoric tension. Arteries, for instance, can be considered as a composite of an isotropic ground substance of elastin fibres and a highly anisotropic network of cross-linked collagen fibrils. Mechanical loading beyond the physiological loading range, e.g. caused by a surgical intervention such as balloon angioplasty, can significantly reduce the elastic properties of the artery. Physically related to Mullins-type effects, these phenomena can be attributed to the continuous degradation of particular collagen fibres and to the corresponding overstretch of neighbouring cross-links leading to pronounced softening.

Based on the classic work by Kachanov [153] who interpreted the damage effect as a consequence of an area reduction of the stress-bearing region, material degradation can be modelled by means of standard continuum damage formulations, i.e. in a local sense. Up to now, a large variety of models exist where we refer the reader to classic monographs and textbooks as, e.g., Kachanov [153], Kachanov [154], Krajcinovic and Lemaitre [162], Lemaitre and Chaboche [182], Lemaitre [181] or Krajcinovic [161], to name only a few. However, the assumption of a purely *local* continuum damage may, as a major drawback, imply a loss of well-posedness, such as loss of ellipticity, of the underlying boundary value problem. With regard to related numerical methods such as the finite element method, this results in a significant mesh-dependence of the solutions,

in other words in a vanishing localised damage zone upon mesh refinement, and hence physically meaningless—or at least questionable—simulations.

In order to regularise the problem, and thereby to circumvent the aforementioned deficiencies, several approaches have been proposed in the literature as, for instance, viscous regularisation, or the concept of generalised *nonlocal* continua such as micro-morphic continua, see the monograph on nonlocal continuum field theories by Eringen [94], the articles by Aifantis [7, 8] or the contributions in Eringen [93] and Rogula [253]. Here, intrinsic or rather internal length scales are introduced into the continuum formulation. A nonlocal continuum formulation can generally be established by either introducing an integral- or a gradient-type equation.

Nonlocal *integral* models are inherently associated with a global averaging procedure which complicates the linearisation of the equations and from the computational point of view, are far more expensive than related gradient-type models. With regard to continuum damage formulations, nonlocal integral models are advocated by Pijaudier-Cabot and Bažant [238] and Bažant [27] and extensively studied by Jirásek [150] or Bažant and Ožbolt [33] and Bažant and Di Luzio [28], the latter referring to microplane models.

As a convenient alternative, Lasry and Belytschko [178], Mühlhaus and Aifantis [212] and Polizzotto et al. [241] suggested nonlocal *gradient* models. Here, the non-locality is incorporated by means of an additional gradient-based Euler-Lagrange equation, to be fulfilled in a weak sense, accompanied by a nonlocal quantity taking the interpretation of an additional independent variable. Nonlocal gradient-based continuum damage formulations were first discussed in de Vree et al. [280], Peerlings et al. [235] and de Borst and Pamin [48]; see also the comparison by Pamin [231] or the coupled damage-plasticity approach by Svedberg and Runesson [271].

A large variety of gradient-extended damage formulations exists for the geometrical *linear* case, see e.g. the contributions by Kuhl and Ramm [167], Kuhl et al. [169] for anisotropic gradient damage, the article by Liebe et al. [186] or the work by Dimitrijević and Hackl [85] for isotropic gradient damage. However, there is a comparatively small number of contributions for the geometrical *non-linear* case. The article by Steinmann [269] can be considered as a starting point wherein the nonlocal strain energy density is introduced as an additional primary variable. This approach was used in Liebe and Steinmann [185], and similarly with application to softening-plasticity in Liebe et al. [184], and compared to an alternative model which takes the damage field as an independent variable. Both approaches used a global active-set-search to account for the Kuhn-Tucker conditions. Recently, Weisło et al. [289] proposed a gradient-enhanced large-strain damage-plasticity model where gradient averaging is applied to the deformation measure which determines the damage evolution. Following the concept by Frémond and Nedjar [101], the article by Nedjar [222] considered a damage-related formalism based on the principle of virtual power where the power of the internal forces depends, in addition to the strain rates, on the damage rate itself as well as on the gradient of the damage rate. The series of papers by Abu Al-Rub and Voyiadjis [6] and

Voyiadjis and Abu Al-Rub [279], proposed a nonlocal gradient-enhanced plastic-damage model coupled to visco-inelasticity where ‘explicit and implicit microstructural length scales’ are introduced by means of viscosity and gradient localisation limiters.

As mentioned above, damage processes in biomaterials such as arteries are of major significance with regard to surgical treatments. In recent years, the mechanics of damage and failure in soft biological tissue have extensively been studied from the experimental and modelling point of view. A multitude of damage and failure formulations has been published, such as the article by Calvo et al. [55], the contribution by Volokh [278], or the recent publication by Balzani et al. [22], amongst others. However, to the author’s knowledge, almost all of these works consider damage as a purely local phenomenon without robust regularisation techniques involved, which, in view of finite element applications, may result in highly mesh-dependent and physically questionable simulations. A visco-type regularisation-approach is adopted in, e.g., Peña et al. [236]. So far, a fully nonlocal gradient-extended damage formulation allowing for large deformations with special regard to biological tissues has not yet been established for anisotropic biological tissues.

1.1.3 Remodelling effects in soft biological tissues

Adaptation is a key biomechanical phenomenon occurring in hard as well as in soft biological tissues. Modelling and simulation of such growth and remodelling processes constitutes an active and continuously increasing field of research; for an overview the reader is referred to the monographs by Fung [102] and Humphrey and Rajagopal [145] as well as to the contributions in Holzapfel and Ogden [136], the survey by Taber [272], the contribution by Cowin [72] and the review article by Ambrosi et al. [16]. Various biological and chemical effects determine the macroscopic behaviour of the particular biological tissue of interest. In general, biological tissues exhibit changes in mass, denoted as growth, and internal structure, referred to as remodelling.

Fibrous soft biological tissues—for example ligaments, tendons, muscles, and skin—possess a pronounced composite-type multiscale structure together with strongly direction-dependent or rather anisotropic mechanical properties; see, for instance, Silver et al. [260]. The local mechanical response of these material structures is typically determined by elastin and collagen fibres, or cable-like bundles thereof. Placing special emphasis on the latter, collagen molecules are secreted by so-called fibroblasts which arrange themselves as polymeric collagen fibrils. Based on these, cable-like collagen fibres are formed which turn out to be aligned with respect to the fibroblasts; see Alberts et al. [13] for detailed background information. Influenced by genetic information as well as by local mechanical loading conditions, remodelling and self-assembly of these oriented fibre networks occur—the related processes often being denoted as fibre reorientation or, rather, turnover. Several experimental investigations on these remodelling effects are reported in the literature, even though the underlying mechanisms, based on which the respective cells sense the various mechanical and biochemical stimuli, still remain

fairly unknown. An overview on the adaptation of different types of biological tissue is provided in the survey by Wang and Thampatty [287]. To give two particular examples, adaptation of tendon-related tissue is discussed by Calve et al. [54], whereas Breen [52] studies tissue remodelling of the lung.

Several continuum modelling approaches to describe the anisotropic material properties of soft biological tissues have been suggested in the literature; see, for instance, Almeida and Spilker [15], the contributions in Cowin and Humphrey [75], the popular model by Holzapfel et al. [135] and Menzel and Steinmann [204] for a comparison of two different modelling approaches. While phenomenological formulations used to consider individual fibre families to be perfectly aligned with pre-defined directions, recent investigations additionally account for the dispersion of fibres; see Gasser et al. [107] for a formulation based on generalised structural tensors, and Marquez [194] in view of experimental investigations to identify the orientation of fibre distributions. Alastrué et al. [9] proposed an anisotropic microsphere model applied to the simulation of blood vessels. The computational modelling based on such a multiscale-type unit-sphere ansatz dates back to the introduction of so-called ‘microplane models’ as embedded into small strain kinematics, see the early contribution by Bažant and Oh [31]. To give a short background on the history of microsphere models, we subsequently give a brief outline of the progress of microsphere-based and related models proposed basically during the last three decades.

Background – from microplane to microsphere models The term ‘microsphere model’ was first introduced almost one decade ago in the paper by Miehe et al. [218] and dealt with a non-affine constitutive model for rubber-like materials at large strains. The basic idea of the microsphere model which considers the surface of the microsphere as a *continuous distribution of* (polymer chain) *orientations* in space, is clearly characteristic but exhibits several conceptual and numerical similarities to the related class of ‘microplane models’ which had already been established at that time. A detailed overview of the historical background, different mathematical formulations and related references on microplane models can be found, for instance, in the textbook by Jirásek and Bažant [151], the collection edited by Stein et al. [267] or the article by Carol et al. [60] which provides a review of small strain as well as a first extension to large strain microplane formulations.

Motivated by the *slip theory of plasticity* established in the classic works by Taylor [273], Batdorf and Budiansky [24] and others, one of the first microplane models—if not *the* first—was proposed by Bažant and Oh [30] even if the term ‘microplane’ itself was introduced a little later by the same authors (Bažant and Oh [29]). The guiding idea, common in all of these contributions, is to “define the inelastic behaviour independently on planes of different orientation within the material, and then in some way superimposing the inelastic effects from all planes”, cf. Bažant and Oh [29]. This superposition of responses on all microplanes is performed in an integral mean, which, algorithmi-

cally, reduces to a *numerical integration scheme over the unit-sphere*, since closed-form solutions to the averaging integrals over the sphere are generally not available.

While the slip theory of plasticity is based on a *static constraint*, i.e. assuming the stress traction on each (slip) plane to be associated with the projection of the macroscopic stress tensor, Bažant and Oh [29] proposed a *kinematic (micro-macro) constraint* assuming the *normal* and *tangential* strain on each microplane to correspond to the projection of the macroscopic strain tensor. This proves to be more appropriate to characterise the softening behaviour of quasi-brittle materials, as, for instance, concrete and rock, to which most of the first microplane models were referred to. As this *normal-tangential* strain-split turns out to be inadequate to cover the whole range of Poisson's ratio, a *volumetric-deviatoric-tangential* split was subsequently proposed by Bažant and Prat [34, 35], see also the article by Kuhl and Ramm [168]. This split, however, disables a unique determination of the elastic constants which motivated Leukart and Ramm [183] to suggest the *volumetric-deviatoric* split, thereby eliminating the deficits related to the aforementioned strain-splits.

Furthermore, the *static micro-macro relations* or rather *constraints* between microstresses on each microplane and the macroscopic stress tensor need to be specified such that the kinematic micro-macro constraints and the fundamental constitutive laws at the microplane level are satisfied simultaneously. In classic microplane formulations these relations are intuitively deduced by means of the *principle of virtual work* relating the microplane and the macroscopic level. However, in doing so, the requirement of *thermodynamic consistency* cannot be ensured. For a long time this was an unsolved issue until the first thermodynamic consistent microplane model was proposed by Carol et al. [59] and extended to inelastic problems by Kuhl et al. [174]. They assumed a *free energy potential for each microplane* which—integrated over the sphere—resulted in the macroscopic free energy. According to Carol et al. [60], “this concept, combined with the kinematic constraint, provides a thermodynamically consistent procedure to define conjugate microplane stresses, and to develop the correct integral static relations needed.”

The microplane approach proves to be extremely versatile and flexible to naturally include inelastic and load-induced anisotropic behaviour, due to the fact that each microplane in the system is exposed to a characteristic loading history and thus may exhibit a different mechanical response. During the years, it was applied to the modelling of quasi-brittle materials such as concrete (Bažant et al. [36, 37]), to the incorporation of inelasticity in the form of damage or plasticity (Carol and Bažant [58], Kuhl et al. [170, 174]) or to the modelling of shape memory alloys (Brocca et al. [53], Kadkhodaei et al. [155, 156]), to name only a few typical examples amongst many others.

However, all of the aforementioned microplane formulations are restricted to small strains. The first thermodynamically consistent microplane formulation accounting for *large strains* was published by Carol et al. [60] who investigated several microplane models of neo-Hookean and Mooney-Rivlin-type with regard to their hyperelastic continuum counterparts; see Appendix B for a related detailed discussion. Subsequently, an ap-

plication to fibrous blood vessel tissue was provided by Caner and Carol [56]. In this regard, the physical justification of the microplanes to be considered as a finite number of characteristic slip planes is slightly misleading and may be reinterpreted, for instance, as a finite number of representative polymer chains or collagen fibres associated with the integration points defined on the sphere.

Almost at the same time, Miehe et al. [218] proposed the so-called *non-affine microsphere model of rubber elasticity*, which was extended to rubber viscoelasticity (Miehe and Göktepe [217]) and anisotropic Mullins-type damage (Göktepe and Miehe [111]). The non-affine microsphere model of rubber elasticity is a micromechanically motivated network model for rubber-like materials at large strains. Interpreting the surface of the microsphere as a continuous distribution of chain orientations in space, the model combines two new essential features. First, the micro-mechanical response of a *single polymer chain is assumed to be governed by a constrained environment defined by two micro-kinematic variables*: the stretch of the chain and the contraction of a micro-tube containing the chain, thus incorporating polymer cross-links and entanglements. Secondly, a *non-affine micro-to-macro transition* is assumed to link micro and macro line-stretches and area-stretches by means of a fluctuation field on the microsphere where this fluctuation field is determined by a minimisation of the macroscopic free energy.

However, there is some confusion over the classification of criteria being characteristic for microplane and microsphere formulations. The terminology often differs; some authors rely on the classic term ‘microplane’, while others prefer ‘microsphere’ and yet others do not use any of the aforementioned terminology but introduce alternative denominations describing the same or at least closely related approaches as, for instance, proposed in terms of a statistical fibre orientation by Lanir [176, 177] or Federico and Gasser [96]. It becomes obvious that the criterion determining that microplane models are restricted to small strains does not hold since large strain microplane approaches are also used (Caner and Carol [56], Carol et al. [60]). Vice versa, the denomination as microsphere model was also applied to small-strain formulations (Ostwald et al. [229, 230]). Furthermore, both formulations are introduced to rely on *two* kinematic variables, i.e. by means of the *distortional microplane stretch* λ_N in Carol et al. [60] which is equivalent to the affine stretch $\bar{\lambda}$ in Miehe et al. [218], accompanied by the *distortional microplane thickening* $\bar{\lambda}_N$ in Carol et al. [60] which is equivalent to the reciprocal of the affine area stretch $\bar{\nu}$ in Miehe et al. [218]. Finally, common to both formulations is a numerical integration scheme over the sphere, since closed-form solutions to the averaging integrals over the unit-sphere are generally not available.

As a crucial distinction with respect to the non-affine microsphere approach, however, the microplane formulation is restricted to purely *affine* deformations, i.e. “the assumption that the lengths of individual chains are changed in the same proportion as the dimensions of the bulk rubber”, which, in the microplane context, “is equivalent to the kinematic constraint”, cf. Carol et al. [60]. The affinity assumption, however, results in a model response that is not completely in agreement with experimental observations, particularly for large deformations. Consequently, the original microsphere

model as proposed by Miehe et al. [218] is inherently associated with a *non-affine* micro-to-macro transition of the aforementioned micro-kinematic variables to the macroscopic line-stretch and area-stretch. For a more detailed background and a review of affine and non-affine network models, the reader is referred to Miehe et al. [218].

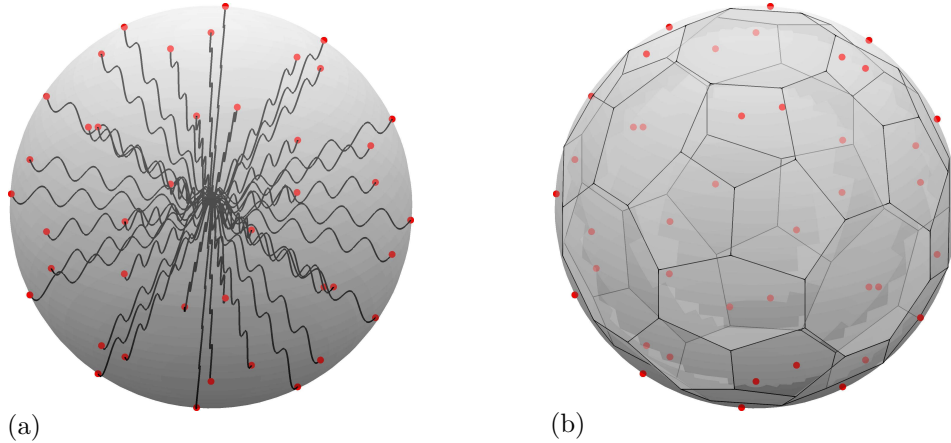


Figure 1.4: Microsphere and microplane concept. Illustration of an orthogonally symmetric cubature scheme with $m = 21$ integration points, represented by the red dots; see Bažant and Oh [32] and Table 4.4. (a) Fiber-like discrete integration directions and (b) plane-like discrete integration areas approximating the surface of the unit-sphere \mathbb{U}^2 .

Therefore, most of the recent so-called microsphere models are in fact microplane models as they are mostly restricted to consider only the *affine* stretch part and to neglect the tube part as well as the non-affine micro-macro transition. Nevertheless, in view of its historical background, the term ‘microplane’ seems to be more closely related to brittle or ductile (slip) plane-like microstructures such as concrete or metals, rather than to fiber-like network microstructures as rubbery polymers or biological tissues. Consequently, the term ‘microsphere’ appears to be more appropriate with regard to a physical sound interpretation of the approach; see Figure 1.4 for a microstructural interpretation of the microsphere/microplane concept. Therefore, the notion ‘microsphere model’ is used throughout this work, even if we continuously neglect the tube-part and restrict ourselves to purely affine deformations at some places.

The microplane and microsphere concept, respectively, contributes to recent extensions and applications in different research fields and disciplines, as for the modelling of polycrystalline ferroelectrics (Kurzhofer [175]), phase transformations in metals (Ostwald et al. [229, 230]), electromechanical modelling of electrostrictive polymers (Thylander et al. [275]), advanced micromechanically motivated network models (Linder et al. [187], Tkachuk and Linder [276]) and magneto-sensitive elastomers. Furthermore, this approach turns out to be attractive for the modelling and simulation of soft and hard biological tissues, as, for instance, published by Menzel et al. [201], Alastrué et al. [9], Alastrué et al. [10], Federico and Gasser [96], Sáez et al. [254] and partially done in the

present work, see Chapters 4 and 5.

Recently, the microsphere model has also been applied to the simulation of elastic but anisotropic and pre-stressed blood vessels; see Alastrué et al. [9], where the integration over the underlying unit-sphere \mathbb{U}^2 was additionally weighted by an orientation distribution function (ODF) ρ with

$$\rho(\mathbf{e}) = \rho(-\mathbf{e}) \quad \forall \mathbf{e} \in \mathbb{U}^2 \quad \text{and} \quad \frac{1}{4\pi} \int_{\mathbb{U}^2} \rho \, dA = 1.$$

To give a brief classification of some generic homogenisation schemes, consider $\langle \bullet \rangle$ to represent an appropriate averaging, respectively homogenisation operator in orientation space that may include directional dependencies by means of ρ . Moreover, let \mathbf{S} denote a suitable stress measure, the computation of which may be based on:

$$(i) \quad \mathbf{S}(\mathbf{C}, \langle \mathbf{e} \otimes \mathbf{e} \rangle) \quad (ii) \quad \mathbf{S} = \langle S_e \mathbf{e} \otimes \mathbf{e} \rangle \quad (iii) \quad \mathbf{S}|_{\text{bvp}}$$

In order to capture the material's anisotropy, a generalised structural tensor $\langle \mathbf{e} \otimes \mathbf{e} \rangle$ can be introduced which, together with the stretch quantity \mathbf{C} , determines the stresses. A remodelling formulation of this approach (i) is proposed in Menzel et al. [201]. In view of further background information on the simulation of deformation-induced anisotropy evolution based on evolving structural tensors, the reader is referred to Menzel and Steinmann [207], Menzel and Steinmann [206] and references cited therein. Alternatively, one may adopt approach (ii), such as the microsphere model, and extend it to the incorporation of remodelling effects. The underlying anisotropy evolution may thereby be directly linked to the numerical integration scheme applied to the unit-sphere. Typical integration schemes are provided in, for instance, Bažant and Oh [32] or Heo and Xu [128], while their respective properties with application to anisotropic elasticity are extensively discussed in Alastrué et al. [9] and particularly in Ehret et al. [91]. Additional modifications of such integration algorithms set to efficiently recapture the materials anisotropy are elaborated in Alastrué et al. [10] with emphasis on uniaxial ODFs. Even though not elaborated in this work, both approaches (i) and (ii) can, in general, be extended to the incorporation of higher-order moments such as $\langle \mathbf{e} \otimes \mathbf{e} \otimes \mathbf{e} \otimes \mathbf{e} \rangle$, etc. Furthermore, the evolution of the ODF—in contrast to the direct local form of evolution equations used here—can alternatively be captured by means of global balance equations; see, for example, Papenfuss [233] or the monograph by Virga [277] with application to liquid crystals. Finally, a so-called FE² strategy could be adopted, wherein the macroscopic constitutive behaviour is determined from the solution of a sub-boundary value problem; see Miehe and Koch [219] or Kouznetsova et al. [160] amongst others.

The continuum modelling of the adaptation of biological tissues is usually either embedded into the framework of open system thermodynamics or based on the theory of mixtures. A survey on open systems is provided in the monograph by Katchalsky and Curran [157], whereas related continuum approaches with particular emphasis on

growth phenomena have been addressed by, for example, Epstein and Maugin [92], Di-Carlo and Quiligotti [83], Lubarda and Hoger [188], Kuhl and Steinmann [171, 172], Garikipati et al. [105], and Guillou and Ogden [114]. In view of mixture-theory-based growth formulations, we refer the reader to the references by Humphrey and Rajagopal [145], Quiligotti [243], and Klisch and Hoger [158]. The majority of articles focus on the remodelling of a single solid phase. Reorientation formulations proposed for the alignment of individual fibre directions are discussed in, e.g., Imatani and Maugin [147], Driessen et al. [89], Menzel [197, 199] or Himpel et al. [130]. Similar approaches have also been applied to the modelling of glassy polymers; see, for instance, Warren [288] or Chen et al. [66], where macroscopic evolution equations were derived from ODFs.

Long-chain molecules within fibrous soft biological tissues can, similarly to rubber, appropriately be modelled within the framework of statistical mechanics; see the monograph by Flory [99] for detailed background information. To be specific, the constitutive behaviour of a single chain may be referred to the so-called worm-like chain model; see Beatty [38] for a review. While the isotropic chain network response can be determined by means of representative unit-cells aligned with the principal stretch directions—a typical example being the eight-chain model advocated by Arruda and Boyce [17]—anisotropic extensions reflecting transversely isotropic or orthotropic response have also been suggested in the literature; see, for example, Kuhl et al. [165] and Bischoff et al. [42].

1.1.4 Growth effects in hard biological tissues

Bone tissue is the main supporting tissue of the human skeleton and, with the exception of dental material, the hardest substance in the human body. It is characterised by a very stable behaviour under both tension and compression and is extraordinarily resistant to mechanical deformation. The structure of cancellous bone is represented by an outer compact layer and an inner trabeculated spongy layer; see the schematic sketch of a femur in Figure 1.5(a). While the compact layer is particularly developed in the shaft, the spongy bone material is especially prominent at the ends of a bone. Due to this ‘lightweight’ construction, bone attains maximum strength with minimal material; see Faller et al. [95] for a more detailed characterisation of bone material. Generally, bones are able to adapt their local density to mechanical loading. This is typically represented by the orientation of their trabecular structure which develops in the form of compression and tension trabeculae under the influence of deformation stresses as illustrated in Figure 1.5(b). Such growth processes result in densification of the bone in regions of high loading levels and in resorption of the material in regions of low loading levels. This evolution and optimisation process generates heterogeneous distributions of bone density accompanied by pronounced anisotropic mechanical properties.

The tibia is the strongest weight bearing and—after the femur—the second largest bone of the human skeleton. Although it plays a critical role in osteoarthritis—the most prevalent joint disorder in the world—the tibia remains much less studied than other

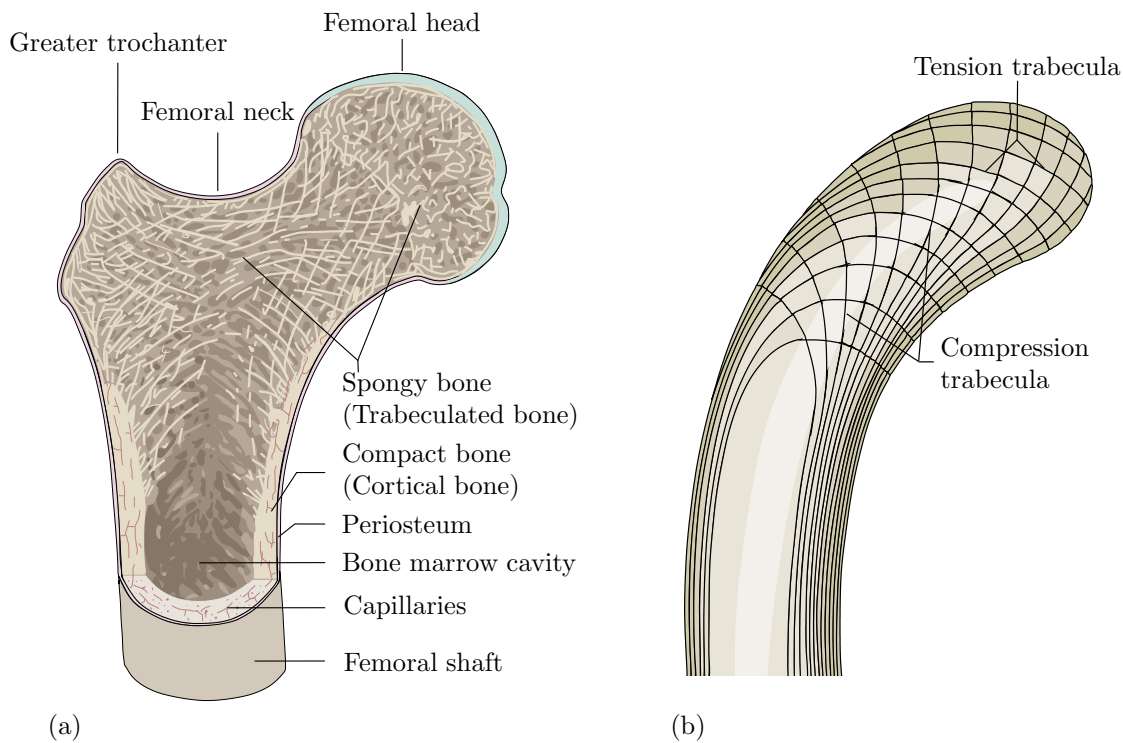


Figure 1.5: Trabecular microstructure of bone tissue, here exemplified by the femur. (a) Outer compact layer and an inner trabeculated spongy layer. (b) Compression and tension trabeculae adapting according to the influence of mechanical stimuli. Modified from Faller et al. [95].

long bones; see, for instance, Hulet et al. [143]. Since the seminal work by Julius Wolff [298], we know that long bones can adapt their local density to mechanical loading. During normal walking, for example, a majority of the generated load is transmitted through the medial side of the knee as reported by Baliunas et al. [21]. As a result, the tibia's bone mineral density is typically significantly larger in the medial than in the lateral regions, see Hurwitz et al. [146].

Figure 1.6(a) illustrates the *isotropic functional adaption* in the healthy proximal tibia characterised through a Dual-Energy X-ray Absorptiometry scan. The different grey scales indicate the heterogeneous bone density distribution with a characteristic dense region in the medial plateau, a less dense region in the lateral plateau, and a low density in the central region, see the recent publication by Pang et al. [232]. Dual-Energy X-ray Absorptiometry is currently the most common diagnostic tool to quantify bone mineral density profiles. However, it fails to visualise microstructural anisotropy, a characteristic feature of spongy bone that was recognised more than a century ago by von Meyer [211]. Figure 1.6(b) displays the *anisotropic functional adaption* in the healthy proximal tibia characterised by a photograph of a thin frontal longitudinal section of the bone taken from Wolff [297]. It clearly documents the alignment of the trabecular architecture

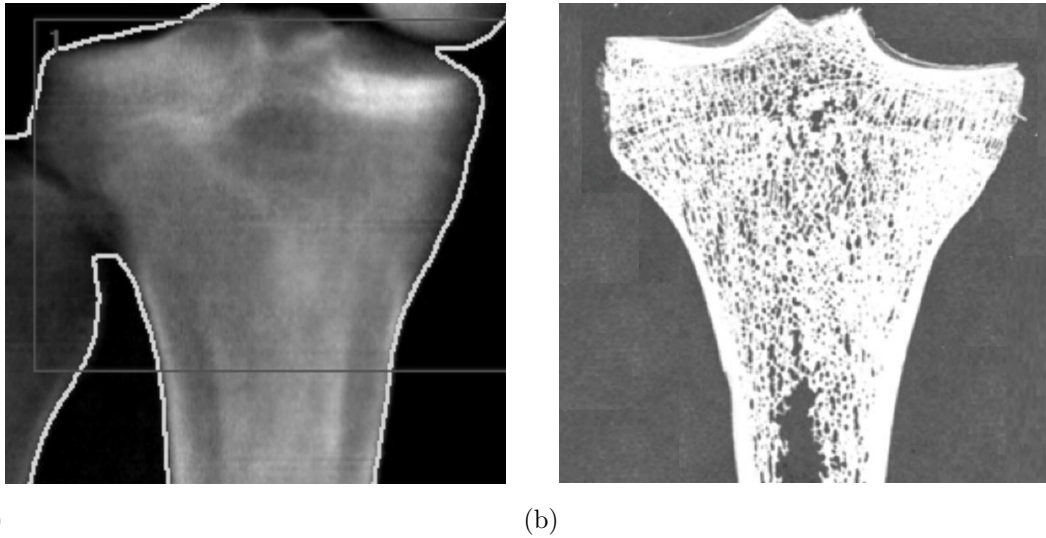


Figure 1.6: Healthy proximal tibia. (a) Isotropic density distribution visualised through a Dual-Energy X-ray Absorptiometry scan of the proximal tibia. The scan displays the characteristic heterogeneous density distribution, with a dense region in the medial plateau, a lower density region in the lateral plateau, and the lowest density in the central region, cf. Pang et al. [232]. (b) Anisotropic density distribution visualised through a thin section of the proximal tibia. The photograph displays the microstructural arrangement of the trabeculae aligned with the axis of maximum principal loading, cf. Wolff [297].

with the directions of maximum principal loading as, for instance, reported by Carter and Beaupré [62].

In the mid 1970s, biomechanical engineers proposed the first mechanistic models to characterise the *isotropic functional adaptation* of bone in response to mechanical loading, see Carter and Hayes [63], Cowin and Hegedus [74] and Cowin and Doty [73]. These approaches model bone growth within the framework of open system thermodynamics, as discussed by Kuhl and Steinmann [171], using an enhanced balance of mass which allows bone to adapt its density driven by stress, strain or energy; see Himpel et al. [129] and Kuhl and Steinmann [171] amongst others. Within the past two decades, we have recognised finite element analysis as a powerful tool to investigate the isotropic functional adaptation in the form of regional variations in density profiles, see Ambrosi et al. [16] and Huiskes et al. [142]. As discussed in a comparative overview by Kuhl et al. [166], finite element algorithms for growing tissue typically introduce the density as nodal degree of freedom (Jacobs et al. [148], Kuhl and Steinmann [173]), as internal variable (Harrigan and Hamilton [116]), or as local degree of freedom which can be condensed on the element level (Beaupré et al. [39]). Finite element models allow us to predict bone growth and resorption in response to virtually any loading scenario, which would not be experimentally feasible, see Reina-Romo et al. [246] or Weinans et al. [290]. They also allow for efficient parametric studies to identify key contributors

to bone straightening (Carpenter and Carter [61]), bone torsion (Taylor et al. [274]), or to bone failure (Gitman et al. [109], Zhang et al. [300]).

While the initial growth models for hard biological tissues are exclusively isotropic and fail to reproduce the characteristic microstructural architecture of spongy bone, only few studies focus on the *anisotropic functional adaptation* we can observe in vivo, as reported by Taber [272]. Most of the models proposed are directly motivated by the so-called ‘trajectorial hypothesis’ introduced by Wolff [298] which states that—in addition to the change in apparent density of the bone tissue resulting from the growth and remodelling process—we also observe a time-dependent alignment of the trabecular architecture with the directions of maximum principal loading directions, in other words anisotropy evolution. To give a short overview, we shall give a brief description of different anisotropic bone remodelling approaches.

As one of the first contributions on anisotropic bone remodelling considered here, Carter et al. [64] introduced a mathematical formulation for the functional adaptation of trabecular bone. The formulation is based on a self-optimisation concept, which takes into account the influence of different load cases weighted by the corresponding number of load cycles. For a single load case, it is discussed that an alignment of the principal material axes with the principal stress axes will result in an optimal material microstructure orientation in the context of local stiffness maximisation. Almost a decade later after Carter, Jacobs et al. [149] proposed to add a remodelling rule for the rate-of-change of the full anisotropic elasticity tensor to the density rate-of-change rule adapted from an existing isotropic remodelling theory. In a review paper on existing bone remodelling formulations, Petteermann et al. [237] discussed a micro-macro mechanical description of bone in its different microstructural configurations and derived a remodelling algorithm accompanied by a new unified material model for describing the linear elastic orthotropic behaviour of bone. Based on a hypoelastic material model, Weng [295] applied a formulation which—conceptually similar to Jacobs et al. [149]—assumed an evolution of the stiffness tensor. Inspired by mathematical optimisation approaches, Fernandes et al. [97] and Rodrigues et al. [252] proposed an analytical parametric microstructural model from which a global material model was obtained by making use of homogenisation concepts. An optimal material structure constructed by means of homogenised material properties could be found by optimising a cost function. This cost or rather goal function accounts for both, the structural stiffness and the biological costs associated with metabolic maintenance of the bone tissue. In a series of papers, Doblaré and García [87] introduced internal remodelling from general damage-repair theories adopting the framework of continuum damage mechanics. Therein, a damage-repair-tensor is defined in terms of the apparent density and a fabric tensor is associated with the porosity and directionality of the trabeculae; see also Cowin [71, 76] or Zysset and Curnier [302]. In a follow-up paper, García et al. [104] also considered external remodelling, whereas a subsequent contribution analysed the proximal femur before and after total hip replacement, Doblaré and García [87]. Similar to the contributions above, Nackenhorst et al. [221] and Krstin et al. [163] applied a fabric tensor description for porous materials to

extend the isotropic theory to anisotropic material behaviour. In some recent publications, Coelho et al. [70] and Coelho et al. [69] proposed a hierarchical model based on the above mentioned topology-optimisation-related approaches to model the bone apparent density distribution at the macro scale and the trabecular structure at the micro scale. Bone at global macroscopic scale is consequently assumed as a continuum characterised by equivalent or rather homogenised material properties.

1.2 Scope and outline

In order to acquaint the reader with the structure and the main issues of the present work, we give a brief overview and summary of each chapter of this thesis which is organised as follows:

In **Chapter 2**, the overall energetic properties of an artery are discussed by means of the inflation, bending and extension of a double-layered cylindrical tube. Different states of residual stresses and different fibre orientations are considered so that, for instance, representative fibre angles that result in extremal states of the total potential energy can be identified. In view of turnover and remodelling processes, these orientations are considered to constitute preferred directions of fibre alignment. In summary, the main goal of this chapter is to calculate optimal material, structural and loading parameters by concepts of energy-minimisation. Several numerical studies show that the obtained values—such as the fibre orientations, the residual axial stretch and the opening angle—are in good agreement with respective physiological parameters reported in the literature. This chapter is supplemented by **Appendix A** which deals with the thin-wall membrane approximation of the cylindrical tube.

Chapter 3 presents a nonlocal gradient-based damage formulation within a geometrically non-linear setting. The hyperelastic constitutive response at local material point level is governed by a strain energy which is additively composed of an isotropic matrix and of an anisotropic fibre-reinforced material, respectively. The inelastic constitutive response is governed by a scalar $[1-d]$ -type damage formulation, where only the anisotropic elastic part is assumed to be affected by the damage. Following the concept in Dimitrijević and Hackl [85], the local free energy function is enhanced by a gradient-term. This term essentially contains the gradient of the nonlocal damage variable which, itself, is introduced as an additional independent variable. In order to guarantee the equivalence between the local and nonlocal damage variable, a penalisation term is incorporated within the free energy function. Based on the principle of minimum total potential energy, a coupled system of Euler-Lagrange equations, i.e. the balance of linear momentum and the balance of the nonlocal damage field, is obtained and solved in weak form. The resulting coupled, highly non-linear system of equations is symmetric and can conveniently be solved by a standard incremental-iterative Newton-Raphson-type solution scheme. Several three-dimensional displacement- and force-driven boundary value problems—partially motivated by biomechanical application—highlight the mesh-

objective characteristics and constitutive properties of the model and illustratively underline the capabilities of the formulation proposed. This chapter is supplemented by **Appendices D, E, F, G** which provide details with regard to an implementation into the commercial finite-element-software Abaqus. To be specific, **Appendices D** and **E** provide crucial aspects of non-linear coupled finite element formulations and general constitutive relations when implemented into Abaqus while **Appendices F** and **G** address the implementation of deformation-dependent loads and usage of arc-length methods in connection with Abaqus.

The main goal of **Chapter 4** is a new remodelling approach that, on the one hand, reflects the alignment of fibrous soft biological tissue with respect to representative loading directions. On the other hand, the continuum approach proposed is based on a sound micro-mechanically motivated formulation. To be specific, use of a worm-like chain model is made to describe the behaviour of long-chain molecules as present in, for instance, collagenous tissues. The extension of such a one-dimensional constitutive equation to the three-dimensional macroscopic level is performed by means of a microsphere formulation. Inherent with the algorithmic treatment of this type of modelling approach, a finite number of unit-vectors is considered for the numerical integration over the domain of the unit-sphere. As a key aspect of this chapter, remodelling is incorporated by setting up evolution equations for the referential orientations of these integration directions. Accordingly, the unit-vectors considered now allow interpretation as internal variables which characterise the material's anisotropic properties. Several numerical studies underline the applicability of the model that, moreover, fits well in iterative finite element formulations so that general boundary value problems can be solved.

The objective of **Chapter 5** is to generalise a well-established framework of energy-driven isotropic functional adaptation to anisotropic microstructural growth and density evolution. We adopt the microsphere concept, which proves to be extremely versatile and flexible to extend sophisticated one-dimensional constitutive relations to the three-dimensional case. In this chapter we apply this framework to the modelling and simulation of anisotropic functional adaptation by means of a directional density distribution, which evolves in time and in response to the mechanical loading condition. Several numerical studies highlight the characteristics and properties of the anisotropic growth model we establish. The formulation is embedded into an iterative finite element algorithm to solve complex boundary value problems. In particular, we consider the finite-element-simulation of a subject-specific proximal tibia bone. The proposed model is able to appropriately represent the heterogeneous bone density distribution. Furthermore, we investigate the anisotropic growth formulation with a special emphasis on its application to structural design problems. To this end, four illustrative three-dimensional benchmark-type boundary value problems are discussed and compared qualitatively with the results obtained by classic structural optimisation strategies. As an advantage over several other computational growth models proposed in the literature, a pronounced local anisotropy evolution is identified and illustrated by means of orientation-distribution-type density plots. This chapter is supplemented by **Appendices B** and **C** where the

former deals with a comparison of macroscopic and microsphere-based constitutive models and the latter is dedicated to different techniques used in this chapter to visualise anisotropic material properties.

2 Extremal states of energy of a double-layered thick-walled tube

This chapter discusses the overall energetic properties of an artery by means of the inflation, bending and extension of a double-layered cylindrical tube. The material presented is based on the ideas outlined in the recent work by Waffenschmidt and Menzel [282]. Within this chapter, an attempt towards the interpretation of the interactions between loading conditions, states of residual stresses and fibre orientations is made by means of energy-based arguments. As an exemplary constitutive relation, the model proposed by Holzapfel et al. [135] is adopted and, by analogy with that work, a thick-walled double-layered cylindrical tube subjected to combined bending, inflation and extension is considered. As an advantage of this idealised test case, the underlying boundary value problem can be solved (almost) analytically without the need for extensive numerical methods such as the finite element method. Nevertheless, all representative characteristics of the loading conditions and the geometry can be captured; see Holzapfel and Ogden [136, 137] and references cited therein. For the present application of a residually stressed artery subjected to different blood pressures, commonly combined loading cases including inflation, bending, and axial extension of the thick-walled tube are considered. The bending and extension modes are typically related to residual stress states within the arterial wall.

The main goal of the present chapter is to obtain additional information on optimal, say material, structural and loading parameters—such as the distribution of residual stresses and angles characterising the orientation of fibre families—by direct minimisation concepts applied to the total potential energy of the underlying boundary value problem. In other words, the total potential energy is minimised with respect to one or several primary variables, such as the inner circumferential stretch and a representative fibre angle, to indicate one example. Thus, results previously established in the literature can be reproduced on the one hand and, as a main goal of this chapter, characteristic settings of material, structural and loading parameters which render the total potential energy to take extremal states can also be investigated on the other. Such extremal states are assumed to identify configurations that, from the design point of view, are favourable.

The present energy-based approach will be restricted to the special case of a perfect cylindrical geometry. Any further geometries accompanied by non-uniform loading cases, as these intrinsically occur in real patient-specific applications, are beyond the scope of this chapter but constitute future work in combination with advanced finite element techniques. Moreover, arterial tissue possesses active properties which are not accounted for in this chapter.

Several numerical studies are discussed and show that the values calculated for, e.g., the axial residual stretch, the opening angle or the fibre angles, are in good agreement with the respective physiological parameters reported in the literature. As expected, these values correspond to an extremal state of the total potential energy and lead to a reduced, but interestingly not minimal, inner circumferential stretch as compared to the physiological values reported in the literature.

This chapter is organised as follows: Section 2.1 provides a short summary of basic equations in the context of anisotropic finite hyperelasticity intended to introduce essential quantities frequently used throughout this thesis. The analytical expression for the total potential energy for bending, inflation, extension, and torsion of a thick-walled tube is established in Section 2.2. With this total potential energy function at hand, the Euler-Lagrange equations are derived. Section 2.3 includes the investigation of characteristic properties of an arterial tube for a specific constitutive model. Several parameter studies are performed by means of a double-layered thick-walled residually stressed tube in response to different loading levels.

2.1 Finite anisotropic hyperelasticity

This introductory section provides a short summary of basic equations characterising the non-linear elastic deformation of solids and its related hyperelastic stress response in the context of finite deformation continuum mechanics. This section is not intended to provide an extensive review of the detailed continuum mechanical background; in this regard, we refer, for instance, to the textbook by Ogden [225]. Here, we basically aim at introducing the notation by means of summarising essential quantities commonly used throughout this work. The relevant governing balance relations are specified within the respective chapters along with the theoretical discussion of the particular elastic and inelastic material models.

2.1.1 Basic kinematics

Let $\mathbf{x} = \boldsymbol{\varphi}(\mathbf{X}, t)$ describe the deformation of the body, which transforms referential placements $\mathbf{X} \in \mathcal{B}_0$ to their spatial counterparts $\mathbf{x} \in \mathcal{B}_t$. Based on this, the deformation gradient is defined as

$$\mathbf{F} = \nabla_{\mathbf{X}} \boldsymbol{\varphi} \tag{2.1}$$

which transforms infinitesimal referential line elements $d\mathbf{X}$ onto their spatial counterparts $d\mathbf{x}$. Furthermore, let dV and dv denote an infinitesimal volume element in referential and spatial setting. Accordingly, the Jacobian

$$J = \frac{dv}{dV} = \det(\mathbf{F}) > 0 \quad (2.2)$$

is the ratio of the deformed to the undeformed volume. Finally, let $d\mathbf{A} = \mathbf{N} dA$ and $d\mathbf{a} = \mathbf{n} da$ define the reference and spatial area normals. Then, Nanson's formula

$$\mathbf{n} da = \text{cof}(\mathbf{F}) \cdot \mathbf{N} dA \quad (2.3)$$

describes the transformation of infinitesimal area elements between the reference and the spatial configuration.

Following Flory [99], the deformation gradient \mathbf{F} can be decomposed multiplicatively into a spherical and unimodular part, i.e.

$$\mathbf{F} = J^{1/3} \mathbf{I} \cdot \bar{\mathbf{F}}. \quad (2.4)$$

Based upon this, the right Cauchy-Green deformation tensor \mathbf{C} and its isochoric counterpart $\bar{\mathbf{C}}$ are denoted by standard notations, i.e.

$$\mathbf{C} = \mathbf{F}^t \cdot \mathbf{F} = J^{2/3} \bar{\mathbf{C}}, \quad \bar{\mathbf{C}} = \bar{\mathbf{F}}^t \cdot \bar{\mathbf{F}}. \quad (2.5)$$

Fibre-reinforcement of the material is considered by assuming N families of fibres to be embedded in the continuum. Their orientation is characterised by referential unit vectors \mathbf{a}_{0i} , $i = 1, \dots, N$ with $\|\mathbf{a}_{0i}\| = 1$. The deformation $\varphi(\mathbf{X}, t)$ transforms the fibre into its current configuration, where the vector $\mathbf{a}_i = \mathbf{F} \cdot \mathbf{a}_{0i}$ defines the spatial orientation with $\|\mathbf{a}_i\| \neq 1$ denoting the stretch in the direction of the particular fibre.

2.1.2 Decoupled volumetric-isochoric stress response

The quasi-incompressible anisotropic non-linear elastic material response of biological tissues is assumed to be governed by a strain energy function Ψ defined per unit reference volume. In this regard, the anisotropy due to the fibre-reinforcement of the material is incorporated by introducing a set of symmetric second-order tensors

$$\mathbf{A}_i = \mathbf{a}_{0i} \otimes \mathbf{a}_{0i}, \quad i = 1, \dots, N. \quad (2.6)$$

In order to take account of the incompressibility, we adopt a volumetric-isochoric split, which results in the following decoupled format

$$\Psi(\mathbf{C}, \mathbf{A}_i) = \Psi_{\text{vol}}(J) + \Psi_{\text{ich}}(\mathbf{C}, \mathbf{A}_i). \quad (2.7)$$

Utilisation of the Clausius-Planck inequality enables the Piola-Kirchhoff stress tensor to be expressed in standard form

$$\mathbf{S} = 2 \partial_{\mathbf{C}} \Psi. \quad (2.8)$$

Based on equation (2.7), the hyperelastic form of the Piola-Kirchhoff stress results in

$$\mathbf{S} = \mathbf{S}_{\text{vol}} + \mathbf{S}_{\text{ich}}. \quad (2.9)$$

Herein, the respective volumetric and isochoric contributions to the Piola-Kirchhoff stress can be expressed as

$$\mathbf{S}_{\text{vol}} = p J \mathbf{C}^{-1} \quad \text{with} \quad p := \partial_J \Psi_{\text{vol}}, \quad (2.10)$$

$$\mathbf{S}_{\text{ich}} = \bar{\mathbf{S}}_{\text{ich}} : \mathbf{P} \quad \text{with} \quad \bar{\mathbf{S}}_{\text{ich}} := 2 \partial_{\bar{\mathbf{C}}} \Psi_{\text{ich}}, \quad (2.11)$$

where we employ the partial derivative $\partial_{\mathbf{C}} J = J \mathbf{C}^{-1}/2$ and introduce the definition of the fourth-order deviatoric projection tensor $\mathbf{P} := \partial_{\mathbf{C}} \bar{\mathbf{C}} = J^{-2/3} [\mathbf{I}_{\text{sym}} - \frac{1}{3} \mathbf{C} \otimes \mathbf{C}^{-1}]$.

A push forward transformation of equations (2.9)–(2.11) allows the Cauchy stress tensor $\boldsymbol{\sigma} = J^{-1} \mathbf{F} \cdot \mathbf{S} \cdot \mathbf{F}^t$ to be expressed in decoupled form as

$$\boldsymbol{\sigma} = \boldsymbol{\sigma}_{\text{vol}} + \boldsymbol{\sigma}_{\text{ich}}. \quad (2.12)$$

Herein, the respective volumetric and isochoric contributions to the Cauchy stress are specified as

$$\boldsymbol{\sigma}_{\text{vol}} = p \mathbf{I}, \quad (2.13)$$

$$\boldsymbol{\sigma}_{\text{ich}} = \bar{\boldsymbol{\sigma}}_{\text{ich}} : \mathbf{l}_{\text{dev}} \quad \text{with} \quad \bar{\boldsymbol{\sigma}}_{\text{ich}} := J^{-1} \bar{\mathbf{F}} \cdot \bar{\mathbf{S}}_{\text{ich}} \cdot \bar{\mathbf{F}}^t. \quad (2.14)$$

Furthermore, the Piola stress tensor is introduced as $\mathbf{P} = \partial_{\mathbf{F}} \Psi = \mathbf{F} \cdot \mathbf{S}$ and the relation for the Kirchhoff stress tensor is represented by $\boldsymbol{\tau} = J \boldsymbol{\sigma}$.

2.2 Basic equations of a thick-walled tube

This section first discusses the basic kinematics of an incompressible thick-walled cylindrical tube, which represents an artery, in Sections 2.2.1 and 2.2.2. The basic modes of deformation considered are combined bending, inflation, extension and torsion, see Ogden [225], Holzapfel et al. [135] or Ogden [226]. Section 2.2.3 establishes the representation of the total potential energy for the problem at hand and the related Euler-Lagrange equations are summarised in Section 2.2.4.

2.2.1 Kinematics

The kinematics of a thick-walled tube B can conveniently be described by cylindrical polar coordinates. Adopting common notation, these coordinates are introduced as R , Θ and Z with respect to a chosen reference configuration \mathcal{B}_0 . An orthonormal referential frame can be defined in terms of these coordinates as

$$\mathbf{E}_R(\Theta) = \cos(\Theta) \mathbf{e}_1 + \sin(\Theta) \mathbf{e}_2, \quad (2.15)$$

$$\mathbf{E}_\Theta(\Theta) = -\sin(\Theta) \mathbf{e}_1 + \cos(\Theta) \mathbf{e}_2, \quad (2.16)$$

$$\mathbf{E}_Z = \mathbf{e}_3, \quad (2.17)$$

wherein $\{\mathbf{e}_1, \mathbf{e}_2, \mathbf{e}_3\}$ is a Cartesian frame fixed in space. Related coordinates with respect to the current configuration \mathcal{B}_t are introduced as r, θ, z so that the corresponding spatial orthonormal frame reads

$$\mathbf{e}_r(\theta) = \cos(\theta) \mathbf{e}_1 + \sin(\theta) \mathbf{e}_2, \quad (2.18)$$

$$\mathbf{e}_\theta(\theta) = -\sin(\theta) \mathbf{e}_1 + \cos(\theta) \mathbf{e}_2, \quad (2.19)$$

$$\mathbf{e}_z = \mathbf{e}_3. \quad (2.20)$$

The geometry of the tube considered is visualised in Figure 2.1 and its material and spatial settings are specified by

$$R_i \leq R \leq R_o, \quad 0 \leq \Theta \leq 2\pi - \alpha, \quad 0 \leq Z \leq L, \quad (2.21)$$

$$r_i \leq r \leq r_o, \quad 0 \leq \theta \leq 2\pi, \quad 0 \leq z \leq l. \quad (2.22)$$

where R_i, R_o and L represent the inner and outer radii and the length of the tube in a (undeformed) reference configuration \mathcal{B}_0 while r_i, r_o and l represent the corresponding quantities in the (deformed) current configuration \mathcal{B}_t ; see Figure 2.1. With these quantities, the deformation modes of bending, extension and torsion of an incompressible tube—the deformation due to inflation under internal pressure p will be discussed later on—can be represented by the spatial position vector

$$\mathbf{x} = \boldsymbol{\varphi}(\mathbf{X}, t) = r \mathbf{e}_r(\theta) + z \mathbf{e}_z \quad (2.23)$$

specified by means of

$$r(R) = \sqrt{\frac{R^2 - R_i^2}{k \lambda_z} + r_i^2}, \quad (2.24)$$

$$\theta(\Theta, Z) = k \Theta + Z \frac{\phi}{L}, \quad (2.25)$$

$$z = \lambda_z Z. \quad (2.26)$$

The parameter k is defined in terms of the so-called opening angle α , i.e.

$$k = \frac{2\pi}{2\pi - \alpha} \quad (2.27)$$

as used in Holzapfel et al. [135], so that $k|_{\alpha=0} = 1$ and $k|_{\alpha \rightarrow 2\pi} \rightarrow \infty$. The positive scalar λ_z represents the axial stretch and ϕ is the angle of twist. Equation (2.24) reflects the assumption of incompressibility: for the isochoric deformation of the tube considered the referential sub-volume $V(R) = \pi L [R^2 - R_i^2]$ coincides with the current sub-volume $v(r) = \pi k l [r^2 - r_i^2]$ from which, together with (2.26), equation (2.24) can be concluded; cf. Ogden [225, ch. 2.2.6, p. 112]. The angle θ defined in equation (2.25) is a linear function in Θ, Z and ϕ . As a consequence, the radial spatial base vector \mathbf{e}_r does not depend on Θ alone in the case of $\phi \neq 0$.

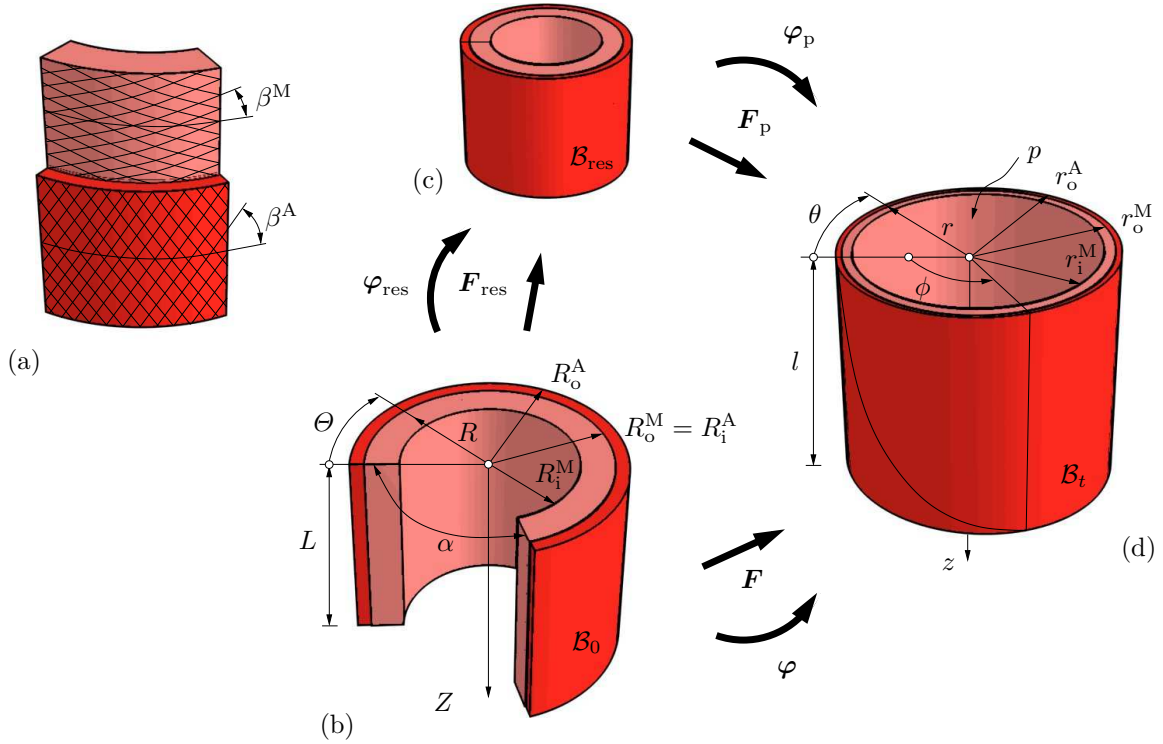


Figure 2.1: Deformation modes of a double-layered thick-walled cylindrical tube, Holzapfel et al. [135]: bending (opening angle α), inflation (internal pressure p), longitudinal extension (axial stretch $\lambda_z = l/L$), and torsion (angle of twist ϕ); (a) segment of the arterial wall consisting of media (superscript M) and adventitia (superscript A) reinforced by two families of fibres with fibre angles β^M and β^A defined in (b) a stress-free reference configuration \mathcal{B}_0 ; (c) residually stressed but load-free configuration \mathcal{B}_{res} ; (d) residually stressed and loaded current configuration \mathcal{B}_t .

Representative deformation measures can conveniently be introduced with respect to the coordinates R, Θ, Z and r, θ, z . To set the stage, equation (2.23) is used together with $\nabla_{\mathbf{X}}[\bullet] = \partial_R[\bullet] \otimes \mathbf{E}_R + R^{-1} \partial_\Theta[\bullet] \otimes \mathbf{E}_\Theta + \partial_Z[\bullet] \otimes \mathbf{E}_Z$ —see, e.g., Malvern [193]—to introduce the deformation gradient as

$$\mathbf{F} = \nabla_{\mathbf{X}}[r \mathbf{e}_r + z \mathbf{e}_z] \quad (2.28)$$

$$\begin{aligned} &= \partial_R[r \mathbf{e}_r + z \mathbf{e}_z] \otimes \mathbf{E}_R \\ &\quad + \partial_\Theta[r \mathbf{e}_r + z \mathbf{e}_z] \otimes \mathbf{E}_\Theta R^{-1} \\ &\quad + \partial_Z[r \mathbf{e}_r + z \mathbf{e}_z] \otimes \mathbf{E}_Z. \end{aligned} \quad (2.29)$$

It is concluded from equations (2.18)–(2.20) and (2.24)–(2.26) that

$$\frac{\partial \mathbf{e}_r}{\partial R} = \mathbf{0}, \quad \frac{\partial \mathbf{e}_r}{\partial \Theta} = \frac{\partial \theta}{\partial \Theta} \mathbf{e}_\theta, \quad \frac{\partial \mathbf{e}_r}{\partial Z} = \frac{\partial \theta}{\partial z} \frac{\partial z}{\partial Z} \mathbf{e}_\theta, \quad (2.30)$$

whereas $\partial_R \mathbf{e}_z = \partial_\Theta \mathbf{e}_z = \partial_Z \mathbf{e}_z = \mathbf{0}$. Based on equations (2.24)–(2.26) and (2.27) one can specify further partial derivatives, such as

$$\frac{\partial r}{\partial R} = \frac{R}{r k \lambda_z}, \quad \frac{\partial z}{\partial Z} = \lambda_z, \quad \frac{\partial \theta}{\partial \Theta} = k, \quad \frac{\partial \theta}{\partial z} = \frac{\phi}{l}, \quad (2.31)$$

and additionally identify $\partial_\Theta r = \partial_Z r = \partial_R z = \partial_\Theta z = 0$. With these relations, the deformation gradient reduces to

$$\mathbf{F} = \frac{R}{r k \lambda_z} \mathbf{e}_r \otimes \mathbf{E}_R + \frac{r k}{R} \mathbf{e}_\theta \otimes \mathbf{E}_\Theta + \lambda_z \mathbf{e}_z \otimes \mathbf{E}_Z + r \frac{\phi}{l} \lambda_z \mathbf{e}_\theta \otimes \mathbf{E}_Z. \quad (2.32)$$

To simplify notation, common abbreviations are adopted and the radial stretch and a shear measure are introduced as

$$\lambda_r = \frac{R}{r k \lambda_z} \quad \text{and} \quad \gamma = r \frac{\phi}{l}. \quad (2.33)$$

The incompressibility assumption, i.e. $J = \lambda_r \lambda_\theta \lambda_z \doteq 1$ so that $\text{cof}(\mathbf{F}) = \mathbf{F}^{-t}$, enables us to express the circumferential stretch, for instance, as

$$\lambda_\theta = [\lambda_r \lambda_z]^{-1} = \frac{r k}{R}, \quad (2.34)$$

so that the deformation gradient, finally, takes the form

$$\mathbf{F} = \lambda_r \mathbf{e}_r \otimes \mathbf{E}_R + \lambda_\theta \mathbf{e}_\theta \otimes \mathbf{E}_\Theta + \lambda_z \mathbf{e}_z \otimes \mathbf{E}_Z + \gamma \lambda_z \mathbf{e}_\theta \otimes \mathbf{E}_Z. \quad (2.35)$$

It is obvious that the matrix of coefficients of \mathbf{F} is not symmetric in the case of activated twist, i.e. $\gamma \neq 0$, so that λ_r represents a principal stretch in the radial direction, whereas λ_θ and λ_z do not constitute principal stretches. Throughout this chapter, however, twist will be neglected so that $\gamma = 0$, the matrix of coefficients of \mathbf{F} becomes symmetric and λ_r , λ_θ , λ_z take the interpretation as principal stretches in radial, circumferential and axial direction.

2.2.2 Residual stresses

The incorporation of residual stresses is of key importance within the modelling and simulation of soft biological tissues. Different concepts have been discussed in the literature to account for these equilibrated stress contributions present in the absence of external loading; see, e.g., Hoger [132] where special emphasis is placed on circular cylinders. Here, a framework discussed by Hoger [133] and Johnson and Hoger [152] is adopted which makes use of an additional configuration. The general concept is similar to the introduction of a local isomorphism, as advocated by Noll [224], but the related energetic contributions are different. Speaking in a conceptual sense, one introduces a

residual strain quantity which, in combination with a hyperelastic form specified later on, induces a residual stress contribution.

In this context, let the overall deformation be formally composed as $\boldsymbol{\varphi} = \boldsymbol{\varphi}_p \circ \boldsymbol{\varphi}_{\text{res}}$, where $\boldsymbol{\varphi}_{\text{res}}$ generates a load-free but residually stressed configuration \mathcal{B}_{res} . The mapping $\boldsymbol{\varphi}_p$ accounts for the motion under the action of external forces. For the present problem, $\boldsymbol{\varphi}_{\text{res}}$ induces circumferential residual stretches, while $\boldsymbol{\varphi}_p$ will be associated with inflation of the tube and, in general, may also include a torsional deformation mode. Axial elongation may either be attached to $\boldsymbol{\varphi}_{\text{res}}$ or $\boldsymbol{\varphi}_p$. As mentioned above, a twist contribution is neglected throughout this chapter. In view of the overall deformation gradient, one obtains the multiplicative composition $\mathbf{F} = \mathbf{F}_p \cdot \mathbf{F}_{\text{res}}$, which is illustrated in Figure 2.1; cf. Holzapfel et al. [135]. The circumferential residual stretch, described by the opening angle α , must directly be included in \mathbf{F}_{res} , whereas an axial residual stretch can either be incorporated in \mathbf{F}_{res} or \mathbf{F}_p , or can be enforced by, e.g., Dirichlet boundary conditions. Moreover, note that this composition of the deformation gradient can conveniently be used to model residual stresses within finite element formulations for the simulation of complex boundary value problems; see Chapter 4.5.3.2 or, e.g., Alastrué et al. [9], Alastrué et al. [11] and references cited in these works.

2.2.3 Total potential energy

The total potential energy of a conservative system considered additively combines the internal contribution Π_{int} , reflecting the action of internal forces, and an external contribution $\Pi_{\text{ext}} = \Pi_{\text{ext}}^{\text{vol}} + \Pi_{\text{ext}}^{\text{sur}}$ due to the volume and surface forces applied, i.e.

$$\Pi = \Pi_{\text{int}} + \Pi_{\text{ext}}^{\text{vol}} + \Pi_{\text{ext}}^{\text{sur}} + \text{const.} \quad (2.36)$$

The existence of a strain energy function $\Psi(\mathbf{F}; \mathbf{X})$ is assumed, with the dependency on \mathbf{X} often not explicitly mentioned in the following, so that the internal energy contribution of B can be represented as

$$\Pi_{\text{int}} = \int_{\mathcal{B}_t} J^{-1} \Psi(\mathbf{F}) \, dv = \int_{\mathcal{B}_0} \Psi(\mathbf{F}) \, dV. \quad (2.37)$$

In view of the specific application considered subsequently, the volume force contribution is neglected—in other words, $-\partial_{\boldsymbol{\varphi}} \Pi_{\text{ext}}^{\text{vol}} = \mathbf{b} \doteq \mathbf{0}$ is consistently assumed. Moreover, for the case of pressure loading the traction vector $\bar{\mathbf{t}}$ is proportional to the outward normal unit vector \mathbf{n} and its length is referred to the volume-related pressure, i.e. $-\partial_{\boldsymbol{\varphi}} \Pi_{\text{ext}}^{\text{sur}} = \bar{\mathbf{t}} \doteq -p^{\text{vol}} \mathbf{n}$. Similarly, the referential volume-related traction vector takes the Piola-transformed representation $\bar{\mathbf{T}} = -p^{\text{vol}} \text{cof}(\mathbf{F}) \cdot \mathbf{N}$, where \mathbf{N} is the referential outward unit vector referring to the referential inner surface of the tube $\partial\mathcal{B}_{0i}$. In case of pressure loading, the referential surface-related energy contribution can be expressed as

$$\tilde{\Pi}_{\text{ext}}^{\text{sur}} = \int_{\partial\mathcal{B}_{0i}} p^{\text{sur}} \boldsymbol{\varphi} \cdot \text{cof}(\mathbf{F}) \cdot \mathbf{N} \, dA \quad (2.38)$$

with $p^{\text{sur}} = \int_0^1 p^{\text{vol}}(\alpha \mathbf{v}) \alpha^2 d\alpha$ being the surface-related pressure for any sufficiently smooth vector function \mathbf{v} ; cf. Podio-Guidugli and Vergara Caffarelli [240] and Šilhavý [259, sect. 13]. For the loading case considered in the present chapter, one obtains with regard to equation (2.38) the equivalent volume-related external energy contribution

$$\tilde{\Pi}_{\text{ext}}^{\text{vol}} = - \int_{\mathcal{V}_t} p^{\text{vol}} dv = - \int_{\mathcal{V}_0} J p^{\text{vol}} dV. \quad (2.39)$$

The equivalence between $\tilde{\Pi}_{\text{ext}}^{\text{sur}}$ and $\tilde{\Pi}_{\text{ext}}^{\text{vol}}$ can be illustrated by relating the surface integral in equation (2.38) to a volume integral by means of Gauss's theorem. To be specific, one obtains

$$\begin{aligned} \tilde{\Pi}_{\text{ext}}^{\text{sur}} &= - \int_{\partial\mathcal{V}_0} p^{\text{sur}} \boldsymbol{\varphi} \cdot \text{cof}(\mathbf{F}) \cdot \mathbf{N} dA \\ &= - \int_{\mathcal{V}_0} \nabla_{\mathbf{X}} \cdot [p^{\text{sur}} \boldsymbol{\varphi} \cdot \text{cof}(\mathbf{F})] dV \\ &= - \int_{\mathcal{V}_0} p^{\text{sur}} \mathbf{F} : \text{cof}(\mathbf{F}) + \boldsymbol{\varphi} \cdot \text{cof}(\mathbf{F}) \cdot \nabla_{\mathbf{X}} p^{\text{sur}} dV \\ &= - \int_{\mathcal{V}_t} 3p^{\text{sur}} + \boldsymbol{\varphi} \cdot \nabla_{\mathbf{x}} p^{\text{sur}} dv \\ &= - \int_{\mathcal{V}_t} p^{\text{vol}} dv = \tilde{\Pi}_{\text{ext}}^{\text{vol}} \end{aligned} \quad (2.40)$$

wherein the Piola identity $\nabla_{\mathbf{X}} \cdot \text{cof}(\mathbf{F}) = \mathbf{0}$ is applied; cf. Podio-Guidugli and Vergara Caffarelli [240]. Note, that the change in sign from equation (2.38) to (2.40)₁ refers to the change in direction of the outward normal vectors related to the inner lateral surface of the tube, $\partial\mathcal{B}_{0i}$, and the surface of the inner volume of the tube, $\partial\mathcal{V}_0$. Furthermore, it becomes apparent that the relation between p^{sur} and p^{vol} is in line with the definition mentioned above, and as a special case, i.e. if $\nabla_{\mathbf{x}} p^{\text{sur}} = \mathbf{0}$, one observes the relation $p^{\text{sur}} = \frac{1}{3} p^{\text{vol}}$. An alternative derivation based on the introduction of \mathbf{n} in terms of the vector product of two surface tangent vectors is included in, e.g., Bonet and Wood [45, ch. 6].

Summarising the total potential energy for the tube problem and applying coordinates and deformation measures introduced above, one obtains

$$\begin{aligned} \Pi &= \int_{z=0}^l \int_{\theta=0}^{2\pi} \int_{r=r_i}^{r_o} \tilde{\Psi}(\lambda_{\theta}(r), \lambda_z) r dr d\theta dz \\ &\quad - \int_{z=0}^l \int_{\theta=0}^{2\pi} \int_{r=0}^{r_i} p r dr d\theta dz + \text{const.} \\ &= 2\pi l \int_{r=r_i}^{r_o} \tilde{\Psi}(\lambda_{\theta}(r), \lambda_z) r dr - p \pi r_i^2 l + \text{const}, \end{aligned} \quad (2.41)$$

wherein it is assumed that the internal energy density can be expressed as a function of the principal stretches and the in-compressibility constraint has been accounted for. Moreover, external contributions acting on the outer surface boundary are assumed to vanish identically. The volume-related pressure is homogeneously distributed within \mathcal{V}_t , so that $\nabla_x p^{\text{vol}} = \mathbf{0}$, for the inflation of the thick-walled tube addressed in this chapter. Moreover, the notation is simplified by the abbreviation $p = p^{\text{vol}}$.

Due to the non-linear dependency of $\tilde{\Psi}$ on r , the integral expression in equation (2.41) can in general not be evaluated analytically. A possible numerical integration scheme will be discussed in Section 2.3.

2.2.4 Euler-Lagrange equations

In order to derive the Euler-Lagrange equations, i.e. the equations of equilibrium, the variation of the total potential energy is calculated to identify stationary points of $\Pi(\mathbf{F}, \varphi)$. Starting with the representation of the total potential energy with respect to referential volumes and surfaces and assuming dead traction loading on the outer boundary, one obtains the following relations

$$\delta \Pi|_{\mathbf{X}} = \delta \int_{\mathcal{B}_0} \Psi \, dV - \delta \int_{\mathcal{V}_0} p J \, dV - \delta \int_{\partial \mathcal{B}_{0o}} \varphi \cdot \bar{\mathbf{T}}_o \, dA \quad (2.42)$$

$$\begin{aligned} &= \int_{\mathcal{B}_0} \partial_{\mathbf{F}} \Psi : \nabla_{\mathbf{X}} \delta \varphi \, dV \\ &\quad - \int_{\mathcal{V}_0} J \partial_{\varphi} p \cdot \delta \varphi + p \operatorname{cof}(\mathbf{F}) : \nabla_{\mathbf{X}} \delta \varphi \, dV - \int_{\partial \mathcal{B}_{0o}} \delta \varphi \cdot \bar{\mathbf{T}}_o \, dA \end{aligned} \quad (2.43)$$

$$\begin{aligned} &= \int_{\mathcal{B}_0} \nabla_{\mathbf{X}} \cdot [\delta \varphi \cdot \partial_{\mathbf{F}} \Psi] - \delta \varphi \cdot [\nabla_{\mathbf{X}} \cdot \partial_{\mathbf{F}} \Psi] \, dV \\ &\quad - \int_{\mathcal{V}_0} J \partial_{\varphi} p \cdot \delta \varphi + p \nabla_{\mathbf{X}} \cdot [\delta \varphi \cdot \operatorname{cof}(\mathbf{F})] \, dV - \int_{\partial \mathcal{B}_{0o}} \delta \varphi \cdot \bar{\mathbf{T}}_o \, dA \end{aligned} \quad (2.44)$$

$$\begin{aligned} &= \int_{\partial \mathcal{B}_0} \delta \varphi \cdot \partial_{\mathbf{F}} \Psi \cdot \mathbf{N} \, dA - \int_{\mathcal{B}_0} \delta \varphi \cdot [\nabla_{\mathbf{X}} \cdot \partial_{\mathbf{F}} \Psi] \, dV \\ &\quad - \int_{\mathcal{V}_0} \nabla_{\mathbf{X}} \cdot [p \delta \varphi \cdot \operatorname{cof}(\mathbf{F})] \, dV - \int_{\partial \mathcal{B}_{0o}} \delta \varphi \cdot \bar{\mathbf{T}}_o \, dA \end{aligned} \quad (2.45)$$

$$\begin{aligned} &= \int_{\partial \mathcal{B}_0} \delta \varphi \cdot \mathbf{P} \cdot \mathbf{N} \, dA - \int_{\mathcal{B}_0} \delta \varphi \cdot [\nabla_{\mathbf{X}} \cdot \mathbf{P}] \, dV \\ &\quad - \int_{\partial \mathcal{V}_0} p \delta \varphi \cdot \operatorname{cof}(\mathbf{F}) \cdot \mathbf{N} \, dA - \int_{\partial \mathcal{B}_{0o}} \delta \varphi \cdot \bar{\mathbf{T}}_o \, dA \doteq 0, \end{aligned} \quad (2.46)$$

wherein Gauss's theorem, the Piola identity and $J \partial_{\varphi} p = \operatorname{cof}(\mathbf{F}) \cdot \nabla_{\mathbf{X}} p$ have been applied; cf. Podio-Guidugli and Vergara Caffarelli [240] and Haughton [121]. Moreover,

the traction vector prescribed at the outer boundary $\partial\mathcal{B}_{0o}$ is denoted as $\bar{\mathbf{T}}_o \doteq \text{const.}$ Based on this, the local Euler-Lagrange equations take the representation

$$\mathbf{0} = \nabla_{\mathbf{X}} \cdot \mathbf{P} \quad \text{in} \quad \mathcal{B}_0 \quad (2.47)$$

$$\bar{\mathbf{T}} = \mathbf{P} \cdot \mathbf{N} = \bar{\mathbf{T}}_o \quad \text{on} \quad \partial\mathcal{B}_{0o} \quad (2.48)$$

$$\bar{\mathbf{T}} = \mathbf{P} \cdot \mathbf{N} = -p \text{cof}(\mathbf{F}) \cdot \mathbf{N} \quad \text{on} \quad \partial\mathcal{B}_{0i}. \quad (2.49)$$

As indicated above, the referential outward normals \mathbf{N} in the first and third term of equation (2.46) refer to differently oriented surfaces, i.e. the surface of tube $\partial\mathcal{B}_0$ and the surface of the inner volume of the tube $\partial\mathcal{V}_0$, respectively. Consequently, a change in sign from the third term in equation (2.46) to equation (2.49) is considered. By analogy with equation (2.41), the Piola stresses are next assumed to take a spectral form with respect to the base systems introduced in equations (2.15)–(2.20), i.e. $\mathbf{P} = P_{rR} \mathbf{e}_r \otimes \mathbf{E}_R + P_{\theta\Theta} \mathbf{e}_\theta \otimes \mathbf{E}_\Theta + P_{zZ} \mathbf{e}_z \otimes \mathbf{E}_Z$. Note that this form, together with equation (2.35) and $\gamma \doteq 0$, includes coaxiality of conjugated stresses and strain measures which, however, does not generally restrict the underlying constitutive relation to isotropy. With this assumption in hand and $\mathbf{N} = \pm \mathbf{E}_R$ for the particular application considered, the Euler-Lagrange equations can be represented as

$$\mathbf{0} = \left[\frac{\partial P_{rR}}{\partial R} + \frac{P_{rR}}{R} - \frac{P_{\theta\Theta}}{R} \right] \mathbf{e}_r + \frac{1}{R} \frac{\partial P_{\theta\Theta}}{\partial \Theta} \mathbf{e}_\theta + \frac{\partial P_{zZ}}{\partial Z} \mathbf{e}_z \quad \text{in} \quad \mathcal{B}_0 \quad (2.50)$$

$$\bar{\mathbf{T}} = P_{rR} \mathbf{e}_r \quad \text{on} \quad \partial\mathcal{B}_{0o} \quad (2.51)$$

$$\bar{\mathbf{T}} = p \lambda_r^{-1} \mathbf{e}_r \quad \text{on} \quad \partial\mathcal{B}_{0i}. \quad (2.52)$$

Instead of choosing representations in terms of the Piola stresses \mathbf{P} , which refer to referential area elements, the Euler-Lagrange equations can be formulated in terms of the Cauchy stresses $\boldsymbol{\sigma} = \mathbf{P} \cdot \text{cof}(\mathbf{F}^{-1})$, which refer to spatial area elements. Applying the Piola identity, the variation of the total potential can be rewritten as

$$\begin{aligned} \delta II|_{\mathbf{X}} &= \int_{\partial\mathcal{B}_t} \delta\varphi \cdot \boldsymbol{\sigma} \cdot \mathbf{n} \, da - \int_{\mathcal{B}_t} \delta\varphi \cdot [\nabla_{\mathbf{x}} \cdot \boldsymbol{\sigma}] \, dv \\ &\quad - \int_{\partial\mathcal{V}_t} p \delta\varphi \cdot \mathbf{n} \, da - \int_{\partial\mathcal{B}_o} \delta\varphi \cdot \bar{\mathbf{t}}_o \, da \doteq 0. \end{aligned} \quad (2.53)$$

Based on this, the Euler-Lagrange equation in terms of spatial arguments take the representation

$$\mathbf{0} = \nabla_{\mathbf{x}} \cdot \boldsymbol{\sigma} \quad \text{in} \quad \mathcal{B}_t \quad (2.54)$$

$$\bar{\mathbf{t}} = \boldsymbol{\sigma} \cdot \mathbf{n} = \bar{\mathbf{t}}_o \quad \text{on} \quad \partial\mathcal{B}_{to} \quad (2.55)$$

$$\bar{\mathbf{t}} = \boldsymbol{\sigma} \cdot \mathbf{n} = -p \mathbf{n} \quad \text{on} \quad \partial\mathcal{B}_{ti}. \quad (2.56)$$

In view of the base system introduced in equations (2.18)–(2.20), together with the assumed coaxiality of conjugated stresses and strain measures, the Cauchy stresses allow

2 Extremal states of energy of a double-layered thick-walled tube

representation in spectral form as $\boldsymbol{\sigma} = \sigma_{rr} \mathbf{e}_r \otimes \mathbf{e}_r + \sigma_{\theta\theta} \mathbf{e}_\theta \otimes \mathbf{e}_\theta + \sigma_{zz} \mathbf{e}_z \otimes \mathbf{e}_z$. By analogy with the derivations reviewed above and with $\mathbf{n} = \pm \mathbf{e}_r$, the Euler-Lagrange equations can be summarised as

$$\mathbf{0} = \left[\frac{\partial \sigma_{rr}}{\partial r} + \frac{\sigma_{rr}}{r} - \frac{\sigma_{\theta\theta}}{r} \right] \mathbf{e}_r + \frac{1}{r} \frac{\partial \sigma_{\theta\theta}}{\partial \theta} \mathbf{e}_\theta + \frac{\partial \sigma_{zz}}{\partial z} \mathbf{e}_z \quad \text{in} \quad \mathcal{B}_t \quad (2.57)$$

$$\bar{\mathbf{t}} = \sigma_{rr} \mathbf{e}_r \quad \text{on} \quad \partial \mathcal{B}_{t_o} \quad (2.58)$$

$$\bar{\mathbf{t}} = p \mathbf{e}_r \quad \text{on} \quad \partial \mathcal{B}_{t_i}. \quad (2.59)$$

Note, that relation (2.57) is the basis for the derivation of the underlying equilibrium equations for the *thin-walled* cylindrical tube, also referred to as *membrane approximation*, which is addressed in Appendix A.

In summary, stationary points of $\Pi(\mathbf{F}, \boldsymbol{\varphi})$ for the rotationally symmetric inflation of a thick-walled tube can be represented with respect to the base systems in (2.15)–(2.20) as

$$\begin{aligned} \delta \Pi|_{\mathbf{X}} &= \int_{\partial \mathcal{B}_o} \delta \varphi_r P_{rR} R \, d\Theta \, dZ - \int_{\mathcal{B}_o} \left[\delta \varphi_r \left[\frac{\partial [R P_{rR}]}{\partial R} - P_{\theta\theta} \right] \right. \\ &\quad \left. + \delta \varphi_\theta \frac{\partial P_{\theta\theta}}{\partial \Theta} + \delta \varphi_z \frac{\partial [R P_{zz}]}{\partial Z} \right] dR \, d\Theta \, dZ \\ &\quad - \int_{\partial \mathcal{B}_{t_i}} \delta \varphi_r p \lambda_r^{-1} R \, d\Theta \, dZ - \int_{\partial \mathcal{B}_{o_o}} \delta \varphi_r \bar{t}_r R \, d\Theta \, dZ \quad (2.60) \\ &= \int_{\partial \mathcal{B}_t} \delta \varphi_r \sigma_{rr} r \, d\theta \, dz - \int_{\mathcal{B}_t} \left[\delta \varphi_r \left[\frac{\partial [r \sigma_{rr}]}{\partial r} - \sigma_{\theta\theta} \right] \right. \\ &\quad \left. + \delta \varphi_\theta \frac{\partial \sigma_{\theta\theta}}{\partial \theta} + \delta \varphi_z \frac{\partial [r \sigma_{zz}]}{\partial z} \right] dr \, d\theta \, dz \\ &\quad - \int_{\partial \mathcal{B}_{t_i}} \delta \varphi_r p r \, d\theta \, dz - \int_{\partial \mathcal{B}_{t_o}} \delta \varphi_r t_r r \, d\theta \, dz \doteq 0 \quad (2.61) \end{aligned}$$

with $\delta \boldsymbol{\varphi} = \delta \varphi_r \mathbf{e}_r + \delta \varphi_\theta \mathbf{e}_\theta + \delta \varphi_z \mathbf{e}_z$. Throughout this chapter, $P_{rR} = 0$ on $\partial \mathcal{B}_{o_o}$ is assumed, respectively $\sigma_{rr} = 0$ on $\partial \mathcal{B}_{t_o}$, but the tube could also interact with the ambient space such that the radial stresses do not vanish identically on the outer surface boundary. Note, that in the case of shear stresses being activated at the outer surface boundary, the stresses do not remain coaxial with respect to conjugated strain measures for the constitutive relations considered later on.

2.3 Analysis of a double-layered thick-walled tube

The structural response of a thick-walled double-layered arterial tube subjected to combined bending, inflation and extension is investigated by means of minimising the total

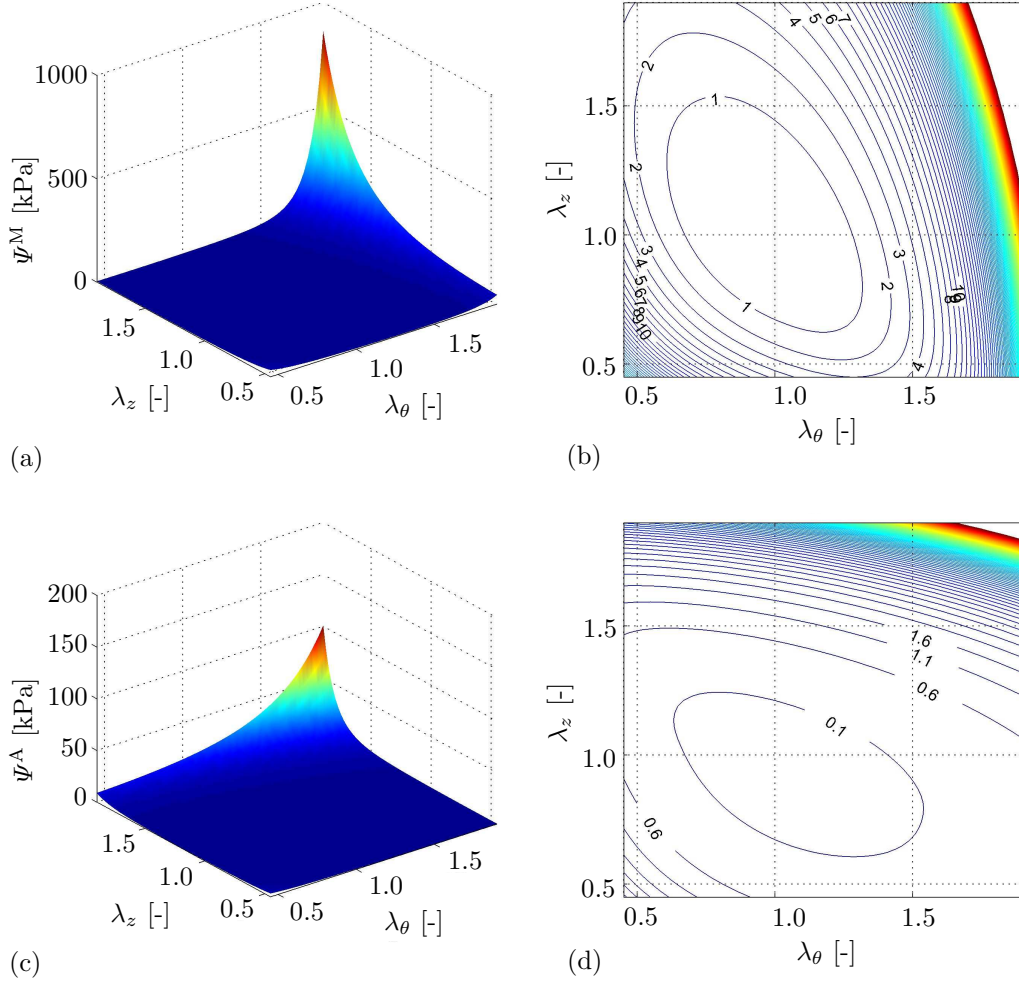


Figure 2.2: Contour plots of the strain energy density (2.62) for the media (a, b) and for the adventitia (c, d) based on the material parameters given in Table 2.1.

potential energy functional (2.41). Several multivariable optimisation problems with respect to combinations of up to five variables of loading-type and structure-type are set up and solved. The computational results are discussed and compared to physiological values taken from the literature.

2.3.1 Constitutive model

To set the stage, the underlying constitutive model adopted for the following investigations is briefly reviewed. To be specific, use of an orthotropic model with two families of fibres is made as introduced by Holzapfel et al. [135]; for a general review on the modelling of fibre reinforced materials the reader is also referred to Spencer [264] and the contributions in Spencer [265] and Boehler [43]. The strain energy density of this

2 Extremal states of energy of a double-layered thick-walled tube

model is assumed to additively decompose into an isotropic part $\Psi_{\text{iso}}^{\text{n}}$, representing the contribution of the non-collagenous ground material, and into an anisotropic part $\Psi_{\text{ani}}^{\text{n}}$, representing the contributions of the different families of collagen fibres, i.e.

$$\Psi^{\text{n}}(\mathbf{F}, \mathbf{a}_{01, \dots, N}^{\text{n}}) = \Psi_{\text{iso}}^{\text{n}}(\mathbf{F}) + \Psi_{\text{ani}}^{\text{n}}(\mathbf{F}, \mathbf{a}_{01, \dots, N}^{\text{n}}), \quad (2.62)$$

wherein $\text{n} = \text{M}$ represents the media and $\text{n} = \text{A}$ the adventitia. Moreover, $\mathbf{a}_{01, \dots, N}$ denotes a set of N referential unit-vectors characterising the fibre families considered. The isotropic part of the strain energy is specified by a common neo-Hookean format

$$\Psi_{\text{iso}}^{\text{n}}(\mathbf{F}) = \frac{\mu^{\text{n}}}{2} [I_1 - 3], \quad (2.63)$$

with

$$I_1 = \mathbf{F} : \mathbf{F} = \lambda_{\theta}^2 + \lambda_z^2 + \lambda_{\theta}^{-2} \lambda_z^{-2} \quad (2.64)$$

for $J \doteq 1$ so that $\Psi_{\text{iso}}^{\text{n}} = \Psi_{\text{ich}}^{\text{n}}$. The anisotropic part adopted takes the following exponential form

$$\Psi_{\text{ani}}^{\text{n}}(\mathbf{F}, \mathbf{a}_{01, \dots, N}^{\text{n}}) = \frac{k_1^{\text{n}}}{2 k_2^{\text{n}}} \sum_{i=1}^N [\exp(k_2^{\text{n}} \langle E_i^{\text{n}} \rangle^2) - 1], \quad (2.65)$$

wherein it is assumed that the fibres within each layer n are mechanically equivalent. The notation $\langle \bullet \rangle = [|\bullet| + \bullet]/2$ reflects the Macaulay brackets. These allow activation of the fibre contributions in the tension regime only. To be specific, the referential strain measure E_i^{n} is introduced as

$$E_i^{\text{n}} = \mathbf{a}_{0i}^{\text{n}} \cdot \mathbf{C} \cdot \mathbf{a}_{0i}^{\text{n}} - 1 = I_{4i}^{\text{n}} - 1. \quad (2.66)$$

Even though equation (2.66) does not include any dispersion of fibre contributions, the formulation can be extended to account for these as discussed in, for instance, Gasser et al. [107] and Menzel et al. [201]. The number of mechanically equivalent fibre families per layer is restricted to $N = 2$ and, moreover, their initial orientations are assumed as

$$\mathbf{a}_{01,2}^{\text{n}} = \sin(\beta^{\text{n}}) \mathbf{E}_Z \pm \cos(\beta^{\text{n}}) \mathbf{E}_{\theta}, \quad (2.67)$$

see the illustration in Figure 2.1(a). This kinematic relation together with equation (2.35) and $\gamma = 0$ renders stresses and conjugated strain measures to be coaxial. Furthermore, one observes $E_1^{\text{n}} = E_2^{\text{n}} \doteq E^{\text{n}}$ and the invariant introduced in equation (2.66) can be expressed as

$$I_{4i}^{\text{n}} = \mathbf{a}_{0i}^{\text{n}} \cdot \mathbf{C} \cdot \mathbf{a}_{0i}^{\text{n}} = \sin^2(\beta^{\text{n}}) \lambda_z^2 + \cos^2(\beta^{\text{n}}) \lambda_{\theta}^2. \quad (2.68)$$

In conclusion, the strain energy can be written as a function in terms of the circumferential and longitudinal stretch, i.e. $\tilde{\Psi}^{\text{n}}(\lambda_{\theta}, \lambda_z)$, as indicated in equation (2.41).

Table 2.1: Material, structural and geometrical parameters for a carotid artery of a rabbit adopted from Holzapfel et al. [135], respectively Chuong and Fung [68]. The index $n = M$ refers to the media, whereas $n = A$ refers to the adventitia. This parameter set is used throughout if not otherwise stated. Note, that the inner referential radii R_i^n are assumed to linearly depend on the opening angle α ; cf. equation (2.73).

| Type | Symbol | Description | Value | | Unit |
|-------------|---------------------------------|----------------------------|--------|------------|-------|
| | | | Media | Adventitia | |
| material | μ^n | elastic constant | 3.0 | 0.3 | [kPa] |
| | k_1^n | elastic constant | 2.3632 | 0.5620 | [kPa] |
| | k_2^n | elastic constant | 0.8393 | 0.7112 | [-] |
| structural | β^n | fibre angle | 29.0 | 62.0 | [deg] |
| geometrical | H^n | referential wall thickness | 0.26 | 0.13 | [mm] |
| | $L^n = R_i^M _{\alpha=0^\circ}$ | referential length | 0.71 | 0.71 | [mm] |
| | $R_i^n _{\alpha=0^\circ}$ | inner referential radius | 0.71 | 0.97 | [mm] |
| | $R_o^n _{\alpha=0^\circ}$ | outer referential radius | 0.97 | 1.1 | [mm] |
| | $R_i^n _{\alpha=160^\circ}$ | inner referential radius | 1.43 | 1.69 | [mm] |
| | $R_o^n _{\alpha=160^\circ}$ | outer referential radius | 1.69 | 1.82 | [mm] |

With these relations, the Cauchy stress tensor $\boldsymbol{\sigma}^n = \partial_{\mathbf{F}} \Psi^n \cdot \text{cof}(\mathbf{F}^{-1})$ can be specified, i.e.

$$\boldsymbol{\sigma}^n = \mu^n \mathbf{b} + 4 k_1^n E^n \exp(k_2 \langle E^n \rangle^2) [\mathbf{a}_1^n \otimes \mathbf{a}_1^n + \mathbf{a}_2^n \otimes \mathbf{a}_2^n] \quad (2.69)$$

with $\mathbf{a}_{1,2}^n = \mathbf{F} \cdot \mathbf{a}_{01,2}^n$. Alternatively, the Cauchy stress tensor can be expressed with respect to the base system introduced in equations (2.18)–(2.20), or rather in spectral form, as

$$\sigma_{rr}^n = \mu^n \lambda_\theta^{-2} \lambda_z^{-2} \quad (2.70)$$

$$\sigma_{\theta\theta}^n = \mu^n \lambda_\theta^2 + 4 \cos^2(\beta^n) k_1^n \lambda_\theta^2 E^n \exp(k_2 \langle E^n \rangle^2) \quad (2.71)$$

$$\sigma_{zz}^n = \mu^n \lambda_z^2 + 4 \sin^2(\beta^n) k_1^n \lambda_z^2 E^n \exp(k_2 \langle E^n \rangle^2) \quad (2.72)$$

Even though not highlighted, the Piola stresses can be represented by analogy with equations (2.69)–(2.72).

2.3.2 Material, structural and geometrical parameters

For reasons of comparability, the material, structural and geometrical parameters used in this chapter are adopted from Holzapfel et al. [135] as originally identified by Chuong and Fung [68]; see Table 2.1. Note, that in Holzapfel et al. [135] the inner referential radii

2 Extremal states of energy of a double-layered thick-walled tube

Table 2.2: Loading parameters included in the total potential energy (2.41). The pressure p directly enters the external potential energy, whereas the axial stretch λ_z and the opening angle α are included in the internal potential energy via the deformation gradient \mathbf{F} , see equation (2.35). The physiological values are adopted from Holzapfel et al. [135] and correspond to an inner circumferential stretch of $\lambda_{\theta_i}^{\text{phys}} = 1.604$, see equation (2.74). The discrete pressure values are related to the systolic blood pressure $p = 17.4$ [kPa], the diastolic blood pressure $p = 8.0$ [kPa] and the mean blood pressure $p = 13.33$ [kPa].

| Description | Load case | Physiological value | Value range | | Unit | |
|-------------|-------------------|---------------------|---------------------------------|-----------|--------------------|-------|
| | | | Continuous | Discrete | | |
| p | internal pressure | inflation | $p^{\text{phys}} = 13.33$ | 0.0–21.33 | {8.0, 13.33, 17.4} | [kPa] |
| λ_z | axial stretch | elongation | $\lambda_z^{\text{phys}} = 1.7$ | 0.2–1.9 | {0.2, 1.0, 1.9} | [–] |
| α | opening angle | bending | $\alpha^{\text{phys}} = 160.0$ | 0.0–160.0 | {0.0, 80.0, 160.0} | [deg] |

R_i^n are assumed to depend on the opening angle α . For the subsequent studies, where different opening angles α are considered, the inner referential radius R_i^M is linearly interpolated by means of

$$R_i^M(\alpha) = \frac{R_i^M|_{\alpha=160} - R_i^M|_{\alpha=0}}{160} \alpha + R_i^M|_{\alpha=0} \quad (2.73)$$

depending on the actual value of α , here included in unit-free form.

For illustration and comparison purposes, contour plots of the strain energy density (2.62) for the media and adventitia based on the parameters summarised in Table 2.1 are depicted in Figure 2.2; cf. Holzapfel et al. [135]. According to the constitutive assumption that only the ground substance contributes in case of compressive loading, one observes an isotropic behaviour in the in-plane compression range, i.e. for $\lambda_\theta < 1$ and $\lambda_z < 1$, which is reflected by the symmetric contour lines within this region. In contrast, for in-plane tensile loading, i.e. $\lambda_\theta > 1$ and $\lambda_z > 1$, the collagen fibres essentially affect the constitutive behaviour, and one consequently obtains an anisotropic response. In this regard, one observes that the directions of largest ascent are essentially different for the media and adventitia, see Figure 2.2(b, d).

2.3.3 Loading parameters

In the following, parameters essentially affecting the deformation of the specimen are referred to as ‘loading parameters’. The loading parameters used in this chapter are adopted from Holzapfel et al. [135] and summarised in Table 2.2. For later evaluation and comparison, the physiological inner circumferential stretch $\lambda_{\theta_i}^{\text{phys}}$ corresponding to the physiological values in Table (2.2) can be computed by means of the relation

$$\lambda_{\theta_i}^{\text{phys}} = \frac{k r_i}{R_i}. \quad (2.74)$$

For $\alpha = 160$ [deg], $r_i = 1.274$ [mm] and $R_i = 1.43$ [mm], this results in a value of $\lambda_{\theta_i}^{\text{phys}} = 1.604$.

2.3.4 Algorithmic treatment

The solution of the underlying boundary value problem is obtained by means of the minimisation of the related total potential energy functional (2.41), i.e.

$$\lambda_{\theta_i}^{\min} = \arg \min_{\lambda_{\theta_i}} \Pi(\lambda_{\theta_i}, \lambda_z \doteq \text{const}; \lambda_{\theta_i}^0, \boldsymbol{\kappa}), \quad (2.75)$$

with respect to the primary variable λ_{θ_i} using an initial guess $\lambda_{\theta_i}^0$ and a pseudo-vector $\boldsymbol{\kappa}$ which summarises the material, structural and geometrical parameters as well as the loading parameters.

Such minimisation problems may conveniently be solved by typical optimisation techniques available in commercial software packages used for numerical calculations as, e.g., Matlab. In this study, the Matlab optimisation-algorithm `fmincon` is used which is based on a sequential quadratic programming (SQP) method. Without discussing specific algorithmic details at this stage, this algorithm allows us to find a constrained minimum of a scalar function of one or more variables, whereby initial estimate values must be set. For detailed background information on such constrained nonlinear optimisation problems, the reader is referred to the monographs by Luenberger [190], Bertsekas [41] and Dennis, Jr., and Schnabel [81].

Solving the aforementioned minimisation problem (2.75) for the single primary variable λ_{θ_i} , see Tables 2.3 and 2.4, is equivalent to solving the corresponding Euler Lagrange equations in form of equations (2.47)–(2.49) or equations (2.54)–(2.56). In addition to minimising Π with respect to λ_{θ_i} , one could also think of solving for extrema of the total or internal potential energy functional with respect to the loading parameters or structural parameters or combinations thereof. In the following, settings of structural or loading parameters, which lead to stationary points of the total or internal potential energy in states of equilibrium, are calculated and it is discussed whether such extremal states of energy can be referred to an optimal or rather natural design of arterial walls.

In view of the algorithm implemented, it is important to note that those problems involving the fibre angles β^n as variable quantities rely on a modified computational strategy: the minimisation is first performed for those variables not related to the fibre angles β^n , then followed by a maximisation with respect to the fibre angles β^n . Alternatively, one could also think of minimising the energy with respect to β^n . The physical interpretation of an adaptive biological tissue suggests, however, that its loading capacity is maximised so that the internal energy is maximised in the case of Dirichlet

2 Extremal states of energy of a double-layered thick-walled tube

Table 2.3: Algorithm to minimise $\Pi(\lambda_{\theta i}, \lambda_z \doteq \text{const}; \lambda_{\theta i}^0, \boldsymbol{\kappa})$ as given in equation (2.41).

1. set up material, structural and geometrical parameters from Table 2.1 for media, $n = M$, and adventitia, $n = A$, as well as loading parameters from Table 2.2 and collect these in pseudo-vector $\boldsymbol{\kappa}$
2. perform initial guess $\lambda_{\theta i}^0$ for the primary variable, which is the inner circumferential stretch
3. compute argument of minimum of total energy (2.41)

$$\lambda_{\theta i}^{\min} = \arg \min_{\lambda_{\theta i}} \Pi(\lambda_{\theta i}, \lambda_z \doteq \text{const}; \lambda_{\theta i}^0, \boldsymbol{\kappa}) ,$$
 wherein Π is determined by the algorithm given in Table 2.4 and the minimisation can be performed by, e.g., the Matlab `fmincon`-optimisation-function

boundary conditions. To give an example, the optimisation in the present context can be understood as

$$\left\{ \beta^{M \text{opt}}, \beta^{A \text{opt}} \right\} = \arg \underset{\beta^M, \beta^A; \lambda_{\theta i}, \lambda_z, \alpha}{\text{opt}} \Pi^*(\lambda_{\theta i}, \lambda_z, \alpha, \beta^M, \beta^A; \boldsymbol{\kappa}^*) \quad (2.76)$$

$$= \arg \max_{\beta^M, \beta^A} \left\{ \min_{\lambda_{\theta i}, \lambda_z, \alpha} \Pi^*(\lambda_{\theta i}, \lambda_z, \alpha, \beta^M, \beta^A; \boldsymbol{\kappa}^*) \right\}. \quad (2.77)$$

In other words, the total potential energy Π is first minimised with respect to variables $\{\lambda_{\theta i}, \lambda_z, \alpha\}$, which results in the quadruple $\{\lambda_{\theta i}^{\min}, \lambda_z^{\min}, \alpha^{\min}, \Pi^{\min}\}$. Thereafter, the result is studied by means of a simple max-function applied to Π^{\min} , which renders $\{\beta^{M \text{opt}}, \beta^{A \text{opt}}\}$ that maximise Π^{\min} in states of equilibrium.

Remark 2.3.1 *Note, that a closed-form evaluation of the integral in equation (2.41) is generally not available due to the non-linearity of the constitutive model. In analogy to Holzapfel et al. [135], an $m = 3$ -point Gaussian integration scheme with fifth-order accuracy is applied, see Table 2.4, which turns out to be sufficiently accurate for the computation of the energy expressions and stress contributions of interest within the range of deformations considered.*

2.3.5 Results

In the following, the results of the optimisation of the total potential energy functional (2.41) with respect to different parameters are presented and discussed. The underlying multivariable optimisation problems are performed in view of combinations of five, four, three and two parameters of loading type, $\{\lambda_z, \alpha, p\}$, and structural type, $\{\beta^n\}$, i.e.

Table 2.4: Algorithmic determination of functional $\Pi(\lambda_{\theta_i}, \lambda_z \doteq \text{const}; \lambda_{\theta_i}^0, \boldsymbol{\kappa})$ as given in equation (2.41).

1. given: material, structural and geometrical parameters, see Table 2.1, and loading parameters, see Table 2.2, summarised in pseudo-vector $\boldsymbol{\kappa}$
2. calculate opening angle measure

$$k = 2\pi / [2\pi - \alpha]$$
3. calculate current radii of media

$$r_i^M = \lambda_{\theta_i} R_i^M / k$$

$$r_o^M = \sqrt{[R_o^M]^2 - [R_i^M]^2} / [k \lambda_z] + [r_i^M]^2$$
4. calculate current radii of adventitia

$$r_i^A = r_o^M$$

$$r_o^A = \sqrt{[R_o^A]^2 - [R_i^A]^2} / [k \lambda_z] + [r_i^A]^2$$
5. apply $m = 3$ -point Gaussian quadrature rule for $n = M, A$ with quadrature points $\xi_j = \{-\sqrt{3/5} \ 0 \ \sqrt{3/5}\}$ and weights $w_j = \{5/9 \ 8/9 \ 5/9\}$:
 loop over number of quadrature points $j = 1, \dots, m$
 - (a) calculate current radius

$$r_j = [r_i^n + r_o^n] / 2 + \xi_j [r_o^n - r_i^n] / 2$$
 - (b) calculate referential radius

$$R_j = \sqrt{k \lambda_z [r_j^2 - [r_i^n]^2] + [R_i^n]^2}$$
 - (c) calculate circumferential stretch

$$\lambda_{\theta_j} = k r_j / R_j$$
 - (d) calculate strain energy density

$$\Psi_j^n = \tilde{\Psi}^n(\lambda_{\theta_j}, \lambda_z \doteq \text{const})$$
 by means of equations (2.62, 2.63, 2.65)
 calculate internal potential energy

$$\Pi_{\text{int}}^n \approx \pi l [r_o^n - r_i^n] \sum_{j=1}^m \Psi_j^n r_j w_j$$
6. calculate external potential energy

$$\Pi_{\text{ext}} = -p \pi [r_i^M]^2 l$$
7. calculate total potential energy

$$\Pi = \Pi_{\text{int}}^M + \Pi_{\text{int}}^A + \Pi_{\text{ext}}$$

$$\min_{\lambda_{\theta_i}, \lambda_z, \alpha} \bar{\Pi}(\lambda_{\theta_i}, \lambda_z, \alpha; \bar{\boldsymbol{\kappa}}) \quad (2.78)$$

$$\text{opt}_{\beta^M, \beta^A; \lambda_{\theta_i}, \lambda_z, \alpha} \Pi^*(\lambda_{\theta_i}, \lambda_z, \alpha, \beta^M, \beta^A; \boldsymbol{\kappa}^*) \quad (2.79)$$

$$\min_{\lambda_{\theta_i}, \lambda_z} \tilde{\Pi}(\lambda_{\theta_i}, \lambda_z; \tilde{\boldsymbol{\kappa}}) \quad (2.80)$$

$$\text{opt}_{\beta^M, \beta^A; \lambda_{\theta_i}, \lambda_z} \Pi^*(\lambda_{\theta_i}, \lambda_z, \beta^M, \beta^A; \boldsymbol{\kappa}^*) \quad (2.81)$$

$$\text{opt}_{\beta; \lambda_{\theta_i}, \lambda_z} \Pi^*(\lambda_{\theta_i}, \lambda_z, \beta, \beta; \boldsymbol{\kappa}^*) \quad (2.82)$$

$$\min_{\lambda_{\theta_i}, \alpha} \check{\Pi}(\lambda_{\theta_i}, \alpha; \check{\boldsymbol{\kappa}}) \quad (2.83)$$

$$\text{opt}_{\beta^M, \beta^A; \lambda_{\theta_i}, \alpha} \Pi^\diamond(\lambda_{\theta_i}, \alpha, \beta^M, \beta^A; \boldsymbol{\kappa}^\diamond) \quad (2.84)$$

$$\text{opt}_{\beta; \lambda_{\theta_i}, \alpha} \Pi^\diamond(\lambda_{\theta_i}, \alpha, \beta, \beta; \boldsymbol{\kappa}^\diamond) \quad (2.85)$$

$$\min_{\lambda_{\theta_i}, p} \hat{\Pi}(\lambda_{\theta_i}, p; \hat{\boldsymbol{\kappa}}) \quad (2.86)$$

$$\text{opt}_{\beta^M, \beta^A; \lambda_{\theta_i}} \Pi^\Delta(\lambda_{\theta_i}, \beta^M, \beta^A; \boldsymbol{\kappa}^\Delta) \quad (2.87)$$

$$\text{opt}_{\beta; \lambda_{\theta_i}} \Pi^\Delta(\lambda_{\theta_i}, \beta, \beta; \boldsymbol{\kappa}^\Delta) \quad (2.88)$$

Note, that $\lambda_{\theta_i}^0$ is not explicitly indicated in the energy function above. Moreover, identical fibre orientations within the media and adventitia are assumed, i.e. $\beta^M = \beta^A = \beta$, for some of the subsequent investigations; see equations (2.82, 2.85, 2.88). In order to structure the examples discussed in the following, minimisation problems are typically investigated first, followed by related optimisation studies. Furthermore, the most general cases are addressed first and thereafter reduced to specific applications. In other words, results from the more general cases are transferred to simpler minimisation and optimisation problems in order to render a better illustration of the results obtained.

2.3.5.1 Minimisation of $\bar{\Pi}(\lambda_{\theta_i}, \lambda_z, \alpha; \bar{\boldsymbol{\kappa}})$

In the following, the minimisation of the three-variable energy functional $\bar{\Pi}$ with respect to the inner circumferential stretch λ_{θ_i} , the axial (residual) stretch λ_z and the opening angle α is investigated; cf. (2.78). The pressure is set to the physiological value $p^{\text{phys}} = 13.33$ [kPa].

Figure 2.3(a) depicts the solution space $\{\lambda_{\theta_i}^{\min}, \lambda_z, \alpha\}$ of the minimisation of $\bar{\Pi}$. The colour code used in Figure 2.3(a) illustrates the value of the total potential energy Π^{\min} ; cf. (2.75). Moreover, Figure 2.3(b) shows the total potential energy Π^{\min} over λ_z and α , the colour code refers to the primary variable $\lambda_{\theta_i}^{\min}$. The red spot at $\lambda_{\theta_i}^{\min} = 1.657$,

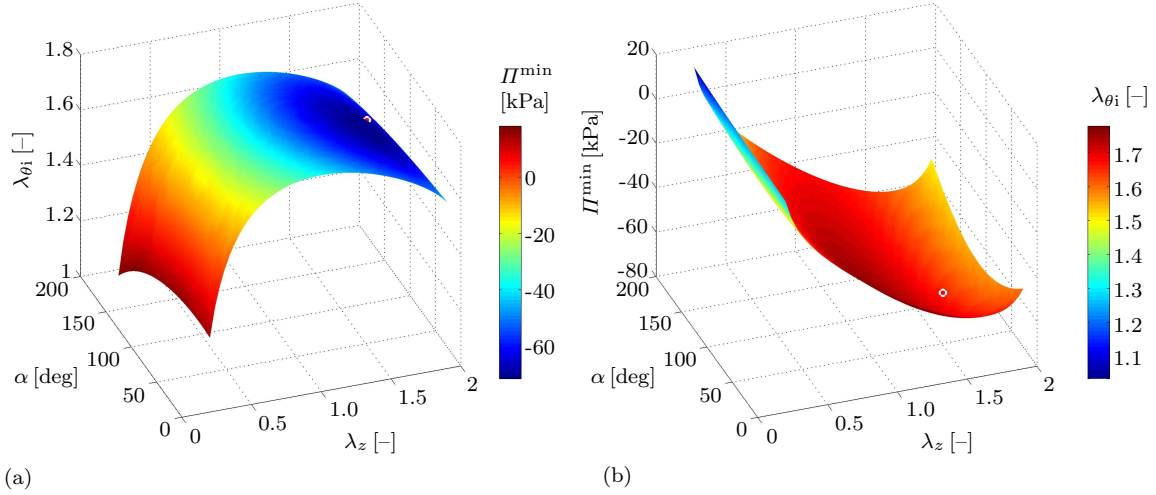


Figure 2.3: Plots of the solution space of minimisation problem (2.78). Figure (a) depicts the inner circumferential stretch λ_{θ_i} over the axial stretch λ_z and the opening angle α , whereby the colour code refers to the total potential energy Π^{\min} . Figure (b) shows the total potential energy Π^{\min} over λ_z and α , whereby the colour code refers to the primary variable λ_{θ_i} . The red spot at $\lambda_{\theta_i}^{\min} = 1.657$, $\lambda_z^{\min} = 1.654$ and $\alpha^{\min} = 90.609$ [deg] corresponds to the minimal total potential energy Π^{\min} on this constrained equilibrium-surface, see also Table 2.5.

Table 2.5: Results of the minimisation problem (2.78). The initial values are set to $\lambda_{\theta_i}^0 = 1.0$, $\lambda_z^0 = 1.0$ and $\alpha^0 = 90.0$ [deg]. The superscript \bullet^{\min} is omitted.

| λ_{θ_i} [-] | λ_z [-] | α [deg] | $\bar{\Pi}$ [kPa] |
|--------------------------|-----------------|----------------|-------------------|
| 1.657 | 1.654 | 90.609 | -71.724 |

$\lambda_z^{\min} = 1.654$ and $\alpha^{\min} = 90.609$ [deg], associated with the solution of the minimisation problem (2.78), corresponds to the minimal total potential energy $\bar{\Pi}^{\min}$ on this constrained equilibrium-surface, see also Table 2.5.

Interestingly, the stretch-values $\lambda_{\theta_i}^{\min} = 1.657$ and $\lambda_z^{\min} = 1.654$ correspond quite well to the physiological values $\lambda_{\theta_i}^{\text{phys}} = 1.604$ and $\lambda_z^{\text{phys}} = 1.7$. The corresponding opening angle $\alpha^{\min} = 90.609$ [deg], however, differs significantly from its physiological counterpart $\alpha^{\text{phys}} = 160.0$ [deg]. From Figure 2.3(a), one observes that in the case of a constant axial stretch λ_z and an increasing opening angle α the inner circumferential stretch λ_{θ_i} decreases, whereas the potential energy Π in Figure 2.3(b) increases.

2.3.5.2 Optimisation of $\Pi^*(\lambda_{\theta_i}, \lambda_z, \alpha, \beta^M, \beta^A; \kappa^*)$

The optimisation of the five-variable energy functional Π^* with respect to the inner circumferential stretch λ_{θ_i} , the axial (residual) stretch λ_z , the opening angle α and both fibre angles β^M and β^A is discussed next; cf. (2.79). The pressure is set to the physiological value $p^{\text{phys}} = 13.33$ [kPa].

2 Extremal states of energy of a double-layered thick-walled tube

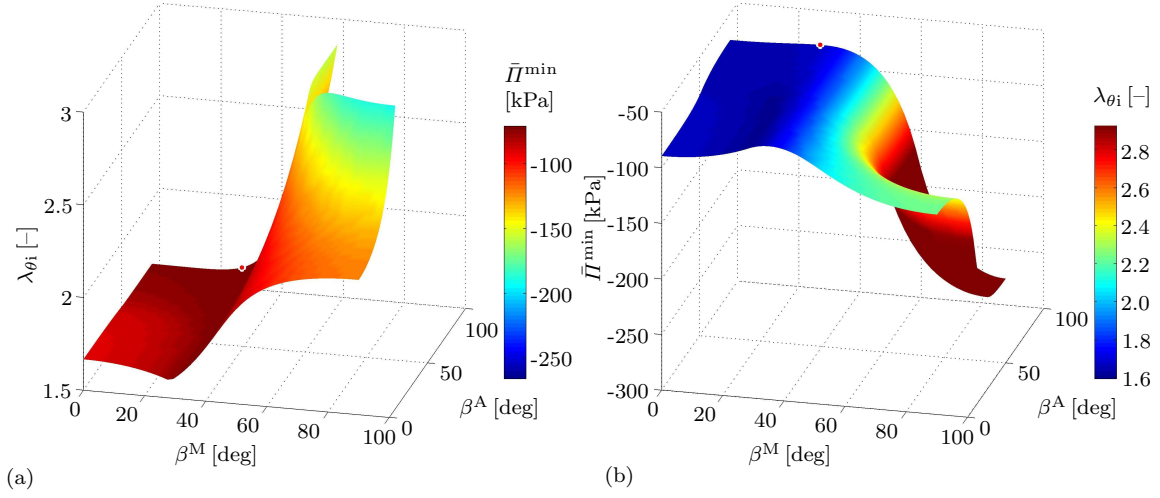


Figure 2.4: Plots of subsets of the solution space of optimisation problem (2.79). Figure (a) depicts the inner circumferential stretch $\lambda_{\theta_i}^{\min}$ over the medial and adventitial fibre angle β^M and β^A , whereby the colour code refers to the total potential energy $\bar{\Pi}^{\min}$. Figure (b) shows the total potential energy $\bar{\Pi}^{\min}$ over β^M, β^A , whereby the colour code refers to the primary variable $\lambda_{\theta_i}^{\min}$. The red spot at $\lambda_{\theta_i}^{\text{opt}} = 1.676$, $\beta^M \text{ opt} = 29.388$ [deg] and $\beta^A \text{ opt} = 90.000$ [deg] corresponds to the optimal total potential energy $\Pi^{*\text{opt}}$ on this constrained equilibrium-surface, see also Table 2.6.

Table 2.6: Results of the optimisation problem (2.79). The initial values are set to $\lambda_{\theta_i}^0 = 1.0$, $\lambda_z^0 = 1.0$, $\alpha^0 = 90.0$ [deg]. The superscript \bullet^{opt} is omitted.

| λ_{θ_i} [-] | λ_z [-] | α [deg] | β^M [deg] | β^A [deg] | Π^* [kPa] |
|--------------------------|-----------------|----------------|-----------------|-----------------|---------------|
| 1.676 | 1.593 | 91.263 | 29.388 | 90.000 | -70.833 |

Figure 2.4(a) depicts the subset $\{\lambda_{\theta_i}^{\min}, \beta^M, \beta^A\}$ of the solution space of the corresponding minimisation of $\bar{\Pi}$. The colour code used in Figure 2.4(a) illustrates the value of the minimised total potential energy $\bar{\Pi}^{\min}$; cf. (2.78). Moreover, Figure 2.4(b) shows the total potential energy $\bar{\Pi}^{\min}$ over β^M and β^A , the colour code refers to the primary variable $\lambda_{\theta_i}^{\min}$. The red spot at $\lambda_{\theta_i}^{\text{opt}} = 1.676$, $\beta^M \text{ opt} = 29.388$ [deg] and $\beta^A \text{ opt} = 90.000$ [deg], associated with the solution of the optimisation problem (2.79), corresponds to the optimal total potential energy $\Pi^{*\text{opt}}$ on this constrained equilibrium-surface. For ease of reference, essential results are also summarised in Table 2.6.

Even though the opening angle $\alpha^{\min} = 91.263$ [deg] significantly deviates from the physiological value of $\alpha^{\text{phys}} = 160.0$ [deg], the resulting values for the inner circumferential stretch $\lambda_{\theta_i}^{\text{opt}} = 1.676$, the axial (residual) stretch $\lambda_z^{\text{opt}} = 1.593$ and especially the result for the fibre angle in the media $\beta^M \text{ opt} = 29.388$ [deg] correspond remarkably well to their physiological counterparts $\lambda_{\theta_i}^{\text{phys}} = 1.604$, $\lambda_z^{\text{phys}} = 1.7$ and $\beta^M \text{ phys} = 29.0$ [deg], see Tables 2.1 and 2.2.

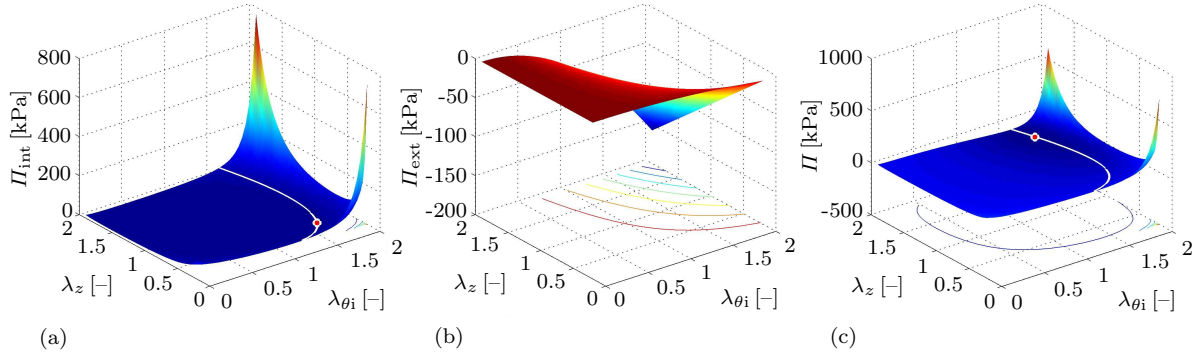


Figure 2.5: Illustration of minimisation problem (2.80). Surface plot of the (a) internal, (b) external and (c) total potential energy over $\lambda_{\theta i}$ and λ_z for the material, structural and geometrical parameters as given in Table 2.1 and an internal pressure of $p^{\text{phys}} = 13.33$ [kPa]. The opening angle α is assumed as $\alpha^{\text{min}} = 90.609$ [deg] as identified by the minimisation problem (2.78), see Table 2.5. The white lines in (a) and (c) illustrate the equilibrium-path. The red spot in (a) at $\lambda_{\theta i} = 1.624$ and $\lambda_z = 0.478$ represents the minimal internal potential energy on this constrained equilibrium-path. The red spot in (c) at $\lambda_{\theta i}^{\text{min}} = 1.657$ and $\lambda_z^{\text{min}} = 1.654$ represents the minimal total potential energy on this constrained equilibrium-path.

Table 2.7: Parameter study of the minimisation problem (2.80) prescribing different combinations of the internal pressure p and the opening angle α . Within rows 1–4, parameters according to Table 2.1 are used whereas row 5 results from the minimisation problem (2.78) and provides the numerical values of the red spot in Figure 2.5. The superscript \bullet^{min} is omitted.

| Input | | Output | | |
|-----------|----------------|--------------------------|-----------------|---------------------|
| p [kPa] | α [deg] | $\lambda_{\theta i}$ [-] | λ_z [-] | $\tilde{\Pi}$ [kPa] |
| 0.000 | 0.000 | 1.000 | 1.000 | 0.000 |
| 13.330 | 0.000 | 1.693 | 1.642 | -53.230 |
| 0.000 | 160.000 | 0.915 | 1.002 | 0.015 |
| 13.330 | 160.000 | 1.616 | 1.657 | -60.600 |
| 13.330 | 90.609 | 1.657 | 1.654 | -71.720 |

With regard to the medial fibre angle $\beta^{\text{M opt}}$, the good correspondence may be explained by the fact that the media is by far the stiffest component of a (healthy) artery which consequently carries the main load, especially for the present case of a mean pressure level of $p^{\text{phys}} = 13.33$ [kPa]. In contrast, the influence of the adventitial fibre angle β^{A} on the total potential energy $\bar{\Pi}^{\text{min}}$ for medial fibre angles in the range $\beta^{\text{M}} = 25.0\text{--}50.0$ [deg] is almost negligible, i.e. $\bar{\Pi}^{\text{min}} \approx \text{const}$ for $\beta^{\text{A}} \in [0, 90]$ [deg] in the range $\beta^{\text{M}} = 25.0\text{--}50.0$ [deg], see Figure 2.4(b). This means that—within this range— β^{A} can take any value between 0.0 [deg] and 90.0 [deg] without significant changes in total potential energy $\bar{\Pi}^{\text{min}}$. For larger values of both fibre angles in a range of $\beta^{\text{n}} = 60.0\text{--}90.0$ [deg], however, a sudden decrease in total potential energy $\bar{\Pi}^{\text{min}}$ is observed which

clearly illustrates the reduced load bearing capability for fibre angles oriented in almost axial direction of the artery at this particular state of deformation.

Interestingly, fibre angles of $\beta^M = 27.551$ [deg] and $\beta^A = 34.898$ [deg] lead to a minimal inner circumferential stretch $\lambda_{\theta_i} = 1.594$ which obviously is not identical with the location where the optimal total potential energy $\Pi^{*\text{opt}}$ is obtained. Even if, in this case, the medial fibre angle corresponds quite well to the physiological value again, a significant deviation with respect to the adventitial fibre angle and a large deviation with respect to the inner circumferential stretch is obtained.

2.3.5.3 Minimisation of $\tilde{\Pi}(\lambda_{\theta_i}, \lambda_z; \tilde{\kappa})$

The minimisation of the two-variable energy functional $\tilde{\Pi}$ with respect to the inner circumferential stretch λ_{θ_i} and the axial (residual) stretch λ_z is discussed; cf. (2.80). The material, structural and geometrical parameters used are chosen as given in Table 2.1 and the internal pressure is set to the physiological value of $p^{\text{phys}} = 13.33$ [kPa]. Moreover, the opening angle α , associated with the circumferential residual stretch, is assumed as $\alpha^{\text{min}} = 90.609$ [deg] which corresponds to the value calculated for the minimisation problem (2.78), see also Table 2.5. Practically speaking, the minimisation problem addressed here constitutes a special case of the problem discussed in Section 2.3.5.3, but allows us to conveniently visualise quantities of interest for a pre-fixed value for α .

Figure 2.5 shows the (a) internal, (b) external and (c) total potential energy Π over λ_{θ_i} and λ_z . Figures 2.5(a) and 2.5(b) underline the significant influence of the axial stretch λ_z on the internal, as well as on the external potential energy contribution. Using the algorithm summarised in Table 2.3, the white line within the plot of the total potential energy in Figure 2.5(c) is associated with the solution of the minimisation problem (2.75) and, in consequence, represents the equilibrium-path. The red spot at $\lambda_{\theta_i}^{\text{min}} = 1.657$ and $\lambda_z^{\text{min}} = 1.654$, associated with the solution of the minimisation problem (2.80), represents the minimum value of the total potential energy on this constrained equilibrium-path; see also the last row in Table 2.7. It is remarkable that the related value of the (residual) axial stretch value corresponds very well to the assumed physiological value of $\lambda_z^{\text{phys}} = 1.7$, cf. also the values in Table 2.2 which are considered to be physiological.

Moreover, a small parameter study for the minimisation problem (2.80) is performed by prescribing different combinations of the internal pressure p and the opening angle α . The corresponding results are summarised in Table 2.7. Within rows 1–4, parameters according to Table 2.1 are used, whereas row 5 results from the minimisation problem (2.78) and provides the numerical values of the red spot in Figure 2.5. Interestingly, the minimum total potential energy is obtained for $\alpha = 90.609$ [deg], which, however does not yield the minimal inner circumferential stretch λ_{θ_i} , which is obtained for $\alpha = 160.0$ [deg]. In addition, one observes that the values of the axial stretch λ_z are very similar in the case of $p^{\text{phys}} = 13.33$ [kPa] and correspond very well to the assumed physiological value of $\lambda_z^{\text{phys}} = 1.7$.

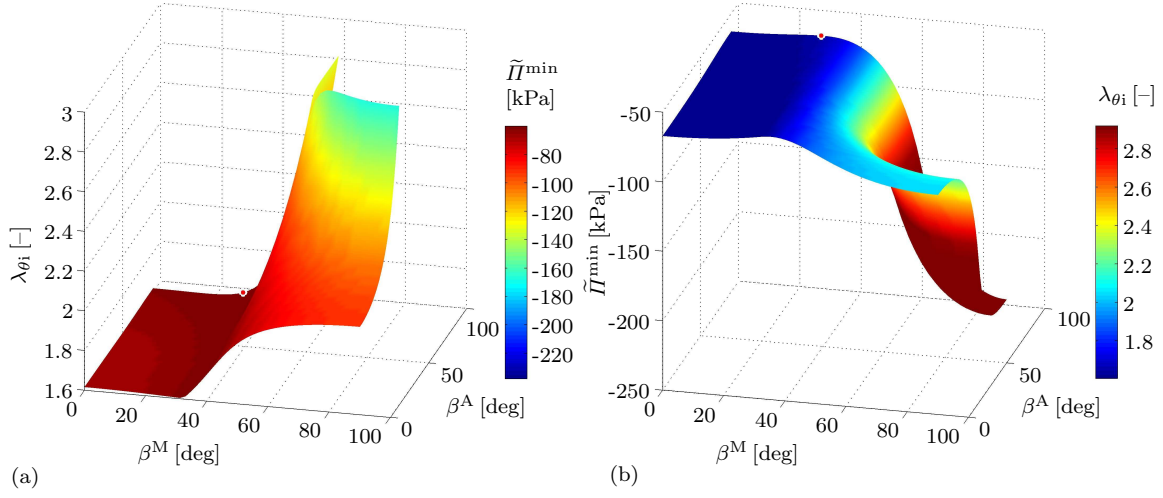


Figure 2.6: Plots of subsets of the solution space of optimisation problem (2.81). Figure (a) depicts the inner circumferential stretch $\lambda_{\theta_i}^{\min}$ over the medial and adventitial fibre angle β^M and β^A , whereby the colour code refers to the total potential energy $\tilde{\Pi}^{\min}$. Figure (b) shows the total potential energy $\tilde{\Pi}^{\min}$ with respect to β^M, β^A , whereby the colour code refers to the primary variable $\lambda_{\theta_i}^{\min}$. The red spot at $\lambda_{\theta_i}^{\text{opt}} = 1.638$, $\beta^M{}^{\text{opt}} = 29.388$ [deg] and $\beta^A{}^{\text{opt}} = 90.000$ [deg] corresponds to the optimal total potential energy $\Pi^{*\text{opt}}$ on this constrained equilibrium-surface, see also Table 2.8.

Table 2.8: Results of the minimisation problem (2.81). The initial values are set to $\lambda_{\theta_i}^0 = 1.0$ and $\lambda_z^0 = 1.0$. The superscript \bullet^{opt} is omitted.

| λ_{θ_i} [-] | λ_z [-] | β^M [deg] | β^A [deg] | Π^* [kPa] |
|--------------------------|-----------------|-----------------|-----------------|---------------|
| 1.638 | 1.587 | 29.388 | 90.000 | -60.053 |

2.3.5.4 Optimisation of $\Pi^*(\lambda_{\theta_i}, \lambda_z, \beta^M, \beta^A; \kappa^*)$

The optimisation of the four-variable energy functional Π^* with respect to the inner circumferential stretch λ_{θ_i} , the axial (residual) stretch λ_z and both fibre angles β^M and β^A is addressed in this subsection; cf. (2.81). The pressure is set to the physiological value $p^{\text{phys}} = 13.33$ [kPa] and the opening angle is fixed as $\alpha^{\text{phys}} = 160.0$ [deg].

Figure 2.6(a) depicts the subset $\{\lambda_{\theta_i}^{\min}, \beta^M, \beta^A\}$ of the solution space of the corresponding minimisation of $\tilde{\Pi}$; cf. (2.80). The colour code illustrates the value of the minimised total potential energy $\tilde{\Pi}^{\min}$. Moreover, Figure 2.6(b) shows the total potential energy $\tilde{\Pi}^{\min}$ over β^M and β^A , the colour code refers to the primary variable $\lambda_{\theta_i}^{\min}$. The red spot at $\lambda_{\theta_i}^{\text{opt}} = 1.638$, $\beta^M{}^{\text{opt}} = 29.388$ [deg] and $\beta^A{}^{\text{opt}} = 90.000$ [deg], associated with the solution of the optimisation problem (2.81), corresponds to the optimal total potential energy $\Pi^{*\text{opt}}$ on this constrained equilibrium-surface. Essential results are summarised in Table 2.8. The results obtained, especially with regard to the optimal fibre angles $\beta^M{}^{\text{opt}}$ and $\beta^A{}^{\text{opt}}$, are qualitatively and quantitatively very similar to the previous ones

summarised in Table 2.6 and illustrated in Figures 2.4. In fact, the optimisation problem considered in this subsection is a special case of the problem discussed in Section 2.3.5.2 but with the value of α fixed.

2.3.5.5 Optimisation of $\Pi^*(\lambda_{\theta_i}, \lambda_z, \beta, \beta; \kappa^*)$

As a special case of the optimisation problem in Section 2.3.5.4, the optimisation of the three-variable energy functional Π^* with respect to the inner circumferential stretch λ_{θ_i} , the axial (residual) stretch λ_z and the (identical) fibre angle for the media and adventitia $\beta = \beta^M = \beta^A$ is performed next; cf. (2.82). The pressure is set to the physiological value $p^{\text{phys}} = 13.33$ [kPa], and the opening angle is prescribed as $\alpha^{\text{phys}} = 160.0$ [deg].

Figure 2.7(a) depicts the subset $\{\lambda_{\theta_i}^{\text{min}}, \lambda_z, \beta\}$ of the solution space of the corresponding minimisation of $\tilde{\Pi}$. The colour code used in Figure 2.7(a) illustrates the value of the total potential energy $\tilde{\Pi}^{\text{min}}$. Figure 2.7(b) shows the total potential energy $\tilde{\Pi}^{\text{min}}$ over λ_z and β ; cf. (2.80). The colour code refers to the primary variable $\lambda_{\theta_i}^{\text{min}}$. The red spot at $\lambda_{\theta_i}^{\text{opt}} = 1.625$, $\lambda_z^{\text{opt}} = 1.637$ and $\beta^{\text{opt}} = 33.158$ [deg], associated with the solution of the optimisation problem (2.82), corresponds to the optimal total potential energy $\Pi^{*\text{opt}}$ on this constrained equilibrium-surface, see also Table 2.9.

One observes from Figure 2.7(a, b) that, for smaller axial stretch values in a range of $\lambda_z = 0.2$ – 1.75 , the inner circumferential stretch $\lambda_{\theta_i}^{\text{min}}$ increases continuously with an increasing fibre angle β . This is a consequence of the fact that—within this range—the pressure p dominates the response in the arterial wall. It becomes apparent that fibres predominantly aligned with respect to the circumferential direction are more appropriate to support the pressure-dominated loading, and thus enable lower circumferential stretches within the arterial wall. Interestingly, this effect is reversed upon a limit axial stretch value of about $\lambda_z = 1.7$ – 1.8 . To be specific, a plateau-like region can be identified for almost constant axial stretches of $\lambda_z = 1.7$ – $1.8 \approx \text{const}$ and fibre angles of $\beta = 60.0$ – 80.0 [deg], which lead to a significant decrease of the inner circumferential stretch $\lambda_{\theta_i}^{\text{min}}$. A similar interpretation can, later on, be taken from Figure 2.15 which is based on minimisation problem (2.88).

2.3.5.6 Minimisation of $\check{\Pi}(\lambda_{\theta_i}, \alpha; \check{\kappa})$

The minimisation of the two-variable energy functional $\check{\Pi}$ with respect to the inner circumferential stretch λ_{θ_i} and the opening angle α is elaborated on next; cf. (2.83).

Figure 2.8 shows the (a) internal, (b) external and (c) total potential energy $\check{\Pi}$ over λ_{θ_i} and α for the parameters as given in Table 2.1. The axial (residual) stretch is assumed as $\lambda_z^{\text{min}} = 1.654$ and the opening angle, associated with the circumferential residual stretch, is set to $\alpha^{\text{min}} = 90.609$ [deg] as identified by the minimisation problem (2.78), see also Table 2.5.

One observes from Figure 2.8(a) that the internal potential energy changes slightly with varying opening angle α , while Figure 2.8(b) highlights the dependency of the

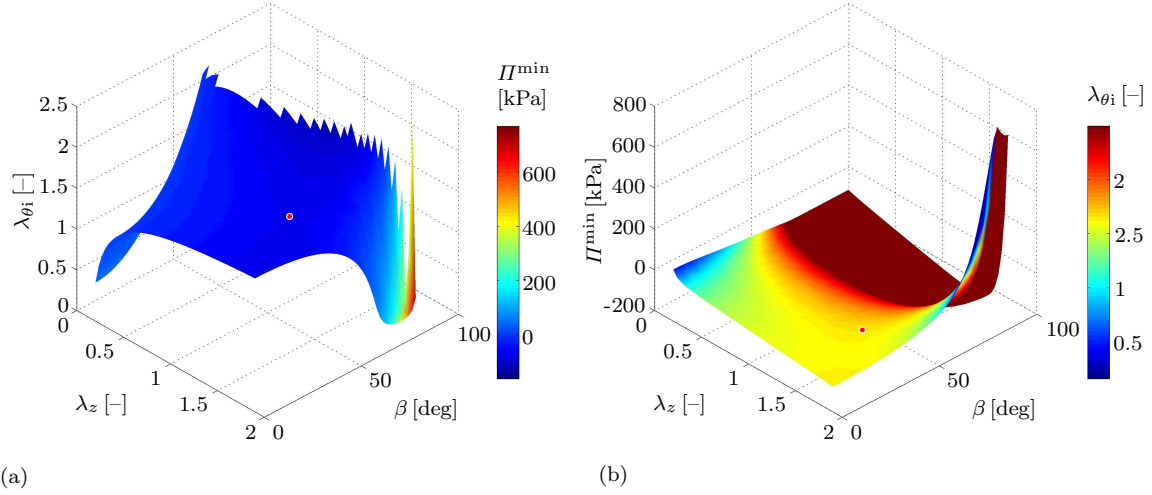


Figure 2.7: Plots of the solution space of optimisation problem (2.82). Figure (a) depicts the inner circumferential stretch $\lambda_{\theta_i}^{\min}$ over the axial stretch λ_z and the fibre angle β , whereby the colour code refers to the total potential energy Π^{\min} . Figure (b) shows the total potential energy Π^{\min} over λ_z and β , whereby the colour code refers to the primary variable $\lambda_{\theta_i}^{\min}$. The red spot at $\lambda_{\theta_i}^{\text{opt}} = 1.625$, $\lambda_z^{\text{opt}} = 1.637$ and $\beta^{\text{opt}} = 33.158$ [deg] corresponds to the optimal total potential energy $\Pi^{*\text{opt}}$ on this constrained equilibrium-surface, see also Table 2.9.

Table 2.9: Results of the optimisation problem (2.82). The initial values are set to $\lambda_{\theta_i}^0 = 1.0$ and $\lambda_z^0 = 1.0$. The superscript \bullet^{opt} is omitted.

| λ_{θ_i} [-] | λ_z [-] | β [deg] | Π^* [kPa] |
|--------------------------|-----------------|---------------|---------------|
| 1.625 | 1.637 | 33.158 | -160.750 |

external potential energy on α with minimal values of λ_{θ_i} obtained at approximately $\alpha = 100 \pm 10$ [deg]. The white line in the plot of the total potential energy in Figure 2.8(c) is associated with the solution of the minimisation problem (2.75) and, in consequence, represents the equilibrium-path for a prescribed internal pressure of $p^{\text{phys}} = 13.33$ [kPa] and an axial stretch $\lambda_z = 1.654$. The red spot at $\lambda_{\theta_i}^{\min} = 1.657$ and $\alpha^{\min} = 90.610$ [deg], associated with the solution of the minimisation problem (2.83), represents the minimal total potential energy on this constrained equilibrium-path, see also the last row in Table 2.10.

Moreover, a small parameter study of the minimisation problem (2.83) is performed by prescribing different combinations of the pressure p and the axial stretch λ_z . The corresponding results are summarised in Table 2.10. Within rows 1–4, parameters according to Table 2.1 are used, whereas row 5 results from the minimisation of (2.78) and gives the numerical values of the red spot in Figure 2.8. Interestingly, the minimum total potential energy is obtained for $\lambda_z = 1.654$ which, however, does not yield the minimal inner circumferential stretch λ_{θ_i} , obtained for $\lambda_z = 1.7$.

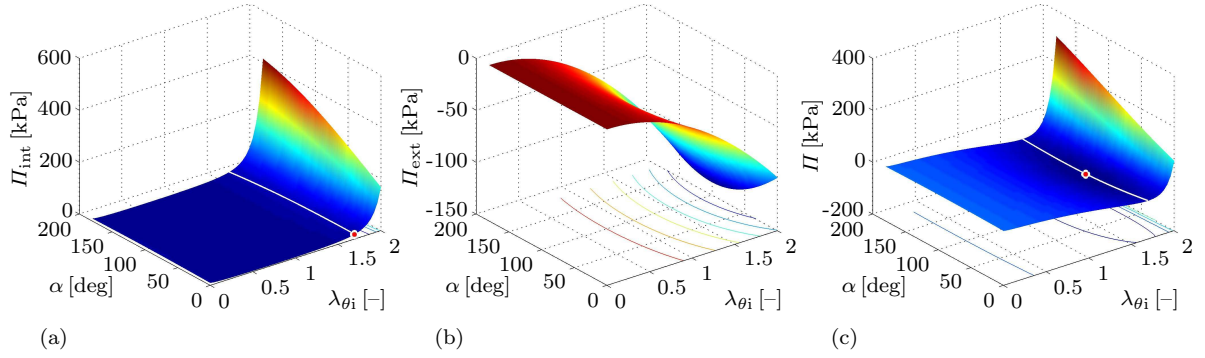


Figure 2.8: Illustration of minimisation problem (2.83). Surface plot of the (a) internal, (b) external and (c) total potential energy over $\lambda_{\theta i}$ and α for the parameters as given in Table 2.1. The axial residual stretch λ_z is assumed as $\lambda_z^{\min} = 1.654$ and the opening angle α , associated with the circumferential residual stretch, is set to $\alpha^{\min} = 90.609$ [deg] as identified by the minimisation problem (2.79), see also Table 2.5. The white lines in (a) and (c) illustrate the equilibrium-path. The red spot in (a) at $\lambda_{\theta i} = 1.6895$ and $\alpha = 0.0$ [deg] represents the minimal internal potential energy on this constrained equilibrium-path. The red spot in (c) at $\lambda_{\theta i}^{\min} = 1.657$ and $\alpha^{\min} = 90.610$ [deg] represents the minimal total potential energy on this constrained equilibrium-path.

Table 2.10: Parameter study of the minimisation problem (2.83) prescribing different combinations of the pressure p and the axial stretch λ_z . Within rows 1–4, parameters according to Table 2.1 are used, whereas row 5 results from the minimisation problem (2.78) and provides the numerical values of the red spot in Figure 2.8. The superscript \bullet^{\min} is omitted.

| Input | | Output | | |
|-----------|-----------------|--------------------------|----------------|-------------------|
| p [kPa] | λ_z [-] | $\lambda_{\theta i}$ [-] | α [deg] | \check{I} [kPa] |
| 0.000 | 1.000 | 1.000 | -0.001 | 0.000 |
| 13.330 | 1.000 | 1.743 | 90.040 | -50.920 |
| 0.000 | 1.700 | - | - | - |
| 13.330 | 1.700 | 1.644 | 90.460 | -71.510 |
| 13.330 | 1.654 | 1.657 | 90.610 | -71.720 |

2.3.5.7 Optimisation of $\check{I}^\diamond(\lambda_{\theta i}, \alpha, \beta^M, \beta^A; \kappa^\diamond)$

The optimisation of the four-variable energy functional \check{I}^\diamond with respect to the inner circumferential stretch $\lambda_{\theta i}$, the opening angle α and both fibre angles β^M and β^A is performed next; cf. (2.84). The pressure is set to the physiological value $p^{\text{phys}} = 13.33$ [kPa] and the axial (residual) stretch is fixed to $\lambda_z^{\text{phys}} = 1.7$.

Figure 2.9(a) depicts the subset $\{\lambda_{\theta i}^{\min}, \beta^M, \beta^A\}$ of the solution space of the corresponding minimisation of \check{I} . The colour code used in Figure 2.9(a) illustrates the value of the minimised total potential energy \check{I}^{\min} ; cf. (2.83). Moreover, Figure 2.9(b) shows the total potential energy \check{I}^{\min} over β^M and β^A , the colour code refers to the primary variable $\lambda_{\theta i}^{\min}$. The red spot at $\lambda_{\theta i}^{\text{opt}} = 1.832$, $\beta^M{}^{\text{opt}} = 62.449$ [deg] and $\beta^A{}^{\text{opt}} = 90.000$ [deg], asso-

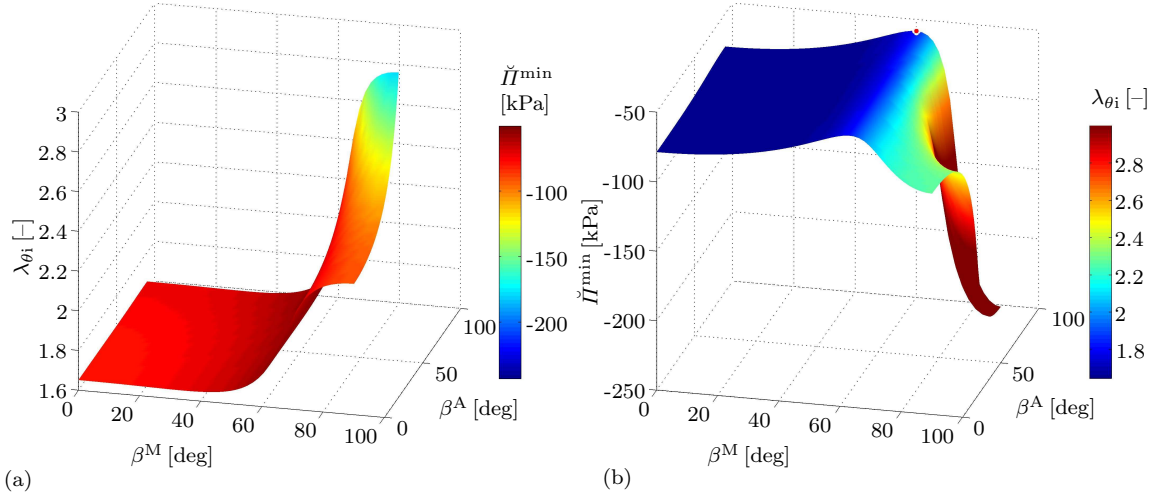


Figure 2.9: Plots of subsets of the solution space of optimisation problem (2.84). Figure (a) depicts the inner circumferential stretch $\lambda_{\theta_i}^{\min}$ over the medial and adventitial fibre angle β^M and β^A , whereby the colour code refers to the total potential energy $\check{\Pi}^{\min}$. Figure (b) shows the total potential energy $\check{\Pi}^{\min}$ with respect to β^M and β^A , whereby the colour code refers to the primary variable $\lambda_{\theta_i}^{\min}$. The red spot at $\lambda_{\theta_i}^{\text{opt}} = 1.8323$, $\beta^M \text{opt} = 62.449$ [deg] and $\beta^A \text{opt} = 90.000$ [deg] corresponds to the optimal total potential energy $\Pi^{\circ \text{opt}}$ on this constrained equilibrium-surface, see also Table 2.11.

Table 2.11: Results of the optimisation problem (2.84). The initial values are set to $\lambda_{\theta_i}^0 = 1.0$ and $\alpha^0 = 90.0$ [deg]. The superscript \bullet^{opt} is omitted.

| λ_{θ_i} [-] | α [deg] | β^M [deg] | β^A [deg] | Π° [kPa] |
|--------------------------|----------------|-----------------|-----------------|---------------------|
| 1.832 | 89.861 | 62.449 | 90.000 | -50.298 |

ciated with the solution of the optimisation problem (2.84), corresponds to the optimal total potential energy $\Pi^{\circ \text{opt}}$ on this constrained equilibrium-surface. Essential results are summarised in Table 2.11.

Even if it turns out that the resulting values, as summarised in Table 2.11, are quite different compared to the physiological values, it is worth noting that, in this case, the medial fibre angle of $\beta^M \text{opt} = 62.449$ [deg] coincidentally corresponds very well to the assumed physiological adventitial value of $\beta^A \text{phys} = 62.0$ [deg]. This enlarged value for the medial fibre angle can be considered as a consequence of the—compared to the previous problems—higher prescribed axial (residual) stretch $\lambda_z = 1.7 = \text{const}$. This results in fibre directions β^M closer, but not fully, oriented with respect to the axial direction; see Figure 2.10 and the remark below. Similar to the previous observations, however, the adventitial fibre angle seems to be unaffected by these effects and always results in $\beta^A \text{opt} = 90.0$ [deg]. Interestingly, fibre angles of $\beta^M = 34.898$ [deg] and $\beta^A = 53.265$ [deg] lead to a minimal inner circumferential stretch $\lambda_{\theta_i} = 1.643$ which again is not identical with the state at which the minimal total potential energy is obtained.

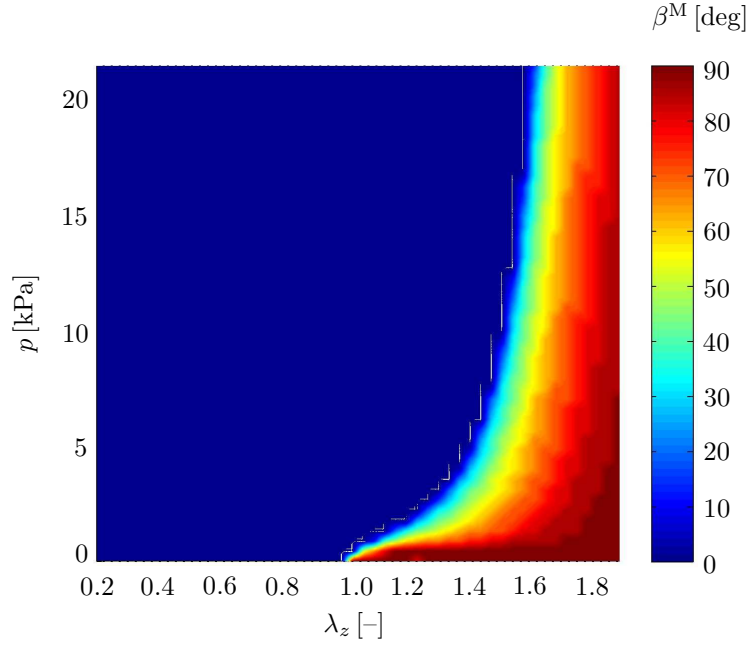


Figure 2.10: Illustration of the relation between the axial stretch λ_z , internal pressure p and (optimal) fibre angle $\beta^{M \text{ opt}}$ as indicated by the colour code. The opening angle is assumed as $\alpha^{\text{phys}} = 160.0$ [deg]. The white rectangle is associated with the physiological region corresponding to $p^{\text{phys}} = 8.0\text{--}17.4$ [kPa] and $\lambda_z^{\text{phys}} = 1.65\text{--}1.75$.

In addition to the results displayed in Figure 2.9, the relation between the axial stretch λ_z , internal pressure p and medial fibre angle $\beta^{M \text{ opt}}$ is illustrated in Figure 2.10, where the colour code refers to the optimal fibre angle $\beta^{M \text{ opt}}$ corresponding to a particular loading state defined by λ_z and p . The opening angle is assumed as $\alpha^{\text{phys}} = 160.0$ [deg]. The physiological region corresponding to $p^{\text{phys}} = 8.0\text{--}17.4$ [kPa] and $\lambda_z^{\text{phys}} = 1.65\text{--}1.75$ is marked by a white-shaded rectangle.

It is obvious from Figure 2.10 that for low axial stretch values but for high pressure values, favourable fibre angles are oriented towards the circumferential direction, i.e. $\beta^{M \text{ opt}} = 0.0$ [deg], which is indicated by the dark blue colour in the upper left region. In contrast, a fibre angle aligned with respect to the axial direction, i.e. $\beta^{M \text{ opt}} = 90.0$ [deg], is obtained for high values of the axial stretch but for low pressure values as indicated by the dark red colour in the lower right. However, for high axial stretch values of $\lambda_z = 1.8\text{--}1.9$, irrespective of the pressure magnitude, one permanently obtains a fibre angle aligned with respect to the axial direction. Interestingly, there is a physiologically characteristic region indicated in yellow, where the fibre angle and the axial stretch remain almost constant, i.e. $\beta^{M \text{ opt}} \approx 62.0$ [deg] and $\lambda_z \approx 1.7$, respectively. For pressures being located within the physiological range, i.e. $p = 8.0\text{--}17.4$ [kPa], one consequently observes only slight variations with respect to the axial stretch, i.e. $\lambda_z \approx 1.7$ for a fibre

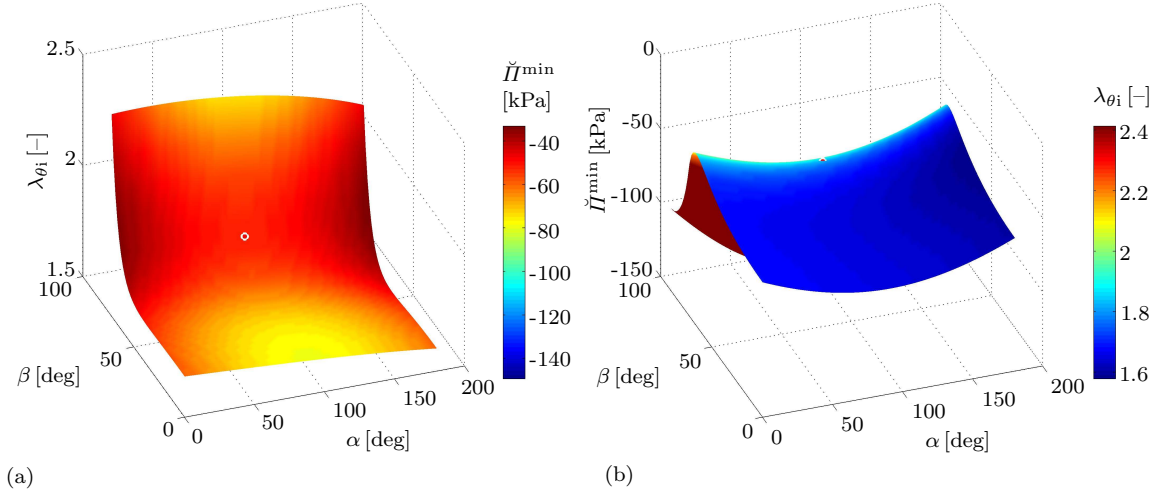


Figure 2.11: Plots of subsets of the solution space of optimisation problem (2.85). Figure (a) depicts the inner circumferential stretch $\lambda_{\theta_i}^{\min}$ over the opening angle α and the fibre angle β , whereby the colour code refers to the total potential energy \check{I}^{\min} . Figure (b) shows the total potential energy \check{I}^{\min} with respect to α and β , whereby the colour code refers to the primary variable $\lambda_{\theta_i}^{\min}$. The red spot at $\lambda_{\theta_i}^{\text{opt}} = 1.815$, $\alpha^{\text{opt}} = 88.362$ [deg] and $\beta^{\text{opt}} = 62.449$ [deg] corresponds to the optimal total potential energy $\check{I}^{\circ \text{opt}}$ on this constrained equilibrium-surface, see also Table 2.12.

Table 2.12: Results of the optimisation problem (2.85). The initial values are set to $\lambda_{\theta_i}^0 = 1.0$, $\alpha = 90$ [deg]. The superscript \bullet^{opt} is omitted.

| λ_{θ_i} [-] | α [deg] | β [deg] | \check{I}° [kPa] |
|--------------------------|----------------|---------------|---------------------------|
| 1.815 | 88.362 | 62.449 | -149.310 |

angle of $\beta^{\text{M opt}} \approx 62.0$ [deg], which illustratively underlines the physiological suitability of these values.

2.3.5.8 Optimisation of $\check{I}^{\circ}(\lambda_{\theta_i}, \alpha, \beta, \beta; \kappa^{\circ})$

The optimisation of the three-variable energy functional \check{I}° with respect to the inner circumferential stretch λ_{θ_i} , the opening angle α and the (identical) fibre angle for the media and adventitia $\beta = \beta^{\text{M}} = \beta^{\text{A}}$ are investigated; cf. (2.85). The pressure is set to the physiological value $p^{\text{phys}} = 13.33$ [kPa] and the axial (residual) stretch is fixed as $\lambda_z^{\text{phys}} = 1.7$.

Figure 2.11(a) depicts the subset $\{\lambda_{\theta_i}^{\min}, \alpha, \beta\}$ of the solution space of the corresponding minimisation of \check{I} ; cf. (2.85). The colour code used in Figure 2.11(a) illustrates the value of the total potential energy \check{I}^{\min} . Moreover, Figure 2.11(b) shows the total potential energy \check{I}^{\min} over α and β , the colour code refers to the primary variable $\lambda_{\theta_i}^{\min}$. The red spot at $\lambda_{\theta_i}^{\text{opt}} = 1.815$, $\alpha^{\text{opt}} = 88.362$ [deg] and $\beta^{\text{opt}} = 62.449$ [deg], associated

with the solution of the optimisation problem (2.85), corresponds to the optimal total potential energy $\hat{\Pi}^{\text{opt}}$ on this constrained equilibrium-surface, see also Table 2.12.

One observes from Figure 2.11(a) that, for an increasing opening angle α , the inner circumferential stretch $\lambda_{\theta_i}^{\text{min}}$ slightly decreases. Interestingly, this is not the case for the total potential energy $\hat{\Pi}^{\text{min}}$ as can be seen from Figure 2.11(b). Here, the saddle-shaped energy landscape renders a minimal energy for an opening angle range of $\alpha = 80.0\text{--}100.0$ [deg]. Furthermore, as indicated in Figure 2.11(a), smaller fibre angles β close to the circumferential direction, i.e. $\beta \rightarrow 0.0$, render smaller circumferential stretches for the present case of an assumed physiological axial stretch of $\lambda_z^{\text{phys}} = 1.7$. This is a consequence of the stiffening behaviour caused by the fibres with respect to the circumferential direction. Interestingly, the maximal total potential energy with regard to the fibre angle β is always obtained for values of $\beta \approx 60.0$ [deg], which corresponds very well to the assumed physiological fibre angle $\beta^{\text{Aphys}} = 62.0$ [deg] of the adventitia, which actually is less important compared to the media in view of the respective loading carrying capacities. This can be considered as a consequence of the higher prescribed axial (residual) stretch $\lambda_z = 1.7 = \text{const.}$ This results in fibre directions β^{M} oriented closer, but not fully, with respect to the axial direction.

2.3.5.9 Minimisation of $\hat{\Pi}(\lambda_{\theta_i}, p; \hat{\kappa})$

The minimisation of the two-variable energy functional $\hat{\Pi}$ with respect to the inner circumferential stretch λ_{θ_i} and the internal pressure p is studied next; cf. (2.86). Figure 2.12 shows the (a) internal, (b) external and (c) total potential energy $\hat{\Pi}$ over λ_{θ_i} and p for the parameters as given in Table 2.1. The axial residual stretch λ_z is assumed as $\lambda_z^{\text{min}} = 1.654$ and the opening angle α , associated with the circumferential residual stretch, is set to $\alpha^{\text{min}} = 90.609$ [deg] as identified by the minimisation problem (2.78), see also Table 2.5.

As expected, Figure 2.12(a) shows the internal potential energy to be rather constant for varying internal pressure p , whereas Figure 2.12(b) shows the linear dependence of the external potential energy on p . The white line shown in the plot of the total potential energy in Figure 2.12(c) is associated with the solution of the minimisation problem (2.75) and, consequently, represents the equilibrium-path for a prescribed axial stretch $\lambda_z = 1.654$ and an opening angle of $\alpha^{\text{min}} = 90.609$ [deg]. The red spot at $\lambda_{\theta_i} = 1.722$ and $p = 21.33$ [kPa], associated with the solution of the minimisation problem (2.86), represents the minimal total potential energy on this constrained equilibrium-path, see also the last row in Table 2.13.

Moreover, a small parameter study of the minimisation problem (2.86) is performed by prescribing different combinations of the axial (residual) stretch λ_z and the opening angle α . The corresponding results are summarised in Table 2.13. Within rows 1–4, parameters according to Table 2.1 are used, whereas row 5 results from the minimisation problem (2.78) and gives the numerical values of the red spot in Figure 2.12. It becomes apparent that the incorporation of a circumferential residual stress by means of an

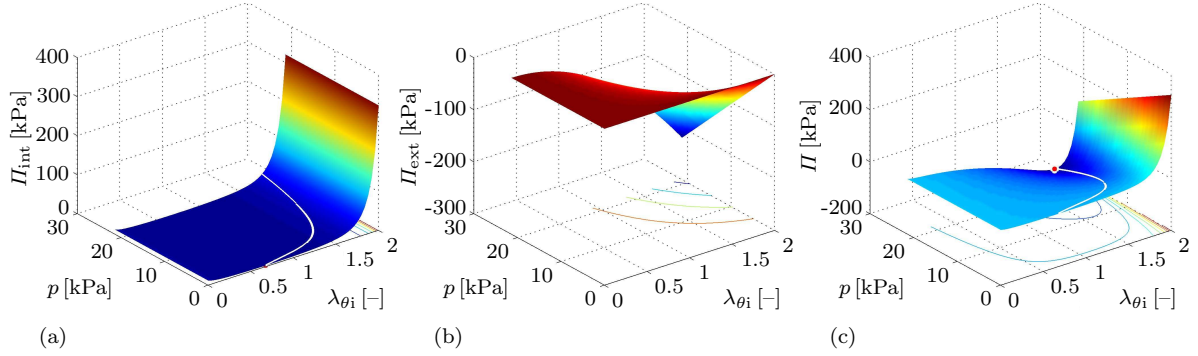


Figure 2.12: Illustration of minimisation problem (2.86). Surface plot of the (a) internal, (b) external and (c) total potential energy over λ_{θ_i} and p for the parameters as given in Table 2.1. The axial residual stretch λ_z is assumed as $\lambda_z^{\min} = 1.654$ and the opening angle α , associated with the circumferential residual stretch, is set to $\alpha^{\min} = 90.609$ [deg] as identified by the minimisation problem (2.78), see also Table 2.5. The white lines in (a) and (c) illustrate the equilibrium-path. The red spot in (a) at $\lambda_{\theta_i} = 0.67399$ and $p = 0.0$ [kPa] represents the minimal internal potential energy on this constrained equilibrium-path. The red spot in (c) at $\lambda_{\theta_i} = 1.722$ and $p = 21.33$ [kPa] represents the minimal total potential energy on this constrained equilibrium-path.

Table 2.13: Parameter study of the minimisation problem (2.86) prescribing different combinations of the axial stretch λ_z and the opening angle α . Within rows 1–4, parameters according to Table 2.1 are used, whereas row 5 results from the minimisation problem (2.78) and provides the numerical values of the red spot in Figure 2.12. The superscript \bullet^{\min} is omitted.

| Input | | Output | | |
|-----------------|----------------|--------------------------|-----------|-------------------|
| λ_z [-] | α [deg] | λ_{θ_i} [-] | p [kPa] | $\hat{\Pi}$ [kPa] |
| 1.000 | 0.000 | 1.846 | 21.330 | -67.900 |
| 1.700 | 0.000 | 1.743 | 21.330 | -97.890 |
| 1.000 | 160.000 | 1.767 | 21.330 | -76.990 |
| 1.700 | 160.000 | 1.673 | 21.330 | -111.900 |
| 1.654 | 90.609 | 1.722 | 21.330 | -130.900 |

opening angle $\alpha > 0.0$ reduces the obtained circumferential stretch λ_{θ_i} as well as the total potential energy $\hat{\Pi}$. Interestingly, the minimum total potential energy is obtained for $\alpha = 90.609$ [deg] which, however, does not yield the minimal inner circumferential stretch λ_{θ_i} , obtained for $\alpha = 160.0$ [deg].

2.3.5.10 Optimisation of $\Pi^{\Delta}(\lambda_{\theta_i}, \beta^M, \beta^A; \kappa^{\Delta})$

As a last type of optimisation problem the three-variable energy functional Π^{Δ} , with respect to the inner circumferential stretch λ_{θ_i} and the fibre angles for the media and adventitia β^M and β^A , is discussed; cf. (2.87). The pressure is set to the physiological

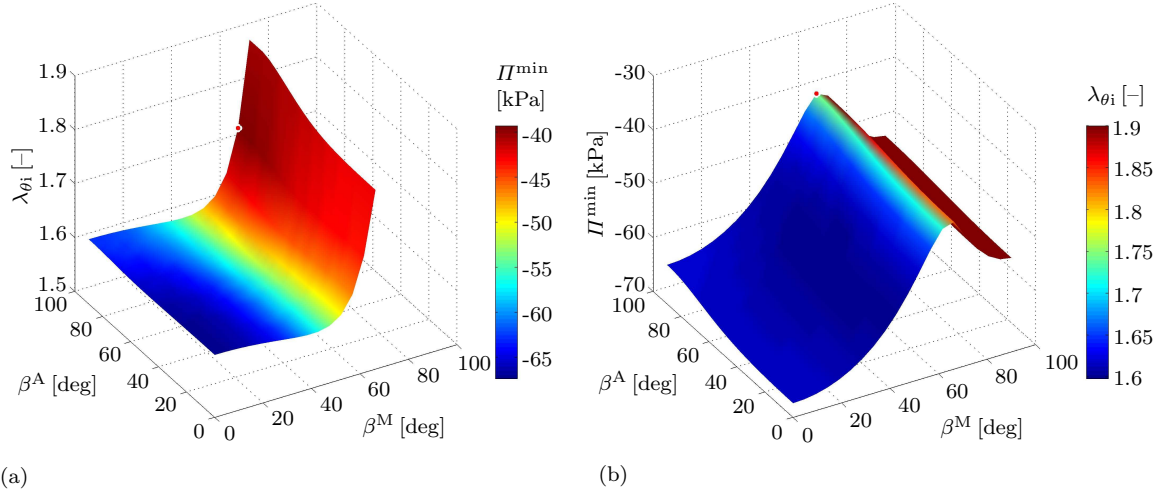


Figure 2.13: Plots of the solution space of optimisation problem (2.87). Figure (a) depicts the inner circumferential stretch λ_{θ_i} over the medial and adventitial fibre angle β^M and β^A , whereby the colour code refers to the total potential energy Π^{\min} . Figure (b) shows the total potential energy Π^{\min} with respect to β^M and β^A , whereby the colour code refers to the primary variable λ_{θ_i} . The red spot at $\lambda_{\theta_i}^{\text{opt}} = 1.765$, $\beta^M{}^{\text{opt}} = 62.449$ [deg] and $\beta^A{}^{\text{opt}} = 90.000$ [deg] represents the optimal total potential energy on this constrained equilibrium-surface, see also Table 2.14.

Table 2.14: Results of the optimisation problem (2.87), where the initial value is set to $\lambda_{\theta_i}^0 = 1.0$. The superscript \bullet^{opt} is omitted.

| λ_{θ_i} [-] | β^M [deg] | β^A [deg] | Π^Δ [kPa] |
|--------------------------|-----------------|-----------------|--------------------|
| 1.765 | 62.449 | 90.000 | -39.089 |

value of $p^{\text{phys}} = 13.33$ [kPa] and the axial (residual) stretch is fixed to $\lambda_z^{\text{phys}} = 1.7$ while the opening angle is assumed as $\alpha^{\text{phys}} = 160.0$ [deg].

Figure 2.13(a) depicts the solution space $\{\lambda_{\theta_i}^{\min}, \beta^M, \beta^A\}$, whereby the colour code represents the value of the total potential energy Π^{\min} . Moreover, Figure 2.13(b) shows the total potential energy Π^{\min} over β^M and β^A , the colour code refers to the primary variable $\lambda_{\theta_i}^{\min}$. The red spot at $\lambda_{\theta_i}^{\text{opt}} = 1.765$, $\beta^M{}^{\text{opt}} = 62.449$ [deg] and $\beta^A{}^{\text{opt}} = 90.000$ [deg], associated with the solution of the optimisation problem (2.87), corresponds to the optimal total potential energy on this constrained equilibrium-surface, see also Table 2.14.

In Figure 2.13, the medial fibre angle β^M strongly influences the contour plots visualised, whereas the adventitial fibre angle β^A possesses only a slight influence on the results shown. One observes in Figure 2.13(a) that the inner circumferential stretch $\lambda_{\theta_i}^{\min}$ significantly increases with increasing medial fibre angle β^M . The total potential energy, however, shows different characteristics. As can be seen from Figure 2.13(b), one obtains a saddle-shaped energy landscape, maxima of which are obtained at $\beta^M \approx 60.0$ [deg] which correspond very well to the assumed physiological fibre angle $\beta^A{}^{\text{phys}} = 62.0$ [deg]

of the adventitia. This is a consequence of the large prescribed axial stretch $\lambda_z = 1.7 = \text{const}$ which, in the context of the optimisation problem addressed, favours fibre directions β^M aligned with the axial direction. Regarding the adventitial fibre angle β^A , one observes that the inner circumferential stretch λ_{θ_i} as well as the total potential energy tend to increase with increasing β^A .

2.3.5.11 Optimisation of $\Pi^\Delta(\lambda_{\theta_i}, \beta, \beta; \kappa^\Delta)$

The optimisation of the two-variable energy functional Π^Δ with respect to the inner circumferential stretch λ_{θ_i} and the fibre angle β is focussed on in this section, cf. (2.88). This constitutes a special case of the optimisation problem discussed in Section 2.3.5.10.

Figure 2.14 shows the (a) internal, (b) external and (c) total potential energy with respect to λ_{θ_i} and β for the parameters as given in Table 2.1. The fibre angles β^M and β^A are assumed to be identical for both layers, i.e. $\beta = \beta^M = \beta^A$. The axial residual stretch λ_z is assumed as $\lambda_z^{\text{min}} = 1.654$ and the opening angle α , associated with the circumferential residual stretch, is set to $\alpha^{\text{min}} = 90.609$ [deg] as identified by the minimisation problem (2.78), see also Table 2.5. One observes from Figure 2.14(a) that the internal potential energy landscape varies significantly with the fibre angle β while Figure 2.14(b) shows, as expected, the external potential energy to be constant in β . The white line in the plot of the total potential energy in Figure 2.14(c) is associated with the solution of the minimisation problem (2.75) and consequently represents the equilibrium-path for a prescribed internal pressure of $p^{\text{phys}} = 13.33$ [kPa], an axial stretch of $\lambda_z = 1.654$ and an opening angle of $\alpha = 90.609$ [deg]. The red spot at $\lambda_{\theta_i}^{\text{opt}} = 1.765$ and $\beta^{\text{opt}} = 53.265$ [deg], associated with the solution of the optimisation problem (2.88), represents an extremum of the total potential energy on this constrained equilibrium-path; see also the last row in Table 2.15.

Moreover, a small parameter study of the optimisation problem (2.88) is performed prescribing different combinations of the pressure p , the axial stretch λ_z and the opening angle α . The corresponding results are summarised in Table 2.15. Within rows 1–8, parameters according to Table 2.1 are used, whereas row 9 results from the minimisation problem (2.78) and provides the numerical values of the red spot in Figure 2.14. It becomes apparent that the incorporation of a circumferential residual stress by means of an opening angle $\alpha > 0.0$ tends to reduce the obtained circumferential stretch λ_{θ_i} . As expected, one obtains a fibre angle of $\beta = 0.0$ [deg] for parameter combinations including $p \neq 0.0$ [kPa] and $\lambda_z = 1.0$. Similarly, a fibre angle of $\beta = 90.0$ [deg] is observed for a parameter combination considered with $p = 0.0$ [kPa] and $\lambda_z \neq 1.0$. Furthermore, the minimum total potential energy is obtained for $\lambda_z = 1.654$ and $\alpha = 90.609$ [deg] which, however, does not yield the minimal inner circumferential stretch λ_{θ_i} for the parameter settings considered—the related minimal values are $\lambda_z = 1.0$ and $\alpha = 160.0$ [deg].

Based on optimisation problem (2.88), the interaction between the pressure p , the opening angle α , the fibre angle β and the axial stretch λ_z is investigated. A physiological value of the axial (residual) stretch of $\lambda_z^{\text{phys}} = 1.7$ is used according to Holzapfel et al.

2 Extremal states of energy of a double-layered thick-walled tube

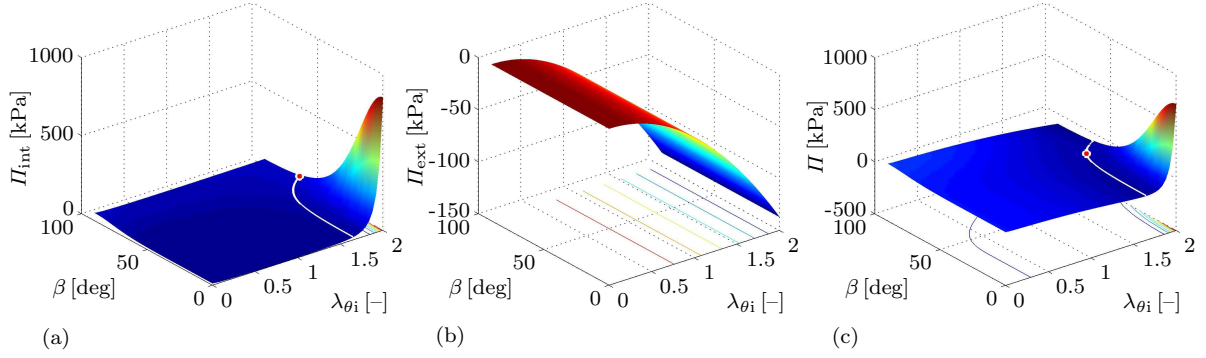


Figure 2.14: Illustration of optimisation problem (2.88). Surface plot of the (a) internal, (b) external and (c) total potential energy Π over $\lambda_{\theta i}$ and β for the parameters as given in Table 2.1 with $\beta = \beta^M = \beta^A$. The axial residual stretch λ_z is assumed as $\lambda_z^{\min} = 1.654$ and the opening angle α , associated with the circumferential residual stretch, is set to $\alpha^{\min} = 90.609$ [deg] as identified by the minimisation problem (2.78), see also Table 2.5. The white lines in (a) and (c) illustrate the equilibrium-path. The red spot in (a) at $\lambda_{\theta i} = 1.9797$ and $\beta = 62.449$ [deg] represents the minimal internal potential energy on this constrained equilibrium-path. The red spot in (c) at $\lambda_{\theta i}^{\text{opt}} = 1.765$ and $\beta^{\text{opt}} = 53.265$ [deg] represents the minimal total potential energy on this constrained equilibrium-path.

Table 2.15: Parameter study of the optimisation problem (2.88) prescribing different combinations of the pressure p , the axial stretch λ_z and the opening angle α . Within rows 1–8, parameters according to Table 2.1 are used, whereas row 9 results from the minimisation problem (2.78) and provides the numerical values of the red spot in Figure 2.14. The superscript \bullet^{opt} is omitted.

| Input | | | Output | | |
|-----------|-----------------|----------------|--------------------------|---------------|--------------------|
| p [kPa] | λ_z [-] | α [deg] | $\lambda_{\theta i}$ [-] | β [deg] | Π^Δ [kPa] |
| 13.330 | 1.000 | 0.000 | 1.594 | 0.000 | -31.074 |
| 0.000 | 1.700 | 0.000 | 0.767 | 90.000 | 59.448 |
| 13.330 | 1.700 | 0.000 | 1.896 | 64.286 | -34.256 |
| 13.330 | 1.000 | 160.000 | 1.510 | 0.000 | -34.329 |
| 13.330 | 1.700 | 160.000 | 1.798 | 64.286 | -40.034 |
| 13.330 | 1.654 | 90.609 | 1.765 | 53.265 | -66.907 |

[135]. Under the action of real blood flow, i.e. changing values of internal pressure p , it is obvious that the axial elongation of an artery should not vary significantly. In other words, a change of λ_z for different values of p should not significantly influence other quantities of interest such as the inner circumferential stretch $\lambda_{\theta i}$. In this context, the primal aim is to find out whether parameter sets exist with regard to p , α and especially β , which render the optimal axial stretch to remain almost unchanged, i.e. $\lambda_z = \text{const}$.

Figure 2.15 shows the axial stretch λ_z over the inner circumferential stretch $\lambda_{\theta i}$ and the fibre angle β for different pressures of $p = \{8.0, 13.3, 17.4\}$ [kPa] (from top to bottom) and for different opening angles $\alpha = \{0.0, 80.0, 160.0\}$ [deg] (from left to right). With regard to the constant axial stretch range of about $\lambda_z = 0.0$ – 1.7 , one observes that

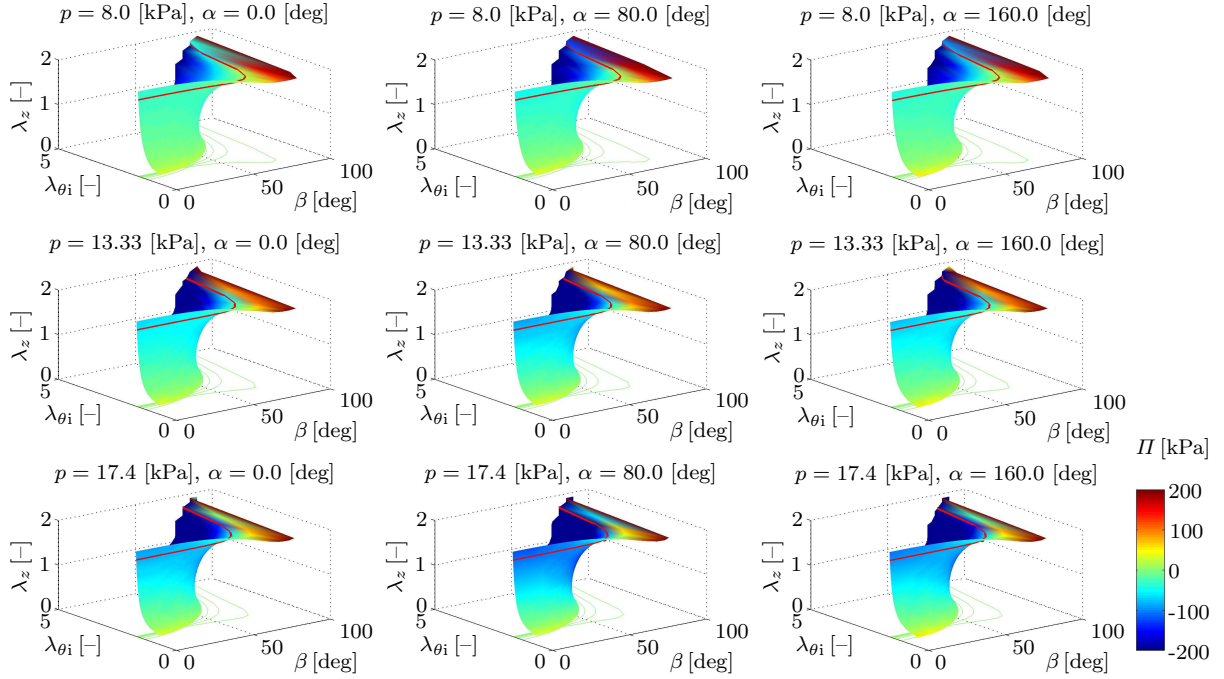


Figure 2.15: Axial stretch λ_z plotted over the inner circumferential stretch λ_{θ_i} and the fibre angle β for different pressures $p = \{8.0, 13.3, 17.4\}$ [kPa] (from top to bottom) and different opening angles $\alpha = \{0.0, 80.0, 160.0\}$ [deg] (from left to right). The colour code illustrates the total potential energy Π and the red line represents an exemplary isoline for $\lambda_z = \text{const}$ to be further studied in Figure 2.16.

the inner circumferential stretch λ_{θ_i} increases with increasing values of the fibre angle β . It is of interest to note that this effect is reversed for approximately $\lambda_z > 1.7$. In other words, λ_{θ_i} first may decrease with β but for larger values of β significantly increases with β , which clearly is a consequence of the pronounced material properties in these directions. Moreover, one observes that a plateau-type characteristic exists for $\beta = 60.0\text{--}80.0$ [deg], where the axial stretch remains almost unchanged within the range $\lambda_z \in [1.7, 1.8]$. Furthermore, even if not clearly illustrated in Figure 2.15, the values of the inner circumferential stretch λ_{θ_i} increase with increasing internal pressure p . Practically speaking, the entire surface is shifted towards larger values of λ_{θ_i} . An increase of the opening angle α , however, causes the inner circumferential stretch λ_{θ_i} to decrease, i.e. the entire surface is shifted towards smaller values of λ_{θ_i} .

Figure 2.16 illustrates the inner circumferential stretch λ_{θ_i} over the fibre angle $\beta = \beta^M = \beta^A$ for different pressures $p = \{8.0, 13.3, 17.4\}$ [kPa] and different axial (residual) stretches $\lambda_z = \{1.6, 1.65, 1.7, 1.75\}$. The opening angle is set to $\alpha = 160.0$ [deg] which corresponds to the red curves in the right column of Figure 2.15. One observes from Figures 2.16(a) and 2.16(b), which respectively refer to axial stretches of $\lambda_z = 1.6$ and $\lambda_z = 1.65$, that λ_{θ_i} increases with increasing fibre angles β (except the curve for $p = 8.0$ [kPa]). This behaviour, however, significantly changes for the graphs in Fig-

2 Extremal states of energy of a double-layered thick-walled tube

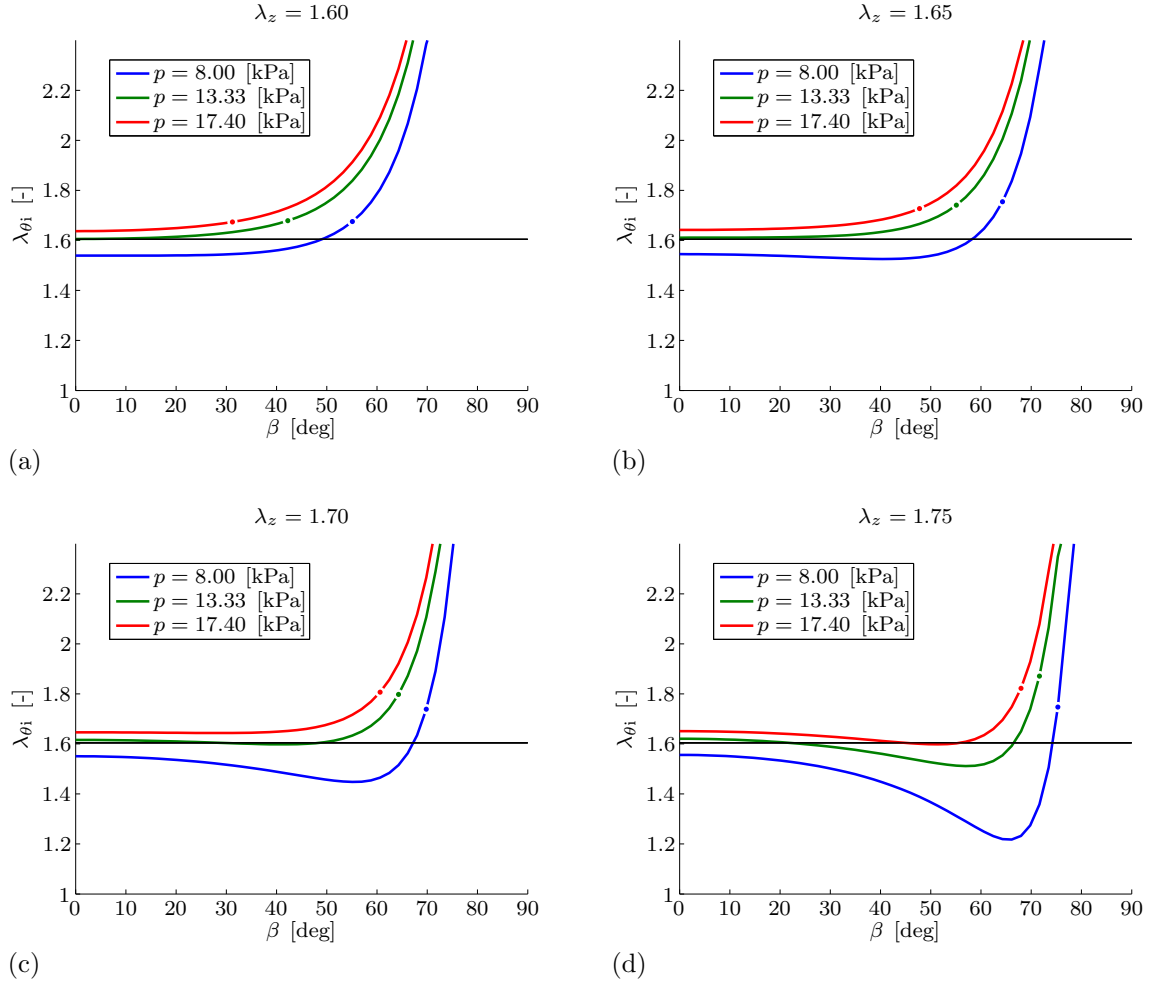


Figure 2.16: Inner circumferential stretch λ_{θ_i} plotted over the fibre angle $\beta = \beta^M = \beta^A$ for different pressures $p = \{8.0, 13.3, 17.4\}$ [kPa] and different axial (residual) stretches $\lambda_z = \{1.6, 1.65, 1.7, 1.75\}$ and an opening angle of $\alpha = 160.0$ [deg] corresponding to the red line in the right column of Figure 2.15. The horizontal black line indicates the physiological value of the circumferential stretch $\lambda_{\theta_i}^{\text{phys}} = 1.604$ which, according to Table 2.2 corresponds to $\lambda_z^{\text{phys}} = 1.7$, $p^{\text{phys}} = 13.33$ [kPa] and $\alpha^{\text{phys}} = 160.0$ [deg]. The spots indicate the values obtained from the optimisation problem (2.88).

ures 2.16(c, d), i.e. for axial stretches of $\lambda_z = 1.7$ and $\lambda_z = 1.75$. In these cases, λ_{θ_i} first decreases with increasing fibre angles β until a minimum value is obtained and then increases with β . It is interesting to note that for the largest axial stretch considered, here $\lambda_z = 1.75$, the smallest inner circumferential stretches are obtained. These minimum values, for the respective pressure values chosen, also refer to different fibre angles β as for smaller axial stretches. Moreover, one observes that in c almost constant values for λ_{θ_i} are obtained for $\beta = 0-40$ [deg], whereas β turns out to remain almost constant for $\lambda_{\theta_i} > 1.8$. The spots in the graphs of Figures 2.16(a)–(d) refer to the optimisation problem (2.88). One observes especially from Figures 2.16(c, d) that the minimal cir-

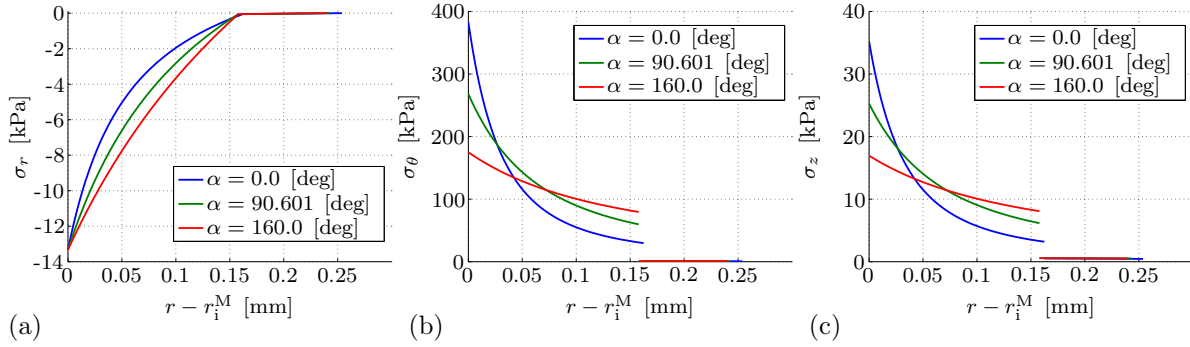


Figure 2.17: Plots of the principal Cauchy stresses $\sigma_{rr, \theta\theta, zz}$ over the width $r - r_i^M$ of the deformed tube for three different opening angles $\alpha = \{0.0, 90.601, 160.0\}$ [deg] together with $p = 13.33$ [kPa] and $\lambda_z = 1.0$: (a) radial stress σ_{rr} , (b) circumferential stress $\sigma_{\theta\theta}$, (c) axial stress σ_{zz} .

cumferential stretch values and the values resulting in a minimal total potential energy are not identical.

In addition to the previous plots, Figure 2.17 shows—by way of illustration and comparison—the distributions of the Cauchy stresses over the width of the deformed tube. Three different cases of residual stress states are considered as represented by the opening angles $\alpha = \{0.0, 90.601, 160.0\}$ [deg] in combination with a physiological pressure of $p^{\text{phys}} = 13.33$ [kPa] and an axial (residual) stretch of $\lambda_z = 1.0$. The opening angle of $\alpha = 90.601$ [deg] corresponds to the solution of the minimisation problem (2.78), see also Table 2.5. Figure 2.17(a) shows that the radial stress σ_{rr} —in contrast to the tangential stresses $\sigma_{\theta\theta}$ and σ_{zz} —turns out to be continuous over the width of the tube, which is a consequence of the contribution of the equilibrium condition in radial direction, see equation (2.57). Note, that the boundary conditions $\sigma_{rr}|_{r_i^M} = -13.33$ [kPa] at the inner boundary and $\sigma_{rr}|_{r_o^A} = 0.0$ [kPa] at the outer boundary are met. Moreover, the circumferential stress $\sigma_{\theta\theta}$ constitutes the dominant stress coefficient within the wall of the tube, since its magnitude is significantly larger compared to the magnitudes of σ_{rr} and σ_{zz} . In the case residual stresses are accounted for via the opening angle α , the circumferential and axial stresses $\sigma_{\theta\theta}$ and σ_{zz} obviously decrease at the inner wall but increase at the outer wall, as can be seen in Figures 2.17(b, c). Practically speaking, the gradient of $\sigma_{\theta\theta}$ and σ_{zz} with respect to r in the media is reduced so that their distributions are more, say, homogenised. As an interesting side aspect, the mean stresses of $\sigma_{\theta\theta}$ and σ_{zz} through the wall-thickness increase in the case residual stresses are included, although residual stress reduces the maximal circumferential and axial stresses at the inner wall significantly. In contrast to this, the radial stress coefficient σ_{rr} increases from the inner boundary of the wall to its outer boundary and, moreover, the related graphs possess a kink at the interface between the media and adventitia due to the change of material parameters.

3 A gradient-enhanced continuum model for the simulation of damage

This chapter deals with a gradient-enhanced continuum damage model reflecting the progressive failure of collagen fibres, and is based on the ideas outlined in the work by Waffenschmidt et al. [284]. We apply a nonlocal gradient-based damage formulation within a geometrically non-linear setting. Following the concept in Dimitrijević and Hackl [85], we enhance the local free energy function by a gradient-term. This term essentially contains the referential gradient of the nonlocal damage variable which itself is introduced as an additional independent variable. In order to guarantee the equivalence between the local and nonlocal damage variable, a penalisation term is incorporated within the free energy function. Basically, this approach is in line with the systematic construction of micromorphic gradient-type dissipative solids proposed by Forest [100], and can be considered as a special application case of the multi-field incremental variational framework for gradient-extended dissipative solids discussed by Miehe [216].

This work presents a geometrically *non-linear* framework allowing for large deformations. Based on the principle of minimum total potential energy, a coupled system of Euler-Lagrange equations, i.e. the balance of linear momentum and the balance corresponding to the non-local damage field contributions, is obtained which will be solved in weak form. As a key aspect of the model proposed in this contribution, the hyperelastic constitutive response at local material point level is governed by a highly non-linear strain energy, additively composed of an isotropic contribution of the matrix material and of an anisotropic contribution related to the fibre-reinforcement. The inelastic constitutive response is governed by a scalar $[1-d]$ -type damage formulation, where only the anisotropic elastic part is assumed to be affected by the damage evolution. The resulting coupled, highly non-linear system of equations is symmetric and can conveniently be solved by a standard incremental-iterative Newton-Raphson-type solution scheme. Essential numerical aspects of the algorithmic setting of the (non-)local inelastic constitutive relations and the coupled finite element approach are presented in detail. Furthermore, an outline on the computer-implementation is provided with a focus on the commercial finite-element-software Abaqus. Several three-dimensional displacement and force-driven boundary value problems, solved with the finite element

method, highlight the mesh-objective characteristics and constitutive properties of the model and illustratively underline the capabilities of the formulation proposed.

The theoretical outline as discussed in Sections 3.1 and 3.2 constitutes a combination of the small-strain-based gradient enhanced continuum damage formulation proposed by Dimitrijević and Hackl [85] on the one hand, and the local scalar $[1-d]$ -damage formulation used, for instance, in Liebe et al. [186] on the other. The difference in the *local* damage formulations used in these articles relies on the usage of the damage *variable*. Dimitrijević and Hackl [85] introduced an internal variable $d \in (0, \infty)$, which in Liebe et al. [186] is denoted as κ . Liebe et al. [186] derived the driving force according to the damage variable $d \in [0, 1)$ as $Y = -\partial_d \Psi$. Dimitrijević and Hackl [85] introduced the driving force according to the internal variable as $q = -\partial_d \Psi$ but $d \in (0, \infty)$. These two formulations consequently do *not* coincide even if they seem to be identical at first glance. As a further conceptual difference, Dimitrijević and Hackl [85] introduced the damage *condition* as $\phi - r_1 \leq 0$ with $r_1 = \text{const}$ whereas Liebe et al. [186] used $\phi - \kappa \leq 0$. As a notable consequence, the (local) damage formulation used by Dimitrijević and Hackl [85] may not work appropriately in connection with the exponential constitutive relation used later on in the present framework. This is caused by the effect that the exponential contribution due to the fibre-related anisotropic part of the free energy ‘over-compensates’ the damage contribution, resulting in an increase of the local stress vs. stretch response at a formally almost fully degraded material state. We therefore adopt the classic scalar $[1-d]$ -damage formulation in the following. For the general case of *anisotropic* damage, tensorial variables would also have to be taken into account; see, e.g., Menzel and Steinmann [203] and Menzel et al. [200] for local anisotropic damage approaches at large strains or the contributions by Kuhl and Ramm [167] and Kuhl et al. [169] with regard to gradient-enhanced anisotropic damage models at small strains.

The present approach offers several advantages over other gradient-enhanced damage formulations proposed in the literature. As a major benefit, due to its conceptual simplicity, the present formulation can be solved by standard Newton-Raphson-type solution procedures without any need for advanced and computationally expensive solution methods such as a global active-set-search as applied by Liebe et al. [186]. The present gradient-enhanced damage approach proves to be quite robust, even at high levels of degradation, and allows the straightforward incorporation of practically any suitable scalar-valued damage formulation, ensuring the damage function to decrease faster with deformation than the respective (undamaged) stress measure would increase with deformation.

This chapter is organised as follows. In Section 3.1, we give a brief summary of kinematic relations for the geometrically non-linear case and establish generic balance equations of the coupled boundary value problem in weak and strong form on the basis of the principle of minimum total potential energy. Next, in Section 3.2, we specify the underlying constitutive equations, containing the isotropic and anisotropic non-linear elastic and gradient-enhanced free energies, as well as the continuum damage formulation in its continuous format and corresponding algorithmic setting. In Section 3.3, we discretise

the governing weak forms by means of the finite-element method resulting in a coupled non-linear system of equations which can be solved appropriately with incremental-iterative Newton-Raphson-type solution procedures. Finally, in Section 3.4, we apply the proposed model to representative three-dimensional homogeneous and inhomogeneous deformation problems. In order to illustrate the basic constitutive characteristic of the formulation, we first investigate a homogeneous model problem under uniaxial tension. Secondly, to emphasise the regularisation properties of the model due to the gradient-enhancement strategy, we consider a displacement-driven anisotropic plate with a hole. Thirdly, to show the capabilities of the approach with regard to biomechanics-related problems, we study a force-driven example by means of an anisotropic artery-like tube subjected to internal pressure.

3.1 Gradient enhancement of a continuum damage formulation

This section derives the governing coupled balance equations of the boundary value problem on the basis of the principle of minimum total potential energy. Especially the corresponding variational and strong forms are elaborated both in referential and spatial description, where the latter provides the basis for the finite-element discretisation described in Section 3.3.

3.1.1 General gradient-enhanced format of the free energy function

As a starting point, we assume the existence of a local free energy function Ψ_{loc} defined per unit reference volume

$$\Psi_{\text{loc}}(\mathbf{F}, \mathbf{A}_i, \kappa) = \Psi_{\text{iso}}(\mathbf{F}) + f_d(\kappa) \Psi_{\text{ani}}(\mathbf{F}, \mathbf{A}_i) \quad (3.1)$$

that accounts for anisotropic non-linear elastic material response under the influence of scalar damage. Basically, the effective free energy function of the hypothetical undamaged material is composed additively of an isotropic contribution Ψ_{iso} , representing the ground substance, i.e. the matrix material, and of an anisotropic contribution Ψ_{ani} associated with the embedded fibres. It is assumed that only the anisotropic part is subjected to damage, whereas the isotropic matrix material remains elastic. In equation (3.1), $\kappa \in [0, \infty)$ is a scalar internal damage variable, characterising a material stiffness loss of the fibres, while $f_d(\kappa) = 1 - d$ represents an appropriate damage function that is at least twice differentiable and satisfies

$$f_d(\kappa) : \mathbb{R}^+ \rightarrow (0, 1] \left| \left\{ f_d(0) = 1, \lim_{\kappa \rightarrow \infty} f_d(\kappa) \rightarrow 0 \right\} . \quad (3.2)$$

These conditions assure purely elastic behaviour of the undamaged material and result in a complete loss of the related material stiffness in the limiting case $\kappa \rightarrow \infty$, cf. Dimitrijević and Hackl [85].

Furthermore, a set of symmetric second-order tensors

$$\mathbf{A}_i = \mathbf{a}_{0i} \otimes \mathbf{a}_{0i}, \quad i = 1, 2 \quad (3.3)$$

is introduced in Ψ_{ani} to describe the anisotropic and hyperelastic stress response of the fibre-reinforced material.

Following the approach by Dimitrijević and Hackl [85], who considered an analogous framework for the geometrically linear case, a gradient-enhanced non-local free energy function Ψ^{nlloc} is introduced as

$$\Psi_{\text{nlloc}}(\phi, \nabla_{\mathbf{X}}\phi, \kappa; \mathbf{F}) = \Psi_{\text{nlloc}}^{\text{grd}}(\nabla_{\mathbf{X}}\phi; \mathbf{F}) + \Psi_{\text{nlloc}}^{\text{plty}}(\phi, \kappa), \quad (3.4)$$

where $\Psi_{\text{nlloc}}^{\text{grd}}$ contains the referential gradient of the nonlocal damage field variable ϕ essentially representing the first-order term of a Taylor series expansion of ϕ at a material point. Moreover, the contribution $\Psi_{\text{nlloc}}^{\text{plty}}$ incorporates a penalisation term which links the non-local damage variable ϕ to the local damage variable κ . Consequently, we obtain an enhanced free energy function as

$$\begin{aligned} \Psi_{\text{int}}(\mathbf{F}, \phi, \nabla_{\mathbf{X}}\phi, \mathbf{A}_i, \kappa) &= \Psi_{\text{loc}}(\mathbf{F}, \mathbf{A}_i, \kappa) + \Psi_{\text{nlloc}}(\phi, \nabla_{\mathbf{X}}\phi, \kappa; \mathbf{F}) \\ &= \Psi_{\text{iso}}(\mathbf{F}) + f_{\text{d}}(\kappa) \Psi_{\text{ani}}(\mathbf{F}, \mathbf{A}_i) \\ &\quad + \Psi_{\text{nlloc}}^{\text{grd}}(\nabla_{\mathbf{X}}\phi; \mathbf{F}) + \Psi_{\text{nlloc}}^{\text{plty}}(\phi, \kappa). \end{aligned} \quad (3.5)$$

Provided that the external load can be derived from a potential, the local external energy function can be specified as $\Psi_{\text{ext}}(\varphi)$.

In summary, the total potential energy function is additively composed of the internal and external contribution so that its local form reads

$$\Psi(\varphi, \mathbf{F}, \phi, \nabla_{\mathbf{X}}\phi, \mathbf{A}_i, \kappa) = \Psi_{\text{int}}(\mathbf{F}, \phi, \nabla_{\mathbf{X}}\phi, \mathbf{A}_i, \kappa) + \Psi_{\text{ext}}(\varphi). \quad (3.6)$$

3.1.2 Total potential energy

The total potential energy of a system additively combines the internal contribution Π_{int} , reflecting the action of internal forces, and an external contribution $\Pi_{\text{ext}} = \Pi_{\text{ext}}^{\text{vol}} + \Pi_{\text{ext}}^{\text{sur}}$ due to volume and surface forces, i.e.

$$\Pi(\varphi, \mathbf{F}, \phi, \nabla_{\mathbf{X}}\phi; \mathbf{A}_i, \kappa) = \Pi_{\text{int}} + \Pi_{\text{ext}}. \quad (3.7)$$

The existence of the strain energy function (3.5) provided, the internal energy contribution can be written as

$$\Pi_{\text{int}}(\mathbf{F}, \phi, \nabla_{\mathbf{X}}\phi; \mathbf{A}_i, \kappa) = \int_{B_0} \Psi_{\text{int}} \, dV. \quad (3.8)$$

Assuming 'dead' loads, the external contributions take the representation

$$\Pi_{\text{ext}}^{\text{vol}}(\boldsymbol{\varphi}) = \int_{\mathcal{B}_0} \Psi_{\text{ext}}^{\text{vol}} dV = - \int_{\mathcal{B}_0} \bar{\mathbf{B}} \cdot \boldsymbol{\varphi} dV, \quad (3.9)$$

$$\Pi_{\text{ext}}^{\text{sur}}(\boldsymbol{\varphi}) = \int_{\partial\mathcal{B}_0} \Psi_{\text{ext}}^{\text{sur}} dA = - \int_{\partial\mathcal{B}_0} \bar{\mathbf{T}} \cdot \boldsymbol{\varphi} dA, \quad (3.10)$$

where $\bar{\mathbf{B}}$ denotes the body force vector per unit reference volume and where $\bar{\mathbf{T}}$ characterises the traction vector per unit reference surface area.

3.1.3 Variational form

The boundary problem is governed by the principle of minimum potential energy

$$\min_{\boldsymbol{\varphi}, \phi} \Pi(\boldsymbol{\varphi}, \mathbf{F}, \phi, \nabla_{\mathbf{X}}\phi; \mathbf{A}_i, \kappa), \quad (3.11)$$

which is specified by requiring the first variation of the total potential energy with respect to $\boldsymbol{\varphi}$ and ϕ to vanish identically, i.e.

$$\delta_{\boldsymbol{\varphi}} \Pi(\boldsymbol{\varphi}, \mathbf{F}, \phi, \nabla_{\mathbf{X}}\phi; \mathbf{A}_i, \kappa) \doteq \mathbf{0} \quad \forall \delta\boldsymbol{\varphi}, \quad (3.12)$$

$$\delta_{\phi} \Pi(\boldsymbol{\varphi}, \mathbf{F}, \phi, \nabla_{\mathbf{X}}\phi; \mathbf{A}_i, \kappa) \doteq 0 \quad \forall \delta\phi. \quad (3.13)$$

In detail, the resulting coupled system of equations in *material* description can be deduced as

$$\int_{\mathcal{B}_0} \mathbf{P} : \nabla_{\mathbf{X}}\delta\boldsymbol{\varphi} dV - \int_{\mathcal{B}_0} \bar{\mathbf{B}} \cdot \delta\boldsymbol{\varphi} dV - \int_{\partial\mathcal{B}_0} \bar{\mathbf{T}} \cdot \delta\boldsymbol{\varphi} dA \doteq 0, \quad (3.14)$$

$$\int_{\mathcal{B}_0} \mathbf{Y} \cdot \nabla_{\mathbf{X}}\delta\phi dV - \int_{\mathcal{B}_0} Y \delta\phi dV \doteq 0, \quad (3.15)$$

where the Piola stress \mathbf{P} and the vectorial damage quantity \mathbf{Y} are related to *flux* terms, whereas the body force $\bar{\mathbf{B}}$ and the scalar damage quantity Y are associated to *source* terms. They are defined as

$$\mathbf{P} = \partial_{\mathbf{F}}\Psi, \quad \bar{\mathbf{B}} = - \partial_{\boldsymbol{\varphi}}\Psi_{\text{ext}}^{\text{vol}}, \quad (3.16)$$

$$\mathbf{Y} = \partial_{\nabla_{\mathbf{X}}\phi}\Psi, \quad Y = - \partial_{\phi}\Psi, \quad (3.17)$$

together with $\bar{\mathbf{T}} = - \partial_{\boldsymbol{\varphi}}\Psi_{\text{ext}}^{\text{sur}}$. The corresponding spatial quantities are given by

$$\boldsymbol{\sigma} = \mathbf{P} \cdot \text{cof}(\mathbf{F}^{-1}), \quad \bar{\mathbf{b}} = J^{-1}\bar{\mathbf{B}}, \quad (3.18)$$

$$\mathbf{y} = \mathbf{Y} \cdot \text{cof}(\mathbf{F}^{-1}), \quad y = J^{-1}Y. \quad (3.19)$$

Applying relation $\nabla_{\mathbf{X}}\delta\boldsymbol{\varphi} = \nabla_{\mathbf{x}}\delta\boldsymbol{\varphi}\cdot\mathbf{F}$ as well as $\nabla_{\mathbf{X}}\delta\phi = \nabla_{\mathbf{x}}\delta\phi\cdot\mathbf{F}$ together with equations (2.2) and (2.3) results in the variational forms in *spatial* description,

$$\int_{\mathcal{B}_t} \boldsymbol{\sigma} : \nabla_{\mathbf{x}}\delta\boldsymbol{\varphi} \, dv - \int_{\mathcal{B}_t} \bar{\mathbf{b}} \cdot \delta\boldsymbol{\varphi} \, dv - \int_{\partial\mathcal{B}_t} \bar{\mathbf{t}} \cdot \delta\boldsymbol{\varphi} \, da \doteq 0, \quad (3.20)$$

$$\int_{\mathcal{B}_t} \mathbf{y} \cdot \nabla_{\mathbf{x}}\delta\phi \, dv - \int_{\mathcal{B}_t} y \delta\phi \, dv \doteq 0. \quad (3.21)$$

The first terms in equations (3.14) and (3.20) represent the internal virtual work $\delta_{\boldsymbol{\varphi}}W_{\text{int}} = \delta_{\boldsymbol{\varphi}}\Pi_{\text{int}}$, while the remaining terms characterise the external virtual work $\delta_{\boldsymbol{\varphi}}W_{\text{ext}} = -\delta_{\boldsymbol{\varphi}}\Pi_{\text{ext}}$. Consequently, equations (3.14), (3.20) and (3.15), (3.21) can be expressed in compact form as

$$\delta_{\boldsymbol{\varphi}}W = \delta_{\boldsymbol{\varphi}}W_{\text{int}} - \delta_{\boldsymbol{\varphi}}W_{\text{ext}} = \mathbf{0} \quad \forall \delta\boldsymbol{\varphi}, \quad (3.22)$$

$$\delta_{\phi}W = \delta_{\phi}W_{\text{int}} - \delta_{\phi}W_{\text{ext}} = 0 \quad \forall \delta\phi, \quad (3.23)$$

where the internal and external contributions are given in spatial form as

$$\delta_{\boldsymbol{\varphi}}W_{\text{int}} = \int_{\mathcal{B}_t} \boldsymbol{\sigma} : \nabla_{\mathbf{x}}\delta\boldsymbol{\varphi} \, dv, \quad (3.24)$$

$$\delta_{\boldsymbol{\varphi}}W_{\text{ext}} = \int_{\mathcal{B}_t} \bar{\mathbf{b}} \cdot \delta\boldsymbol{\varphi} \, dv + \int_{\partial\mathcal{B}_t} \bar{\mathbf{t}} \cdot \delta\boldsymbol{\varphi} \, da, \quad (3.25)$$

$$\delta_{\phi}W_{\text{int}} = \int_{\mathcal{B}_t} \mathbf{y} \cdot \nabla_{\mathbf{x}}\delta\phi \, dv, \quad (3.26)$$

$$\delta_{\phi}W_{\text{ext}} = \int_{\mathcal{B}_t} y \delta\phi \, dv. \quad (3.27)$$

These relations provide the basis for the finite-element discretisation described in Section 3.3.

3.1.4 Strong form – Euler-Lagrange equations

For the sake of completeness, the corresponding local Euler-Lagrange equations in material and spatial description are derived in this subsection. By means of the well-established relations

$$\mathbf{P} : \nabla_{\mathbf{X}}\delta\boldsymbol{\varphi} = \nabla_{\mathbf{X}} \cdot [\delta\boldsymbol{\varphi} \cdot \mathbf{P}] - \delta\boldsymbol{\varphi} \cdot [\nabla_{\mathbf{X}} \cdot \mathbf{P}], \quad (3.28)$$

$$\mathbf{Y} \cdot \nabla_{\mathbf{X}}\delta\phi = \nabla_{\mathbf{X}} \cdot [\delta\phi \mathbf{Y}] - \delta\phi \nabla_{\mathbf{X}} \cdot \mathbf{Y}, \quad (3.29)$$

and Gauss's divergence theorem applied to (3.14) and (3.15), we obtain the Euler-Lagrange equations in referential form as

$$\nabla_{\mathbf{X}} \cdot \mathbf{P} + \bar{\mathbf{B}} = \mathbf{0} \quad \text{in} \quad \mathcal{B}_0, \quad (3.30)$$

$$\mathbf{P} \cdot \mathbf{N} = \bar{\mathbf{T}} \quad \text{on} \quad \partial\mathcal{B}_0, \quad (3.31)$$

$$\text{and} \quad \nabla_{\mathbf{X}} \cdot \mathbf{Y} + Y = 0 \quad \text{in} \quad \mathcal{B}_0, \quad (3.32)$$

$$\mathbf{Y} \cdot \mathbf{N} = 0 \quad \text{on} \quad \partial\mathcal{B}_0. \quad (3.33)$$

Equations (3.30), (3.31) represent the common quasi-static balance of linear momentum in local form with respect to the reference configuration \mathcal{B}_0 . Equations (3.32), (3.33) represent the governing local balance relations associated with the nonlocal damage field ϕ with respect to the reference configuration \mathcal{B}_0 . In this regard, it is important to note that—as implied in equation (3.33)—a *natural boundary condition of vanishing flux of the nonlocal damage variable* across the boundary $\partial\mathcal{B}_0$ is assumed, as applied for instance by de Borst and Pamin [48], Peerlings et al. [234] and Simone et al. [263], amongst others.

Using analogous arguments, the Euler-Lagrange equations in spatial description can be provided. Using the relations

$$\boldsymbol{\sigma} : \nabla_x \delta \boldsymbol{\varphi} = \nabla_x \cdot [\delta \boldsymbol{\varphi} \cdot \boldsymbol{\sigma}] - \delta \boldsymbol{\varphi} \cdot [\nabla_x \cdot \boldsymbol{\sigma}], \quad (3.34)$$

$$\mathbf{y} \cdot \nabla_x \delta \phi = \nabla_x \cdot [\delta \phi \mathbf{y}] - \delta \phi \nabla_x \cdot \mathbf{y}, \quad (3.35)$$

and Gauss's divergence theorem applied to (3.20) and (3.21), gives the Euler-Lagrange equations in spatial form as

$$\nabla_x \cdot \boldsymbol{\sigma} + \bar{\mathbf{b}} = \mathbf{0} \quad \text{in} \quad \mathcal{B}_t, \quad (3.36)$$

$$\boldsymbol{\sigma} \cdot \mathbf{n} = \bar{\mathbf{t}} \quad \text{on} \quad \partial\mathcal{B}_t, \quad (3.37)$$

$$\text{and} \quad \nabla_x \cdot \mathbf{y} + y = 0 \quad \text{in} \quad \mathcal{B}_t, \quad (3.38)$$

$$\mathbf{y} \cdot \mathbf{n} = 0 \quad \text{on} \quad \partial\mathcal{B}_t. \quad (3.39)$$

3.2 Constitutive relations

In this section, we first briefly review the hyperelastic constitutive equations adopted on the basis of an isotropic compressible neo-Hookean relation and an anisotropic contribution, cf. Gasser et al. [107]. These relations essentially characterise the *elastic* anisotropic response of the fibre-reinforced materials considered. As a key aspect of this section, the gradient-enhanced, nonlocal contribution to the free energy function is specified, followed by the formulation of continuum damage and its related algorithmic implementation.

3.2.1 Hyperelastic part of the free energy function

From Section 3.1.1, we recall the local free energy density Ψ_{loc} , equation (3.1), to be additively composed of an isotropic part Ψ_{iso} , representing the contribution of an isotropic matrix material, and of an anisotropic part Ψ_{ani} , representing the contributions of the individual families of fibres. In the following, we assume the isotropic part to be specified by a compressible neo-Hookean format

$$\Psi_{\text{iso}} = \frac{\mu_e}{2} [I_1 - 3] - \mu_e \ln(J) + \frac{\lambda_e}{2} [\ln(J)]^2, \quad (3.40)$$

3 A gradient-enhanced continuum model for the simulation of damage

Table 3.1: Structural, elastic and damage-related parameters as used in constitutive equations specified in Sections 3.2.1–3.2.3.

| Type | Symbol | Description | Unit |
|----------------|-------------------|--------------------------|--------------------------------------|
| structural | \mathbf{a}_{0i} | fibre orientation vector | [-] |
| | \varkappa | dispersion parameter | [-] |
| elastic | μ_e | shear modulus | [kPa] |
| | κ_e | bulk modulus | [kPa] |
| | k_1 | elastic constant | [kPa] |
| | k_2 | elastic constant | [-] |
| regularisation | c_d | degree of regularisation | [kPa ⁻¹ mm ²] |
| | β_d | penalty parameter | [kPa ⁻¹] |
| | γ_d | (non-)local switch | [-] |
| damage | η_d | saturation parameter | [kPa ⁻¹] |
| | κ_d | damage threshold | [kPa] |

with $I_1 = \mathbf{C} : \mathbf{I} = \mathbf{b} : \mathbf{I}$ denoting the first principal invariant and the Finger tensor $\mathbf{b} = \mathbf{F} \cdot \mathbf{F}^t$. The elastic constants are represented by the Lamé-parameters μ_e and $\lambda_e = \kappa_e - 2/3 \mu_e$ in terms of the shear modulus μ_e and the bulk modulus κ_e . The corresponding Cauchy stress tensor can be derived by means of the constitutive equation for hyperelastic materials, i.e. equations (3.16)₁ and (3.18)₁, and takes the same additive structure as (3.1), i.e.

$$\boldsymbol{\sigma} = \boldsymbol{\sigma}_{\text{iso}} + f_d(\kappa) \boldsymbol{\sigma}_{\text{ani}}. \quad (3.41)$$

For the particular strain energy density (3.40), the isotropic contribution to the Cauchy stresses can be specified as

$$\boldsymbol{\sigma}_{\text{iso}} = \frac{\mu_e}{J} [\mathbf{b} - \mathbf{I}] + \frac{\lambda_e}{J} \ln(J) \mathbf{I}. \quad (3.42)$$

The anisotropic contribution of the local free energy (3.1) is based on a modified version of an orthotropic exponential model with two families of fibres, as originally proposed by Holzapfel et al. [135]. This also includes the effect of fibre dispersion, see Gasser et al. [107], the review article by Holzapfel and Ogden [138] or Menzel et al. [201]. The free energy adopted is represented by the exponential format

$$\Psi_{\text{ani}} = \frac{k_1}{2k_2} \sum_{i=1}^N [\exp(k_2 \langle E_i \rangle^2) - 1], \quad (3.43)$$

with the strain-like quantity $E_i = \varkappa I_1 + [1 - 3\varkappa] I_{4i} - 1$ and the invariant $I_{4i} = \mathbf{C} : \mathbf{A}_i = \mathbf{C} : [\mathbf{a}_{0i} \otimes \mathbf{a}_{0i}]$ for $N = 2$ the number of fibre families. The term $\langle E_i \rangle$, where

$\langle \bullet \rangle = [|\bullet| + \bullet]/2$ is the Macaulay bracket, reflects the basic assumption that fibres can support tension only. Consequently, the anisotropic strain energy density Ψ_{ani} can only contribute if the fibre-related strain is positive, i.e. $E_i > 0$. Fibre dispersion is introduced by means of the parameter $\varkappa \in [0, 1/2]$, where $\varkappa = 0$ corresponds to no dispersion, i.e. transverse isotropy, and where $\varkappa = 1/3$ provides an isotropic distribution, whereas $\varkappa = 1/2$ represents an isotropic distribution in the plane perpendicular to \mathbf{a}_{0i} . The corresponding anisotropic contribution to the Cauchy stress tensor can, for the particular strain energy density (3.43), be represented as

$$\boldsymbol{\sigma}_{\text{ani}} = 2k_1 \sum_{i=1}^N [E_i \exp(k_2 \langle E_i \rangle^2) \mathbf{h}_i] \quad (3.44)$$

with the generalised structural tensor $\mathbf{h}_i = \varkappa \mathbf{b} + [1 - 3\varkappa] \mathbf{a}_i \otimes \mathbf{a}_i$. Table 3.1 summarises the structural and elastic material quantities included in constitutive equations (3.40)–(3.44) together with their units. It is important to note that the fibre orientations may be defined arbitrarily, but that the present formulation uses only *one* nonlocal damage variable so that both fibre families undergo identical degradation. This is physically meaningful if both families of fibers possess one and the same stretch history, otherwise a second nonlocal damage variable may be included in the formulation.

3.2.2 Gradient-enhanced part of the free energy function

According to equation (3.4), the nonlocal part of the free energy function is assumed to be additively composed of a gradient-related contribution $\Psi_{\text{nloc}}^{\text{grd}}$ and of a penalty term $\Psi_{\text{nloc}}^{\text{plty}}$. These free energy terms are specified as

$$\Psi_{\text{nloc}}^{\text{grd}}(\nabla_{\mathbf{X}}\phi; \mathbf{F}) = \frac{c_d}{2} \nabla_{\mathbf{X}}\phi \cdot \mathbf{C}^{-1} \cdot \nabla_{\mathbf{X}}\phi = \frac{c_d}{2} \nabla_{\mathbf{x}}\phi \cdot \nabla_{\mathbf{x}}\phi, \quad (3.45)$$

$$\Psi_{\text{nloc}}^{\text{plty}}(\phi, \kappa) = \frac{\beta_d}{2} [\phi - \gamma_d \kappa]^2. \quad (3.46)$$

The energy-related penalty parameter β_d approximately enforces the local damage field κ and the nonlocal field ϕ to coincide. Furthermore, the gradient parameter c_d controls the quasi-nonlocal character of the formulation and characterises the degree of gradient regularisation. Finally, a switch-parameter $\gamma_d \in \{0, 1\}$ is introduced to change between the local and nonlocal gradient-enhanced model: $\gamma_d = 0$ or $c_d = 0$ results in a local model, while $\gamma_d = 1$ and $c_d \neq 0$ leads to the regularised gradient-enhanced model. For the particular nonlocal free energy functions (3.45) and (3.46), the scalar and vectorial quantities, y and \mathbf{y} , can be specified by means of relations (3.17) and (3.19) as

$$y = -J^{-1} \beta_d [\phi - \gamma_d \kappa], \quad (3.47)$$

$$\mathbf{y} = J^{-1} c_d \nabla_{\mathbf{x}}\phi. \quad (3.48)$$

The damage-related parameters included in constitutive equations (3.45)–(3.46) together with their units are summarised in Table 3.1.

Remark 3.2.1 *Based on the general format of the variational form for the nonlocal damage field variable (3.21) and using relations (3.47) and (3.48), the variational form can be formulated as*

$$\int_{\mathcal{B}_t} J^{-1} c_d \nabla_{\mathbf{x}} \phi \cdot \nabla_{\mathbf{x}} \delta \phi \, dv + \int_{\mathcal{B}_t} J^{-1} \beta_d [\phi - \gamma_d \kappa] \delta \phi \, dv \doteq 0. \quad (3.49)$$

Using the identity $\nabla_{\mathbf{x}} \phi \cdot \nabla_{\mathbf{x}} \delta \phi = \nabla_{\mathbf{x}} \cdot [\nabla_{\mathbf{x}} \phi \delta \phi] - \delta \phi \Delta_{\mathbf{x}} \phi$ with the Laplace operator $\Delta_{\mathbf{x}}(\bullet) = \nabla_{\mathbf{x}} \cdot [\nabla_{\mathbf{x}}(\bullet)]$ and Gauss's divergence theorem, the first integral can be expressed as

$$\int_{\mathcal{B}_t} J^{-1} c_d \nabla_{\mathbf{x}} \phi \cdot \nabla_{\mathbf{x}} \delta \phi \, dv = \int_{\partial \mathcal{B}_t} J^{-1} c_d [\delta \phi \nabla_{\mathbf{x}} \phi] \cdot \mathbf{n} \, da - \int_{\mathcal{B}_t} J^{-1} c_d \delta \phi \Delta_{\mathbf{x}} \phi \, dv. \quad (3.50)$$

Assuming homogeneous Neumann boundary conditions, i.e. $\nabla_{\mathbf{x}} \phi \cdot \mathbf{n} = 0$ on $\partial \mathcal{B}_t$, the weak form finally takes the representation

$$\int_{\mathcal{B}_t} J^{-1} c_d \Delta_{\mathbf{x}} \phi \delta \phi \, dv - \int_{\mathcal{B}_t} J^{-1} \beta_d [\phi - \gamma_d \kappa] \delta \phi \, dv \doteq 0. \quad (3.51)$$

Based on this, the Euler-Lagrange equation for the nonlocal damage field variable in spatial format results in

$$c_d \Delta_{\mathbf{x}} \phi - \beta_d [\phi - \gamma_d \kappa] = 0 \quad \text{in} \quad \mathcal{B}_t, \quad (3.52)$$

$$\nabla_{\mathbf{x}} \phi \cdot \mathbf{n} = 0 \quad \text{on} \quad \partial \mathcal{B}_t. \quad (3.53)$$

Equation (3.52) is a second order differential equation governing the evolution of the nonlocal damage variable ϕ , cf. Dimitrijević and Hackl [85]. An illustrative interpretation of this differential equation is provided by Liebe et al. [186], where the term $\Delta_{\mathbf{x}} \phi$ is related to the curvature of the damage profile, i.e. the driving force increases (decreases) in regions with positive (negative) curvature and consequently ‘broadens’ the damage profile.

Remark 3.2.2 *As an alternative to the gradient-related contribution (3.45) to the free energy function, one could similarly assume the format*

$$\Psi_{\text{nlloc}}^{\text{grd}}(\nabla_{\mathbf{X}} \phi) = \frac{c_d}{2} \nabla_{\mathbf{X}} \phi \cdot \nabla_{\mathbf{X}} \phi = \frac{c_d}{2} \nabla_{\mathbf{x}} \phi \cdot \mathbf{b} \cdot \nabla_{\mathbf{x}} \phi. \quad (3.54)$$

In this context, the reader is referred to Steinmann [269], who considered the nonlocal strain energy density as an additional primary variable and who investigated four different options for their specification—basically motivated from material and spatial averaging procedures and combinations thereof. The free energy (3.45), as used in the course of this chapter, results in stress-like quantities (3.47) and (3.48) which, in spatial

form, formally coincide with the expressions for the small strain case, apart from the factor J^{-1} , cf. Dimitrijević and Hackl [85]. This simplifies the formulation in terms of spatial arguments as compared to the analogous expression based on equation (3.54). As a finite element formulation in terms of spatial arguments is used, equation (3.45) is applied in the following.

3.2.3 Gradient-enhanced damage model – continuous formulation

In order to obtain the stress-like thermodynamic forces driving the local dissipative damage process, we follow standard thermodynamic arguments; see, e.g., Lemaitre and Chaboche [182], and Dimitrijević [84]. The total temperature-weighted production of entropy $\dot{\mathcal{S}}$ for an isothermal, irreversible damage process is governed by

$$\dot{\mathcal{S}} = \int_{\mathcal{B}_0} [\mathbf{P} : \dot{\mathbf{F}} - \dot{\Psi}] \, dV \geq 0. \quad (3.55)$$

Differentiation of the general format of the free energy function (3.5) with respect to time allows us to specify relation (3.55) as

$$\begin{aligned} \dot{\mathcal{S}} = \int_{\mathcal{B}_0} & \left[[\mathbf{P} - \partial_{\mathbf{F}}\Psi] : \dot{\mathbf{F}} - \partial_{\kappa}\Psi \dot{\kappa} \right. \\ & \left. - \partial_{\nabla_{\mathbf{X}}\phi}\Psi \cdot \nabla_{\mathbf{X}}\dot{\phi} - \partial_{\phi}\Psi \dot{\phi} \right] \, dV \geq 0. \end{aligned} \quad (3.56)$$

Taking into account equation (3.15) together with the definitions (3.17) and the rate form considered here, the last two terms in (3.56) depending on $\dot{\phi}$ vanish. The Clausius-Planck inequality can be formulated in local form defining the internal dissipation \mathcal{D} as

$$\mathcal{D} = [\mathbf{P} - \partial_{\mathbf{F}}\Psi] : \dot{\mathbf{F}} - \partial_{\kappa}\Psi \dot{\kappa} \geq 0. \quad (3.57)$$

By means of the Coleman-Noll procedure, one recovers the Piola stresses as introduced in equation (3.16) based on variational arguments. The reduced dissipation inequality in local form results in

$$\mathcal{D}_{\text{red}} = g \dot{\kappa} \geq 0 \quad (3.58)$$

including the thermodynamic force $g \geq 0$ conjugate to the damage variable $\kappa \in [0, \infty)$, i.e.

$$g = -\partial_{\kappa}\Psi = -\partial_{\kappa}\Psi^{\text{loc}} - \partial_{\kappa}\Psi^{\text{nloc}} = g^{\text{loc}} + g^{\text{nloc}}, \quad (3.59)$$

which ensures thermodynamic consistency, i.e. $\mathcal{D}_{\text{red}} \geq 0$, if g and $\dot{\kappa}$ are non-negative.

As indicated in the introduction, the exponential contribution due to the fibre-related anisotropic part of the free energy may ‘over-compensate’ the damage contribution and result in an increase of the local stress vs. stretch response even for $\kappa \rightarrow \infty$. In order

to avoid this undesired effect, we adopt the classic scalar $[1-d]$ -damage formulation in the following and introduce the thermodynamic force $q \geq 0$ conjugate to the damage variable $d \in [0, 1)$, i.e.

$$q = -\partial_d \Psi = -\partial_\kappa \Psi \partial_d \kappa = g \partial_d \kappa. \quad (3.60)$$

The reduced dissipation inequality is satisfied, i.e. $\mathcal{D}_{\text{red}} \geq 0$, if $\partial_d \kappa > 0$.

In this context, note the relation $f_d(\kappa) = 1 - d$ so that $-\partial_d(\bullet) = \partial_{f_d}(\bullet)$. The thermodynamic force q takes the interpretation of the effective strain energy of the fibre contributions released per unit current volume, also called energy release rate. It becomes apparent that the Cauchy stress tensor $\boldsymbol{\sigma}$ maintains its form associated to a standard local free energy function, whereas the energy release rate q is composed of a local and nonlocal contribution $q_{\text{loc}} = -\partial_d \Psi_{\text{loc}}$ and $q_{\text{nloc}} = -\partial_d \Psi_{\text{nloc}} = -\partial_\kappa \Psi_{\text{nloc}} \partial_d \kappa$, respectively. To be specific, we obtain

$$q_{\text{loc}} = \Psi_{\text{ani}} \quad \text{and} \quad q_{\text{nloc}} = \beta_d \gamma_d [\phi - \gamma_d \kappa] \partial_d \kappa. \quad (3.61)$$

By means of relation (3.52), the nonlocal energy release rate can alternatively be expressed as $q_{\text{nloc}} = \gamma_d c_d \Delta_{\mathbf{x}} \phi \partial_d \kappa$.

We now adopt a damage condition, at any time of the loading process, as

$$\Phi_d = q - \kappa \leq 0 \quad (3.62)$$

where $\Phi_d < 0$ refers to the purely elastic case and where $\Phi_d = 0$ includes damage evolution. Based on the postulate of maximum dissipation, a constrained optimisation problem involving the Lagrange multiplier λ can be constructed which results in the following associated representation of the evolution of the damage variable

$$\dot{\kappa} = \lambda \frac{\partial \Phi_d}{\partial q} = \lambda \quad \text{with} \quad \kappa|_{t=0} = \kappa_d. \quad (3.63)$$

Initiation as well as termination of damage are assumed to be governed by the Karush-Kuhn-Tucker complementary conditions

$$\lambda \geq 0, \quad \Phi_d \leq 0, \quad \lambda \Phi_d = 0, \quad (3.64)$$

which, equivalently but more illustratively, can be reformulated as

$$\left\{ \begin{array}{l} \Phi_d < 0 \\ \Phi_d = 0 \end{array} \right. \quad \text{and} \quad \left\{ \begin{array}{ll} \lambda < 0 & \text{elastic unloading} \\ \lambda = 0 & \text{neutral loading} \\ \lambda > 0 & \text{damage loading} \end{array} \right. \quad \text{elastic} \quad (3.65)$$

see Simo and Hughes [262] and Figure 3.2 for a graphical representation.

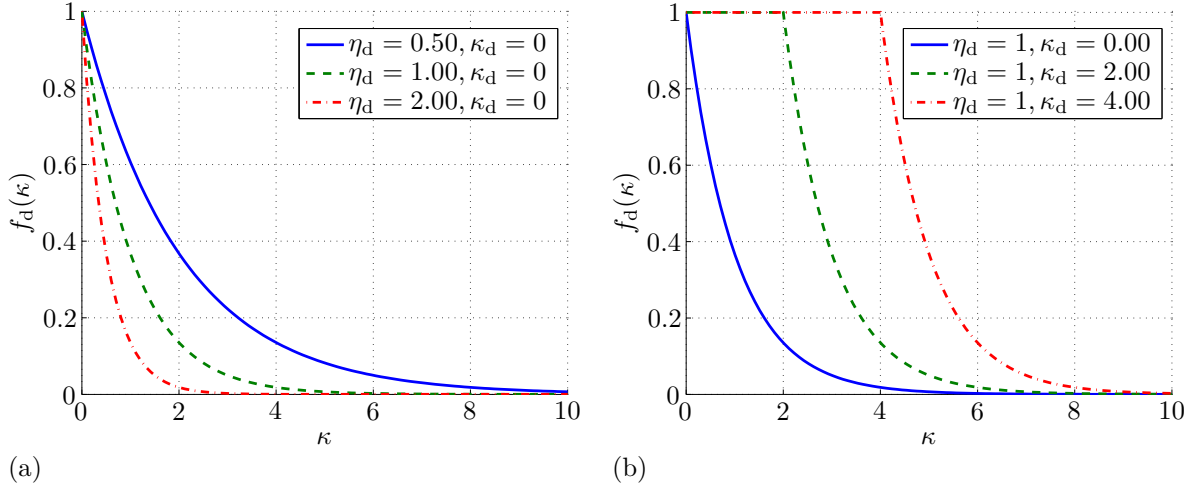


Figure 3.1: Exponential damage function $f_d(\kappa)$, see equation (3.66). (a) Different values of the damage saturation parameter η_d . (b) Different values of the damage threshold parameter κ_d where the function $f_d(\kappa) = \exp(-\eta_d \langle \kappa - \kappa_d \rangle)$ is plotted for purpose of illustration.

For the damage function $f_d(\kappa)$, we adopt a simple exponential-type law

$$f_d(\kappa) = 1 - d = \exp(\eta_d [\kappa_d - \kappa]), \quad (3.66)$$

with $\eta_d > 0$ so that $\partial_d \kappa = [\eta_d f_d(\kappa)]^{-1} > 0$. We use an initial damage threshold κ_d , which must be exceeded in order to activate damage evolution; in this regard, the initial condition in (3.63) is of major importance. Furthermore, an exponential saturation parameter η_d is included. Note, that for $\kappa_d = 0$ and $\eta_d = 1$, relation (3.66) reduces to the format $f_d(\kappa) = \exp(-\kappa)$ applied by Dimitrijević and Hackl [85]. The driving force introduced in (3.60) is, however, different and possesses the property $q^{\text{loc}} = \Psi^{\text{loc}} > 0 \forall \mathbf{F} \neq \mathbf{I}$, whereas $g^{\text{loc}} = \eta_d f_d(\kappa) \Psi^{\text{loc}} \rightarrow 0$ for $\kappa \rightarrow \infty$, which turns out to be essential for the energy function Ψ^{loc} chosen later on. Figure 3.1 illustrates the characteristics of function (3.66) for different parameters. It becomes apparent that larger values of η_d accelerate the damage process, cf. Figure 3.1(a), whereas larger values of κ_d lead to a delay of the damage initiation, cf. Figure 3.1(b). Note, that for the limiting case where $\kappa_d = 0$, damage is initiated from the very beginning of the loading process, whereas no damage evolution is obtained for $\kappa_d \rightarrow \infty$.

Remark 3.2.3 Relation (3.66) represents a constitutive assumption which is required to be at least twice differentiable and has to satisfy condition (3.2). In this regard, one could specify alternative formats for the damage function $f_d(\kappa)$ giving more flexibility in calibration and a possibly smoother transition from the undamaged to the damaged state. Two possible damage functions including a maximum damage value d_∞ were suggested by Miehe [214], who introduced

$$f_d^\diamond(\kappa) = 1 - d_\infty [1 - \exp(-\eta_d \kappa)], \quad (3.67)$$

and Leukart and Ramm [183], who adopted an extended format

$$f_d^*(\kappa) = \frac{\kappa_d}{\kappa} [1 - d_\infty [1 - \exp(\eta_d [\kappa_d - \kappa])]] , \quad (3.68)$$

incorporating an initial damage threshold κ_d . The format proposed by S  ez et al. [254],

$$f_d^\Delta(\kappa) = \frac{1}{1 + \exp(\eta_d [\kappa - \kappa_d])} , \quad (3.69)$$

however, does not fulfill the basic requirements (3.2) for all parameter sets $\{\eta_d, \kappa_d\}$, to give an example: $\eta_d = 1$, $\kappa_d = 1$. Similar observations hold for the tanh-related format

$$f_d^\bullet(\kappa) = -\frac{1}{2} [\tanh(\eta_d [\kappa - \kappa_d]) - 1] . \quad (3.70)$$

As an advantage of the gradient-enhanced damage model elaborated in the present work, any damage function satisfying (3.2) can be adopted.

3.2.4 Gradient-enhanced damage model – algorithmic setting

Evolution equation (3.63) represents a non-linear ordinary differential equation, which is integrated numerically in order to obtain the internal damage variable κ at a current time step $n + 1$. In this context, we introduce respective intervals in time, $\Delta t = t_{n+1} - t_n \geq 0$, and apply an implicit, unconditionally stable Euler backward integration scheme, which yields

$$\kappa = \kappa_n + \gamma \quad \text{with} \quad \kappa|_{t_0} = \kappa_d \quad (3.71)$$

where $\gamma := \Delta t \lambda$ is the incremental Lagrange multiplier at time t_{n+1} . Here and in the following, we omit the subscript index $n + 1$ associated with time t_{n+1} for the sake of readability. The incremental Karush-Kuhn-Tucker conditions read

$$\gamma \geq 0, \quad \Phi_d \leq 0, \quad \gamma \Phi_d = 0. \quad (3.72)$$

The stresses are updated according to relations (3.41) and (3.47) by

$$\boldsymbol{\sigma} = \boldsymbol{\sigma}_{\text{iso}} + f_d(\kappa) \boldsymbol{\sigma}_{\text{ani}} , \quad (3.73)$$

$$y = -J^{-1} \beta_d [\phi - \gamma_d \kappa] , \quad (3.74)$$

with $\kappa = \kappa_n$ for an elastic incremental load step. For an *inelastic* incremental load step, the incremental Lagrange multiplier γ is computed by enforcing the incremental consistency condition such that

$$\Phi_d = q - \kappa = 0 \quad (3.75)$$

$$= \Psi_{\text{ani}} + \frac{\beta_d \gamma_d}{\eta_d f_d(\kappa)} [\phi - \gamma_d \kappa] - \kappa \quad (3.76)$$

Table 3.2: Algorithmic box for the gradient-enhanced damage model (to be continued on page 76). Quantities without subscript n are assumed to be associated with t_{n+1} .

0. given: deformation gradient \mathbf{F} , nonlocal damage variable ϕ and gradient $\nabla_{\mathbf{x}}\phi$ at time t and internal damage variable κ_n at time t_n (initialise (non-)local damage field variable as $\kappa|_{t_0} = \phi|_{t_0} = \kappa_d$)
1. compute isotropic elastic contribution of strain energy Ψ_{iso} , Cauchy stress $\boldsymbol{\sigma}_{\text{iso}}$ and elasticity tensor \mathbf{e}_{iso}
2. compute anisotropic elastic contribution of strain energy Ψ_{ani} , Cauchy stress $\boldsymbol{\sigma}_{\text{ani}}$ and elasticity tensor \mathbf{e}_{ani}
3. compute driving force

$$q = \Psi_{\text{ani}} + \frac{\beta_d \gamma_d}{\eta_d f_d(\kappa_n)} [\phi - \gamma_d \kappa_n]$$
 with damage function $f_d(\kappa_n) = \exp(\eta_d [\kappa_d - \kappa_n])$
4. check damage condition

if $\Phi_d = q - \kappa_n \leq 0$, set $\kappa = \kappa_n$ and go to 6.
 else go to 5.
5. perform (damped) local Newton-Raphson scheme to compute incremental Lagrange multiplier γ iteratively
 - (a) compute residual $r^k := \Phi_d(\kappa^k)$

$$r^k = \Psi_{\text{ani}} + \frac{\beta_d \gamma_d}{\eta_d f_d(\kappa^k)} [\phi - \gamma_d \kappa^k] - \kappa^k$$
 - (b) check tolerance

if $|r^k| < \text{tol}$ go to 6.
 else go to 5. (c)
 - (c) compute tangent of residual

$$d_\gamma r^k = \frac{\beta_d \gamma_d}{\eta_d f_d(\kappa^k)} [\eta_d [\phi - \gamma_d \kappa^k] - \gamma_d] - 1$$
 - (d) compute increment

$$\Delta\gamma = - [d_\gamma r^k]^{-1} r^k$$
 - (e) update incremental Lagrange multiplier

$$\gamma^{k+1} = \gamma^k + \eta \Delta\gamma$$
 with η adjusted iteratively by means of damped Newton scheme (see Table 3.3)
 - (f) update internal damage variable

$$\kappa^k = \kappa_n + \gamma^{k+1}$$
 and go to 5. (a)

Table 3.2 (continued): Algorithmic box for the gradient-enhanced damage model. Quantities without subscript n are assumed to be associated with t_{n+1} .

| |
|--|
| <p>6. compute flux and source terms</p> $\boldsymbol{\sigma} = \boldsymbol{\sigma}_{\text{iso}} + f_d(\kappa) \boldsymbol{\sigma}_{\text{ani}}$ $\mathbf{y} = J^{-1} c_d \nabla_{\mathbf{x}} \phi$ $\mathbf{y} = -J^{-1} \beta_d [\phi - \gamma_d \kappa]$ <p>7. compute tangent moduli, see Section 3.3.3</p> $\mathbf{e} = \mathbf{e}_{\text{iso}} + f_d \mathbf{e}_{\text{ani}} + \eta_d f_d \vartheta_d J \boldsymbol{\sigma}_{\text{ani}} \otimes \boldsymbol{\sigma}_{\text{ani}}$ $d\boldsymbol{\sigma} / d\phi = 2 d\mathbf{y} / d\mathbf{g} = \beta_d \gamma_d \vartheta_d \boldsymbol{\sigma}_{\text{ani}}$ $d\mathbf{y} / d\phi = -J^{-1} \beta_d [1 + \beta_d \gamma_d^2 [\eta_d f_d]^{-1} \vartheta_d]$ $d\mathbf{y} / d\nabla_{\mathbf{x}} \phi = J^{-1} c_d \mathbf{I}$ <p>with abbreviation $\vartheta_d = -1 - \frac{\eta_d f_d(\kappa)}{\beta_d \gamma_d [\gamma_d [1 + \eta_d \kappa] - \eta_d \phi]}$</p> |
|--|

which depends non-linearly on γ . This non-linear equation can be solved iteratively by employing a Newton-Raphson method. We expand equation (3.75) in a Taylor series at γ^k with k denoting the particular Newton iteration step. Neglecting terms of second and higher order, we obtain

$$\gamma^{k+1} = \gamma^k - [d_\gamma r^k]^{-1} r^k \quad (3.77)$$

where $r^k := \Phi_d(\kappa^k)$ is the residual in the k -th iteration step. For the particular choice of the damage coefficient function

$$f_d(\kappa) = \exp(\eta_d [\kappa_d - \kappa]), \quad (3.78)$$

the Jacobian of the Newton-Raphson scheme reads

$$d_\gamma r^k = \frac{\beta_d \gamma_d}{\eta_d f_d(\kappa)} [\eta_d [\phi - \gamma_d \kappa] - \gamma_d] - 1. \quad (3.79)$$

With γ determined, the internal damage variable can be updated iteratively according to (3.71) while the norm of the residual is larger than a pre-defined tolerance. Finally, the stresses can be calculated according to (3.73) and (3.74). The algorithm related to the constitutive model is summarised in Table 3.2.

Remark 3.2.4 *Setting $\gamma_d = 0$ results in an entirely local damage formulation. By additionally providing a sufficiently ‘simple’ damage function f_d , the internal damage variable κ can be updated in closed form by $\kappa = \max\{q, \kappa_n, \kappa_d\}$ without any local iterations,*

Table 3.3: Calculation steps for the damped Newton scheme applied for 5. (e) in Table 3.2. Quantities without subscript n are assumed to be associated with t_{n+1} .

| |
|--|
| <p>0. given: internal damage variable κ_n at time t_n, increment $\Delta\gamma$, Lagrange multipliers γ^{k+1}, γ^k and $\eta = 1$</p> <p>1. evaluate $f^k := \Delta\gamma [\Phi_d(\kappa_n + \gamma^k)]$</p> <p>2. perform local iteration with adjusted damping parameter η</p> <p>(a) evaluate $f^{k+1} := \Delta\gamma [\Phi_d(\kappa_n + \gamma^{k+1})]$</p> <p>(b) check condition if $f^{k+1} < f^k$ go to 3. else go to 2. (c)</p> <p>(c) adjust damping parameter $\eta \leftarrow \epsilon \eta$ with $\epsilon = 0.5$</p> <p>(d) adjust update $\gamma^{k+1} = \gamma^k + \eta \Delta\gamma$</p> <p>3. continue with 5. (f) of Table 3.2</p> |
|--|

even though the constitutive update is still fully implicit. In this regard, the reader is referred to Gurtin and Francis [115], Simo [261] and Miehe [214] for related local damage formulations or Steinmann [269] and Liebe et al. [186] for gradient-extended damage approaches.

Remark 3.2.5 Due to the exponential characteristics of the anisotropic contribution of the local free energy, equation (3.43), it may occur that the local Newton-Raphson scheme does not converge for large loading increments, not even for a comparatively high number of iterations. In order to obtain results and to generally improve the convergence rate, we apply a line search method, i.e. a damped Newton-Raphson iteration scheme. Using this technique, the increment $\Delta\gamma = -[\mathbf{d}_\gamma r^k]^{-1} r^k$ obtained from equation (3.79) can be interpreted as an optimal direction of advance towards the solution. The magnitude of $\Delta\gamma$ of the iteration step is controlled (damped) by a parameter η according to

$$\gamma^{k+1} = \gamma^k + \eta \Delta\gamma, \quad (3.80)$$

where η is adjusted (reduced) within every iteration. After starting with $\eta = 1$, which corresponds to the standard Newton-Raphson method, η is then successively scaled by

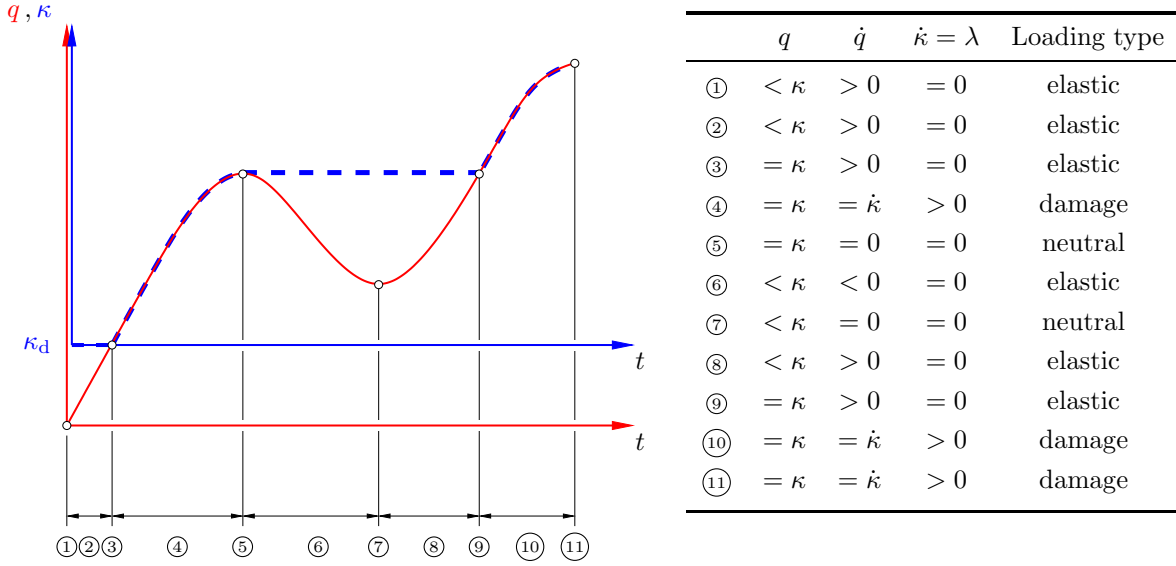


Figure 3.2: Illustration of the Karush-Kuhn-Tucker conditions, i.e. loading-unloading conditions (3.64) or (3.65) in combination with the consistency condition $\lambda \dot{\Phi}_d = 0$.

0.5, i.e. $\eta \leftarrow \epsilon \eta$ with $\epsilon = 0.5$ if the norm of the residual-like quantity $|f^{k+1}|$ is larger than its respective value $|f^k|$ in the previous iteration. The algorithm corresponding to the damped Newton scheme as used in this chapter is summarised in Table 3.3.

3.3 Finite element discretisation

This section deals with the spatial discretisation of the underlying coupled system of non-linear equations by means of the finite element method. In particular, a coupled Bubnov-Galerkin-based finite element discretisation approach with respect to the current configuration is performed. Its specification will include a combination of tri-quadratic serendipity interpolation functions with respect to the displacement field, and tri-linear interpolation functions with respect to the nonlocal damage field variable. As an advantage of the serendipity elements, one and the same eight-point integration scheme can be applied to both types of differently approximated degrees of freedom. The resulting coupled non-linear system of equations can appropriately be solved with an incremental-iterative Newton-Raphson-type solution procedure.

3.3.1 Discretisation

The domain \mathcal{B}_0 is discretised by n_{el} finite elements, so that

$$\mathcal{B}_0 \approx \mathcal{B}_0^h = \bigcup_{e=1}^{n_{el}} \mathcal{B}_0^e, \quad (3.81)$$

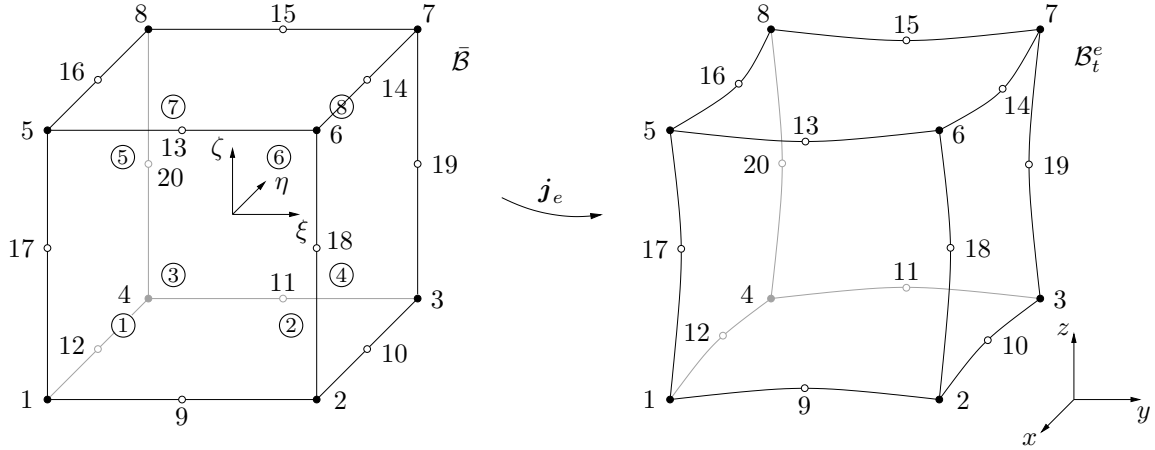


Figure 3.3: Quasi-isoparametric 20-node hexahedral element in reference coordinate space $\{\xi, \eta, \zeta\}$ and in physical coordinate space $\{x, y, z\}$. Deformation-related degrees of freedom φ_I are referred to all nodes (\bullet and \circ) whereas nonlocal-damage-related degrees of freedom ϕ_I are referred to the vertex nodes (\bullet) only. The integration points are consecutively numbered by $\textcircled{1}$ – $\textcircled{8}$.

where every finite element \mathcal{B}_0^e is characterised by n_{en}^φ placement-nodes and n_{en}^ϕ nonlocal-damage-nodes. According to the isoparametric concept, the field variables φ , as well as the geometry \mathbf{X} , are interpolated by the same shape functions N_I , i.e.

$$\mathbf{X} \approx \mathbf{X}^h = \sum_{I=1}^{n_{\text{en}}} N_I(\boldsymbol{\xi}) \mathbf{X}_I, \quad \varphi \approx \varphi^h = \sum_{I=1}^{n_{\text{en}}} N_I(\boldsymbol{\xi}) \varphi_I, \quad (3.82)$$

and are transformed to a hexahedral reference element with coordinates $\boldsymbol{\xi} := \{\xi, \eta, \zeta\} \in \bar{\mathcal{B}}$, where $\bar{\mathcal{B}} := \{\boldsymbol{\xi} \in \mathbb{R}^3 \mid -1 \leq \chi \leq +1; \chi = \xi, \eta, \zeta\}$ denotes the reference domain, see Figure 3.3. In the present context, the number of displacement-nodes and nonlocal-damage-nodes per element—and consequently the related shape functions—do not necessarily have to coincide, i.e. $n_{\text{en}}^\varphi \neq n_{\text{en}}^\phi$ and $N_I^\varphi \neq N_I^\phi$, respectively. Following Dimitrijević [84], we use the denomination *quasi-isoparametric* approximation instead of *isoparametric* approximation, see Figure 3.3. The corresponding field variables, i.e. the placement φ and the nonlocal damage variable ϕ as well as their spatial gradients $\nabla_{\mathbf{x}}\varphi$ and $\nabla_{\mathbf{x}}\phi$, are approximated by means of the product of shape functions $N_I^\alpha(\boldsymbol{\xi})$, $\alpha = \varphi, \phi$ and discrete nodal degrees of freedom φ_I and ϕ_I summed over n_{en}^φ respectively n_{en}^ϕ nodes per element, i.e.

$$\varphi^h = \sum_{I=1}^{n_{\text{en}}^\varphi} N_I^\varphi \varphi_I, \quad \phi^h = \sum_{K=1}^{n_{\text{en}}^\phi} N_K^\phi \phi_K, \quad (3.83)$$

$$\nabla_{\mathbf{x}}\varphi^h = \sum_{I=1}^{n_{\text{en}}^\varphi} \varphi_I \otimes \nabla_{\mathbf{x}}N_I^\varphi, \quad \nabla_{\mathbf{x}}\phi^h = \sum_{K=1}^{n_{\text{en}}^\phi} \phi_K \nabla_{\mathbf{x}}N_K^\phi. \quad (3.84)$$

3 A gradient-enhanced continuum model for the simulation of damage

According to the Bubnov-Galerkin method, an analogous approximation is applied for the variations of field variables and corresponding gradients as

$$\delta \boldsymbol{\varphi}^h = \sum_{I=1}^{n_{\text{en}}^{\varphi}} N_I^{\varphi} \delta \boldsymbol{\varphi}_I, \quad \delta \phi^h = \sum_{K=1}^{n_{\text{en}}^{\phi}} N_K^{\phi} \delta \phi_K, \quad (3.85)$$

$$\nabla_{\mathbf{x}} \delta \boldsymbol{\varphi}^h = \sum_{I=1}^{n_{\text{en}}^{\varphi}} \delta \boldsymbol{\varphi}_I \otimes \nabla_{\mathbf{x}} N_I^{\varphi}, \quad \nabla_{\mathbf{x}} \delta \phi^h = \sum_{K=1}^{n_{\text{en}}^{\phi}} \delta \phi_K \nabla_{\mathbf{x}} N_K^{\phi}, \quad (3.86)$$

where the spatial and material gradients of the shape functions N_I can be expressed as

$$\nabla_{\mathbf{x}} N_I^{\varphi} = \mathbf{j}_e^{-\text{t}} \cdot \nabla_{\boldsymbol{\xi}} N_I^{\varphi} \quad \text{with} \quad \mathbf{j}_e = \nabla_{\boldsymbol{\xi}} \boldsymbol{\varphi}^h = \sum_{I=1}^{n_{\text{en}}^{\varphi}} \boldsymbol{\varphi}_I \otimes \nabla_{\boldsymbol{\xi}} N_I^{\varphi}, \quad (3.87)$$

$$\nabla_{\mathbf{X}} N_I^{\varphi} = \mathbf{J}_e^{-\text{t}} \cdot \nabla_{\boldsymbol{\xi}} N_I^{\varphi} \quad \text{with} \quad \mathbf{J}_e = \nabla_{\boldsymbol{\xi}} \mathbf{X}^h = \sum_{I=1}^{n_{\text{en}}^{\varphi}} \mathbf{X}_I \otimes \nabla_{\boldsymbol{\xi}} N_I^{\varphi}. \quad (3.88)$$

Similar relations for the gradients of N_K^{ϕ} follow by analogy with (3.87), (3.88). As a consequence, the discrete deformation gradient can be represented in terms of the spatial and material Jacobians of the isoparametric transformation as

$$\mathbf{F}^h := \nabla_{\mathbf{X}} \boldsymbol{\varphi}^h = \mathbf{j}_e \cdot \mathbf{J}_e^{-1}. \quad (3.89)$$

Compatibility provided, the discretised weak form on element level can be written as the difference between the element-specific expressions for the internal and external virtual work related expressions $\delta_{\varphi} W_{\text{int}}^e$ and $\delta_{\varphi} W_{\text{ext}}^e$, so that

$$\delta_{\varphi} W^e = \delta_{\varphi} W_{\text{int}}^e - \delta_{\varphi} W_{\text{ext}}^e = \mathbf{0} \quad \forall \quad \delta \boldsymbol{\varphi}_I, \quad (3.90)$$

$$\delta_{\phi} W^e = \delta_{\phi} W_{\text{int}}^e - \delta_{\phi} W_{\text{ext}}^e = 0 \quad \forall \quad \delta \phi_K, \quad (3.91)$$

where the discrete representations take the following forms

$$\delta_{\varphi} W_{\text{int}}^e = \sum_{I=1}^{n_{\text{en}}^{\varphi}} \delta \boldsymbol{\varphi}_I \cdot \mathbf{f}_{\text{int } I}^{\varphi} \quad \text{with} \quad \mathbf{f}_{\text{int } I}^{\varphi} = \int_{B_t^e} \nabla_{\mathbf{x}} N_I^{\varphi} \cdot \boldsymbol{\sigma} \, dv, \quad (3.92)$$

$$\delta_{\varphi} W_{\text{ext}}^e = \sum_{I=1}^{n_{\text{en}}^{\varphi}} \delta \boldsymbol{\varphi}_I \cdot \mathbf{f}_{\text{ext } I}^{\varphi} \quad \text{with} \quad \mathbf{f}_{\text{ext } I}^{\varphi} = \int_{B_t^e} N_I^{\varphi} \bar{\mathbf{b}} \, dv + \int_{\partial B_t^e} N_I^{\varphi} \bar{\mathbf{t}} \, da, \quad (3.93)$$

$$\delta_{\phi} W_{\text{int}}^e = \sum_{K=1}^{n_{\text{en}}^{\phi}} \delta \phi_K f_{\text{int } K}^{\phi} \quad \text{with} \quad f_{\text{int } K}^{\phi} = \int_{B_t^e} \nabla_{\mathbf{x}} N_K^{\phi} \cdot \mathbf{y} \, dv, \quad (3.94)$$

$$\delta_{\phi} W_{\text{ext}}^e = \sum_{K=1}^{n_{\text{en}}^{\phi}} \delta \phi_K f_{\text{ext } K}^{\phi} \quad \text{with} \quad f_{\text{ext } K}^{\phi} = \int_{B_t^e} N_K^{\phi} y \, dv. \quad (3.95)$$

According to the fundamental lemma of calculus of variations, equations (3.90) and (3.91) are equivalent to the equilibrium of internal and external nodal variables in every $I = 1, \dots, n_{\text{en}}^{\varphi}$ placement-node, respectively $K = 1, \dots, n_{\text{en}}^{\phi}$ nonlocal-damage-node of a finite element e . This results in the node-specific residual form of the present coupled problem

$$\mathbf{r}_I^{\varphi} = \mathbf{f}_{\text{int } I}^{\varphi} - \mathbf{f}_{\text{ext } I}^{\varphi} = \mathbf{0} \quad \forall \quad I = 1, \dots, n_{\text{en}}^{\varphi}, \quad (3.96)$$

$$r_K^{\phi} = f_{\text{int } K}^{\phi} - f_{\text{ext } K}^{\phi} = 0 \quad \forall \quad K = 1, \dots, n_{\text{en}}^{\phi}. \quad (3.97)$$

3.3.2 Linearisation

The governing highly non-linear system of equations (3.96) and (3.97) includes coupling between the motion $\boldsymbol{\varphi}$ and the nonlocal damage field ϕ , which itself is linked to the local damage variable κ by means of the penalty contributions. To solve this non-linear system of equations, we use an incremental-iterative Newton-Raphson scheme. In what follows, we omit the subscript index $n + 1$ associated with time t_{n+1} for the sake of readability. A Taylor series expansion around the solution at the current iteration step l —terms of quadratic and higher order being neglected—gives

$$\mathbf{r}_{Il+1}^{\varphi} = \mathbf{r}_{Il}^{\varphi} + \Delta \mathbf{r}_I^{\varphi} = \mathbf{0}, \quad (3.98)$$

$$r_{Kl+1}^{\phi} = r_{Kl}^{\phi} + \Delta r_K^{\phi} = 0, \quad (3.99)$$

with the node-specific increments of the residuals

$$\Delta \mathbf{r}_I^{\varphi} = \sum_{J=1}^{n_{\text{en}}^{\varphi}} \frac{d\mathbf{r}_I^{\varphi}}{d\boldsymbol{\varphi}_J} \cdot \Delta \boldsymbol{\varphi}_J + \sum_{L=1}^{n_{\text{en}}^{\phi}} \frac{d\mathbf{r}_I^{\varphi}}{d\phi_L} \Delta \phi_L, \quad (3.100)$$

$$\Delta r_K^{\phi} = \sum_{J=1}^{n_{\text{en}}^{\varphi}} \frac{dr_K^{\phi}}{d\boldsymbol{\varphi}_J} \cdot \Delta \boldsymbol{\varphi}_J + \sum_{L=1}^{n_{\text{en}}^{\phi}} \frac{dr_K^{\phi}}{d\phi_L} \Delta \phi_L. \quad (3.101)$$

Herein, the increments $\Delta \boldsymbol{\varphi}_J = \boldsymbol{\varphi}_{Jl+1} - \boldsymbol{\varphi}_{Jl}$ and $\Delta \phi_L = \phi_{Ll+1} - \phi_{Ll}$ represent the difference between the discrete nodal degrees of freedom at iteration-steps $l + 1$ and l . Assuming ‘dead loads’, the node-specific sub-matrices of the Jacobian are deduced as

$$\mathbf{K}_{IJ}^{\varphi\varphi} = \frac{d\mathbf{r}_I^{\varphi}}{d\boldsymbol{\varphi}_J} = \int_{B_t^e} \left[\nabla_{\mathbf{x}} N_I^{\varphi} \cdot \mathbf{e} \cdot \nabla_{\mathbf{x}} N_J^{\varphi} + [\nabla_{\mathbf{x}} N_I^{\varphi} \cdot \boldsymbol{\sigma} \cdot \nabla_{\mathbf{x}} N_J^{\varphi}] \mathbf{I} \right] dv, \quad (3.102)$$

$$\mathbf{K}_{IL}^{\varphi\phi} = \frac{d\mathbf{r}_I^{\varphi}}{d\phi_L} = \int_{B_t^e} \nabla_{\mathbf{x}} N_I^{\varphi} \cdot \frac{d\boldsymbol{\sigma}}{d\phi} N_L^{\phi} dv, \quad (3.103)$$

$$\mathbf{K}_{KJ}^{\phi\varphi} = \frac{dr_K^{\phi}}{d\boldsymbol{\varphi}_J} = \int_{B_t^e} N_K^{\phi} 2 \frac{dy}{d\mathbf{g}} \cdot \nabla_{\mathbf{x}} N_J^{\varphi} dv, \quad (3.104)$$

$$K_{KL}^{\phi\phi} = \frac{dr_K^{\phi}}{d\phi_L} = \int_{B_t^e} \left[N_K^{\phi} \frac{dy}{d\phi} N_L^{\phi} + \nabla_{\mathbf{x}} N_K^{\phi} \cdot \frac{d\mathbf{y}}{d\nabla_{\mathbf{x}}\phi} \cdot \nabla_{\mathbf{x}} N_L^{\phi} \right] dv. \quad (3.105)$$

Furthermore, \mathbf{e} , $d\boldsymbol{\sigma}/d\phi$, $2d\mathbf{y}/d\mathbf{g}$, $d\mathbf{y}/d\phi$ and $d\mathbf{y}/d\nabla_{\mathbf{x}}\phi$ denote partitions of the consistent tangent-moduli as specified in Section 3.3.3. The resulting system of equations is clearly symmetric—since a variational framework is used—so that $\mathbf{K}_{IL}^{\varphi\phi} = \mathbf{K}_{KJ}^{\phi\varphi\text{t}}$ which conveniently enables the use of symmetric equation solvers.

The node-specific residual (load) vectors (3.92)₂–(3.95)₂ and the stiffness contributions (3.102)–(3.105) can be summarised as the element-based residual vector, and stiffness matrix

$$\begin{aligned} \mathbf{r}_e^\varphi &:= [\mathbf{r}_I^\varphi], & \mathbf{r}_e^\phi &:= [r_K^\phi], & \Delta\boldsymbol{\varphi}_e &:= [\Delta\boldsymbol{\varphi}_I], & \Delta\boldsymbol{\phi}_e &:= [\Delta\phi_K], \\ \mathbf{K}_e^{\varphi\varphi} &:= [\mathbf{K}_{IJ}^{\varphi\varphi}], & \mathbf{K}_e^{\varphi\phi} &:= [\mathbf{K}_{IL}^{\varphi\phi}], & \mathbf{K}_e^{\phi\varphi} &:= [\mathbf{K}_{KJ}^{\phi\varphi}], & \mathbf{K}_e^{\phi\phi} &:= [K_{KL}^{\phi\phi}]. \end{aligned}$$

This results in the following linearised system of equations on element level

$$\begin{bmatrix} \mathbf{r}_e^\varphi \\ \mathbf{r}_e^\phi \end{bmatrix} + \begin{bmatrix} \mathbf{K}_e^{\varphi\varphi} & \mathbf{K}_e^{\varphi\phi} \\ \mathbf{K}_e^{\phi\varphi} & \mathbf{K}_e^{\phi\phi} \end{bmatrix} \cdot \begin{bmatrix} \Delta\boldsymbol{\varphi}_e \\ \Delta\boldsymbol{\phi}_e \end{bmatrix} = \begin{bmatrix} \mathbf{0} \\ \mathbf{0} \end{bmatrix} \quad (3.106)$$

for the determination of the unknown increments of the element degrees of freedom $\Delta\boldsymbol{\varphi}_e$ and $\Delta\boldsymbol{\phi}_e$. Consequently, the assembly of all elements

$$\mathbf{r} := \mathbf{A}_{e=1}^{n_{el}} \begin{bmatrix} \mathbf{r}_e^\varphi \\ \mathbf{r}_e^\phi \end{bmatrix}, \quad \mathbf{K} = \mathbf{A}_{e=1}^{n_{el}} \begin{bmatrix} \mathbf{K}_e^{\varphi\varphi} & \mathbf{K}_e^{\varphi\phi} \\ \mathbf{K}_e^{\phi\varphi} & \mathbf{K}_e^{\phi\phi} \end{bmatrix}, \quad \Delta\mathbf{d} = \mathbf{A}_{e=1}^{n_{el}} \begin{bmatrix} \Delta\boldsymbol{\varphi}_e \\ \Delta\boldsymbol{\phi}_e \end{bmatrix},$$

results in the global linearised system of equations in the l -th iteration step

$$\mathbf{r}_l + \mathbf{K}_l \cdot \Delta\mathbf{d} = \mathbf{0} \quad \text{with} \quad \Delta\mathbf{d} = \mathbf{d}_{l+1} - \mathbf{d}_l, \quad (3.107)$$

with \mathbf{K}_l being the global tangent stiffness matrix, $\Delta\mathbf{d}$ the global incremental vector of degrees of freedom, \mathbf{r}_l the global residual vector including the internal and external system loads and the incorporation of Dirichlet boundary conditions not explicitly indicated here.

Remark 3.3.1 *The integrals in equations (3.92)–(3.95) and (3.102)–(3.105) are typically evaluated numerically at discrete integration points by means of appropriate integration or rather quadrature rules, such as Gaussian quadrature, see Hughes [140]. For two-dimensional problems, Dimitrijević and Hackl [85] employed a full 3×3 -quadrature. However, following de Borst and Pamin [48], we use a reduced $2 \times 2 \times 2$ Gaussian quadrature rule, see Figure 3.3. As a major benefit, one and the same reduced quadrature rule can conveniently be applied to integrate the expressions related to the tri-quadratic placement field as well as to the tri-linear nonlocal damage field variable. In this regard, we take advantage of the fact that serendipity elements show no zero-energy modes for reduced quadrature rules if more than one element is used, cf. Hughes [140, pp. 240/241].*

3.3.3 Local tangent moduli

The local tangent moduli, contained in the element Jacobians (3.102)–(3.105), can conveniently be derived in material description and then transferred to the spatial description as used for the numerical implementation, by means of push-forward operations. In the following, we omit the subscript index $n + 1$ associated with time t_{n+1} for the sake of readability.

For the present model, the contributions to the Piola-Kirchhoff stresses are given as

$$\mathbf{S}_{\text{iso}} = \mu_e [\mathbf{I} - \mathbf{C}^{-1}] + \lambda_e \ln(J) \mathbf{C}^{-1}, \quad (3.108)$$

$$\mathbf{S}_{\text{ani}} = 2 k_1 \sum_{i=1}^N [E_i \exp(k_2 \langle E_i \rangle^2) \mathbf{H}_i], \quad (3.109)$$

where the material version of the generalised structural tensor $\mathbf{H}_i = \varkappa \mathbf{I} + [1 - 3\varkappa] \mathbf{a}_{0i} \otimes \mathbf{a}_{0i}$ is used. By means of the chain rule together with the definitions $\mathbf{E}_{\text{iso}} := 2 \partial \mathbf{S}_{\text{iso}} / \partial \mathbf{C}$ and $\mathbf{E}_{\text{ani}} := 2 \partial \mathbf{S}_{\text{ani}} / \partial \mathbf{C}$, we obtain

$$\mathbf{E} := 2 \frac{d\mathbf{S}}{d\mathbf{C}} = \mathbf{E}_{\text{iso}} + f_d \mathbf{E}_{\text{ani}} + 2 \mathbf{S}_{\text{ani}} \otimes \frac{\partial f_d}{\partial \kappa} \frac{\partial \kappa}{\partial \mathbf{C}}, \quad (3.110)$$

$$\frac{d\mathbf{S}}{d\phi} = \frac{\partial f_d}{\partial \kappa} \frac{\partial \kappa}{\partial \phi} \mathbf{S}_{\text{ani}}, \quad (3.111)$$

$$2 \frac{dY}{d\mathbf{C}} = 2 \frac{\partial Y}{\partial \kappa} \frac{\partial \kappa}{\partial \mathbf{C}}, \quad (3.112)$$

$$\frac{dY}{d\phi} = \frac{\partial Y}{\partial \phi} + \frac{\partial Y}{\partial \kappa} \frac{\partial \kappa}{\partial \phi}. \quad (3.113)$$

with

$$\mathbf{E}_{\text{iso}} = \lambda_e \mathbf{C}^{-1} \otimes \mathbf{C}^{-1} + 2 [\mu_e - \lambda_e \ln(J)] \mathbf{I}_{\text{sym}}^{\mathbf{C}^{-1}}, \quad (3.114)$$

$$\mathbf{E}_{\text{ani}} = 4 k_1 \sum_{i=1}^N [\exp(k_2 \langle E_i \rangle^2) [1 + 2 k_2 \langle E_i \rangle^2] \mathbf{H}_i \otimes \mathbf{H}_i], \quad (3.115)$$

where the definition of the fourth order tensor $\mathbf{I}_{\text{sym}}^{\mathbf{C}^{-1}} := -\partial \mathbf{C}^{-1} / \partial \mathbf{C} = [\mathbf{C}^{-1} \overline{\otimes} \mathbf{C}^{-1} + \mathbf{C}^{-1} \underline{\otimes} \mathbf{C}^{-1}] / 2$ is used.

The remaining task is to determine the derivatives, on the right hand sides of equations (3.110)–(3.113) as well as $d\mathbf{Y} / d\nabla_{\mathbf{X}} \phi$. We subsequently specify these expressions consecutively according to their appearance in the above mentioned equations.

Recalling that $\Phi_d(q, \kappa) = 0$ for damage evolution, the tensorial derivative $\partial \kappa / \partial \mathbf{C}$ and $\partial \kappa / \partial \phi$ are deduced by means of the implicit function theorem as

$$2 \frac{\partial \kappa}{\partial \mathbf{C}} = -2 \frac{\partial \Phi_d / \partial \mathbf{C}}{\partial \Phi_d / \partial \kappa} = -\vartheta_d \mathbf{S}_{\text{ani}}, \quad (3.116)$$

$$\frac{\partial \kappa}{\partial \phi} = -\frac{\partial \Phi_d / \partial \phi}{\partial \Phi_d / \partial \kappa} = -\vartheta_d \frac{\beta_d \gamma_d}{\eta_d f_d}, \quad (3.117)$$

where the abbreviation

$$\vartheta_d := \left[\frac{\partial \Phi_d}{\partial \kappa} \right]^{-1} = -1 - \frac{\eta_d f_d}{\beta_d \gamma_d [\gamma_d [1 + \eta_d \kappa] - \eta_d \phi]} \quad (3.118)$$

is introduced. Taking into account that $\partial_\kappa f_d = -\eta_d f_d$ and $\partial_\kappa Y = -\beta_d \gamma_d$ as well as $\partial_\phi Y = \beta_d$, we obtain the material tangent moduli as

$$\mathbf{E} = \mathbf{E}_{\text{iso}} + f_d \mathbf{E}_{\text{ani}} + \eta_d f_d \vartheta_d \mathbf{S}_{\text{ani}} \otimes \mathbf{S}_{\text{ani}}, \quad (3.119)$$

$$\frac{d\mathbf{S}}{d\phi} = \beta_d \gamma_d \vartheta_d \mathbf{S}_{\text{ani}}, \quad (3.120)$$

$$2 \frac{dY}{d\mathbf{C}} = \beta_d \gamma_d \vartheta_d \mathbf{S}_{\text{ani}}, \quad (3.121)$$

$$\frac{dY}{d\phi} = \beta_d + [\beta_d \gamma_d]^2 [\eta_d f_d]^{-1} \vartheta_d, \quad (3.122)$$

$$\frac{dY}{d\nabla_{\mathbf{x}}\phi} = c_d \mathbf{C}^{-1}. \quad (3.123)$$

For a purely elastic loading step, the tangent moduli can be reduced to $\mathbf{E} = \mathbf{E}^{\text{iso}} + f_d \mathbf{E}^{\text{ani}}$ and $d\mathbf{S}/d\phi = 2 dY/d\mathbf{C} = \mathbf{0}$ as well as $dY/d\phi = \beta_d$.

Applying standard push-forward operations to equations (3.119)–(3.123), we finally obtain the Cauchy-stress-related spatial tangent moduli as

$$\mathbf{e} = 2 \frac{d\boldsymbol{\sigma}}{d\mathbf{g}} = \mathbf{e}_{\text{iso}} + f_d \mathbf{e}_{\text{ani}} + \eta_d f_d \vartheta_d J \boldsymbol{\sigma}_{\text{ani}} \otimes \boldsymbol{\sigma}_{\text{ani}}, \quad (3.124)$$

$$\frac{d\boldsymbol{\sigma}}{d\phi} = \beta_d \gamma_d \vartheta_d \boldsymbol{\sigma}_{\text{ani}}, \quad (3.125)$$

$$2 \frac{d\mathbf{y}}{d\mathbf{g}} = \beta_d \gamma_d \vartheta_d \boldsymbol{\sigma}_{\text{ani}}, \quad (3.126)$$

$$\frac{d\mathbf{y}}{d\phi} = J^{-1} \beta_d [1 + \beta_d \gamma_d^2 [\eta_d f_d]^{-1} \vartheta_d], \quad (3.127)$$

$$\frac{d\mathbf{y}}{d\nabla_{\mathbf{x}}\phi} = J^{-1} c_d \mathbf{I}. \quad (3.128)$$

Note the relation $\partial_{\mathbf{g}}(\bullet) := \mathbf{F} \cdot \partial_{\mathbf{C}}(\bullet) \cdot \mathbf{F}^t$; for detailed background on the formulation of anisotropic finite elasticity and inelasticity in terms of spatial arguments, the reader is referred to Menzel and Steinmann [205, 207]. The isotropic and anisotropic elasticity tensors in spatial description can be expressed as

$$\mathbf{e}_{\text{iso}} = \lambda_e J^{-1} \mathbf{I} \otimes \mathbf{I} + 2 J^{-1} [\mu_e - \lambda_e \ln(J)] \mathbf{I}_{\text{sym}}, \quad (3.129)$$

$$\mathbf{e}_{\text{ani}} = 4 k_1 J^{-1} \sum_{i=1}^N [\exp(k_2 \langle E_i \rangle^2) [1 + 2 k_2 \langle E_i \rangle^2] \mathbf{h}_i \otimes \mathbf{h}_i]. \quad (3.130)$$

3.4 Numerical examples

In this section, we apply the proposed gradient-enhanced damage model to three representative three-dimensional homogeneous and inhomogeneous deformation problems. We first investigate a homogeneous state under uniaxial tension in order to illustrate the basic constitutive characteristics of the local damage formulation. Secondly, we consider a displacement-driven isotropic and anisotropic plate with a hole in order to emphasise the regularisation properties of the model following the gradient-enhancement strategy. Finally, to show the capabilities of the approach with regard to biomechanics-related problems, we study a force-driven example by means of an anisotropic artery-like tube subjected to internal pressure.

The proposed gradient-enhanced damage model is incorporated within the commercial finite-element software Abaqus/Standard by means of the user subroutine UEL, which allows the implementation of general multi-field non-linear element-formulations, for details see the Abaqus 6.11 Documentation [1] and Appendix D.

Table 3.4: Set of structural and material parameters used for boundary value problems in Sections 3.4.1, 3.4.2, and 3.4.3.

| Type | Symbol | Value | | | Unit |
|----------------|---------------|--|-------------------------|-----------------|--------------------------------------|
| | | Test 1 | Test 2 | Test 3 | |
| structural | $\beta_{1,2}$ | 0.0 | – | 0.0 | [deg] |
| | \varkappa | 0.0 | 1/3 | 0.0 | [–] |
| elastic | μ_e | 14.5805 | 14.5805 | 14.5805 | [kPa] |
| | κ_e | 145.805 | 729.025 | 145.805 | [kPa] |
| | k_1 | 7.290 | 218.708 | 14.5805 | [kPa] |
| | k_2 | 0.1 | 150.0 | 2.1 | [–] |
| regularisation | c_d | – | {0, 10, 100, 500, 1000} | 1000.0 | [kPa ⁻¹ mm ²] |
| | β_d | – | 1000.0 | 1000.0 | [kPa ⁻¹] |
| | γ_d | – | 1.0 | 1.0 | [–] |
| damage | η_d | {1, 10 ⁻¹ , 10 ⁻² , 10 ⁻³ } | 4.0 | 4.0 | [kPa ⁻¹] |
| | κ_d | {0.0, 16.0} | 0.2 | {0.5, 1.0, 2.5} | [kPa] |

3.4.1 Test 1 – homogeneous uniaxial tension

As an introductory numerical example to emphasise the properties of the basic constitutive characteristics of the local damage formulation, we discuss a deformation under isochoric uniaxial tension with

$$\mathbf{F} = \lambda_1 \mathbf{e}_1 \otimes \mathbf{e}_1 + \lambda_1^{-1/2} [\mathbf{e}_2 \otimes \mathbf{e}_2 + \mathbf{e}_3 \otimes \mathbf{e}_3] . \quad (3.131)$$

3 A gradient-enhanced continuum model for the simulation of damage

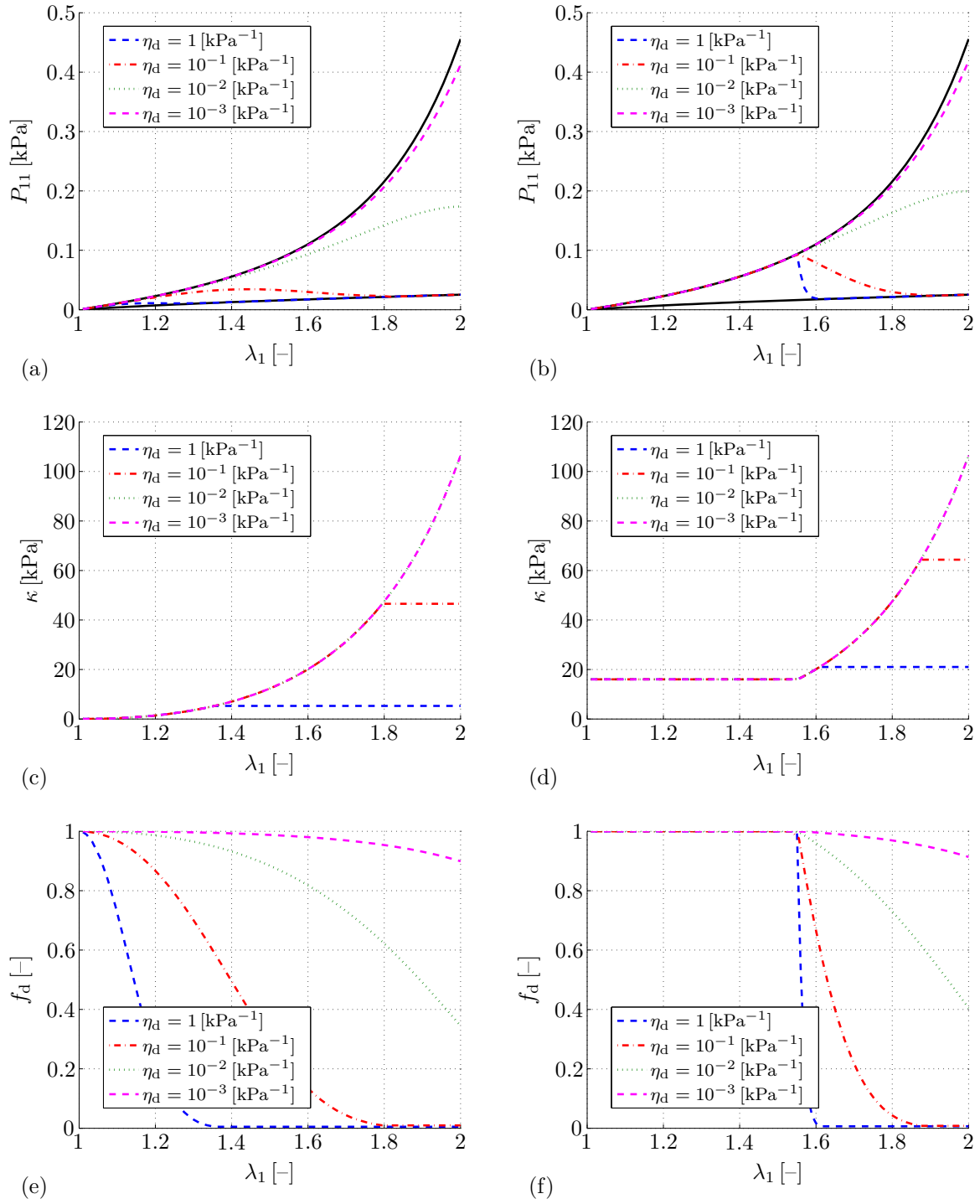


Figure 3.4: Uniaxial isochoric tension: Influence of the saturation parameter η_d . Subfigures (a, c, e) are associated with the damage threshold $\kappa_d = 0.0$ [kPa]. Subfigures (b, d, f) are associated with the damage threshold $\kappa_d = 16.0$ [kPa]. Subfigures (a, b) show the stress-stretch response. The solid black curves represent the elastic response of the isotropic neo-Hookean matrix (lower solid black curve) and the overall elastic response composed of the isotropic neo-Hookean *and* the anisotropic exponential model (upper solid black curve). Subfigures (c, d) show the evolution of the internal damage variable κ . Subfigures (e, f) show the evolution of the damage function $f_d(\kappa) \in (0, 1]$.

The frame $\{\mathbf{e}_1, \mathbf{e}_2, \mathbf{e}_3\}$ represents a fixed orthonormal base system. A monotonically increasing load is applied up to an axial stretch of $\lambda_1 = 2.0$. With regard to the structural properties, both families of fibers are oriented with respect to the axial \mathbf{e}_1 -direction, i.e. $\beta_{1,2} = 0.0$ [deg] where $\beta_{1,2} = \angle(\mathbf{a}_{0,1,2}, \mathbf{e}_1)$. As the dispersion parameter \varkappa is set to zero, ideal transverse isotropy is recovered for every fibre family. The material parameters used for this example are summarised in Table 3.4 in column ‘Test 1’.

For a homogeneous deformation, the gradient-related free energy term (3.45) is not activated, i.e. $\nabla_{\mathbf{x}}\phi = \mathbf{0}$. In consequence, the driving force is represented only by the local term $q = q_{\text{loc}}$ and the damage model’s behaviour is in accordance with a purely local model. Therefore, only the influence of the local damage parameters, i.e. the threshold κ_d and the saturation parameter η_d , is studied in Figure 3.4, where the left column 3.4(a, c, e) is associated with values of $\kappa_d = 0.0$ [kPa], and where the right column 3.4(b, d, f) corresponds to values of $\kappa_d = 16.0$ [kPa]. The stress-stretch response is shown in Figures 3.4(a, b) where $P_{11} = \lambda_1^{-1} \mathbf{e}_1 \cdot \boldsymbol{\sigma} \cdot \mathbf{e}_1$. The two solid black curves represent the fully elastic response of two extreme cases: the isotropic neo-Hookean matrix in the lower solid black curve, and the overall elastic response composed of the isotropic neo-Hookean *and* the anisotropic exponential part, in the upper solid black curve. The inelastic damage-related load-displacement curves can be seen between the two solid black curves. Basically, the material first shows an elastic response according to the exponential constitutive relation. After a certain loading level, the material softens and deviates from the elastic path. Caused by the loss of stiffness, the stress starts to decrease with increasing stretch λ_1 and the curve finally drops towards the black curve which represents the elastic response of the undamaged neo-Hookean ground substance.

It becomes apparent that higher damage saturation values η_d accelerate the damage process. Generally, it is expected that the purely neo-Hookean response is recovered upon complete damage of the fibers. This can be clearly verified for damage saturation values of $\eta_d = \{1, 10^{-1}\}$ [kPa $^{-1}$], whereas for saturation values of $\eta_d = \{10^{-2}, 10^{-3}\}$ [kPa $^{-1}$] complete damage of the fibers cannot be obtained within the deformation range considered. Furthermore, we observe that the higher damage threshold of $\kappa_d = 16.0$ [kPa] leads to a delay of the damage initiation.

The influence of the damage threshold κ_d is illustrated in Figures 3.4(c, d) where the evolution of the internal damage variable κ is shown. Here, we clearly observe how κ_d controls the onset of damage for $\kappa_d = 0.0$ [kPa]. Damage starts at the very beginning of the deformation, see Figure 3.4(c), and continuously evolves, i.e. $\dot{\kappa} > 0$, according to $\kappa = q^{\text{loc}} = \Psi_{\text{ani}}$. The evolution of $\dot{\kappa} > 0$ continues until the fibre-reinforced material is completely damaged. For $\kappa_d = 16.0$ [kPa], see Figure 3.4(d), the damage process is delayed and starts once the driving force $q^{\text{loc}} = \Psi_{\text{ani}}$ exceeds the damage threshold value of $\kappa_d = 16.0$ [kPa], i.e. $q^{\text{loc}} > \kappa_d$. After initiation of the damage process, the damage evolution as represented by $\dot{\kappa} > 0$ continues, up to complete damage of the fibre-reinforced material.

Figures 3.4(e, f) highlight the evolution of the damage function f_d , see equation (3.66). By comparing Figures 3.4(e) and 3.4(f), it becomes apparent how κ_d controls the onset

of damage. Furthermore, we clearly observe that damage evolves faster for higher values of η_d .

3.4.2 Test 2 – isotropic plate with a hole

As a second numerical example, we consider the deformation of an isotropic plate with a hole under Dirichlet boundary conditions. The geometry and its dimensions are depicted in Figure 3.5(a). The plate is assumed to be clamped at the bottom while non-vanishing displacements u are imposed in Y -direction on the top—the remaining displacement degrees of freedom at the top are set to zero. Due to the symmetry and the assumed isotropy of the specimen, only one eighth of the structure is discretised, i.e. the upper right front part of the plate. The nonlocal damage-related field variable ϕ is initialised as the value of the damage threshold κ_d , i.e. $\phi|_{t_0} = \kappa_d$. Full isotropy is ensured by setting the dispersion parameter to $\varkappa = 1/3$ which renders the response to become independent of β_1 and β_2 . The material parameters used for this example are summarised in Table 3.4 in column ‘Test 2’. In view of the choice of the penalty parameter β_d , higher values of β_d generally ensure a better fulfilment of the constraint between ϕ and κ which also turned out to improve the convergence of the *local* Newton-Raphson scheme. For very large values of β_d , however, the global system of equations tends to be ill-conditioned—in the context that the eigenvalues of the global tangent operator possess extremely different orders of magnitude—and the *global* Newton-Raphson scheme may therefore not converge. In either case, a reasonable choice of β_d depends on the specific boundary value problem and on material parameters chosen, so that smaller values of β_d may also result in a good correspondence between ϕ and κ .

For this example, a displacement-controlled cyclic tension test is considered which can be divided in three stages, see Figure 3.5(b): In the first stage the plate is loaded up to a prescribed longitudinal displacement of $u = 24$ [mm] at the top surface. In a second stage the plate is unloaded until the top surface recovers its initial configuration. Finally, in the third stage the plate is once again loaded up to $u = 30$ [mm].

The mechanical response of the plate with hole is illustrated by the load-displacement-curve in Figure 3.5(c). The force f represents the resultant reaction force in Y -direction related to the whole specimen, i.e. not only to one eighth of the plate which is considered for the discretisation. Once more, the two solid black curves represent the fully elastic response of the isotropic neo-Hookean matrix in the lower solid black curve and the overall elastic response composed of the isotropic neo-Hookean *and* the anisotropic exponential part in the upper solid black curve. We observe that the response of the plate initially follows the elastic load-displacement path, also referred to as primary loading path. Upon a certain loading level of approx. $u = 17$ [mm], the response deviates from the elastic path and slightly tends towards the purely neo-Hookean response. Subsequently, the plate is unloaded and completely returns to its unstressed reference state. It becomes apparent that the first loading-unloading cycle is associated with dissipation of energy, represented by the characteristic hysteresis behaviour and the area between the loading

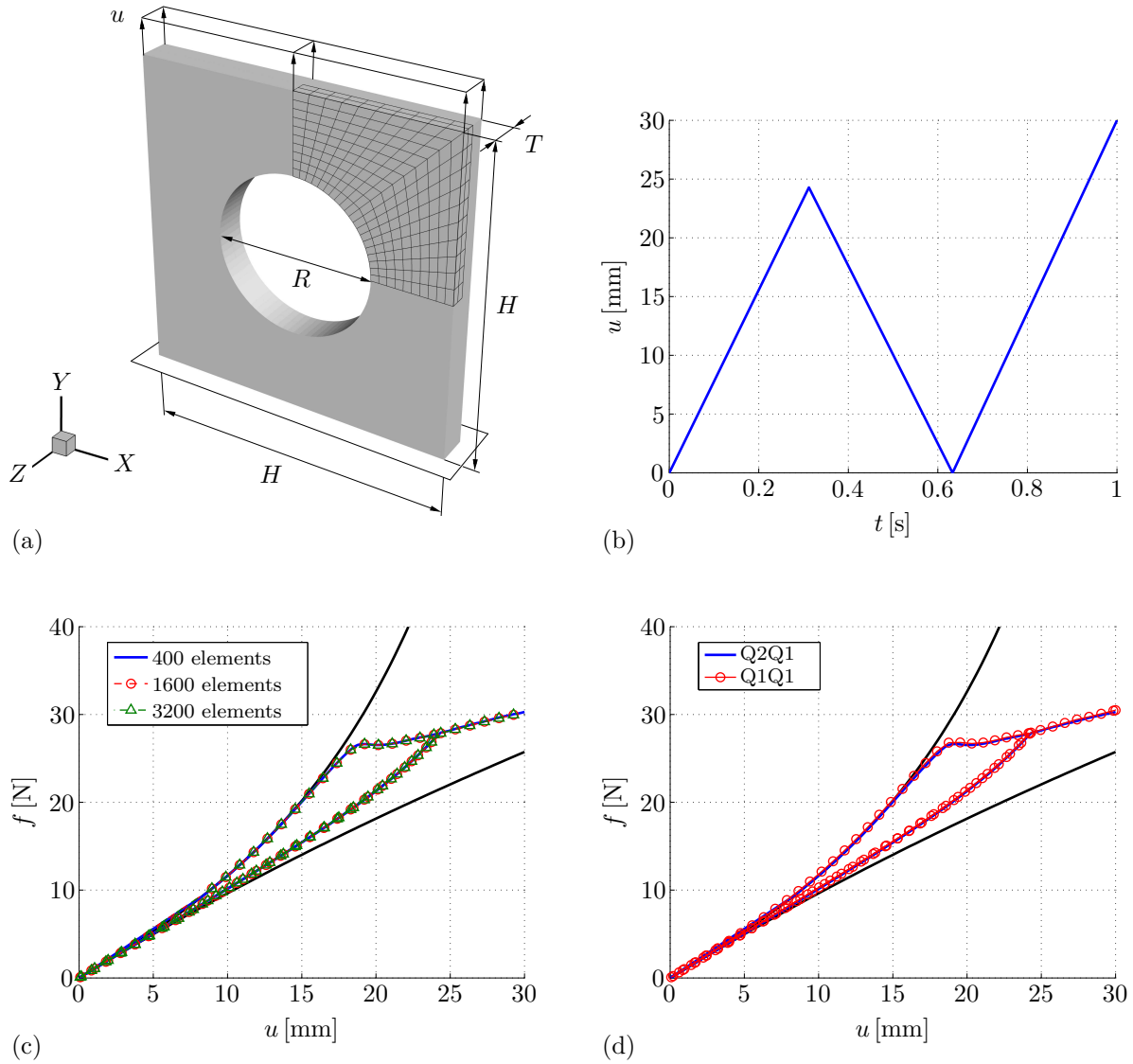


Figure 3.5: Isotropic plate with a hole. (a) Dimensions ($R = 100$ [mm], $H = 200$ [mm], $T = 20$ [mm]) and imposed boundary conditions. Only one eighth of the plate is discretised. (b) Cyclic loading history. (c) Force-displacement response and investigation of mesh-sensitivity. The solid black curves represent the elastic response of the isotropic neo-Hookean matrix (lower solid black curve) and the overall elastic response composed of the isotropic neo-Hookean *and* the anisotropic exponential model (upper solid black curve). (d) Force-displacement response due to cyclic loading for the element types Q2Q1 and Q1Q1 using a 400 element mesh.

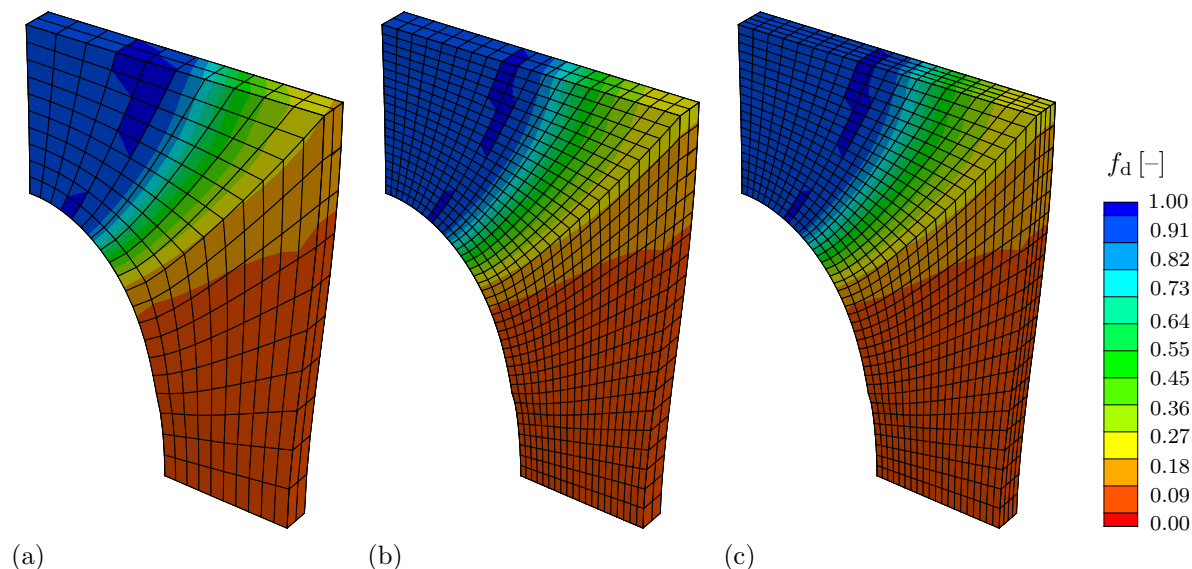


Figure 3.6: Isotropic plate with a hole. Contour plots of the damage function $f_d(\kappa) \in (0, 1]$ at $u = 30$ [mm] and $c_d = 500$ [kPa $^{-1}$] for three different discretisations. (a) 400 elements, (b) 1600 elements, (c) 3200 elements.

and unloading-curves, respectively. When the plate is re-loaded, the load-displacement response first follows the unloading path again, until the continuation of the primary loading path is activated. We note that, in contrast to the homogeneous deformation example discussed above and within the loading levels considered, the curve does not fully drop onto the black curve representing the elastic response of the undamaged neo-Hookean ground substance. Clearly, this is a consequence of the overall inhomogeneous behaviour of the plate with hole, which also involves regions showing less or no damage at all.

One of the major benefits of using a gradient-enhanced damage model lies in the inherent mesh-objectivity of the formulation. In other words, the energy dissipation due to the inelastic processes associated with damage should be independent of the discretisation for sufficiently large values of c_d and sufficiently fine discretisations. In order to illustrate this property, three different discretisations including 400, 1600 and 3200 elements are discussed. The results are presented in Figure 3.5(c) where it becomes apparent that the load-displacement responses almost completely coincide. It can therefore be concluded that, for sufficiently large values of c_d , the dissipation is always the same and the structural response is mesh-independent.

The same conclusion can be drawn from Figure 3.6, where the contour plots of the damage function $f_d(\kappa)$ for the three different meshes turn out to be practically identical. Furthermore, damage is more prominent around the bottom edge of the specimen, the area with the highest stresses. This is consistent with the energy-driven damage formulation, see Section 3.2.3.

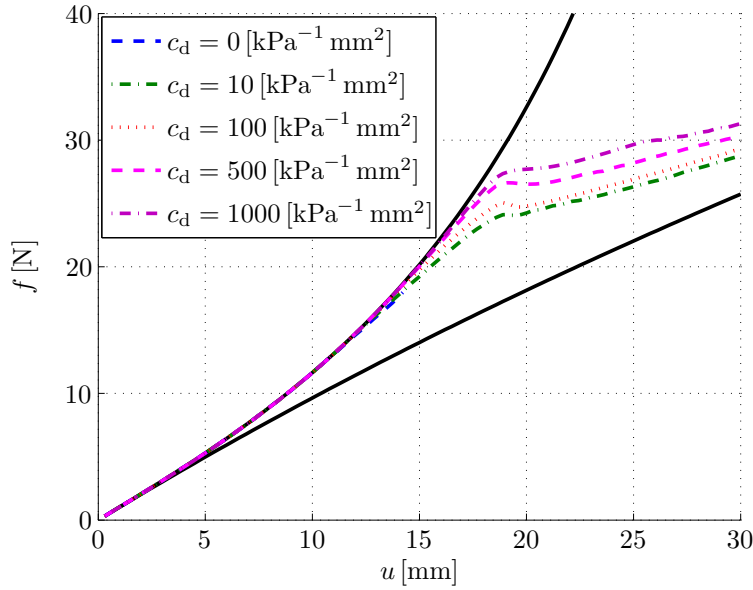


Figure 3.7: Isotropic plate with a hole. Force-displacement response under monotonic loading for different values of the gradient parameter c_d using a 400 element mesh. The solid black curves represent the elastic response of the isotropic neo-Hookean matrix (lower solid black curve) and the overall elastic response composed of the isotropic neo-Hookean *and* the anisotropic exponential model (upper solid black curve).

From Section 3.2.3, we recall that the gradient parameter c_d controls the quasi-nonlocal character of the formulation and characterises the degree of gradient regularisation. As a special case, $c_d = 0$ results in a local model. The strong influence of c_d on the mechanical response is illustrated in Figures 3.7 and 3.8 where values of $c_d = \{0, 10, 100, 500, 1000\}$ [kPa⁻¹ mm²] are investigated for a mesh of 400 elements. Generally, higher values of c_d increase the localisation zone. As a consequence, larger values of c_d increase the dissipation-related area under the load displacement curve in Figure 3.7. Computationally, small values of the gradient parameter $c_d \rightarrow 0$ may lead to numerical instabilities for the solution of the underlying non-linear system of equations, as the local tangent operator might become singular, so that even no global convergence may be obtained. This effect is underlined by Figure 3.7, where the calculation for $c_d = 0.0$ [kPa⁻¹ mm²] cannot be advanced into the softening range but stops at $u = 14.22$ [mm]. With regard to the contour plots of the damage function $f_d(\kappa)$ shown in Figure 3.8, we observe that the deformation patterns are not strongly localised in the form of pronounced narrow damage bands. This is caused by the remaining stiffness of the undamaged isotropic matrix material. A material with a smaller influence of the matrix material would increase the damage evolution on the specimen considerably and, in consequence, would result in a much more pronounced localisation behaviour. This effect is further studied in Section 3.4.3.2.

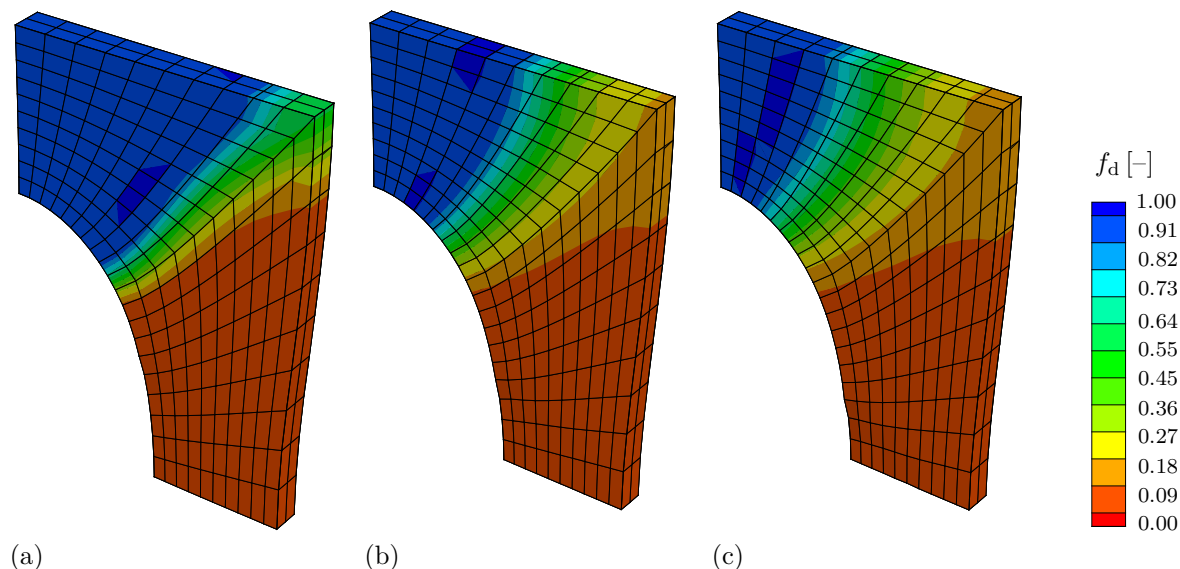


Figure 3.8: Isotropic plate with a hole. Contour plots of the damage function $f_d(\kappa) \in (0, 1]$ at $u = 30$ [mm] for different values of the gradient parameter c_d using a 400 element mesh. (a) $c_d = 100$ [kPa⁻¹], (b) $c_d = 500$ [kPa⁻¹], (c) $c_d = 1000$ [kPa⁻¹].

Up to now, the number of displacement-nodes and nonlocal-damage-nodes per element have been chosen as $n_{\text{en}}^{\varphi} = 20$ and $n_{\text{en}}^{\phi} = 8$, respectively, see Figure 3.3. With regard to the degree of the polynomial interpolation function, this implies a tri-quadratic serendipity interpolation of the displacements and a tri-linear interpolation of the nonlocal damage field variable, the related element type being referred to as Q2Q1-element. In the following, the Q2Q1-element is compared to the Q1Q1-element which is associated with $n_{\text{en}}^{\varphi} = n_{\text{en}}^{\phi} = 8$ and consequently exhibits the same tri-linear interpolation order for the displacement and the nonlocal damage variable field.

Figure 3.5(d) shows the force-displacement response of the isotropic plate with a hole when using the coarsest discretisation considered of 400 elements for both element types Q2Q1 and Q1Q1. It becomes apparent that the Q1Q1-element is able to almost exactly reproduce the force-displacement-curve associated with the Q2Q1-formulation. Only very small deviations can be observed. The same holds for the finer discretisations, $n_{\text{el}} = \{1600, 3200\}$, even though not depicted here. Moreover, the computational speed in terms of the CPU-time T of both formulations is given in Table 3.5. It turns out that, for this particular example, the Q1Q1-element performs three to four-times faster than the Q2Q1-formulation—a finer discretisation even increases this effect.

In summary, Q1Q1-elements seem to be able to reproduce the results obtained by the Q2Q1-formulation and—at the same time—are much more efficient from the computational point of view. Moreover, Q1Q1-elements are much easier to handle, e.g. with regard to contact problems. To give an example for constant pressure, the equivalent nodal force vectors associated with Q1Q1-elements all coincide. This is not the case for

Table 3.5: Isotropic plate with a hole. Comparison of the CPU times T for the element types Q2Q1 and Q1Q1 and different discretisations $n_{\text{el}} = \{400, 1600, 3200\}$.

| n_{el} | T_{Q2Q1} [s] | T_{Q1Q1} [s] | $T_{\text{Q2Q1}}/T_{\text{Q1Q1}}$ |
|-----------------|-----------------------|-----------------------|-----------------------------------|
| 400 | 811.00 | 270.31 | 3.00 |
| 1600 | 4542.20 | 1232.10 | 3.69 |
| 3200 | 13405.00 | 3293.60 | 4.07 |

the Q2Q1-elements where the equivalent nodal force vectors at the middle and vertex nodes differ in magnitude and direction. This would considerably complicate the detection of contact conditions in Q2Q1-elements. In the following, however, we continue to use the Q2Q1-element-formulation as it increases the accuracy.

3.4.3 Test 3 – anisotropic plate with a hole

As a third numerical example, we consider an anisotropic version of the boundary value problem of the plate with a hole as discussed in the previous section. In particular, both families of fibers are oriented with respect to the axial \mathbf{e}_Y -direction, i.e. $\beta_{1,2} = 0.0$ [deg] where $\beta_{1,2} = \angle(\mathbf{a}_{0,1,2}, \mathbf{e}_Y)$, together with $\mathbf{a}_{0,1,2} \cdot \mathbf{e}_Z = 0$, and the dispersion parameter is set to $\varkappa = 0.0$ so that transverse anisotropy is recovered. This ensures that both families of fibers are equally loaded, as the present formulation is restricted to *one* nonlocal damage variable for both fibre families undergoing identical degradation. Alternatively, a second nonlocal damage variable may be included in the formulation. The material parameters used for this example are summarised in Table 3.4 in column ‘Test 3’.

3.4.3.1 Full isotropic contribution

The effect of the damage threshold κ_d is studied in Figure 3.9 for the set of material parameters summarised in Table 3.4. In accordance with the results of the homogeneous uniaxial tension test presented in Figure 3.4, damage initiation is delayed with increasing κ_d .

An even more important aspect of this example is the emergence of the snap-back phenomena in the structural response of the anisotropic plate with a hole. An arc-length method is used to solve this boundary value problem; see Appendix F for a brief review of the arc-length method. Snap-back can be briefly described by taking into consideration that the elastic energy stored by the fibres prior to complete damage has to be released by either an inelastic dissipation process or by unloading of the structure. As stated before, the degree of dissipation is controlled by the parameter c_d . While keeping c_d constant, the only possibility to release elastic energy is unloading the structure which illustrates that snap-back is more prominent for higher values of κ_d . For more detailed

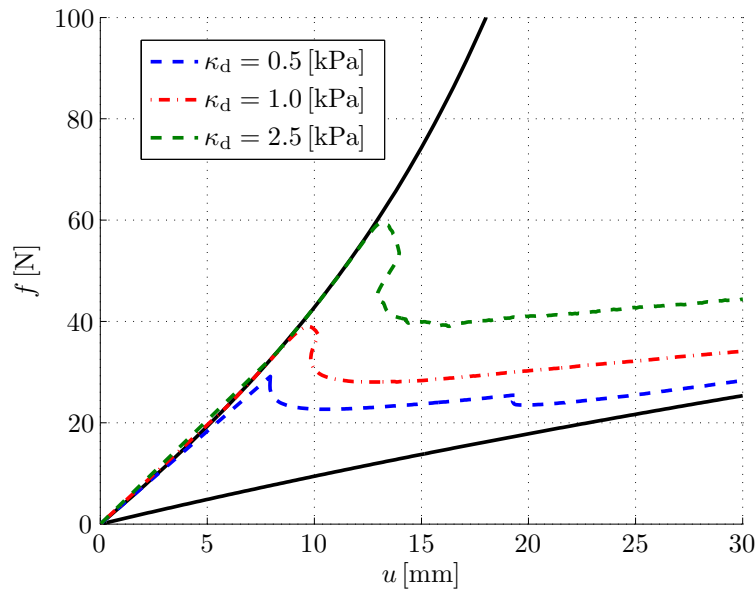


Figure 3.9: Anisotropic plate with a hole. Force-displacement response under monotonic loading for different values of the damage threshold parameter κ_d using a 400 element mesh. The solid black curves represent the elastic response of the isotropic neo-Hookean matrix (lower solid black curve) and the overall elastic response composed of the isotropic neo-Hookean *and* the anisotropic exponential model (upper solid black curve).

background information on snap-back phenomena in structures failure, the reader is referred to, e.g., de Borst [47].

In Figure 3.10, the contour of the damage function is plotted for different damage threshold values of κ_d . As expected, the damaged area decreases with increasing κ_d .

3.4.3.2 Reduced isotropic contribution

As indicated in Section 3.4.2, the contour plots of the damage function $f_d(\kappa)$ in Figure 3.8 do not show strongly localised deformation patterns in the form of pronounced narrow damage bands. This is caused by the remaining stiffness of the undamaged isotropic matrix material. In order to show that a material with a smaller influence of the matrix material would considerably increase the effect of the damage evolution on the specimen, we reduce the elastic parameters governing the isotropic matrix material to $\mu_e = 0.1$ [kPa] and $\kappa_e = 1.0$ [kPa], respectively, and furthermore set the damage threshold to $\kappa_d = 0.001$ [kPa]. The other (material) parameters remain unchanged according to Table 3.4.

The reduction of the elastic parameters μ_e and κ_e results in an almost negligible influence of the neo-Hookean ground substance and in an overall elastic mechanical response which is predominantly governed by the fibre-related anisotropic stress contribution, cf. the solid black curves in Figure 3.11. We observe a strong influence of the regularisation parameter where values of $c_d = \{20, 50, 100, 200, 1000\}$ [kPa⁻¹ mm²] are considered.

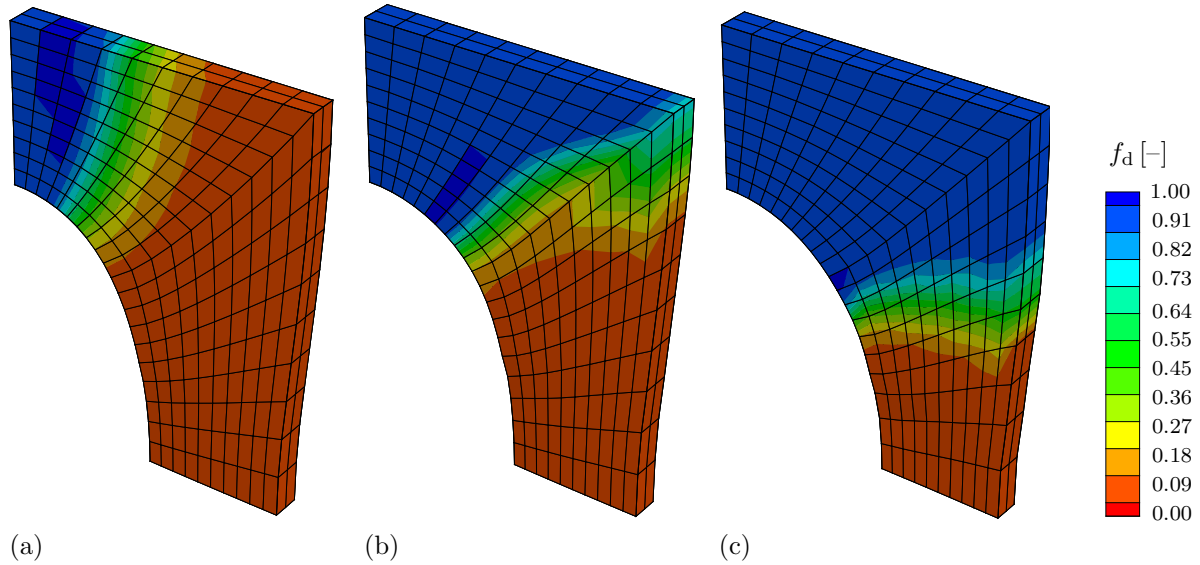


Figure 3.10: Anisotropic plate with a hole. Contour plots of the damage function $f_d(\kappa) \in (0, 1]$ at $u = 30$ [mm] for different values of the damage threshold parameter κ_d using a 400 element mesh. (a) $\kappa_d = 0.5$ [kPa], (b) $\kappa_d = 1.0$ [kPa], (c) $\kappa_d = 2.5$ [kPa].

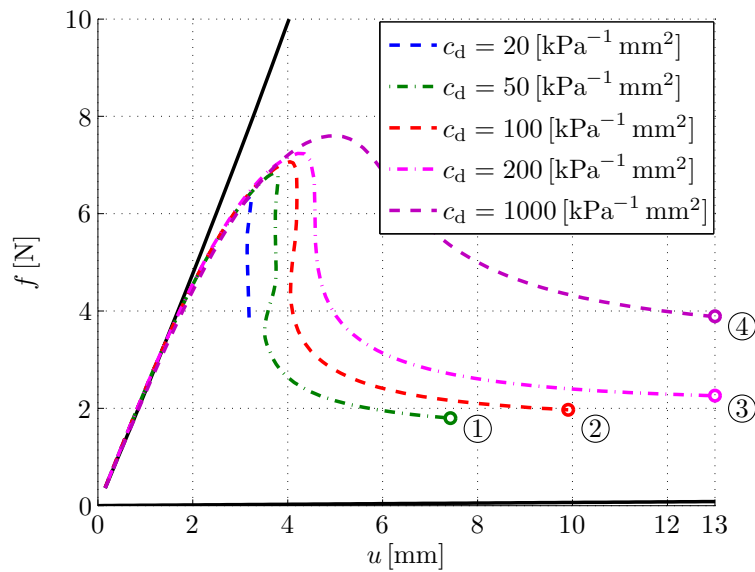


Figure 3.11: Anisotropic plate with a hole with *reduced* isotropic contribution. Force-displacement response under monotonic loading for different values of the gradient parameter c_d using a 400 element mesh. The solid black curves represent the *reduced* elastic response of the isotropic neo-Hookean matrix (lower solid black curve) and the overall elastic response composed of the isotropic neo-Hookean *and* the anisotropic exponential model (upper solid black curve).

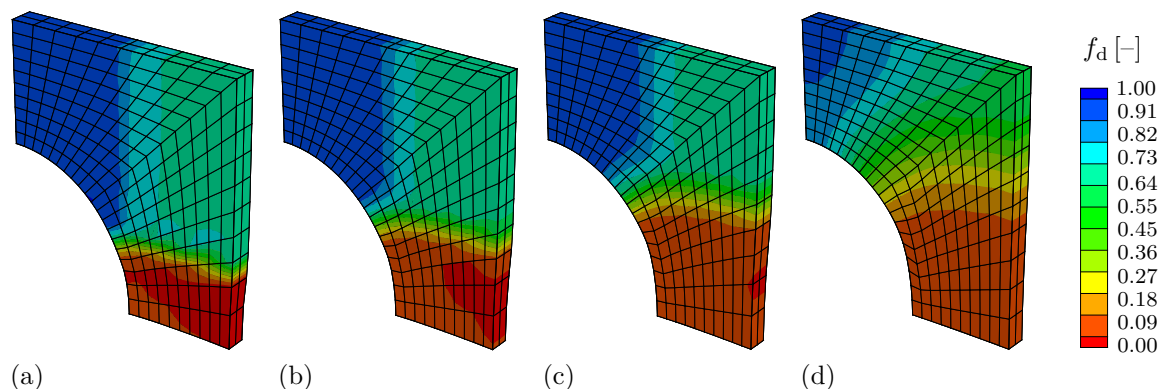


Figure 3.12: Anisotropic plate with a hole with *reduced* isotropic contribution. Contour plots of the damage function $f_d(\kappa) \in (0, 1]$ at different deformation stages ①–④, cf. Figure 3.11, for different values of the gradient parameter c_d using a 400 element mesh. (a) $c_d = 50$ [kPa⁻¹ mm²] at ①, (b) $c_d = 100$ [kPa⁻¹ mm²] at ②, (c) $c_d = 200$ [kPa⁻¹ mm²] at ③, (d) $c_d = 1000$ [kPa⁻¹ mm²] at ④.

For $c_d = \{20, 50, 100\}$ [kPa⁻¹ mm²], we obtain a snap-back effect which necessitates the application of an arc-length solution scheme.

The contour-plots of the damage function $f_d(\kappa)$ in Figure 3.12 illustrate the damage profile for $c_d = \{50, 100, 200, 1000\}$ [kPa⁻¹ mm²]. These are recorded at different stages of deformation marked by ①–④ in Figure 3.11. We observe that higher values of c_d increase the localisation zone. In contrast to the previous examples, however, we obtain a much more pronounced localisation behaviour illustrated by the narrow damage bands, especially for $c_d = \{50, 100\}$ [kPa⁻¹ mm²]. This clearly underlines that a smaller influence of the matrix material considerably increases the effect of the damage localisation on the specimen.

3.4.4 Anisotropic artery-like tube

As a last example, we apply the gradient-enhanced damage formulation proposed to another three-dimensional inhomogeneous biomechanics-related boundary value problem. In particular, we focus on the finite element simulation of a two-layered fibre-reinforced artery-like tube subjected to internal pressure. This idealised setting is commonly used to assess basic capabilities of particular constitutive models for arteries, see, e.g. Holzapfel et al. [135] for an analytical study or Alastrué et al. [9] for a similar finite-element-based investigation. Nevertheless, only very few contributions can be found in the literature which consider a *force-driven* large-deformation problem in connection with a gradient-enhanced damage model.

The particular geometry used in the present context is adopted from Alastrué et al. [9] and essentially reflects the geometry of a healthy coronary artery by means of a perfect cylindrical tube, see Figure 3.13. The tube, characterised by the wall thickness $H = H^M + H^A$ and the inner Radius R_i of the segment, basically includes two main

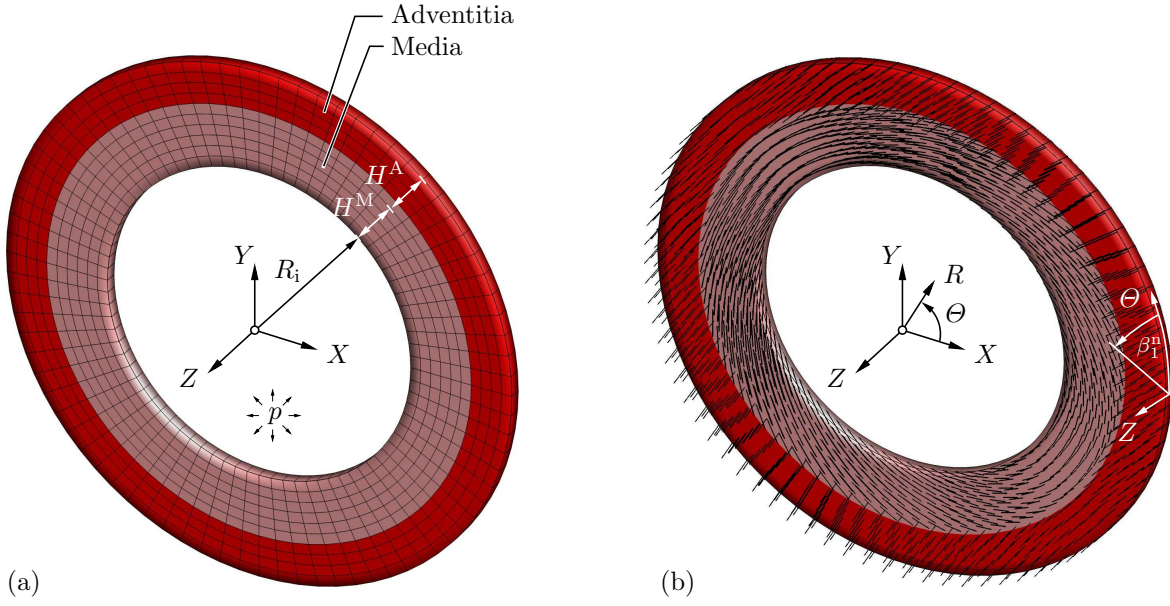


Figure 3.13: Geometry of the thick-walled two-layered cylindrical tube. (a) Finite element mesh with applied internal pressure p and fixed displacements in circumferential and longitudinal direction (not displayed) and (b) fibre orientations for the media and adventitia. The fibre orientation angles β^n are introduced with respect to the circumferential direction Θ .

load-bearing layers, i.e. the media and adventitia, where we assume a wall-thickness ratio H^M/H^A of 3/2. The intima is not included in the model due to its negligible relevance for the mechanical behaviour of a young and healthy artery. The dimensions chosen for the tube are summarised in Table 3.6, whereupon a finite element mesh of 800 hexahedral Q2Q1 elements according to Figure 3.3 is created to model a cross-section of an artery-like tube, see Figure 3.13(a).

Media and adventitia are characterised by individual material and structural parameters, see Table 3.6. The material parameters are taken from Holzapfel and Ogden [136, p. 55], where the shear modulus of the (compressible) neo-Hookean ground substance of the media is assumed to be ten times stiffer than the adventitia, i.e. $\mu_e^A = 10 \mu_e^M$. To enforce nearly-incompressibility, the bulk moduli κ_e^M, κ_e^A are chosen to be 100 times larger than the respective shear moduli, i.e. $\kappa_e^M = 100 \mu_e^M$ and $\kappa_e^A = 100 \mu_e^A$. In this regard, we recall that we do not apply a quasi-incompressible neo-Hookean format based on an isochoric-volumetric split.

The structural parameters are taken from Alastru e et al. [9] and are summarised in Table 3.6. The number of mechanically equivalent fibre families per layer is restricted to $N = 2$ and, moreover, their initial orientations are assumed as $\mathbf{a}_{0,1,2}^n = \sin(\beta^n) \mathbf{e}_Z \pm \cos(\beta^n) \mathbf{e}_\Theta$ with $n = M$ for the media and $n = A$ for the adventitia. In this regard, the layer-specific mean fibre orientation angles β^M and β^A are specified at the integration point level of each finite element so that a helical fibre distribution is included in the model, see Figure 3.13(b). Due to the symmetry of the geometry, the symmetry of the

Table 3.6: Set of geometrical, structural and material parameters as used for the artery-like tube ($n = M$ for the media and $n = A$ for the adventitia). The material parameters are subdivided in elastic- and damage-related parameters. The geometrical and structural parameters are adopted from Alastrué et al. [9], the elastic parameters from Holzapfel and Ogden [136].

| Type | Symbol | Value | | Unit |
|----------------|---------------|--------|------------|--------------------------------------|
| | | Media | Adventitia | |
| geometrical | R_i^n | 1.35 | 1.89 | [mm] |
| | H^n | 0.54 | 0.36 | [mm] |
| structural | β^n | 21.700 | 62.260 | [deg] |
| | \varkappa^n | 0.19 | 0.036 | [-] |
| elastic | μ_e^n | 27.0 | 2.7 | [kPa] |
| | κ_e^n | 2700.0 | 270.0 | [kPa] |
| | k_1^n | 0.64 | 5.1 | [kPa] |
| | k_2^n | 3.54 | 15.4 | [-] |
| regularisation | c_d | | 0.01 | [kPa ⁻¹ mm ²] |
| | β_d | | 1000.0 | [kPa ⁻¹] |
| | γ_d | | 1.0 | [-] |
| damage | η_d | | 0.1 | [kPa ⁻¹] |
| | κ_d | | 3.0 | [kPa] |

fibre orientations as well as the internal pressure loading, both fibre families are equally loaded, so that $E = E_1 = E_2$. Consequently, both fibre families are exposed to identical degradation. This justifies the use of only *one* nonlocal damage variable for both fibre families.

Furthermore, small dispersions of the fibres are considered, i.e. $\varkappa^n \neq 0$. In Alastrué et al. [9], layer-specific values for the related concentration parameter b are provided and can be converted to the dispersion parameter \varkappa as introduced in equation (3.43) by means of

$$\varkappa^n = \frac{1}{4} \int_0^\pi \rho^n(\vartheta^n) \sin^3(\vartheta^n) d\vartheta^n \quad (3.132)$$

with the π -periodic normalised von Mises density function

$$\rho^n(\vartheta) = 4 \sqrt{\frac{b^n}{2\pi}} \frac{\exp(b^n [\cos(2\vartheta^n) + 1])}{\operatorname{erfi}(\sqrt{2} b^n)}. \quad (3.133)$$

Herein, $\vartheta^n \in [0, \pi]$ denotes a ‘dispersion angle’ characterising the rotational symmetric distribution of a given fibre family with respect to the mean referential preferred fibre direction \mathbf{a}_{0i}^n . Furthermore, the concentration parameter $b > 0$ represents a measure

of the degree of anisotropy and $\operatorname{erf} i(x) = i \operatorname{erf}(x)$ denotes the imaginary error function which, according to Weisstein [291], can conveniently be approximated numerically by a series expansion; see, e.g. Alastrué et al. [9] for further details. Relation (3.132) can be evaluated either by numerical integration, see Gasser et al. [107], or by using a polynomial representation as applied in Menzel et al. [201]. For the media, we obtain $\varkappa^M = 0.19$, which indicates a dispersed character of the fibres. In the adventitia, value $\varkappa^A = 0.036$ is very close to zero, reflecting an almost transversely isotropic state for each fibre family. This is in line with the recent experimental results reported by Schriefl et al. [255].

Note, that residual stresses are neglected at this stage, even though they are essential for the mechanical response of arteries, see Holzapfel et al. [135]. However, to emphasise the effects due to the damage, we do not incorporate them in the present chapter. For cylindrical geometries, residual stretches can directly be included in the finite element setting following, e.g. the strategies proposed by Alastrué et al. [9], Alastrué et al. [11] which are based on a multiplicative composition of the deformation gradient.

With regard to boundary conditions, the displacements in circumferential and longitudinal direction are prescribed to zero at the front and back face of the arterial segment, i.e. $u_\theta = u_z = 0.0$ at related nodes. The nonlocal damage-related field variable ϕ is initialised as the value of the damage threshold κ_d , i.e. $\phi|_{t_0} = \kappa_d$. Furthermore, we apply a pressure p at the inner radius of the specimen. This pressure, however, is not prescribed explicitly—typically by a value of $p = 100$ [mmHg] = 13.33 [kPa] representing the mean physiological blood pressure—but is part of the solution itself, the reason being that an arc-length method is applied which enables tracing of the post-peak branch of the load-displacement curves in the damage regime. This proves to be a very advantageous and robust procedure to obtain static equilibrium states for snap-back response or force-driven degradation as discussed here. As the loading magnitude itself is part of the solution, the arc-length algorithm cannot produce a solution at a given load or displacement values directly, as they are treated as unknowns. This complicates a performance of a cyclic force-driven deformation test. Instead, as a termination criterion, the simulation is completed as soon as a prescribed maximum displacement value u_{\max} at a specified degree of freedom is exceeded—here the radial displacement $u_r(r_i)$ at a node located at the inner radius r_i of the tube. In the following, this termination value is set to $u_{\max} = 1.5$ mm. A brief review on the arc-length method in the context of the Abaqus-related UEL-implementation is provided in Appendices D and E.

Figure 3.14 depicts the load-displacement-response of the inflated tube where the pressure p is plotted over the displacement $u_r(r_i)$ at the inner radius of the tube. The lower solid black curve represents the purely elastic mechanical behaviour due to the isotropic neo-Hookean ground substance, see equation (3.40). The upper solid black curve shows the overall elastic response based on the isotropic neo-Hookean part (3.40) as well as the predominant anisotropic exponential contribution (3.43). Both curves give a good illustration of the highly non-linear material behaviour especially at large strains. The blue curve shows the mechanical response due to the damage of the fibre

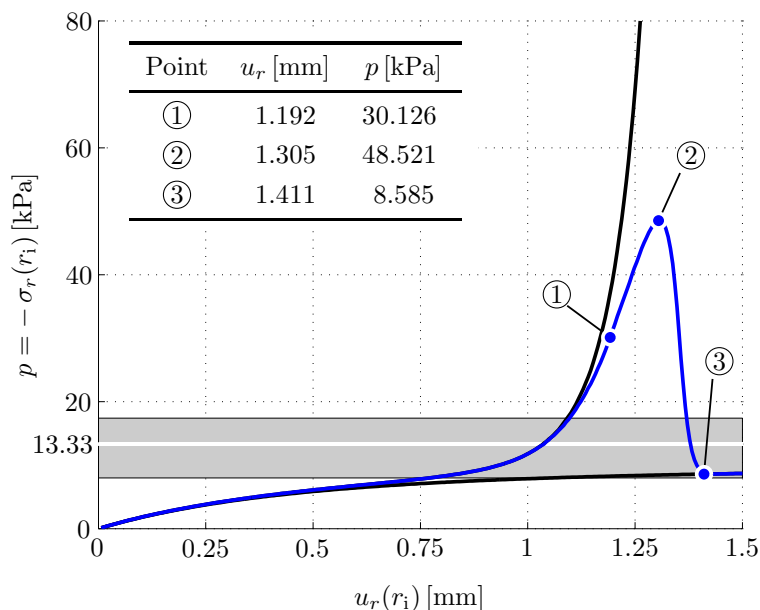


Figure 3.14: Load-displacement-response for the inflated tube: pressure p versus displacement $u_r(r_i)$ at the inner radius of the tube. The lower solid black curve represents the elastic isotropic neo-Hookean ground substance, the upper solid black curve shows the elastic anisotropic fibre-related contribution according to Gasser et al. [107], the blue curve shows the mechanical response due to the gradient-enhanced damage. The gray-shaded region represents the physiological pressure range, determined by the diastolic blood pressure $p = 8.0$ [kPa] (lower black line), the systolic blood pressure $p = 17.4$ [kPa] (upper black line) and the mean blood pressure $p = 13.33$ [kPa] (white line).

contributions. We observe that within the physiological pressure range—determined by the diastolic blood pressure $p = 8.0$ [kPa] and the systolic blood pressure $p = 17.4$ [kPa]—the material responds according to the elastic load path. However, from a pressure value of approx. $p = 20.0$ [kPa] upwards, the material softens significantly and increasingly deviates from the elastic path. The maximal pressure $p_{\max} = 48.521$ [kPa] is obtained at $u_r = 1.305$ [mm]. After that state—caused by the substantial loss of stiffness—the pressure starts to decrease while the displacement still increases and the curve finally drops towards the elastic response of the undamaged neo-Hookean ground substance. Physically, this can be interpreted as a continuous degradation of the fibres contained in an undamaged matrix material, which consequently is expected to carry the full load after complete loss of fibre stiffness.

It becomes apparent that the damage evolution beyond the physiological range results in an increase of the diameter—here measured by the radial displacement u_r —of the tube at the same (mean) pressure. Consequently, at the expense of a loss in stiffness, these damage effects can be beneficially exploited in order to expand an artery and thereby restore and ensure the blood flow of an atherosclerotic or arteriosclerotic blood vessel for instance. One prominent application example from the surgical point of view, which benefits from these effects, is the *balloon angioplasty* where an elastic balloon is inserted

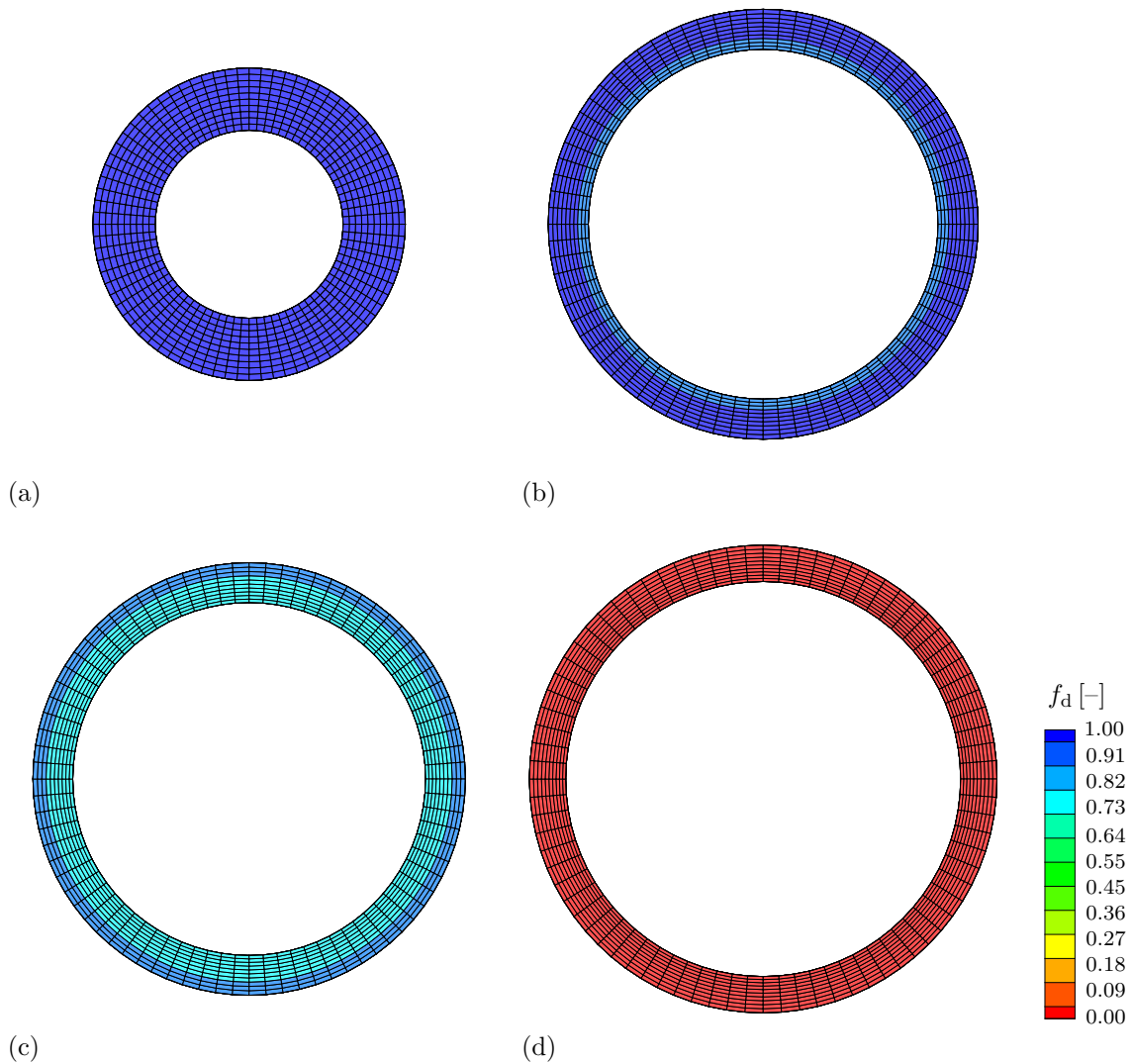


Figure 3.15: Artery-like tube subjected to internal pressure. Contour plot of the distribution of the damage function $f_d(\kappa) \in (0, 1]$ at the referential (undamaged) state and at (b)–(d) representative (damaged) states ①–③, as specified in Figure 3.14, cf. Figure 3.16(b) for an alternative representation.

and inflated inside the constricted artery; see, e.g. Holzapfel et al. [139], Gasser and Holzapfel [106] or Alastrué et al. [12] for detailed studies including experiments and finite element simulations.

It is important to mention that the assumption of an intact matrix and two equally damaging fibre families can provide only a very simplified description of the real biomechanical effects. As a possible refinement or extension of the model, one could, for instance, apply two independent damage variables for matrix and fibres, as proposed in

Calvo et al. [55] for the purely local case, or even three independent damage variables, including matrix-damage and individual damage for each fibre family.

In view of a related finite element implementation, however, this would require three individual nonlocal damage fields in the latter case, possibly accompanied by an active-set search in order to identify the currently damaged fibre family of the multi-surface damage problem, see Dimitrijević and Hackl [86] for a regularisation framework for multi-surface damage-plasticity models.

Figure 3.15 depicts contour-plots of the distribution of the damage function $f_d(\kappa) \in (0, 1]$ at the referential (undamaged) setting \mathcal{B}_0 and at three representative loading points ①–③, as specified in Figure 3.14. In particular, we consider point ① with $u_r = 1.192$ [mm] and $p = 30.126$ [kPa] located close to the state of damage initiation, point ② at the maximal peak pressure $p_{\max} = 48.521$ [kPa] with $u_r = 1.305$ [mm] and ③ at the fully damaged state in the post-peak branch with $u_r = 1.411$ [mm] and $p = 8.585$ [kPa]. As expected, the distribution of the damage function in the undamaged reference state is homogeneous, with $f_d(\kappa) = 1.0$, and in the fully damaged configuration ③ with $f_d(\kappa) \rightarrow 0.0$. At loading points ① and ②, however, we observe a heterogeneous distribution of $f_d(\kappa)$ where higher damage values are obtained at the inner wall of the tube.

Due to the symmetry of the problem, and in order to obtain a better quantitative view of the damage profile over the wall-thickness, it turns out to be appropriate to investigate the distribution of damage-related parameters and stresses over the current width $r - r_i^M$ of the tube recorded at the nodes across the wall-thickness. Once more, we consider three representative loading points ①–③, which, in Figure 3.16, correspond to the red, green and blue curves respectively.

Figure 3.16 shows the distribution of (a) the damage parameters κ and ϕ , (b) the damage function $f_d(\kappa)$ and (c) the driving force q over the current width $r - r_i^M$ of the tube at the aforementioned representative points of the loading path. From Figure 3.16(a), we observe successively increasing damage parameters κ and ϕ for points ①–③, which for ① and ② take their maximum values at the inner wall of the tube and show a decreasing tendency towards the outer radius. For the fully damaged point ③, we obtain an almost constant distribution of the damage variable over the wall-thickness. This corresponds to the curves in Figure 3.16(b) which represent the state of damage by means of the damage function $f_d(\kappa)$, see equation (3.66) where $f_d = 1.0$ for the intact and $f_d \rightarrow 0.0$ for the fully damaged case. At point ① the inner wall is apparently already damaged, whereas the outer radius of the wall is still intact. At point ②, we obtain a similar damage characteristic, now distributed over the wall-thickness until, finally, at point ③ the fibre contributions over the whole wall are fully damaged. The driving force q is depicted in Figure 3.16(c). In agreement with the preceding results, we observe its maximal values at the inner wall of the tube. The maximal overall distribution is obtained at point ② associated with the maximal pressure p_{\max} .

Furthermore, Figure 3.16 shows the (d) radial, (e) circumferential and (f) axial Cauchy stress distributions over the current width $r - r_i^M$ of the tube at the aforementioned

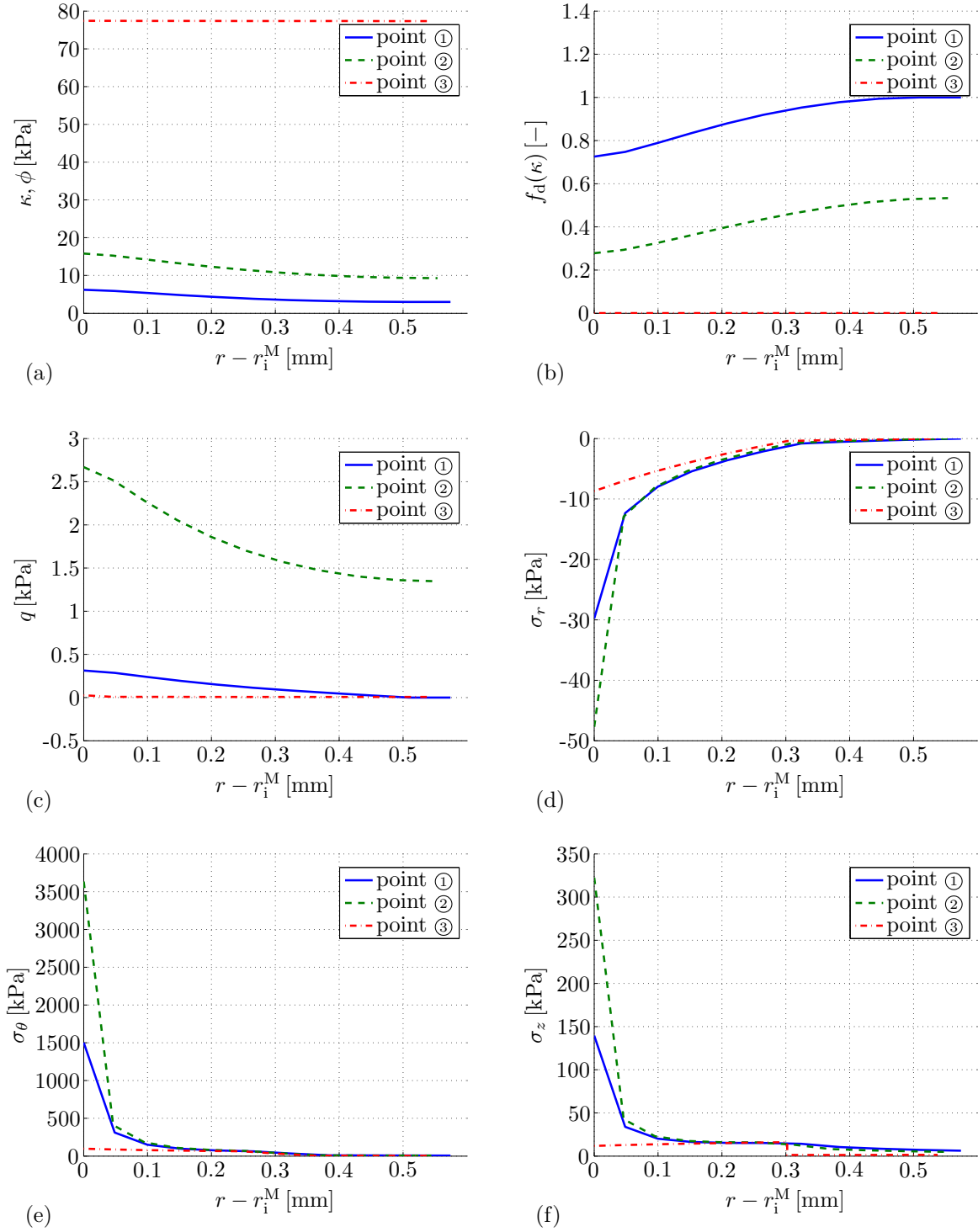


Figure 3.16: Artery-like tube. Distribution of damage-related parameters and the principal Cauchy stresses over the current width $r - r_i^M$ of the tube for representative loading points ①–③, as specified in Figure 3.14. (a) (non-)local damage variable κ and ϕ , (b) damage function $f_d(\kappa) \in (0, 1]$, (c) driving force q , (d) radial stress σ_r , (e) circumferential stress σ_θ , (f) axial stress σ_z .

representative points of the loading. We observe that the circumferential stress σ_θ is the dominant stress component within the wall, since its magnitude is significantly larger compared to the magnitudes of σ_r and σ_z . Note, that the longitudinal stretch is constrained by the boundary condition chosen so that $\lambda_z = 1$. As expected from the load-displacement curve in Figure 3.14, the maximal stresses are obtained for the maximal pressure p_{\max} associated with point ②. For all loading points considered, stress peaks typically occur at the inner wall boundary. Due to the damage evolution, these peaks are significantly reduced which is a consequence of the loss of stiffness of the fibres.

4 A microsphere model for the simulation of remodelling effects

This chapter presents a new micro-mechanically motivated remodelling approach reflecting the alignment of fibrous soft biological tissue with respect to representative loading directions. The material presented is, in large parts, based on the ideas outlined in the work by Menzel and Waffenschmidt [208, 209] and Menzel et al. [210]. The computational remodelling framework subsequently established in this chapter is partly motivated by the investigations reported in Eastwood et al. [90], where a fibroblast-populated collagen lattice was tested. As a result, the macroscopic tension-type mechanical loads—including cell contraction—rendered the initially unstructured collagen fibre network to reorient with the local dominant stretch direction. In this regard, an anisotropic micromechanically motivated model that additionally incorporates this time-dependent remodelling effect is presented.

As various soft biological tissues are reported to behave nearly incompressible, we adopt the classic volumetric-isochoric split of the strain energy density. While we assume its isotropic part to take a standard neo-Hookean form, we incorporate the anisotropic fibre contributions by means of the non-affine microsphere model, as originally proposed by Miehe et al. [218] for rubber elasticity. In this regard, physically sound one-dimensional constitutive models—as for instance the worm-like chain model—can be used and straightforwardly extended to the three-dimensional case. As a key aspect, the microsphere model is extended to the incorporation of remodelling effects. Such deformation-induced anisotropy is introduced by setting up evolution equations for the integration directions used to perform numerical integrations on the unit-sphere. The underlying anisotropy evolution is thereby directly linked to the numerical integration scheme applied to the unit-sphere. Especially two remodelling formulations are proposed for transversely isotropic and orthotropic material behaviour for one and two preferred fibre orientations, respectively. In this regard, we establish evolution equations in terms of shear-related driving forces which reorient the respective unit vectors. The particular models proposed account for saturation effects combined with a visco-elasticity-type time-dependent anisotropy evolution.

The current chapter is set up as follows: Section 4.1 gives a brief preview on essential kinematic relations, which form the basis for key aspects of the microsphere model are addressed in Section 4.2. Section 4.3 constitutes the main body of this chapter, in which two remodelling formulations are established for the transversely isotropic and orthotropic case. Finally, several numerical examples for homogeneous deformations and a non-homogeneous deformation are discussed in Section 4.5

4.1 Basic micro-kinematics and balance equations

In view of the subsequently elaborated computational homogenisation scheme, we introduce the kinematics referred to the underlying unit-sphere \mathbb{U}^2 . In this regard, let $\mathbf{r} \in \mathbb{U}^2$ denote a unit-vector, or rather an element of the unit-sphere, so that the affine isochoric stretch in the direction of \mathbf{r} is determined by means of the macroscopic isochoric right Cauchy-Green deformation tensor via

$$\bar{\lambda} = \sqrt{\mathbf{r} \cdot \bar{\mathbf{C}} \cdot \mathbf{r}}. \quad (4.1)$$

The equilibrium of a single-phased solid continuum can be represented by the balance of linear momentum which, for the quasi static case and in the absence of volume forces, takes the local representation

$$\nabla_{\mathbf{X}} \cdot [\mathbf{F} \cdot \mathbf{S}] = \mathbf{0} \quad \text{in} \quad \mathcal{B}_0, \quad (4.2)$$

$$\mathbf{F} \cdot \mathbf{S} \cdot \mathbf{N} = \bar{\mathbf{T}} \quad \text{on} \quad \partial\mathcal{B}_0, \quad (4.3)$$

where \mathbf{S} denotes the Piola-Kirchhoff stress and $\bar{\mathbf{T}}$ the referential surface traction vector.

4.2 Non-affine hyperelastic microsphere model

In addition to the particular remodelling framework discussed later on, we apply a hyperelastic form so that the stress tensors of interest can be derived from a strain energy potential Ψ as $\mathbf{S} = 2 \partial_{\mathbf{C}} \Psi$. In the following, we do not put emphasis on a full thermodynamical framework which, in this case, should be embedded into the theory of open systems and additionally account for a so-called chemical potential, but solely outline the solid mechanical part of the continuum. Its contribution to the dissipation inequality for the isothermal case results in

$$\mathcal{D}_m^s = \frac{1}{2} \mathbf{S} : \dot{\mathbf{C}} - \dot{\Psi}, \quad (4.4)$$

wherein $(\dot{\bullet}) = \partial_t(\bullet)|_{\mathbf{X}}$ represents the material time derivative. As the material properties of the types of soft tissue we are interested in may be highly anisotropic, this energy function is assumed to not only depend on the deformation gradient \mathbf{F} but also on a finite number of *unit vectors*, denoted by $\mathbf{a}_{0i} \in \mathbb{U}^2$ with $i = 1, \dots, N$, so that

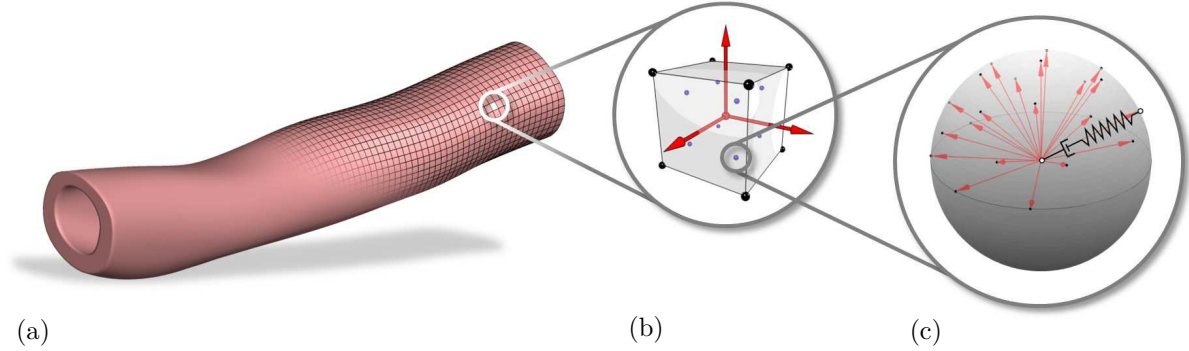


Figure 4.1: Illustration of the microsphere approach. (a) Macroscopic boundary value problem, (b) particular finite element with integration points and (c) microsphere associated with finite number of integration directions \mathbf{r}^i (red) and one-dimensional constitutive law represented by the spring-dashpot device.

$\Psi(\mathbf{C}, \mathbf{a}_{0i}; \mathbf{X})$. Consequently, the hyperelastic form for the Piola-Kirchhoff stresses \mathbf{S} renders the reduced dissipation inequality as

$$\mathcal{D}_{\text{m,red}}^{\text{s}} = \sum_{i=1}^m -\partial_{\mathbf{a}_{0i}} \Psi \cdot \dot{\mathbf{a}}_{0i}. \quad (4.5)$$

It becomes apparent that $\dot{\mathbf{a}}_{0i} \neq \mathbf{0}$ corresponds to deformation-induced anisotropy evolution, i.e. *remodelling*. An essential consequence is that the unit vectors \mathbf{a}_{0i} are treated as internal variables in the following.

As various soft biological tissues have been reported to respond quasi-incompressible, we adopt the well-established volumetric-isochoric split, cf. Section 2.1, and decompose the isochoric part into an isotropic and an anisotropic contribution, to be specific

$$\Psi(\mathbf{C}, \mathbf{a}_{0i}) = \Psi_{\text{vol}}(J) + \Psi_{\text{ich}}(\bar{\mathbf{C}}, \mathbf{a}_{0i}) = \Psi_{\text{vol}}(J) + \Psi_{\text{iso}}(\bar{\mathbf{C}}) + \Psi_{\text{ani}}(\bar{\mathbf{C}}, \mathbf{a}_{0i}), \quad (4.6)$$

wherein possible heterogeneities of the material are not explicitly indicated.

We now further specify the anisotropic part $\Psi_{\text{ani}}(\bar{\mathbf{C}}, \mathbf{a}_{0i})$ of the strain energy, which allows the incorporation of the fibrous properties of the biological tissue. In particular, we adopt a so-called *microsphere formulation*, which allows the macroscopic Piola-Kirchhoff stress \mathbf{S}_{ani} to be represented by

$$\langle\langle \bullet \rangle\rangle = \frac{1}{4\pi} \int_{\mathbb{U}^2} (\bullet) \, dA, \quad (4.7)$$

so that the macroscopic stress quantity corresponding to Ψ_{ani} is determined by integration over the unit-sphere \mathbb{U}^2 . From the micromechanical point of view, the density of fibres, with respect to the particular direction \mathbf{a}_{0i} contributes to these macroscopic stresses.

It is known that the affinity assumption in equation (4.1) is not in good agreement with experimental observations for cross-linked polymer-type materials. Following Miehe et al. [218], we use a *non-affine stretch measure* taking the form

$$\lambda = \langle \bar{\lambda}^{\bar{p}} \rangle^{1/\bar{p}}. \quad (4.8)$$

The non-affine stretch can be interpreted as an averaged stretch over the unit-sphere, with \bar{p} defining a non-affine stretch parameter. As mentioned by Carol et al. [60] and in detail elaborated by Miehe et al. [218], a single collagen chain is constrained by another micro-kinematic variable, i.e. the contraction ν of the cross-section of a micro-tube that contains the related chain. At this stage, however, we restrict ourselves to account only for the non-affine stretch-contributions λ .

When assuming this collection of n fibres per unit volume to be loaded or rather stretched in terms of the macroscopic isochoric deformation measure $\bar{\mathbf{F}}$, and recalling that we deal with a non-affine deformation, then $\bar{\Psi}_{\text{ani}}$ can be computed by means of the one-dimensional fibre-related strain energy $n\psi(\lambda)$ via

$$\bar{\Psi}_{\text{ani}}(\lambda(\bar{\mathbf{C}}, \mathbf{r})) = \langle \rho n \psi(\lambda(\bar{\mathbf{C}}, \mathbf{a}_{0i}, \mathbf{r})) \rangle, \quad (4.9)$$

wherein $\mathbf{r} \in \mathbb{U}^2$ is the respective direction considered for the integration over the unit-sphere. Furthermore, the scalar-valued quantity $\rho(\mathbf{a}_{0i}, \mathbf{r}) = \rho(-\mathbf{a}_{0i}, \mathbf{r})$ characterises a normalised ODF that, in addition to the internal variables \mathbf{a}_{0i} , allows the modelling of the material's anisotropy. For the general case, where $\dot{\rho} \neq 0$, the evolution of this ODF also contributes to the dissipation inequality.

Based on equation (4.6), the hyperelastic form of the Piola-Kirchhoff stresses, $\mathbf{S} = 2 \partial_{\mathbf{C}} \bar{\Psi}$, results in

$$\mathbf{S} = \mathbf{S}_{\text{vol}} + \mathbf{S}_{\text{iso}} + \mathbf{S}_{\text{ani}} \quad (4.10)$$

where the respective volumetric, isotropic and anisotropic contributions to the Piola-Kirchhoff stress can be expressed as

$$\mathbf{S}_{\text{vol}} = \partial_J \bar{\Psi}_{\text{vol}} \mathbf{C}^{-1} \quad (4.11)$$

$$\mathbf{S}_{\text{iso}} = \bar{\mathbf{S}}_{\text{iso}} : \mathbf{P} \quad \text{with} \quad \bar{\mathbf{S}}_{\text{ani}} = 2 \partial_{\bar{\mathbf{C}}} \bar{\Psi}_{\text{ani}} \quad (4.12)$$

$$\mathbf{S}_{\text{ani}} = \bar{\mathbf{S}}_{\text{ani}} : \mathbf{P} \quad \text{with} \quad \bar{\mathbf{S}}_{\text{ani}} = 2 \partial_{\bar{\mathbf{C}}} \bar{\Psi}_{\text{ani}}. \quad (4.13)$$

In view of the microsphere approach adopted, the anisotropic stress contribution is further specified as

$$\bar{\mathbf{S}}_{\text{ani}} = 2 \frac{\partial \bar{\Psi}_{\text{ani}}}{\partial \bar{\mathbf{C}}} = n \psi' \lambda^{1-\bar{p}} \mathbf{H} \quad \text{with} \quad \mathbf{H} := \langle \bar{\lambda}^{\bar{p}-2} \mathbf{r} \otimes \mathbf{r} \rangle \quad (4.14)$$

where the micro-stress is defined as $n \psi' := n \partial_{\lambda} \psi$ and where relation $\partial_{\bar{\mathbf{C}}} \bar{\lambda}^2 = \mathbf{r} \otimes \mathbf{r}$ is used.

4.3 Microsphere-based remodelling formulations

Remodelling, interpreted as a change in the internal structure of the material, is reflected by evolution equations for the unit vectors \mathbf{r}^i . Before discussing particular approaches to incorporate these effects, we shall first refer to additional assumptions on the anisotropic part of the strain energy. On the one hand, Ψ_{ani} is understood to be independent of the orientation (sign) of the unit vectors, in other words $n\psi(\bar{\mathbf{C}}, \mathbf{a}_{0i}, \mathbf{r}) = n\psi(\bar{\mathbf{C}}, -\mathbf{a}_{0i}, \mathbf{r})$. Apart from this rather natural assumption, which is similarly well-established for even-order structural tensors, we directly relate the internal variables to the numerical framework, i.e. the integration of equation (4.9).

The algorithmic integration over the unit-sphere \mathbb{U}^2 reduces to a summation over a finite number of integration directions, say $\mathbf{r}^i \in \mathbb{U}^2$ for $i = 1, \dots, m$, so that continuous representations are approximated as

$$\langle (\bullet) \rangle = \frac{1}{4\pi} \int_{\mathbb{U}^2} (\bullet) \, dA \approx \sum_{i=1}^m w^i (\bullet)^i \quad (4.15)$$

where w^i denotes related weighting factors. Here, we essentially model these integration unit vectors \mathbf{r}^i to coincide with the internal variables so that $m = N$ and $\mathbf{r}^i = \mathbf{a}_{0i}$ with $\sum_{i=1}^m \mathbf{r}^i \doteq \mathbf{0}$. Based on this assumption, equation (4.9) is approximated as

$$\Psi_{\text{ani}}(\lambda(\bar{\mathbf{C}}, \mathbf{r}^i)) \approx \sum_{i=1}^m w^i \rho^i n\psi(\lambda(\bar{\mathbf{C}}, \mathbf{r}^i)), \quad (4.16)$$

where $\lambda = [\sum_{i=1}^m w^i [\bar{\lambda}^i]^{\bar{p}}]^{1/\bar{p}}$ follows by analogy with equation (4.8). In an analogous procedure, the anisotropic Piola-Kirchhoff stress contribution can be approximated as

$$\bar{\mathbf{S}}_{\text{ani}} = n\psi' \lambda^{1-\bar{p}} \mathbf{H} \quad \text{with} \quad \mathbf{H} \approx \sum_{i=1}^m w^i [\bar{\lambda}^i]^{\bar{p}-2} \mathbf{r}^i \otimes \mathbf{r}^i. \quad (4.17)$$

In general, anisotropy evolution—or remodelling—can be incorporated by means of evolving ODF quantities. Here, we combine this idea with the well-established concept of evolving internal variables. In view of the present microsphere model, one may either consider the ODF factors $w^i \rho^i$ or the corresponding integration directions \mathbf{r}^i as internal variables. Combinations of both approaches are also possible. The key aspect of this approach, however, consists in *incorporating remodelling-phenomena by setting up deformation-driven evolution equations for the integration directions \mathbf{r}^i* , which means that these are not constant but evolve in time, i.e. $w^i \rho^i = w^i = \text{const} \forall \mathbf{r}^i$ and $\mathbf{r}^i \neq \text{const}$.

Based on this, we will discuss appropriate remodelling approaches in the following sections, starting with the approach for the transversely isotropic case with one mean fibre direction in Section 4.3.1 as well as for the orthotropic case with two mean fibre directions in Section 4.3.2.

The guiding mechanisms with regard to these deformation-driven reorientation processes are similar for both remodelling approaches and illustrated in Figures 4.3 and 4.5. On the one hand, we assume a particular integration direction \mathbf{r}^i and its rate $\dot{\mathbf{r}}^i$ to be orthogonal such that $\dot{\mathbf{r}}^i \cdot \mathbf{r}^i = 0$. On the other hand, we assume the rate $\dot{\mathbf{r}}^i$ to lie in the plane spanned by \mathbf{r}^i and deformation-dependent mean directions and to be targeted at these mean directions.

With regard to the determination of characteristic preferred—or mean—fibre directions, structural constitutive models are commonly suggested which incorporate different families of preferred fibre directions by means of structural tensors of the type $\mathbf{A}_i = \mathbf{a}_{0i} \otimes \mathbf{a}_{0i}$, where the unit vector \mathbf{a} represents the preferred orientation associated with a particular fibre-family, cf. Section 2.1. Here, we propose a conceptually different approach which is based on two assumptions. First, we assume the preferred fibre directions to be *deformation-dependent* and that they may possibly change their orientation with respect to the progress of deformation. Secondly, we assume this particular deformation-dependent format to reflect *stationary* or rather *extremal states in strain energy*. In this context, one could either choose the principal strain directions $\mathbf{n}_j^{\bar{\mathbf{C}}}$ according to the spectral decomposition of $\bar{\mathbf{C}}$,

$$\bar{\mathbf{C}} = \sum_{j=1}^3 \lambda_j^{\bar{\mathbf{C}}} \mathbf{n}_j^{\bar{\mathbf{C}}} \otimes \mathbf{n}_j^{\bar{\mathbf{C}}} \quad (4.18)$$

with $\lambda_1^{\bar{\mathbf{C}}} > \lambda_2^{\bar{\mathbf{C}}} > \lambda_3^{\bar{\mathbf{C}}}$, or alternatively a set of directions which share identical angles with the principal strain directions. The former approach is used in the context of the transversely isotropic material behaviour with one mean fibre direction in Section 4.3.1. As a special case of the latter approach, we apply the so-called 'limiting directions' in connection with the orthotropic case characterised by two mean fibre directions in Section 4.3.2.

4.3.1 Remodelling for transversely isotropic material behaviour

We subsequently propose a remodelling formulation reflecting macroscopically transversely isotropic behaviour. As a macroscopic measure of anisotropy, we first introduce a second-order generalised structural tensor

$$\mathbf{A} = \sum_{i=1}^m w^i \mathbf{r}^i \otimes \mathbf{r}^i = \sum_{j=1}^3 A_j \mathbf{n}_j \otimes \mathbf{n}_j, \quad (4.19)$$

where $\mathbf{n}_k \cdot \mathbf{n}_l = \delta_{kl}$ and $A_1 \geq A_2 \geq A_3 \geq 0$ with $\sum_j A_j = 1$. Even though initial anisotropy can generally be included, we will consider an initially isotropic setting so that $\mathbf{A}|_{t_0} = \frac{1}{3} \mathbf{I}$. In order to visualise local anisotropic material properties later on, the orientation-distribution-type function $\rho^{\mathbf{A}} = \mathbf{r} \cdot \mathbf{A} \cdot \mathbf{r}$ is introduced with $\mathbf{e} \in \mathbb{U}^2$ denoting a unit-vector. The ODF $\rho^{\mathbf{A}}$ is exemplarily evaluated at different time steps

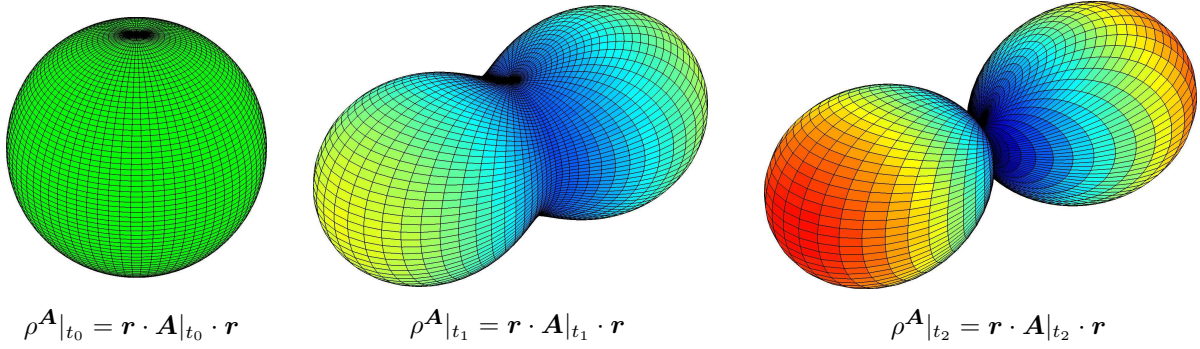


Figure 4.2: Graphical representation of the second order structural tensor \mathbf{A} by means of the orientation-distribution-function $\rho^{\mathbf{A}}$ at different exemplarily chosen time steps t_n , $n = 0, 1, 2$. The spherical distribution at $t = t_0$ corresponds to an initially isotropic setting with $\mathbf{A}|_{t_0} = \frac{1}{3} \mathbf{I}$.

and depicted in Figure 4.2. Note, that deformation-induced anisotropy evolution requires $n \psi'(\lambda = 1) = 0$ in order to be able to recapture a stress-free reference state.

The quantity driving the remodelling process, as captured by deformation-induced anisotropy evolution, is referred to here as the reduced dissipation relation (4.5). In view of an individual integration direction—compare equation (4.16)—one obtains

$$-n \frac{\partial \psi}{\partial \mathbf{r}^i} = -n \frac{\partial \psi}{\partial \lambda} \frac{\partial \lambda}{\partial \bar{\lambda}^i} \frac{\partial \bar{\lambda}^i}{\partial \mathbf{r}^i} = -S^i \bar{\mathbf{C}} \cdot \mathbf{r}^i, \quad (4.20)$$

with $S^i = n \psi' \lambda^{1-\bar{p}} [\bar{\lambda}^i]^{\bar{p}-2} w^i$ where relations $\partial_{\bar{\lambda}^i} \lambda = \lambda^{1-\bar{p}} [\bar{\lambda}^i]^{\bar{p}-1} w^i$ and $\partial_{\mathbf{r}^i} \bar{\lambda}^i = [\bar{\lambda}^i]^{-1} \bar{\mathbf{C}} \cdot \mathbf{r}^i$ are used.

The evolution of \mathbf{r}^i is now motivated by the projection of the driving force (4.20) onto the plane perpendicular to \mathbf{r}^i itself, see Figure 4.3 for an illustration. To that effect, constraint $\dot{\mathbf{r}}^i \cdot \mathbf{r}^i = 0$ for the rate of the unit-vector \mathbf{r}^i is automatically satisfied. From a conceptual point of view, a shear-type deformation measure is considered by means of the projection operator $\mathbf{I} - \mathbf{r}^i \otimes \mathbf{r}^i$. In this regard, we assume the evolution equation

$$\dot{\mathbf{r}}^i = f^i [\mathbf{I} - \mathbf{r}^i \otimes \mathbf{r}^i] \cdot \bar{\mathbf{C}} \cdot \mathbf{r}^i = f^i [\bar{\mathbf{C}} \cdot \mathbf{r}^i - [\mathbf{r}^i \otimes \mathbf{r}^i] \cdot \bar{\mathbf{C}} \cdot \mathbf{r}^i], \quad (4.21)$$

wherein $f^i(\bar{\mathbf{C}}, \mathbf{r}^i)$ is a weighting factor to be specified later on. It becomes obvious that the second term in equation (4.21) can be interpreted in terms of the affine stretch $\bar{\lambda}^i$ oriented with respect to the integration direction \mathbf{r}^i , since $[\mathbf{r}^i \otimes \mathbf{r}^i] \cdot \bar{\mathbf{C}} \cdot \mathbf{r}^i = [\mathbf{r}^i \cdot \bar{\mathbf{C}} \cdot \mathbf{r}^i] \mathbf{r}^i = \bar{\lambda}^2 \mathbf{r}^i$. Note, that $\dot{\mathbf{r}}^i$ is identically zero as \mathbf{r}^i is co-linear with one of the principal directions of $\bar{\mathbf{C}}$. Based on this ansatz, the reduced dissipation inequality results in

$$\mathcal{D}_m^{\text{s,red}} = \sum_{i=1}^m -f^i S^i \mathbf{r}^i \cdot \bar{\mathbf{C}} \cdot [\mathbf{I} - \mathbf{r}^i \otimes \mathbf{r}^i] \cdot \bar{\mathbf{C}} \cdot \mathbf{r}^i, \quad (4.22)$$

which constitutes a semi-definite quadratic form that, by analogy with $\dot{\mathbf{r}}^i$, identically vanishes in case \mathbf{r}^i corresponds to a principal direction of $\bar{\mathbf{C}}$. As a typical example, we

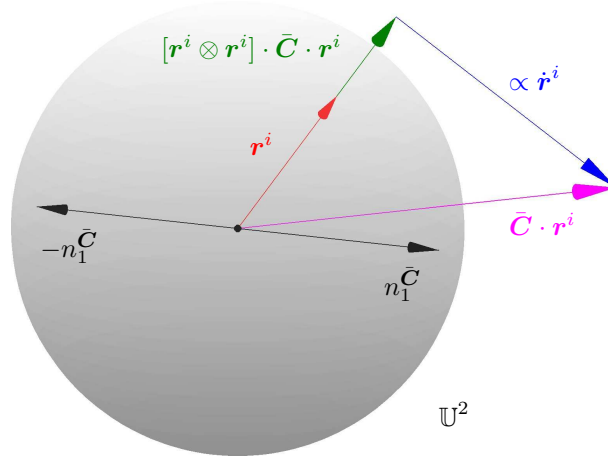


Figure 4.3: Graphical illustration of the evolution equation (4.21) defining the rate of the integration direction \mathbf{r}^i : construction of $\dot{\mathbf{r}}^i$ such that $\dot{\mathbf{r}}^i \cdot \mathbf{r}^i = 0$ resulting in an alignment with respect to one deformation-dependent preferred direction $\mathbf{n}_1^{\bar{\mathbf{C}}}$ for transversely isotropic material behaviour.

have $\dot{\mathbf{r}}^i = \mathbf{0}$ for $\bar{\mathbf{C}} \propto \mathbf{I}$, while $\dot{\mathbf{r}}^i \neq \mathbf{0}$ yields \mathbf{r}^i to align with the dominant principal direction of $\bar{\mathbf{C}}$, i.e. $\mathbf{n}_1^{\bar{\mathbf{C}}}$.

The remaining task is to particularise f^i . It becomes obvious that the standard form of the dissipation inequality for the closed solid mechanical system is satisfied for $f^i = c \bar{S}_i$ with $c \leq 0$. For the present problem, however, a sound description of the adaptation of the biological tissue to be modelled is described by the theory of open systems not outlined in this chapter. A chemical potential might also be included at least formally. In this context, consider a sufficiently loaded body undergoing non-zero Dirichlet boundary conditions fixed in time. An adaptation process should then render the tissue to increase its loading capacity so that the system has to be fed with energy. It becomes obvious that the reduced form of the standard dissipation inequality, as represented by $\mathcal{D}_m^{\text{s,red}}$, is violated in this case, which would be exhibited in a similar way for healing processes. As the adaptation of biological tissues is usually bounded by certain, say biological, limits, the evolution equation for \mathbf{r}^i should account for so-called saturation effects. On the one hand, the evolution of \mathbf{r}^i saturates for \mathbf{r}^i aligning with a principal direction of $\bar{\mathbf{C}}$. On the other hand, we restrict the maximum degree of anisotropy here by applying the spectral decomposition of \mathbf{A} . To be specific, \mathbf{r}^i is assumed to evolve as long as the difference between the largest and smallest eigenvalue of \mathbf{A} , i.e. $A_1 - A_3$, remains smaller than a pre-defined limit value, here denoted as $0 < \tilde{A}_\Delta \leq 1$. Consequently, the proportionality factor f^i introduced in equation (4.21) is assumed as

$$f^i = \begin{cases} \frac{\tilde{A}_\Delta - [A_1 - A_3]}{\tilde{t} \tilde{A}_\Delta} & \text{if } \bar{\lambda}^i > \tilde{\lambda}_c \\ 0 & \text{else} \end{cases} \quad (4.23)$$

Table 4.1: Material parameters for the microsphere-based remodelling formulations.

| Type | Symbol | Description | Unit |
|--|---------------------|------------------------------|-------|
| elastic neo-Hooke model | μ | shear modulus | [kPa] |
| | κ | penalty-like bulk modulus | [kPa] |
| microsphere-based elastic worm-like chain model | B | stress-like parameter | [kPa] |
| | r_0 | undeformed chain-length | [mm] |
| | L | maximal chain-length | [mm] |
| remodelling parameters | \tilde{p} | non-affine stretch parameter | [-] |
| | $\tilde{\lambda}_c$ | activation threshold | [-] |
| | \tilde{A}_Δ | saturation limit value | [-] |
| | \tilde{t} | saturation velocity | [d] |

In addition, a relaxation-type time parameter, $\tilde{t} > 0$, is incorporated and, moreover, we set $\dot{\mathbf{r}}^i = \mathbf{0}$ in case the related affine fibre stretch $\bar{\lambda}^i$ does not exceed a certain threshold, $\tilde{\lambda}_c \geq 0$. Alternatively, one could also set up a dead-zone-type remodelling equation, for instance by setting $f^i = 0$ for $\bar{\lambda}^i$ taking values within a specific interval. For the sake of convenience, the remodelling-related material parameters are summarised in Table 4.1.

With regard to evolution equation (4.21), the deformation-related quantity $\bar{\mathbf{C}} \cdot \mathbf{r}^i$ is assumed to be the essential mechanical stimulus, or driving force, for the reorientation process. As a possible alternative, one could assume the alignment of the fibres to be governed exclusively by the dominant principal strain direction $\mathbf{n}_1^{\bar{\mathbf{C}}}$. We consequently end up with

$$\dot{\mathbf{r}}^i = f^i \text{sign}(\mathbf{r}^i \cdot \mathbf{n}_1^{\bar{\mathbf{C}}}) \left[\mathbf{n}_1^{\bar{\mathbf{C}}} - [\mathbf{r}^i \cdot \mathbf{n}_1^{\bar{\mathbf{C}}}] \mathbf{r}^i \right] = f^i \text{sign}(\mathbf{r}^i \cdot \mathbf{n}_1^{\bar{\mathbf{C}}}) \left[\mathbf{I} - \mathbf{r}^i \otimes \mathbf{r}^i \right] \cdot \mathbf{n}_1^{\bar{\mathbf{C}}}, \quad (4.24)$$

where the sign-function is included to ensure that the integration direction \mathbf{r}^i aligns with $\mathbf{n}_1^{\bar{\mathbf{C}}}$ if \mathbf{r}^i being closer to $\mathbf{n}_1^{\bar{\mathbf{C}}}$ or with $-\mathbf{n}_1^{\bar{\mathbf{C}}}$ if \mathbf{r}^i being closer to $-\mathbf{n}_1^{\bar{\mathbf{C}}}$. It becomes apparent that this alternative format is similar to the format proposed in equation (4.21); essentially $\bar{\mathbf{C}} \cdot \mathbf{r}^i$ is replaced by $\mathbf{n}_1^{\bar{\mathbf{C}}}$ which implies that the principal values of $\bar{\mathbf{C}}$ are not taken into account. As an important consequence, the mechanical response due to the alternative format (4.24) does not depend on the loading history as it was the case for (4.21). The alternative evolution equation (4.24) is the basis for the remodelling approach for orthotropic material behaviour which is discussed in the following section.

4.3.2 Remodelling for orthotropic material behaviour

Since various biological tissues show fibre alignment with more than one single direction, we subsequently propose a remodelling formulation reflecting macroscopically orthotropic behaviour.

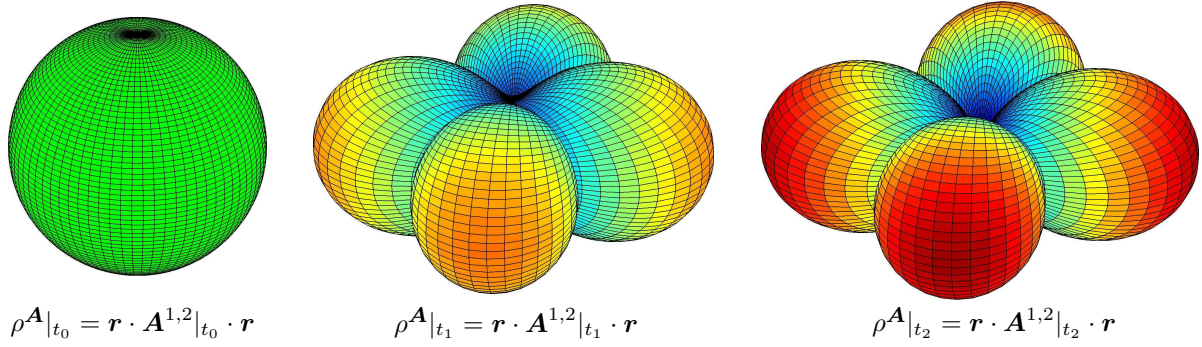


Figure 4.4: Graphical representation of the second order structural tensors $\mathbf{A}^{1,2}$ by means of the orientation-distribution-function $\rho^{\mathbf{A}} = \rho^{\mathbf{A}^1} \cup \rho^{\mathbf{A}^2}$ at different exemplarily chosen time steps t_n , $n = 0, 1, 2$. The spherical distribution at $t = t_0$ corresponds to an initially isotropic setting with $\mathbf{A}|_{t_0} = \frac{1}{6} \mathbf{I}$.

Unlike the approach used in Section 4.3.1 and due to the present assumption of orthotropy with two mean directions, two second-order generalised structural tensors are introduced in this case as

$$\mathbf{A}^{1,2} = \sum_{i=1}^m w^i \mathbf{r}^i \otimes \mathbf{r}^i = \sum_{j=1}^3 A_j^{1,2} \mathbf{n}_j^{1,2} \otimes \mathbf{n}_j^{1,2} \quad \forall \quad \mathbf{r}^i \rightarrow \mathbf{l}^{1,2}, \quad (4.25)$$

where $A_1^{1,2} \geq A_2^{1,2} \geq A_3^{1,2} \geq 0$ with $\sum_j A_j^{1,2} = 1/2$. To give an example, \mathbf{A}^1 will be calculated for those integration directions \mathbf{r}^i , which—due to the deformation—align with the first mean direction \mathbf{l}^1 . In order to visualise local anisotropic material properties later on, the orientation-distribution-type function $\rho^{\mathbf{A}} = \rho^{\mathbf{A}^1} \cup \rho^{\mathbf{A}^2}$ is introduced with $\rho^{\mathbf{A}^{1,2}} = \mathbf{r} \cdot \mathbf{A}^{1,2} \cdot \mathbf{r}$ and $\mathbf{r} \in \mathbb{U}^2$ denoting a unit-vector. The ODF $\rho^{\mathbf{A}^{1,2}}$ is exemplarily evaluated at different time steps and depicted in Figure 4.4.

The evolution of \mathbf{r}^i is based on equation (4.24) and motivated by its alignment with two preferred directions $\mathbf{l}^{1,2}$, see Figure 4.5. Basically, we project $\mathbf{l}^{1,2}$ onto the particular integration direction \mathbf{r}^i which results in the vectorial contribution $[\mathbf{r}^i \cdot \mathbf{l}^{1,2}] \mathbf{r}^i$. The direction of the rate $\dot{\mathbf{r}}^i$ can be constructed accordingly as

$$\dot{\mathbf{r}}^i = f^i \text{sign}(\mathbf{r}^i \cdot \mathbf{l}^{1,2}) [\mathbf{l}^{1,2} - [\mathbf{r}^i \cdot \mathbf{l}^{1,2}] \mathbf{r}^i] \quad \text{so that} \quad \dot{\mathbf{r}}^i \cdot \mathbf{r}^i = 0, \quad (4.26)$$

where the integration direction \mathbf{r}^i aligns either with \mathbf{l}^1 if \mathbf{r}^i being closer to \mathbf{l}^1 or with \mathbf{l}^2 if \mathbf{r}^i being closer to \mathbf{l}^2 , i.e.

$$\mathbf{l}^{1,2} = \begin{cases} \mathbf{l}^1 & \text{if } |\mathbf{r}^i \cdot \mathbf{l}^1| > |\mathbf{r}^i \cdot \mathbf{l}^2| \\ \mathbf{l}^2 & \text{else} \end{cases}. \quad (4.27)$$

Once more, a sign-function is included in the evolution equation (4.26) to ensure that the integration direction \mathbf{r}^i aligns with $\mathbf{l}^{1,2}$ if \mathbf{r}^i being closer to $\mathbf{l}^{1,2}$ or with $-\mathbf{l}^{1,2}$ if \mathbf{r}^i being closer to $-\mathbf{l}^{1,2}$.

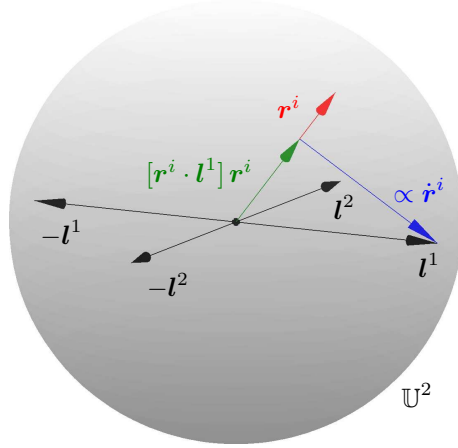


Figure 4.5: Graphical illustration of the evolution equation (4.26) defining the rate of the unit-vector \mathbf{r}^i : construction of $\dot{\mathbf{r}}^i$ such that $\dot{\mathbf{r}}^i \cdot \mathbf{r}^i = 0$ resulting in an alignment with respect to two deformation-dependent preferred directions \mathbf{l}^1 (and \mathbf{l}^2) for orthotropic material behaviour.

In view of the reorientation criterion, a crucial aspect is the identification or rather definition of the deformation-dependent mean directions $\mathbf{l}^{1,2}$. On the one hand, these directions should determine the alignment of the integration directions and, on the other hand, the alignment is assumed to reflect extremal states of strain energy. In this context, one could align the integration directions \mathbf{r}^i with respect to the principal strain directions or alternatively align the directions to share identical angles with the principal strain directions. As a special case of the latter approach, we draw on two particular directions reported in Boulanger and Hayes [49, eq. 3.37] as well as Boulanger and Hayes [50, 51]: the so-called *limiting directions*, which can be calculated via the relation

$$\mathbf{l}^{1,2} = \frac{\sqrt{\lambda_1^{\bar{C}}} \mathbf{n}_2^{\bar{C}} \pm \sqrt{\lambda_2^{\bar{C}}} \mathbf{n}_1^{\bar{C}}}{\sqrt{\lambda_1^{\bar{C}} + \lambda_2^{\bar{C}}}} \quad \text{for } \lambda_1^{\bar{C}} > \lambda_2^{\bar{C}} > 1 \quad (4.28)$$

using the principal values $\lambda_{1,2}^{\bar{C}}$ and principal directions $\mathbf{n}_{1,2}^{\bar{C}}$ of the isochoric right Cauchy-Green strain tensor $\bar{\mathbf{C}}$. Practically speaking, these limiting directions suffer the maximum shear in the considered plane of tension.

The remaining task is to particularise the factor f^i occurring in the evolution equation (4.26). Similar to the format proposed in (4.23), we restrict the maximum degree of anisotropy by assuming \mathbf{r}^i to evolve as long as the difference between the largest and smallest eigenvalue of $\mathbf{A}^{1,2}$ remains smaller than a pre-defined limit value \tilde{A}_Δ . Consequently, the proportionality factor f^i introduced in equation (4.26) is assumed as

$$f^i = \begin{cases} \frac{\tilde{A}_\Delta - [A_1^{1,2} - A_3^{1,2}]}{\tilde{t} \tilde{A}_\Delta} & \text{if } \lambda_2^{\bar{C}} > 1 \quad \text{and} \quad \lambda_1^{\bar{C}} - \lambda_2^{\bar{C}} > \tilde{\lambda}_c \\ 0 & \text{else} \end{cases}, \quad (4.29)$$

where, once more, a relaxation parameter \tilde{t} is incorporated and $\dot{\mathbf{r}}^i = \mathbf{0}$ if the difference between the related fibre stretches is smaller than a certain threshold $\tilde{\lambda}_c$.

4.4 Implementation

In order to integrate the individual unit vectors \mathbf{r}^i in time, we consider a finite time interval, $\Delta t = t_{n+1} - t_n \geq 0$, and apply an Euler-type method, i.e.

$$\tilde{\mathbf{r}}_{n+1}^i = \mathbf{r}_n^i + \Delta t \dot{\mathbf{r}}_n^i. \quad (4.30)$$

together with $\mathbf{r}_{n+1}^i = \tilde{\mathbf{r}}_{n+1}^i / \|\tilde{\mathbf{r}}_{n+1}^i\|$ to satisfy the normalisation constraint. Alternatively, for example, rotation-parameter-based or exponential integration schemes could be adopted, which automatically guarantee $\|\mathbf{r}_{n+1}^i\| = 1$.

Note, that the remodelling formulation itself or rather the evolution of deformation-induced anisotropy, depends on the integration scheme chosen for the unit-sphere. Even though a perfect alignment of all integration directions with respect to one axis of anisotropy, say $\mathbf{a}_0 \in \mathbb{U}^2$, renders $\mathbf{A} = \mathbf{a}_0 \otimes \mathbf{a}_0$ to be independent of the particular integration scheme, any intermediate state obviously depends on the type of the particular algorithmic formulation. Moreover, the orientation of the base-system, with respect to which the fixed coordinates of the initial integration directions $\mathbf{r}^i|_{t_0}$ are referred to, influences the simulation results as well—in particular as unit vectors being co-linear to a principal strain direction, or lying in the plane spanned by two principal strain directions, do not reorient. When considering states of deformation with changing principal directions of deformation, however, this effect is almost negligible and, moreover, higher-order integration schemes show common convergence properties. The algorithmic procedures corresponding to the transversely isotropic and orthotropic remodelling formulations described above are summarised in Tables 4.2 and 4.3, respectively.

4.5 Numerical examples

Before discussing some representative numerical examples, we first specify the particular form of the strain energy (4.6). Based on this, homogeneous as well as inhomogeneous states of deformation are discussed.

4.5.1 Specification of the strain energy

As commonly observed for soft biological tissues, the high water content of the material's ground substance results in an almost incompressible response. In this context, we draw on a related quasi-incompressible neo-Hooke-type model for the volumetric and isotropic isochoric part of the strain energy, i.e.

$$\Psi_{\text{vol}} = \frac{\kappa}{2} [J - 1]^2 \quad \text{and} \quad \Psi_{\text{iso}} = \frac{\mu}{2} [\bar{\mathbf{C}} : \mathbf{I} - 3]. \quad (4.31)$$

Table 4.2: Constitutive box for the three-dimensional microsphere formulation for transversely isotropic remodelling. Quantities without subscript n are associated with t_{n+1} .

| |
|---|
| <p>0. given deformation in terms of the right Cauchy-Green tensor $\bar{\mathbf{C}}$ at time t_{n+1} and history data $\mathbf{r}_n^i \in \mathbb{U}^2$ of all m discrete unit vectors representing the internal variables at time t_n</p> <p>1. compute difference between max. and min. eigenvalue of \mathbf{A}, i.e. $A_1 - A_3$ $\mathbf{A} = \sum_{i=1}^m w^i \mathbf{r}_n^i \otimes \mathbf{r}_n^i = \sum_{j=1}^3 A_j \mathbf{n}_j \otimes \mathbf{n}_j$</p> <p>2. for $i = 1, \dots, m$</p> <p>(a) compute the affine micro-stretches $\bar{\lambda}_n^i = \sqrt{\mathbf{r}_n^i \cdot \bar{\mathbf{C}} \cdot \mathbf{r}_n^i}$</p> <p>(b) update the internal variables $\tilde{\mathbf{r}}^i = \mathbf{r}_n^i + \Delta t f^i [\mathbf{I} - \mathbf{r}_n^i \otimes \mathbf{r}_n^i] \cdot \bar{\mathbf{C}} \cdot \mathbf{r}_n^i$ where $f^i = [\tilde{A}_\Delta - [A_1 - A_3]/[\tilde{t} \tilde{A}_\Delta]]$ if $\bar{\lambda}_n^i > \tilde{\lambda}_c$ or $f^i = 0$ else</p> <p>(c) perform normalisation $\mathbf{r}^i = \tilde{\mathbf{r}}^i / \ \tilde{\mathbf{r}}^i\$</p> <p>(d) update the affine micro-stretches $\bar{\lambda}^i = \sqrt{\mathbf{r}^i \cdot \bar{\mathbf{C}} \cdot \mathbf{r}^i}$</p> <p>3. compute non-affine stretch and derivative $\lambda = [\sum_{i=1}^m \bar{\lambda}^i \bar{w}^i]^{1/\bar{p}}$ and $\mathbf{H} = \sum_{i=1}^m \bar{\lambda}^i [\bar{p}-2] w^i \mathbf{r}^i \otimes \mathbf{r}^i$</p> <p>4. compute micro-stresses according to worm-like chain model $n \psi' = B [4r_0/L[\lambda - 1/\lambda] + 1/[1 - [\lambda r_0]/L]^2 - 1/[\lambda[1 - r_0/L]^2] + 1/\lambda - 1]$ if $\lambda \geq 1$ or $n \psi' = 0$ else</p> <p>5. compute macroscopic Piola-Kirchhoff stresses $\bar{\mathbf{S}}_{\text{ani}} = n \psi' \lambda^{[1-\bar{p}]} \mathbf{H}$ and continue with deviatoric projections defined in equations (4.10)</p> |
|---|

The anisotropic fibre-related part of the strain energy is assumed to be characterised by means of a *worm-like chain model*. While the statistical and entropy-based background of this one-dimensional non-linear model is extensively discussed in the references cited in Section 1.1.3, we shall adopt this approach here without specifying further details. In addition, a repulsive term is incorporated in order to be able to generally recapture

Table 4.3: Constitutive box for the three-dimensional microsphere formulation for orthotropic remodelling. Quantities without subscript n are associated with t_{n+1} .

| |
|--|
| <p>0. given deformation in terms of the right Cauchy-Green tensor $\bar{\mathbf{C}}$ at time t_{n+1} and history data $\mathbf{r}_n^i \in \mathbb{U}^2$ of all m discrete unit vectors representing the internal variables at time t_n</p> <p>1. compute principal values and directions of $\bar{\mathbf{C}}$ $\bar{\mathbf{C}} = \sum_{j=1}^3 \lambda_j^{\bar{\mathbf{C}}} \mathbf{n}_j^{\bar{\mathbf{C}}} \otimes \mathbf{n}_j^{\bar{\mathbf{C}}}$ for $\lambda_1^{\bar{\mathbf{C}}} > \lambda_2^{\bar{\mathbf{C}}} > 1$</p> <p>2. compute limiting directions $\mathbf{l}^{1,2} = \left[\sqrt{\lambda_1^{\bar{\mathbf{C}}} \mathbf{n}_2^{\bar{\mathbf{C}}} \pm \sqrt{\lambda_2^{\bar{\mathbf{C}}} \mathbf{n}_1^{\bar{\mathbf{C}}}}} \right] / \sqrt{\lambda_1^{\bar{\mathbf{C}}} + \lambda_2^{\bar{\mathbf{C}}}}$</p> <p>3. compute difference between max. and min. eigenvalue of $\mathbf{A}^{1,2}$, i.e. $A_1^{1,2} - A_3^{1,2}$ $\mathbf{A}^{1,2} = \sum_{i=1}^m w^i \mathbf{r}_n^i \otimes \mathbf{r}_n^i = \sum_{j=1}^3 A_j^{1,2} \mathbf{n}_j^{1,2} \otimes \mathbf{n}_j^{1,2} \quad \forall \quad \mathbf{r}^i \rightarrow \mathbf{l}^{1,2}$</p> <p>4. for $i = 1, \dots, m$ (a) update the internal variables $\tilde{\mathbf{r}}^i = \mathbf{r}_n^i + \Delta t f^i \text{sign}(\mathbf{r}_n^i \cdot \mathbf{l}) [\mathbf{l} - [\mathbf{r}_n^i \cdot \mathbf{l}] \mathbf{r}_n^i]$ where $\mathbf{l} = \mathbf{l}^1$ if $\mathbf{r}_n^i \cdot \mathbf{l}^1 > \mathbf{r}_n^i \cdot \mathbf{l}^2$ or $\mathbf{l} = \mathbf{l}^2$ else and $f^i = \left[\tilde{A}_\Delta - [A_1^{1,2} - A_3^{1,2}] / [\tilde{t} \tilde{A}_\Delta] \right]$ if $\lambda_2^{\bar{\mathbf{C}}} > 1$ and $\lambda_1^{\bar{\mathbf{C}}} - \lambda_2^{\bar{\mathbf{C}}} > \tilde{\lambda}_c$ or $f^i = 0$ else (b) perform normalisation $\mathbf{r}^i = \tilde{\mathbf{r}}^i / \ \tilde{\mathbf{r}}^i\$ (c) update the affine micro-stretches $\bar{\lambda}^i = \sqrt{\mathbf{r}^i \cdot \bar{\mathbf{C}} \cdot \mathbf{r}^i}$</p> <p>5. compute the non-affine stretch and its derivative $\lambda = \left[\sum_{i=1}^m \bar{\lambda}^i \bar{w}^i \right]^{1/\bar{p}}$ and $\mathbf{H} = \sum_{i=1}^m \bar{\lambda}^i [\bar{p}-2] w^i \mathbf{r}^i \otimes \mathbf{r}^i$</p> <p>6. compute micro-stresses according to worm-like chain model $n \psi' = B [4r_0/L[\lambda - 1/\lambda] + 1/[1 - [\lambda r_0]/L]^2 - 1/[\lambda[1 - r_0/L]^2] + 1/\lambda - 1]$ if $\lambda \geq 1$ or $n \psi' = 0$ else</p> <p>7. compute macroscopic Piola-Kirchhoff stresses $\bar{\mathbf{S}}_{\text{ani}} = n \psi' \lambda^{[1-\bar{p}]} \mathbf{H}$ and continue with deviatoric projections defined in equations (4.10)</p> |
|--|

a stress-free contribution upon unloading, i.e. $\bar{\mathbf{F}} = \mathbf{I}$. In summary, the worm-like chain model considered takes the representation

$$n \psi(\lambda) = \frac{nK\theta L}{4A} \left[2 \frac{r^2}{L^2} + \frac{1}{1 - r/L} - \frac{r}{L} - \frac{\ln(\lambda^{4r_0^2})}{4r_0L} \left[4 \frac{r_0}{L} + \frac{1}{[1 - r_0/L]^2} - 1 \right] - \psi_c \right] \quad (4.32)$$

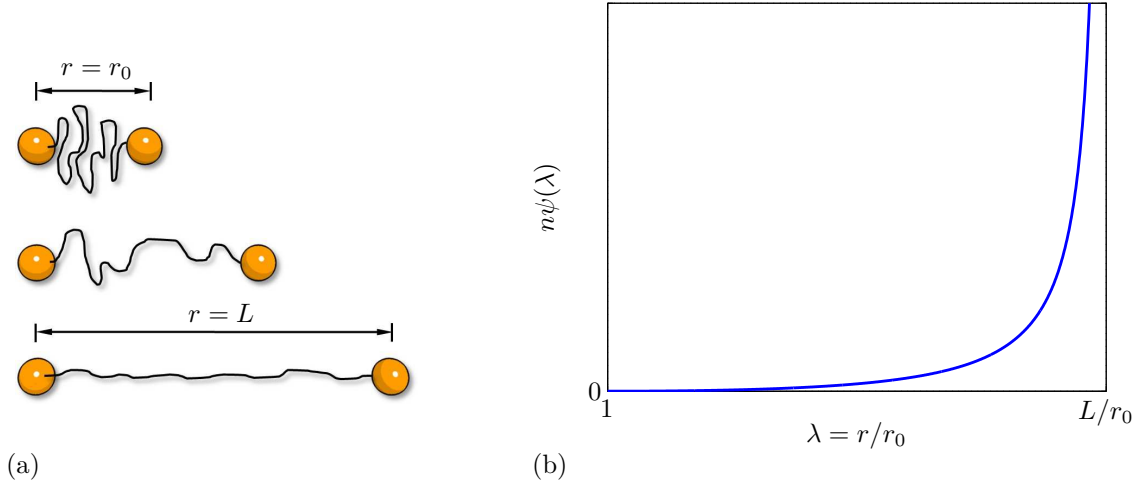


Figure 4.6: Illustration of the one-dimensional constitutive worm-like chain model. (a) Worm-like chain in different states of loading, with chain-length r_0 for the undeformed state at $\lambda = 1$ and chain-length L for the deformed state at the 'locking stretch' $\lambda_{\text{lock}} = L/r_0$. (b) Free energy $n\psi(\lambda)$ against the non-affine stretch λ , $n\psi(\lambda) \rightarrow \infty$ for $\lambda_{\text{lock}} \rightarrow L/r_0$.

for $\lambda \geq 1$ while $n\psi(\lambda) = 0$ is assumed for compression, i.e. $\lambda < 1$. Herein, the Boltzmann constant is denoted by $K = 1.38 \times 10^{-23} [\text{JK}^{-1}]$, θ is the absolute temperature, and A is established as persistent contour length. While r_0 characterises the length of the chain for the undeformed state, i.e. at $\lambda = 1$, the actual chain length follows from $r = \lambda r_0 \in [0, L]$. From the mechanical point of view, it is worth mentioning that the strain energy as well as the related stress contribution both approach towards infinity for $r \rightarrow L$, which reflects one of the main ideas of the worm-like chain model, see Figure 4.6 for an illustration. Furthermore, any response under compression has been excluded and, formally, the constant $\psi_c = 2r_0^2/L^2 + [1 - r_0/L]^{-1} - r_0/L$ is incorporated so that $n\psi = 0$ for $\lambda = 1$. Note, that the worm-like fibre contributions could alternatively have been assumed to depend on the total deformation tensor, \mathbf{C} , rather than on the isochoric part, $\bar{\mathbf{C}}$. The micro-stress can be expressed as

$$n\psi'(\lambda) = B \left[4 \frac{r_0}{L} \left[\lambda - \frac{1}{\lambda} \right] + \frac{1}{[1 - [\lambda r_0]/L]^2} - \frac{1}{\lambda [1 - r_0/L]^2} + \frac{1}{\lambda} - 1 \right], \quad (4.33)$$

wherein the abbreviated notation $B = nK\theta r_0/[4A]$ is applied. For the sake of convenience, the elastic material parameters together with the remodelling-related quantities are summarised in Table 4.1. In view of the particular set of elastic material parameters chosen, we partially adopt constants representing blood vessels as identified in Alastrué et al. [9]. In this regard, the chosen set of worm-like-chain-related material parameters in Figure 4.7(b) could, for instance, correspond to $n = 10^{15} [\text{mm}^{-3}]$ chain segments defined per unit volume with a persistent contour length of $A = 1.1 [\text{mm}]$ and an absolute temperature of $\theta = 310.91 [K]$ which represents body temperature.

Table 4.4: Integration directions $\mathbf{r}^i = r_1^i \mathbf{e}_1 + r_2^i \mathbf{e}_2 + r_3^i \mathbf{e}_3$ and weights w^i for the unit-sphere, cf. Figure 1.4 for an illustration.

| No. | r_1^i | r_2^i | r_3^i | $w^i/2$ |
|-----|-----------------|-----------------|----------------|-----------------|
| 1 | 0.0 | 0.0 | 1.0 | 0.0265214244093 |
| 2 | 0.0 | 1.0 | 0.0 | 0.0265214244093 |
| 3 | 1.0 | 0.0 | 0.0 | 0.0265214244093 |
| 4 | 0.0 | 0.707106781187 | 0.707106781187 | 0.0199301476312 |
| 5 | 0.0 | -0.707106781187 | 0.707106781187 | 0.0199301476312 |
| 6 | 0.707106781187 | 0.0 | 0.707106781187 | 0.0199301476312 |
| 7 | -0.707106781187 | 0.0 | 0.707106781187 | 0.0199301476312 |
| 8 | 0.707106781187 | 0.707106781187 | 0.0 | 0.0199301476312 |
| 9 | -0.707106781187 | 0.707106781187 | 0.0 | 0.0199301476312 |
| 10 | 0.836095596749 | 0.387907304067 | 0.387907304067 | 0.0250712367487 |
| 11 | -0.836095596749 | 0.387907304067 | 0.387907304067 | 0.0250712367487 |
| 12 | 0.836095596749 | -0.387907304067 | 0.387907304067 | 0.0250712367487 |
| 13 | -0.836095596749 | -0.387907304067 | 0.387907304067 | 0.0250712367487 |
| 14 | 0.387907304067 | 0.836095596749 | 0.387907304067 | 0.0250712367487 |
| 15 | -0.387907304067 | 0.836095596749 | 0.387907304067 | 0.0250712367487 |
| 16 | 0.387907304067 | -0.836095596749 | 0.387907304067 | 0.0250712367487 |
| 17 | -0.387907304067 | -0.836095596749 | 0.387907304067 | 0.0250712367487 |
| 18 | 0.387907304067 | 0.387907304067 | 0.836095596749 | 0.0250712367487 |
| 19 | -0.387907304067 | 0.387907304067 | 0.836095596749 | 0.0250712367487 |
| 20 | 0.387907304067 | -0.387907304067 | 0.836095596749 | 0.0250712367487 |
| 21 | -0.387907304067 | -0.387907304067 | 0.836095596749 | 0.0250712367487 |

With regard to the numerical integration on the unit-sphere, a simple scheme with orthogonal symmetry is adopted from Bažant and Oh [32] based on $m = 21$ integration points for half of the sphere, see also Table 4.4 or Miehe et al. [218] and Figure 1.4 for an illustration. A visualisation of the underlying integration directions, together with a graphical illustration of the method of stereographic projection, is highlighted in Figure C.1. Detailed background information on this particular integration scheme, which can nowadays be considered as the standard approach for isotropic materials, is provided in the contributions by Bažant and Oh [32] and Miehe et al. [218]. In view of higher-order methods and modifications of standard integration algorithms, the reader is referred to, for instance, Heo and Xu [128], Alastrué et al. [9], Alastrué et al. [10] and Ehret et al. [91]. As mentioned in Section 4.3, the numerical results strongly depend on the particular integration scheme used. In fact, it turns out that using $m = 21$ cannot capture high degrees of anisotropy if $\mathbf{r}^i = \text{const}$. However, the remodelling formulation proposed is less sensitive to the particular integration algorithm. As indicated above, an illustrative example is given by the fact that all suitable integration schemes render an identical distribution for the fully aligned case, i.e. $\mathbf{A}_i = \mathbf{a}_{0i} \otimes \mathbf{a}_{0i}$.

In the following, we apply the proposed remodelling formulations for transversely isotropic and orthotropic material behaviour to representative three-dimensional ho-

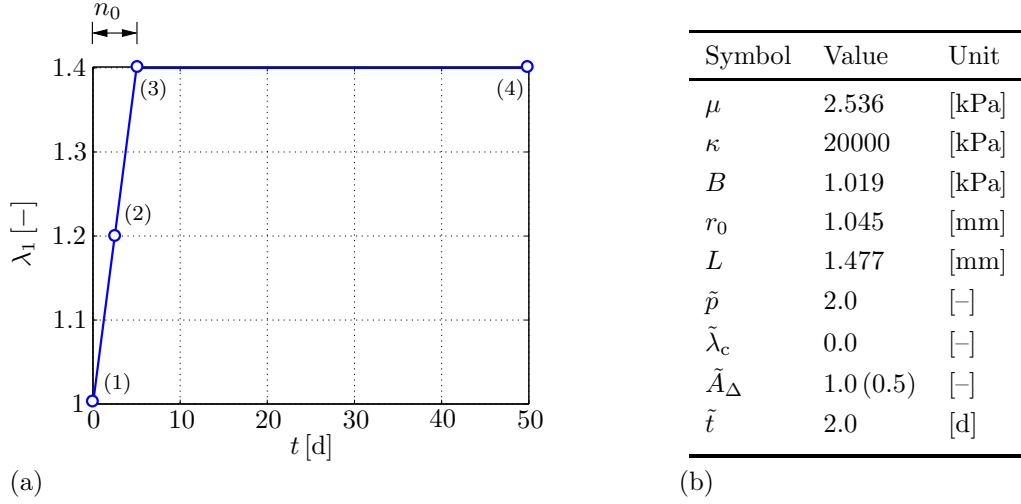


Figure 4.7: Isochoric uniaxial tension. (a) Applied loading history in terms of the stretch λ with (1)–(4) denoting representative points in time at $t = \{0.0, 2.5, 5.0, 50.0\}$ [d]. (b) Material parameters used for the homogeneous uniaxial (biaxial) deformation problem.

homogeneous and non-homogeneous deformation problems. Special emphasis is thereby placed on the evolution of deformation-induced anisotropy. In this regard, we visualise the evolving anisotropic material properties by means of the symmetric second-order structural tensor \mathbf{A} in terms of the ODF-type function $\rho^{\mathbf{A}} = \mathbf{r} \cdot \mathbf{A} \cdot \mathbf{r}$, see equations (4.19) and (4.25), and via the difference between the maximal and minimal principal value of \mathbf{A} , i.e. $A_1 - A_3$, which represents an appropriate measure for the degree of anisotropy. Furthermore, the method of stereographic projection is used to visualise the inhomogeneous distribution of the affine stretches $\bar{\lambda}^i$, see also Appendix C. In this regard, note that the stereographic projection plots are generated based on the *initial* distribution of the integration directions.

4.5.2 Transversely isotropic remodelling

In order to illustrate the basic constitutive characteristics of the transversely isotropic remodelling formulation, we first investigate a homogeneous model problem of isochoric uniaxial tension. Secondly, we consider the displacement-driven deformation of a plate with a cut, in order to show the capabilities of the model with regard to iterative finite-element schemes.

4.5.2.1 Homogeneous uniaxial tension

A state in isochoric uniaxial deformation can be represented via the deformation gradient $\mathbf{F} = \lambda_1 \mathbf{e}_1 \otimes \mathbf{e}_1 + \lambda_1^{-1/2} [\mathbf{e}_2 \otimes \mathbf{e}_2 + \mathbf{e}_3 \otimes \mathbf{e}_3]$. The particular loading history considered is based on the linear increase of the representative loading parameter, i.e. the stretch λ_1 , within a time period of $n_0 = 5$ [d] and then its value is fixed at $\lambda_1 = 1.4$ for a time period

of 45 [d]; see Figure 4.7(a). What we refer to as 1 [d] is related to one time unit which could be in the range of minutes, hours, days, or weeks—here, we choose days. We will also study rate-dependencies during the loading process as the quasi-static transversely isotropic remodelling formulation is of viscoelastic type. Accordingly, setting $n_0 = 5$ [d] reflects a twice as fast loading process as characterised by $n_0 = 10$ [d], while $n_0 = 20$ [d] reduces the speed of loading by a factor of two compared to $n_0 = 10$ [d]. The material parameters applied for this homogeneous deformation case are adopted by analogy with data identified in Alastrué et al. [9] and summarised in Table 4.7(b).

Figure 4.8 shows the saturation-type behaviour of the deformation-induced anisotropy evolution in terms of the degree of anisotropy $A_1 - A_3$. Moreover, the influence of individual material parameters is displayed by choosing values different from those given in Figure 4.7(b). In this regard, Figure 4.8(a) displays the influence of the saturation or rather limit value \tilde{A}_Δ . As mentioned above, $\tilde{A}_\Delta = 1$ constitutes an upper limit for $A_1 - A_3$ so that also larger values $\tilde{A}_\Delta > 1$ render the same saturation plateau. It is also worth mentioning that the extremal value, i.e. $A_1 - A_3 = 1$, is not approached here, since integration directions being either co-linear or orthogonal with respect to the principal stretch direction $\mathbf{n}_1^C = \mathbf{e}_1$ remain constant and do not evolve, see also Figure 4.9(c) at $t = 50$ [d]. In view of the value $\tilde{A}_\Delta = 0.8$, see Figure 4.8(a), one observes in particular that the anisotropy evolution takes place in a viscous manner as the loading parameter λ is fixed after 5 [d] and the graph of $A_1 - A_3$ continues to increase.

The influence of the parameter $\tilde{\lambda}_c$ is highlighted in Figure 4.8(b). As expected, setting $\tilde{\lambda}_c = 0$ ends up with the largest saturation value for $A_1 - A_3$ as directions undergoing all levels of compression also reorient. In case reorientation under compression is excluded, i.e. $\tilde{\lambda}_c \geq 1$, however, the different values of $\tilde{\lambda}_c$ result in the same saturation value here for $A_1 - A_3$, due to the $m = 21$ -point integration scheme applied to the unit-sphere being rather coarse.

Since the remodelling formulation proposed is time-dependent, i.e. of a viscoelastic type, the time interval within which the respective loading is applied strongly influences the adaptation process. By analogy with strain-rate dependencies, Figure 4.8(c) displays the influence of the time period n_0 chosen for the loading interval. It becomes apparent that a higher ‘strain-rate’ yields the remodelling process to develop faster. One could also similarly modify the relaxation-time parameter \tilde{t} , see Figure 4.8(d). It becomes obvious that larger values of \tilde{t} reduce the remodelling velocity.

The deformation-induced anisotropy evolution is additionally depicted in Figure 4.9 for four different states of deformation at $t = \{0.0, 2.5, 5.0, 50.0\}$ [d]. Here, the method of stereographic projection is used to plot the affine stretches $\bar{\lambda}$ for each integration direction in Figure 4.9(a). Furthermore, an ODF-type visualisation for the symmetric second-order tensor \mathbf{A} is applied in Figure 4.9(b), cf. Appendix C.1. The full information is provided by plotting the integration directions themselves in Figure 4.9(c). We observe that the degree of anisotropy continuously evolves with time as the ODF increasingly deviates from its initially spherical distribution at $t = 0$ [d]. Furthermore, Figures 4.9(b) and 4.9(c) illustrate the alignment of the integration directions according to the dominant

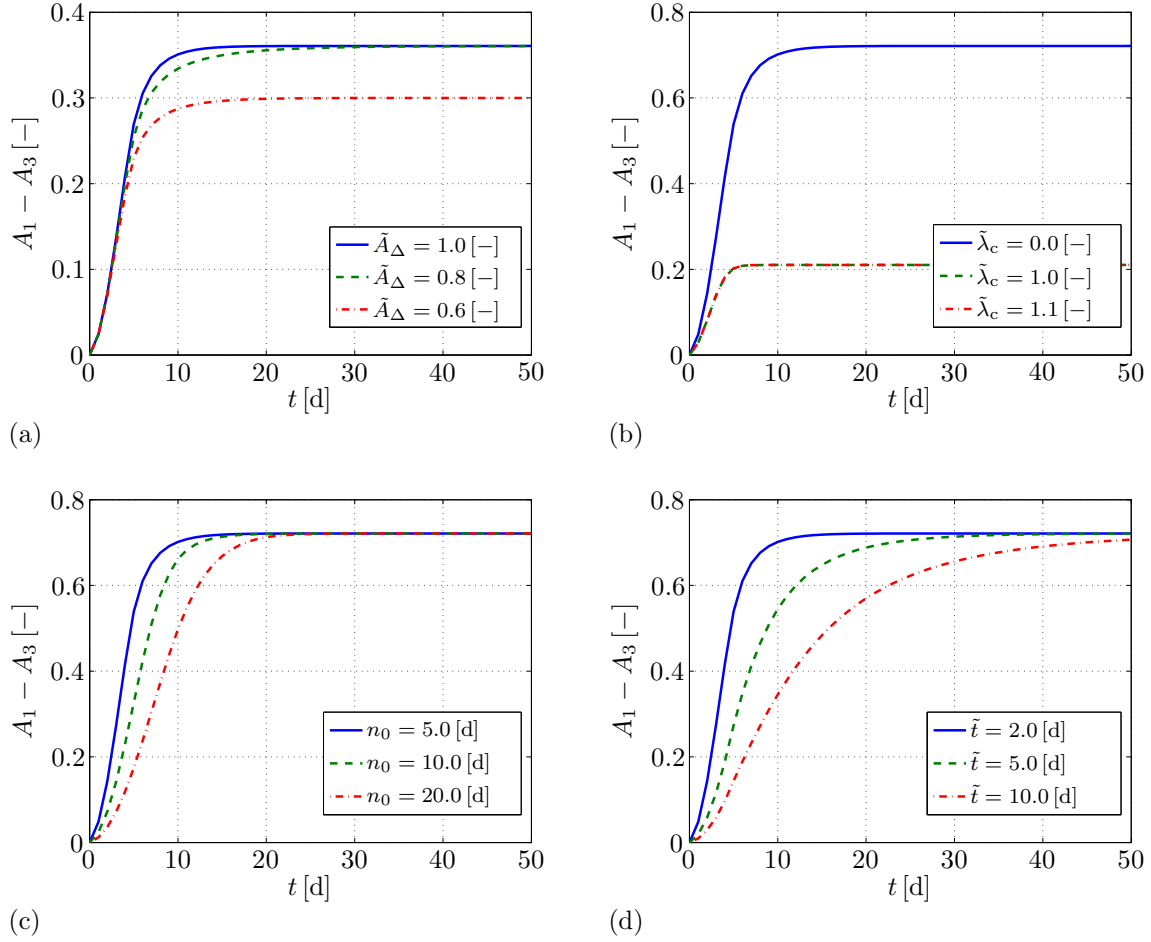


Figure 4.8: Anisotropy-evolution $A_1 - A_3$ of the transversely isotropic remodelling formulation for isochoric uniaxial tension. (a) Influence of remodelling limit \tilde{A}_Δ . (b) Influence of remodelling activation threshold $\tilde{\lambda}_c$. (c) Influence of loading interval n_0 . (d) Influence of remodelling velocity \tilde{t} .

principal stretch direction $\mathbf{n}_1^{\tilde{C}} = \mathbf{e}_1$. To be specific, the uniaxial loading results in a uniaxial distribution of $\rho^{\mathbf{A}}$ so that \mathbf{A} possesses two identical principal values. To give an example, for $t = 50$ [d] we obtain $A_1 = A_2 = 0.0929$ and $A_3 = 0.8142$. It becomes apparent that integration directions being either co-linear or orthogonal with respect to the principal stretch direction $\mathbf{n}_1^{\tilde{C}} = \mathbf{e}_1$, do not reorient, whereas all other integration directions reorient as long as they finally coincide with the principal stretch direction $\mathbf{n}_1^{\tilde{C}} = \mathbf{e}_1$. Note that, for $t = 50$ [d], several integration directions aligned with respect to the \mathbf{e}_1 -direction lie on top of each other. With regard to practical applications including non-homogeneous deformations, however, such an idealised case will hardly occur. Instead, all integration directions will tend to align with respect to the local principal stretch direction.

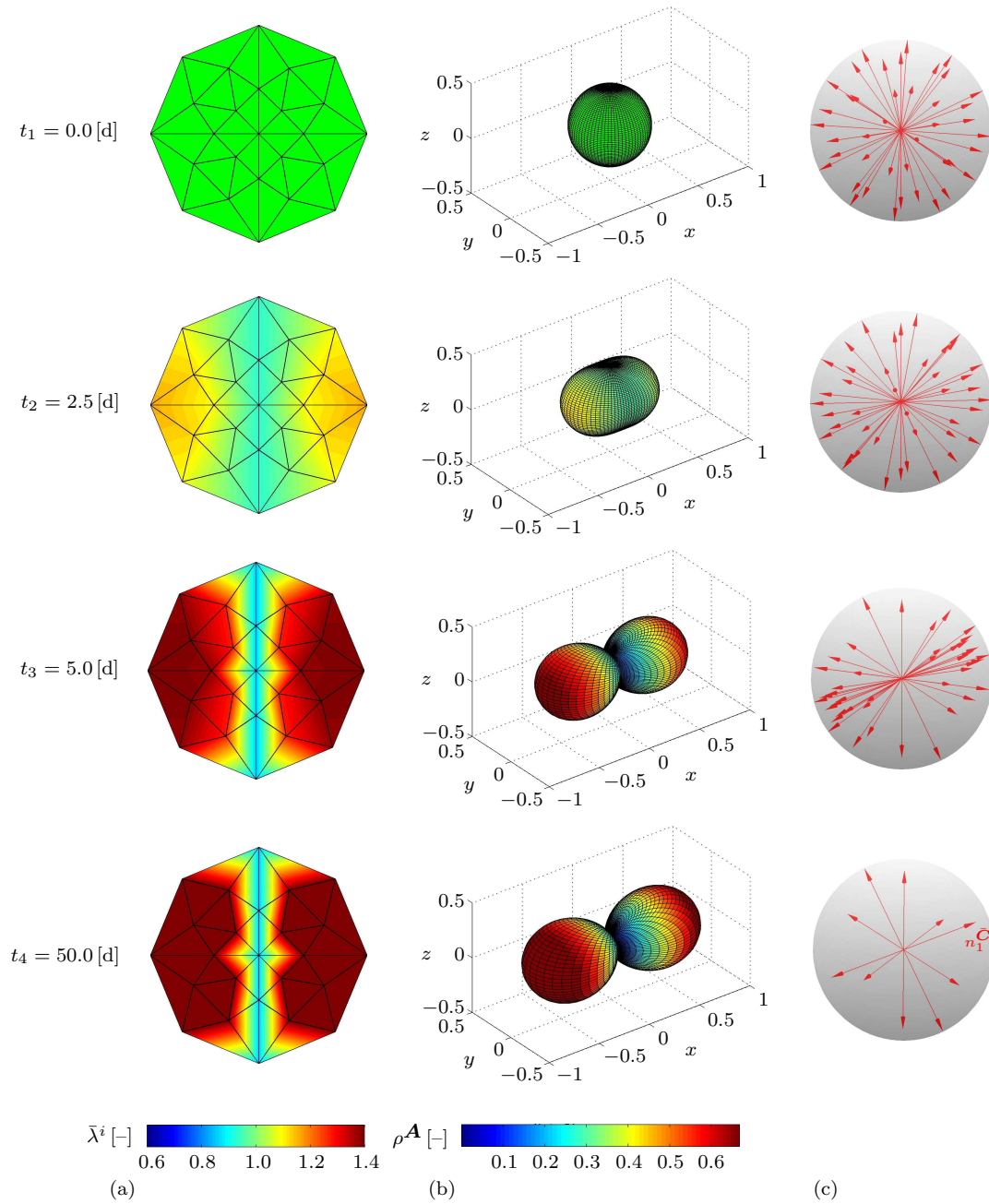


Figure 4.9: Isochoric uniaxial tension. Illustration of the anisotropy evolution at four representative points in time $t = \{0.0, 2.5, 5.0, 50.0\}$ [d] for the loading history and material parameters in Figure 4.7b. (a) Stereographic projection of the affine isochoric stretches $\bar{\lambda}^i$. (b) ODF-type function ρ^A . (c) Alignment of integration directions r^i with respect to principal stretch direction n_1^C .

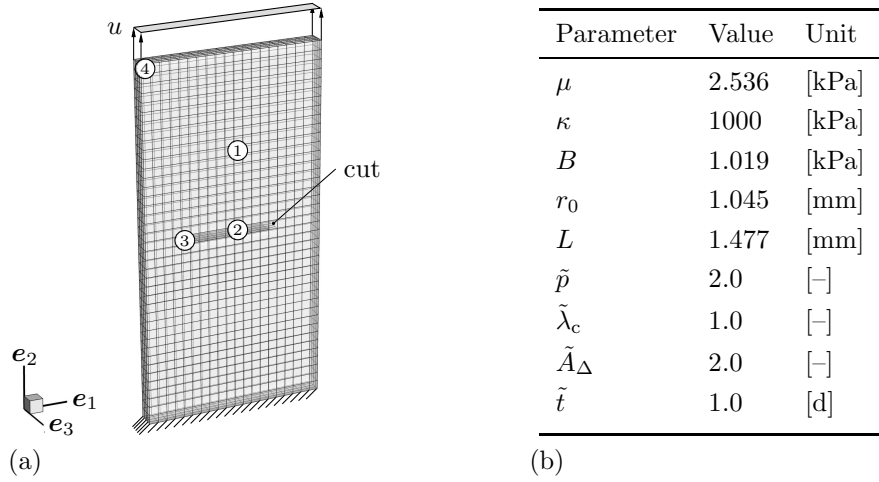


Figure 4.10: Displacement-driven tension of a plate with a cut. (a) Discretised geometry, boundary conditions and four representative Gauss-points ①–④ for anisotropy-visualisation. (b) Material parameters.

4.5.2.2 Tension of a plate with a cut

Motivated by the experimental investigation reported in Eastwood et al. [90], we now carry out a qualitative study on the inhomogeneous deformation of a plate with a cut loaded under displacement-driven tension. The particular specimen considered has the dimensions $80 \times 40 \times 4$ [mm] and its finite-element discretisation is performed with $40 \times 20 \times 4$ Q1P0-type eight node hexahedral elements. The values summarised in Table 4.10(b) are adopted with respect to the set of material parameters. Moreover, quasi static loading conditions are applied by means of Dirichlet boundary conditions so that the plate is longitudinally stretched to a length of 110 [mm]—the transverse displacements at these boundaries being clamped. By analogy with the homogeneous deformations discussed in the previous section, the respective load increments are linearly increased within 40 [d], whereas the boundary conditions thereafter remain fixed for a period of another 60 [d]; related graphical illustrations are highlighted in Figure 4.11(a).

The sum of reaction forces present at the respective Dirichlet boundaries are given in Figure 4.11(b). As expected, we observe that the reaction forces continuously increase. While the slope of this curve increases during the loading interval $0 \leq t \leq 40$ [d] the magnitude of reaction forces tends to saturate for the interval 40 [d] $< t \leq 100$ [d] within which the prescribed degrees of freedom are fixed.

Figure 4.12 displays the distribution of the Cauchy-stresses σ_{22} with respect to the macroscopic longitudinal loading direction for four different points in time at $t = \{1, 40, 70, 100\}$ [d]. It becomes apparent that the maximum stress values are obtained at the cut tip and increase, even for the loading interval within which the prescribed displacements are fixed. This effect clearly underlines the viscous anisotropy evolution and the increase in loading capacity. To investigate the evolution of anisotropy in more

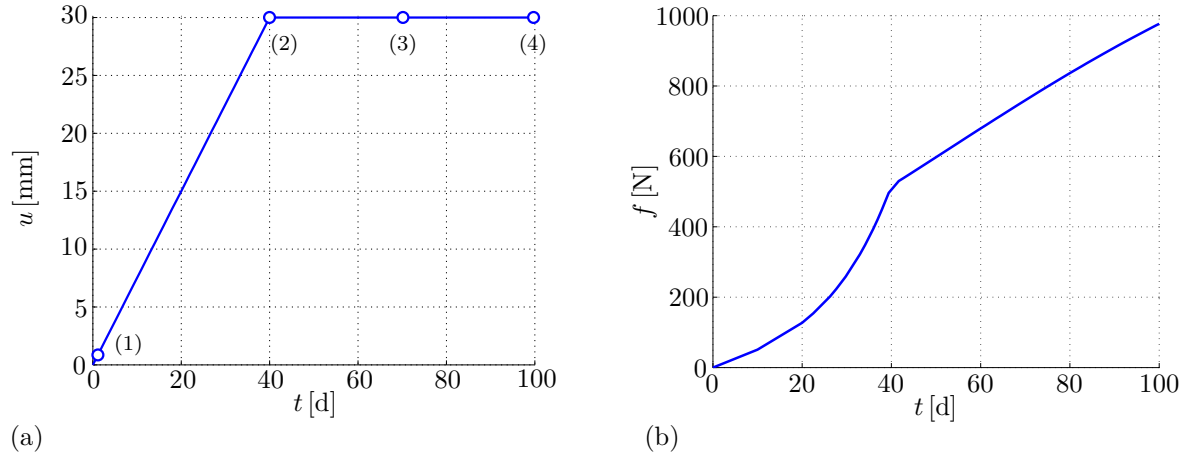


Figure 4.11: Displacement-driven tension of a plate with a cut. (a) Applied loading history in terms of the prescribed longitudinal displacements u with (1)–(4) denoting representative points in time at $t = \{1, 40, 70, 100\}$ [d]. (b) Sum of reaction forces f over time t .

detail, we then focus on four integration points of particular finite elements in order to visualise local anisotropic material properties by means of the ODF $\rho^{\mathbf{A}}$. Generally, we observe that all ODFs ①–④ show transversely isotropic texture evolution, since their shape increasingly deviates from their initial spherical distribution. However, ODFs ① and ②—located in the middle region of the strip and consequently oriented with respect to the longitudinal axis—are only slightly anisotropic. Especially ODF ② remains almost fully spherical and thus isotropic. In contrast, ODF ③—located at the tip of the cut—shows the most significant change in shape, which reflects a pronounced evolution of anisotropy. Interestingly, ODF ③ is aligned according to the opened cut front. Due to the pronounced contraction of the strip at the constrained top of the strip, ODF ④ is oriented towards the opposite direction and also shows considerable anisotropy evolution.

As experimentally observed, the fibre distribution aligns according to the local loading direction. This effect is recaptured by the proposed remodelling formulation and shown in Figure 4.13, where contour-plots of the anisotropy measure $A_1 - A_3$ at different steps of the simulation underline the inhomogeneity of the tension problem considered. The highest anisotropy-values are obtained at the cut-tips, whereas the lowest values can be observed in the middle region of the strip located directly over, respectively under, the cut. The rest of the specimen also shows a distinct anisotropy evolution, whereby the anisotropy distribution over the specimen turns out to be rather homogeneous.

Furthermore, Figure 4.13 illustrates the evolution of the local fibre angle which is determined as the angle $\angle(\mathbf{n}_1^{\bar{\mathbf{C}}}, \mathbf{n}_1^{\mathbf{A}})$ between the macroscopic longitudinal loading direction $\mathbf{n}_1^{\bar{\mathbf{C}}}$ and the principal direction $\mathbf{n}_1^{\mathbf{A}}$ related to the dominant principal value A_1 of the generalised structural tensor \mathbf{A} . Starting from an initially randomly distributed fibre orientation at $t = 0$ [d], the proposed modelling framework reflects an almost perfect

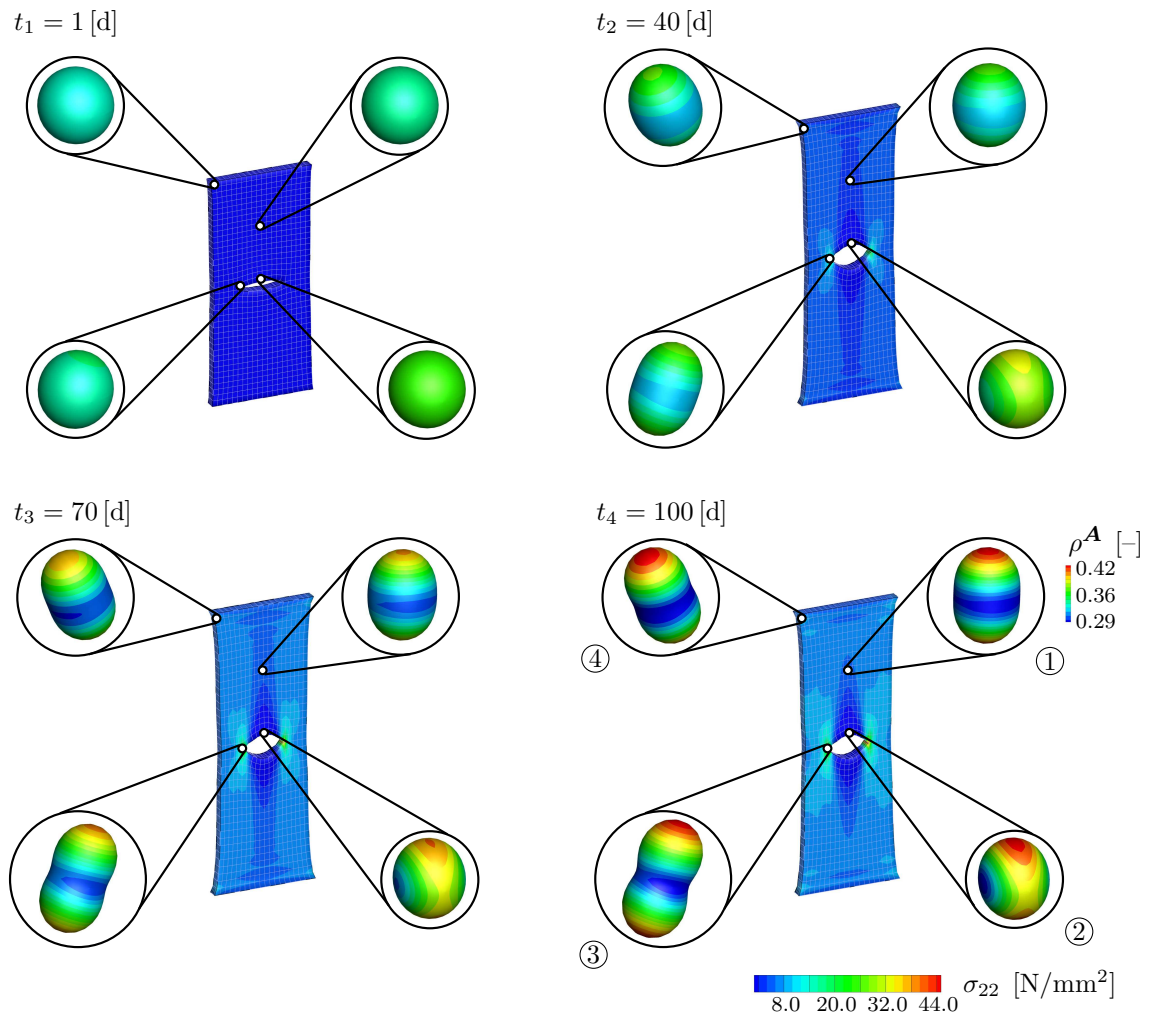


Figure 4.12: Displacement-driven tension of a plate with a cut. Contour-plots of the longitudinal Cauchy-stress σ_{22} for representative points in time at $t = \{1, 40, 70, 100\}$ [d] and ODF-type visualisation ρ^A at four different Gauss-points ①–④.

alignment of the fibres with respect to the average dominant stretch direction \mathbf{e}_2 . This is especially observed in regions away from the cut, whereas the alignment of the fibres is perturbed in the closer surrounding area of the cut.

4.5.3 Orthotropic remodelling

In this section, the constitutive characteristics of the orthotropic remodelling formulation are highlighted by means of a homogeneous biaxial tension test followed by a force-driven inflation of a thick-walled residually-stressed artery-like tube subjected to internal pressure.

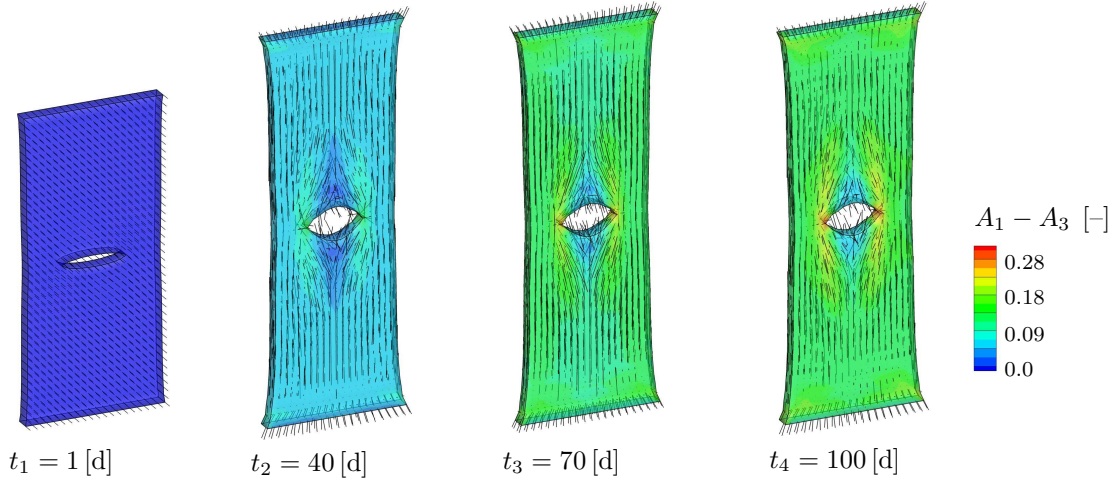


Figure 4.13: Displacement-driven tension of a plate with a cut. Contour-plots of the degree of anisotropy $A_1 - A_3$ for representative points in time at $t = \{1, 40, 70, 100\}$ [d].

4.5.3.1 Homogeneous biaxial tension

A state in isochoric biaxial deformation is associated with the deformation gradient $\mathbf{F} = \lambda_1 \mathbf{e}_1 \otimes \mathbf{e}_1 + \lambda_2 \mathbf{e}_2 \otimes \mathbf{e}_2 + [\lambda_1 \lambda_2]^{-1} \mathbf{e}_3 \otimes \mathbf{e}_3$. The particular loading applied here is based on the linear increase of the representative loading parameters λ_1 and λ_2 —for this particular case we set $\lambda_2 = [1 + \lambda_1]/2$ —within a time period of 5 [d], and then its value is fixed at $\lambda_1 = 1.4$ and $\lambda_2 = 1.2$ for a time period 45 [d]; see Figure 4.14(a). With regard to the set of material parameters, the values summarised in Figure 4.10(b) are adopted by analogy with data identified in Alastrué et al. [9].

Once more, special emphasis is placed on the evolution of deformation-induced anisotropy, illustrated via the difference between maximal and minimal principal values of the second-order generalised structural tensors $\mathbf{A}^{1,2}$, i.e. $A_1^{1,2} - A_3^{1,2}$, cf. equation (4.25). Figure 4.14(b) shows the saturation behaviour of the anisotropy evolution. It obviously takes place in a viscous manner, as the loading is fixed after 5 [d] and the graph of $A_1^{1,2} - A_3^{1,2}$ continues to increase. As mentioned above, $\tilde{A}_\Delta = 1/2$ constitutes an upper limit for $A_1^{1,2} - A_3^{1,2}$ so that also larger values $\tilde{A}_\Delta > 1/2$ render the same saturation plateau. Interestingly, we observe that the curves for $A_1^1 - A_3^1$ and $A_1^2 - A_3^2$ do not coincide. While the former curve yields the extremal value, i.e. $A_1^1 - A_3^1 = 1/2$, this is not the case for the latter curve which gives slightly lower values, i.e. $A_1^2 - A_3^2 = 0.46$. This can be explained by the particular integration scheme used for the calculations. Due to the odd-numbered and non-uniform distribution of the $m = 21$ -point integration scheme over the hemisphere, more integration directions align with limiting direction \mathbf{l}^1 as compared to limiting direction \mathbf{l}^2 . This consequently results in a more pronounced anisotropy evolution with respect to the first limiting direction \mathbf{l}^1 . This effect can be reduced or even completely avoided for uniformly distributed integration schemes, as, for instance, applied by Kurzhöfer [175]. As indicated in Section 4.3.1, the present me-

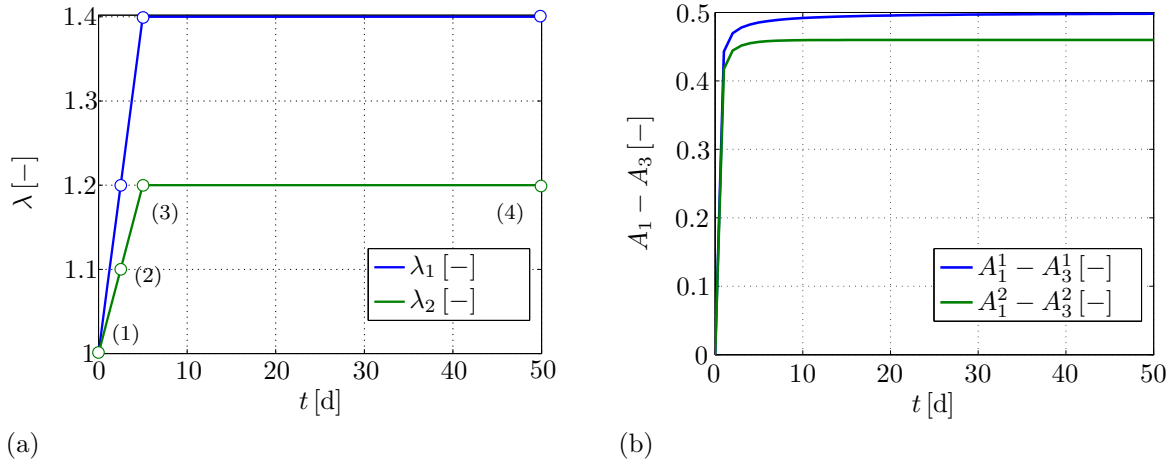


Figure 4.14: Isochoric biaxial tension: (a) Applied loading history in terms of λ_1 and λ_2 with (1)–(4) denoting representative points in time at $t = \{0.0, 2.5, 5.0, 50.0\}$ [d]. (b) Anisotropy-evolution $A_1 - A_3$.

chanical response does not depend on the loading history, as the principal values of $\bar{\mathbf{C}}$ and the particular loading level are not taken into account.

The deformation-induced anisotropy evolution is also depicted in Figure 4.15 for four different states of deformation at $t = \{0.0, 2.5, 5.0, 50.0\}$ [d]. Again, stereographic projections of the affine stretches $\bar{\lambda}$ are adopted in Figure 4.15(a), ODF-type visualisations for the structural tensors $\mathbf{A}^{1,2}$ are applied in Figure 4.15(b) and the integration directions themselves are plotted in Figure 4.15(c). It becomes apparent that the degree of anisotropy continuously evolves with time, and that the integration directions align according to the two limiting directions \mathbf{l}^1 and \mathbf{l}^2 .

The format of the limiting directions for this particular deformation can be computed analytically in terms of the loading parameters $\lambda_1 = [\lambda_1^{\bar{\mathbf{C}}}]^{1/2}$ and $\lambda_2 = [\lambda_2^{\bar{\mathbf{C}}}]^{1/2}$ as $\mathbf{l}^{1,2} = [\lambda_1 \mathbf{e}_2 \pm \lambda_2 \mathbf{e}_1] / \sqrt{\lambda_1^2 + \lambda_2^2}$ where the denominator is included for normalisation purposes. In order to emphasise the orthotropic remodelling behaviour, it is essential to provide a biaxial tensile deformation so that $\lambda_1^{\bar{\mathbf{C}}} > \lambda_2^{\bar{\mathbf{C}}} > 1$. For the present case of biaxial tension with $\lambda_1 > \lambda_2 > 1$, we observe that the limiting directions depend on the deformation level and, for $\lambda_1 = 1.4$ and $\lambda_2 = 1.2$, end up with an angle of $\angle(\mathbf{e}_1, \mathbf{l}^{1,2}) = \pm 49.3987$ [deg], which means that they are slightly more oriented with respect to the \mathbf{e}_2 -axis. *At this stage, we particularly note that an angle considerably deviating from ± 45.0 [deg] can be achieved only for rather high and simultaneously different principal stretch values*—an observation which turns out to be essential for the subsequent investigation of a double-layered residually stressed tube. For the special case of equibiaxial tension, i.e. $\lambda_1^{\bar{\mathbf{C}}} = \lambda_2^{\bar{\mathbf{C}}} > 1$, the angle is exactly $\angle(\mathbf{e}_{1,2}, \mathbf{l}^{1,2}) = \pm 45.0$ [deg].

Another consequence of the odd-numbered and non-uniform integration scheme can be observed from Figure 4.15(c), where, for $t = 50$ [d], the integration directions in \mathbf{l}^2 -direction are already fully aligned (lying on top of each other), whereas the integration

directions associated with the \boldsymbol{l}^1 -direction are still slightly dispersed. In other words, the alignment of the integration directions with respect to \boldsymbol{l}^2 evolves faster compared to their counterparts aligning with \boldsymbol{l}^1 . This can be explained by the lower anisotropy level $A_1^2 - A_3^2$ associated with \boldsymbol{l}^2 , which causes the pre-multiplying factor f^i , defined by equation (4.29), to take larger values, i.e. $f_2^i > f_1^i$. Consequently, the remodelling process evolves faster than for integration directions associated with limiting direction \boldsymbol{l}^2 . Using uniformly distributed integration schemes may significantly reduce this effect.

Furthermore, it becomes obvious that integration directions being orthogonal with respect to the limiting directions $\boldsymbol{l}^{1,2}$ do not reorient, whereas all other integration directions reorient until they finally coincide with the limiting directions $\boldsymbol{l}^{1,2}$. Once more it is worth mentioning that, with regard to practical applications including non-homogeneous deformations, such an idealised case will hardly occur.

4.5.3.2 Inflation of a thick-walled cylindrical tube

As a three-dimensional application example of the orthotropic remodelling formulation, the inflation of a perfectly cylindrical tube is considered next. Moreover, residual strains are taken into account. To be specific, first the influence of the remodelling formulation is studied in response to an internal pressure combined with an axial pre-stretch *without* circumferential residual strains. Thereafter, a technique to incorporate circumferential residual strains is discussed in detail. For validation purposes, we carry out a numerical reproduction of the well-known 'opening angle experiment'. After that we study the remodelling behaviour of the specimen under the influence of both axial *and* circumferential residual stress and strain effects, respectively.

An arterial ring can be approximated by a thick-walled two-layered cylindrical tube, cf. Chapter 2, Holzapfel et al. [135] or Alastrué et al. [10] amongst others. The geometry used in the following is represented by the referential inner radius $r_i = 1.35$ [mm], the wall-thicknesses $h^M = 0.54$ [mm], $h^A = 0.36$ [mm] and the length of the arterial slice $l = 0.10$ [mm]. The three-dimensional discrete boundary value problem consists of 800 Q1P0-type eight node hexahedral elements, see Figure 4.16(a). The values summarised in Table 4.16(b) are adopted for the set of material parameters. Different sets of elastic parameters are used for the media and adventitia by analogy with data identified for both layers in Alastrué et al. [9]. For the present application example, however, the media is assumed to be much stiffer than the adventitia which is a well-known observation from experiments on healthy arterial tissue.

With regard to the boundary conditions, Dirichlet boundary conditions are defined in terms of the cylindrical coordinate system, see Figure 4.16(a). In a first simulation step, all nodes are fixed in circumferential direction, while the back face of the tube is fixed in longitudinal direction. An axial pre-stretch of $\lambda_z = 1.02$, defined in terms of axial displacements applied at the front face of the tube is prescribed until static equilibrium is obtained. Afterwards—retaining these boundary conditions—an internal pressure p is applied linearly at first and then held constant at a mean physiological

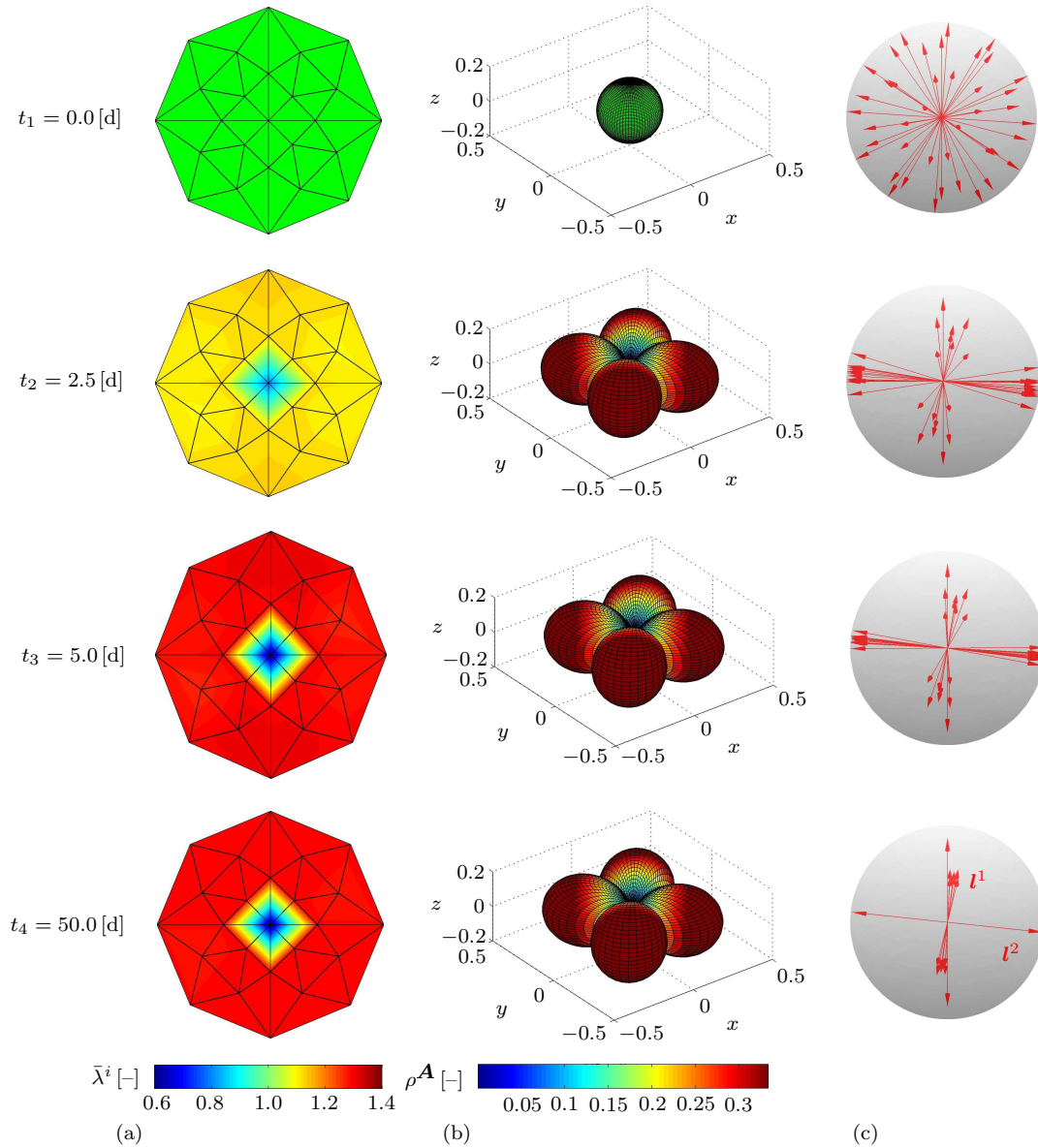


Figure 4.15: Isochoric biaxial tension. Illustration of the anisotropy evolution at four representative points in time $t = \{0.0, 2.5, 5.0, 50.0\}$ [d] for the loading history and material parameters in Figure 4.7. (a) Stereographic projection of the affine isochoric stretches $\bar{\lambda}^i$. (b) ODF-type function ρ^A . (c) Alignment of integration directions \mathbf{r}^i with respect to limiting directions $\mathbf{l}^{1,2}$.

pressure level of $p = 13.33$ [kPa], see Figure 4.16(c). The presence of the axial pre-stretch is motivated by the fact that residual strains in both axial and circumferential direction are commonly observed in arterial tissue. In this first case, however, we neglect the circumferential residual strains in order to exclusively focus on the evolution of anisotropy and the orientation of the limiting directions. In a second case though, we

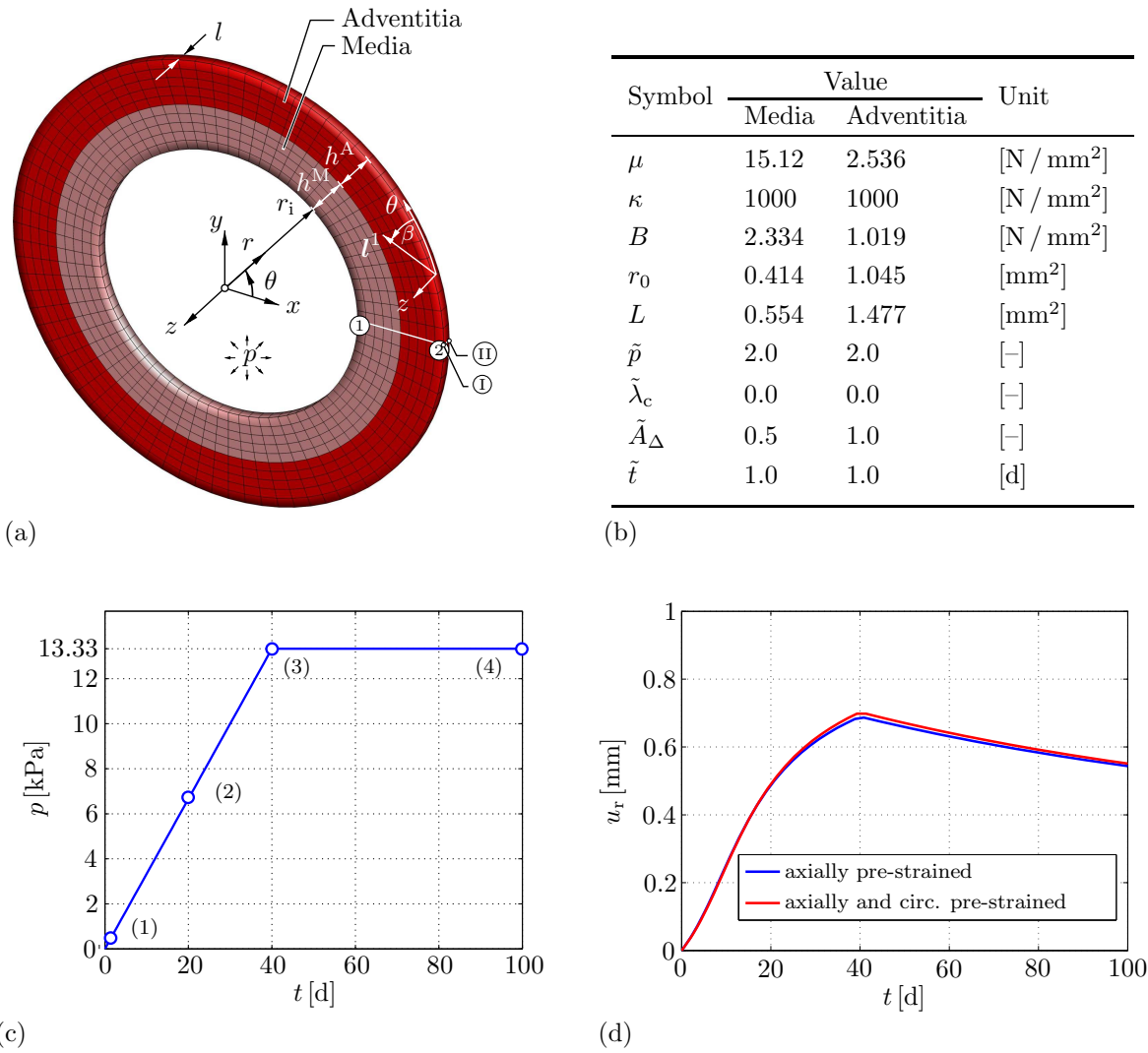


Figure 4.16: Inflation of a thick-walled artery-like tube. (a) Discretised geometry, boundary conditions and two representative Gauss-points ①–② for anisotropy-visualisation. (b) Material parameters. (c) Applied loading history in terms of the prescribed internal pressure p with (1)–(4) denoting representative points in time at $t = \{2, 20, 40, 100\}$ [d]. (d) Radial displacement u_r at the outer tube-diameter over time t for the pre-strained tube.

take the circumferential residual strains into account and compare the resulting pre-strained response to the initially unstrained response.

Remodelling with axial residual strains The radial displacement u_r , recorded at the outer radius of the tube at node ①, is plotted over time t and depicted in Figure 4.16(d). The maximal value of the radial displacement $u_{r, \max} = 0.687$ [mm] is obtained at $t_{\max} = 40.86$ [s]. Due to remodelling, a distinct stiffening behaviour referring to the outer diameter of the tube can be observed, as the radial displacement u_r tends

to decrease during fixed pressure. This effect is caused by the remodelling which drives the artery to adapt in response to the loading.

The circumferential Cauchy-stress $\sigma_{\theta\theta}$ associated with the axially pre-strained tube is depicted in Figure 4.17 at four representative time-steps $t = \{2, 20, 40, 100\}$ [d]. Starting from an initially axially pre-strained configuration at $t_1 = 2$ [d], we observe for the subsequent time-steps that the media carries the main load which is represented by the significantly higher circumferential Cauchy-stress than compared to the adventitia.

Furthermore, an ODF-type visualisation for the tensors $\mathbf{A}^{1,2}$ is applied at two Gauss-points—① related to the inner media and ② to the outer adventitia. It becomes apparent that the limiting directions lie in the tangential \mathbf{e}_θ - \mathbf{e}_z -plane of the considered cylindrical tube. This has also been observed from experiments for the related preferred fibre angle β as introduced in Figure 4.16(a). An essential observation is the alignment of the integration directions with respect to the limiting directions, thereby revealing the anisotropy evolution as the ODF increasingly deviates from its initially spherical distribution. Due to the higher value of $\tilde{A}_\Delta = 1.0$ assumed for the adventitia, the obtained adventitial anisotropy level turns out to be higher than the medial anisotropy level illustrated by the more pronounced shape and the associated contours of ODF ②. The included fibre angles of both families of fibres, however, seem to be approximately the same, regardless of the different material parameters in both layers. This effect shall be briefly discussed in the following.

Depending on the particular loading case, it becomes obvious that the sequence of the principal strain directions $\mathbf{n}_i^{\tilde{C}}$, $i = 1, 2, 3$ does not remain constant in the cylindrical specimen considered here. Assuming that the tube is only loaded by an internal pressure without any axial or circumferential pre-strain, the dominant principal strain directions $\mathbf{n}_1^{\tilde{C}}$ associated with the maximal principal strain value $\lambda_1^{\tilde{C}}$ are oriented in circumferential direction, i.e. $\mathbf{n}_1^{\tilde{C}} = \mathbf{e}_\theta$. For an elongated tube, the dominant principal strain directions are similarly oriented in axial direction, i.e. $\mathbf{n}_1^{\tilde{C}} = \mathbf{e}_z$. Here, we assume the tube to be axially pre-stretched and subsequently loaded by increasing internal pressure. Consequently, the dominant principal strain directions are first oriented in axial direction, i.e. $\mathbf{n}_1^{\tilde{C}} = \mathbf{e}_z$. When the pressure increases over a certain limit, the orientation of the dominant principal strain directions gradually changes—initiated at the inner radius of the media—to the circumferential direction, i.e. $\mathbf{n}_1^{\tilde{C}} = \mathbf{e}_\theta$. This process, of course, highly depends on the particular pre-stretch and the pressure value.

Assuming the principal strain values to be related as $\lambda_\theta > \lambda_z > 1$, the (deformation-dependent) limiting directions can be represented by $\mathbf{l}^{1,2} = [\sqrt{\lambda_\theta} \mathbf{e}_z \pm \sqrt{\lambda_z} \mathbf{e}_\theta] / \sqrt{\lambda_\theta + \lambda_z}$, the denominator included for normalisation purposes. The limiting directions lie in the tangential \mathbf{e}_θ - \mathbf{e}_z -plane of the considered cylindrical tube. This has also been observed from experiments for the preferred structural fibre angle β as introduced in Figure 4.16(a). However, as an important restriction for $\lambda_\theta > \lambda_z > 1$, the angle β , characterised here by the limiting direction \mathbf{l}^1 and the \mathbf{e}_θ -axis, a priori takes values within a range of 45 [deg] $< \beta < 90$ [deg]. On the other hand, for $\lambda_z > \lambda_\theta > 1$, the

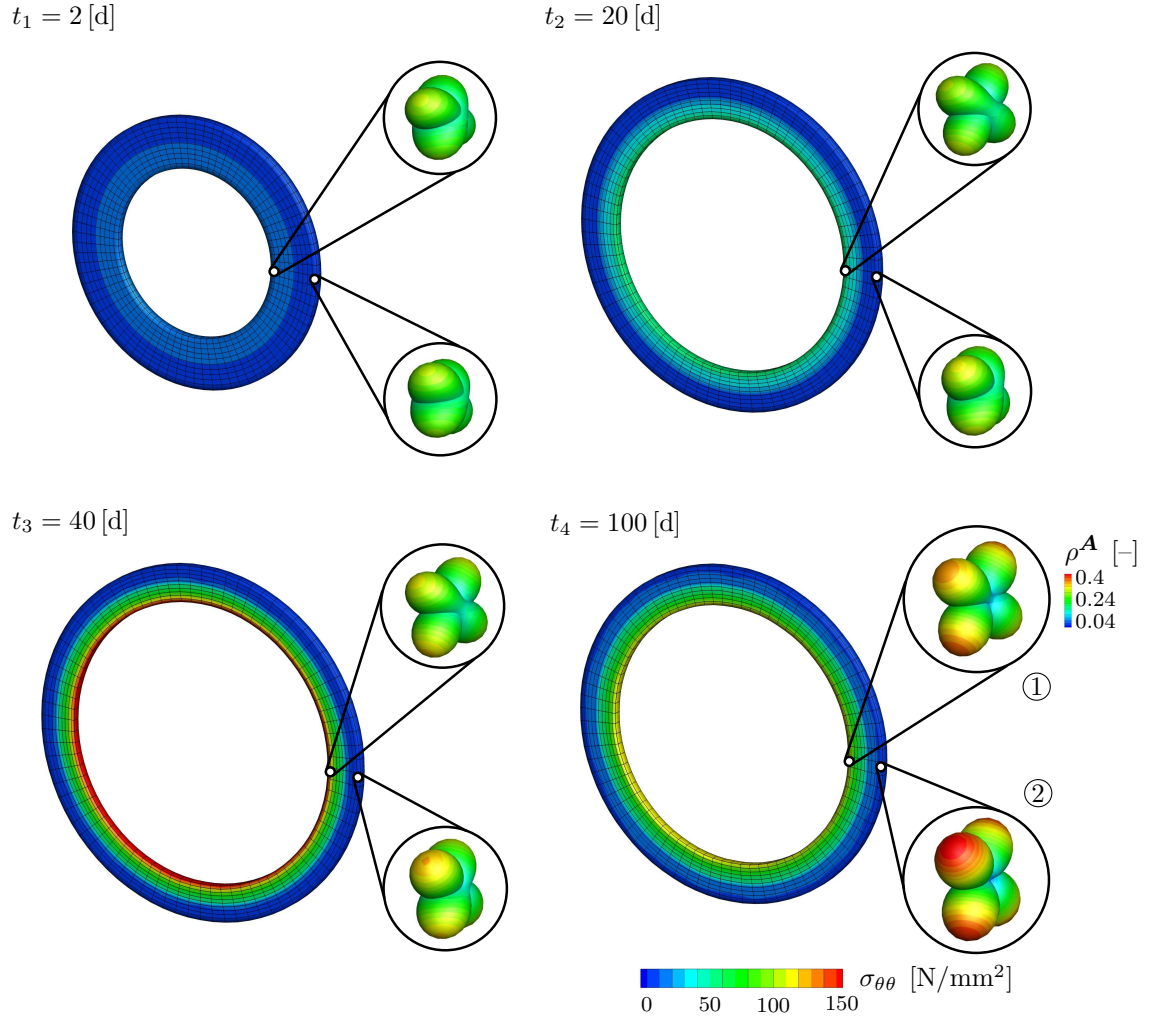


Figure 4.17: Inflation of an axially pre-strained thick-walled artery-like tube. Contour-plots of the circumferential Cauchy-stress $\sigma_{\theta\theta}$ for representative points in time at $t = \{0, 40, 70, 100\}$ [d] and ODF-type visualisation ρ^A at two different Gauss-points located in the media ① and adventitia ②.

angle β a priori takes values within a range of $0 [\text{deg}] < \beta < 45 [\text{deg}]$. The limiting case, $\lambda_z = \lambda_\theta$, results in an angle of $\beta = 45 [\text{deg}]$.

With regard to the experimentally obtained preferred fibre angles β^M and β^A , we typically observe a preferentially circumferential orientation $0 [\text{deg}] < \beta^M < 45 [\text{deg}]$ for the media and a preferentially axial orientation $45 [\text{deg}] < \beta^A < 90 [\text{deg}]$ for the adventitia, i.e. $\beta^M < \beta^A$. To meet these restrictions with regard to the present model, this implies that the principal strain values have to ensure $\lambda_z^M > \lambda_\theta^M$ for the media and $\lambda_\theta^A > \lambda_z^A$ for the adventitia.

While the condition for the adventitia can be met rather easily since $\lambda_\theta^A > \lambda_z^A$ for a mean physiological pressure level of $p = 13.33 [\text{kPa}]$, the condition for the media can

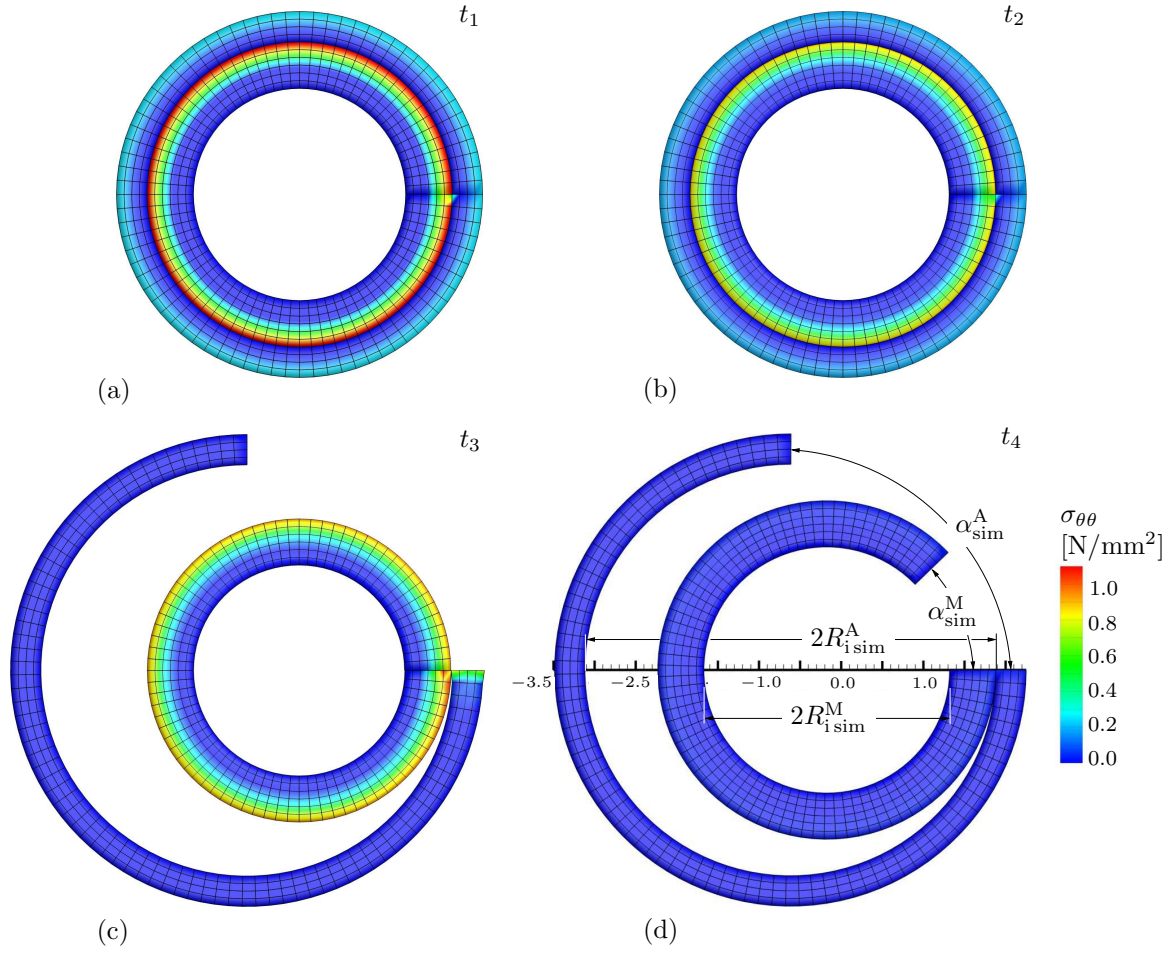


Figure 4.18: Reproduction of the opening angle experiment with prescribed values $R_i^M = 1.5$ [mm], $R_i^A = 2.5$ [mm], $\alpha^M = 45.0$ [deg], $\alpha^A = 90.0$ [deg]. Configuration at different steps of the simulation after (a) the application of the residual strain field, (b) the longitudinal cut, (c) the adventitial radial cut and (d) the medial radial cut.

be met only by increasing the axial residual strains directly and/or by decreasing the circumferential residual strains by significantly decreasing the opening angle α^M .

Another way of fulfilling the above-mentioned conditions is associated with the consideration of a wider pressure range. It is well-known that the blood pressure range can be viewed in between the diastolic blood pressure of $p \approx 8.0$ [kPa] and the systolic blood pressure of $p \approx 17.4$ [kPa], while $p = 13.33$ [kPa] represents an appropriate mean blood pressure. A lower (diastolic) pressure possibly results in $\lambda_z^M > \lambda_\theta^M$ such that 0 [deg] $< \beta^M < 45$ [deg] for the medial fibre angle which is in line with, e.g., Holzapfel et al. [135], who reported the medial response to be associated with lower pressures and fibres to be oriented almost circumferentially. For higher pressures of $p = 13.33$ [kPa] and beyond, we obtain $\lambda_\theta^M > \lambda_z^M$, which consequently results in a pronounced orientation of the fibre directions such that 45 [deg] $< \beta^M < 90$ [deg].

Opening angle experiment Residual circumferential stresses can be revealed by the *opening angle experiment*, where a short ring of an artery is cut in radial direction. The residual stresses through the artery cause the ring to spring open to form an open sector.

The procedure employed here to incorporate such effects is based on a multiplicative composition of the total deformation gradient, cf. Section 2.2.2 for details. To be specific, we consider a stress-free reference configuration \mathcal{B}_0 , a load-free residually stressed configuration \mathcal{B}_{res} and a current configuration \mathcal{B}_t . In this regard, we—on the one hand—introduce a deformation gradient-type tensor \mathbf{F}_{res} which transform line elements from the stress-free reference configuration \mathcal{B}_0 to the residually stressed configuration \mathcal{B}_{res} and—on the other hand—another deformation gradient-type tensor \mathbf{F}_p which transform line elements from the residually stressed configuration \mathcal{B}_{res} to the current configuration \mathcal{B}_t . The resulting deformation gradient tensor can then be written as

$$\mathbf{F} = \mathbf{F}_p \cdot \mathbf{F}_{\text{res}}. \quad (4.34)$$

The technique described above also allows for the inclusion of different opening angles for the different arterial layers within only one simulation, making it more efficient compared to, e.g., imposing residual stresses by means of a numerical inverse reproduction of the opening angle method. For this purpose, it is necessary to create an initial deformation gradient \mathbf{F}_{res} at each Gauss-point of a related finite-element mesh. This deformation gradient field has to be provided in terms of the underlying coordinate system used by the finite-element code which is typically described by a Cartesian basis. The procedure to calculate the initial residual strain field by means of the deformation gradient tensor \mathbf{F}_{res} is summarised in Table 4.5, where the inner radii of the closed and opened configuration r_i and R_i , the opening angle α as well as the longitudinal stretch λ_z have to be prescribed as given input parameters. Even though described for a single layered tube, this procedure can easily be extended in an analogous way to create residual strain fields for two or more layers.

In order to assess whether this method yields accurate results, we now carry out a numerical reproduction of the opening angle experiment. Since we prescribe the radius of the opened configuration and the opening angle as input parameters to create the residual strain field, we expect to reproduce these values at least approximately as well as a complete stress release at the end of the simulation. Basically the FE-simulation of the opening angle experiment is subdivided into a sequence of three calculation steps:

1. *Application of the residual strain field* at Gauss-point-level, see Table 4.5: apply homogeneous Dirichlet boundary conditions at all nodes in circumferential \mathbf{e}_θ - and longitudinal \mathbf{e}_z -direction
2. *Longitudinal cut*: apply homogeneous Dirichlet boundary conditions at all nodes in circumferential \mathbf{e}_θ -direction and at nodes of back face in longitudinal \mathbf{e}_z -direction
3. *Radial cut*: apply homogeneous Dirichlet boundary conditions at nodes ① and ② in radial \mathbf{e}_r -direction, see Figure 4.16(a), at nodes located at the cut in circumferential \mathbf{e}_θ -direction and at all nodes at back face in longitudinal \mathbf{e}_z -direction

Table 4.5: Procedure to calculate the initial residual strain field of a cylindrical FE-mesh by means of the deformation gradient tensor \mathbf{F}_{res} .

| |
|---|
| <ol style="list-style-type: none"> 1. given: prescribe inner radius of closed configuration r_i, inner radius of opened configuration R_i, opening angle α, longitudinal stretch λ_z 2. calculate opening angle parameter $k = 2\pi/[2\pi - \alpha]$ 3. determine physical Cartesian coordinates (x, y, z) of the Gauss-points for the closed configuration and convert these into cylindrical coordinates (r, θ, z) 4. calculate Cartesian base vectors for the closed configuration <ul style="list-style-type: none"> $\mathbf{e}_x = \cos(\theta) \mathbf{e}_r + \sin(\theta) \mathbf{e}_\theta$ $\mathbf{e}_y = -\sin(\theta) \mathbf{e}_r + \cos(\theta) \mathbf{e}_\theta$ $\mathbf{e}_z = \mathbf{e}_x \times \mathbf{e}_y$ 5. calculate cylindrical coordinates (R, Θ, Z) for the opened configuration <ul style="list-style-type: none"> $R = \sqrt{k \lambda_z [r^2 - r_i^2] + R_i^2}$ $\Theta = \theta/k$ $Z = z/\lambda_z$ 6. calculate Cartesian base vectors for the opened configuration <ul style="list-style-type: none"> $\mathbf{E}_X = \cos(\Theta) \mathbf{E}_R + \sin(\Theta) \mathbf{E}_\Theta$ $\mathbf{E}_Y = -\sin(\Theta) \mathbf{E}_R + \cos(\Theta) \mathbf{E}_\Theta$ $\mathbf{E}_Z = \mathbf{E}_X \times \mathbf{E}_Y$ 7. calculate radial and circumferential stretches <ul style="list-style-type: none"> $\lambda_r = R/[r k \lambda_z]$ $\lambda_\theta = r k/R$ 8. calculate initial deformation gradient at each Gauss-point in Cartesian coordinates <ul style="list-style-type: none"> $\mathbf{F}_{\text{res}} = \lambda_r \mathbf{e}_x \otimes \mathbf{E}_X + \lambda_\theta \mathbf{e}_y \otimes \mathbf{E}_Y + \lambda_z \mathbf{e}_z \otimes \mathbf{E}_Z$ |
|---|

In this regard, all boundary conditions are removed from one step to another and re-specified for those boundary conditions that are to be retained. If a boundary condition is removed, it will be replaced by a concentrated force equal to the reaction force calculated at the restrained degree of freedom at the end of the previous step. This concentrated force will then be linearly reduced to zero over the period of the step. In this case, both layers are separated from each other in order to give an illustrative view of the effect of different prescribed opening angles and radii which, for the purpose of illustration, are set to values of $R_i^M = 1.5$ [mm], $R_i^A = 2.5$ [mm], $\alpha^M = 45.0$ [deg], $\alpha^A = 90.0$ [deg]. As a consequence of the initial imposition of the residual strain field, we

obtain a stretching and warping of the cross-section of the tube. As both layers are separated from each other, this consequently results in an undesired penetration. In order to avoid this, a contact condition is prescribed between outer media and inner adventitia in the first simulation step. Figure 4.18 illustrates the configurations at different steps of the simulation associated with the opening angle experiment. It becomes apparent that the technique described above is able to appropriately reproduce the prescribed input parameters, so that $R_{i\text{sim}}^M \approx R_i^M$, $R_{i\text{sim}}^A \approx R_i^A$, $\alpha_{\text{sim}}^M \approx \alpha^M$ and $\alpha_{\text{sim}}^A \approx \alpha^A$ and $\sigma_{\theta\theta} \approx 0$.

Remodelling with axial and circumferential residual strains After having assessed the applicability of the technique for the residual-strain-incorporation, we now perform a similar simulation as for the previous merely axially pre-strained case described in Section 4.5.3.2. In contrast, however, we apply a circumferential strain field which is represented by the parameters $R_i^M = 2.135$ [mm], $R_i^A = 3.65$ [mm], $\alpha^M = 120.0$ [deg], $\alpha^A = 160.0$ [deg]. The mechanical response due to the applied pressure-ramp, see Figure 4.16(c), is plotted in terms of the radial displacement u_r at the outer radius of the tube over time t and depicted in Figure 4.16(d). As in the previous case, a pronounced remodelling-induced stiffening behaviour can be observed which tends to decrease the radial displacement u_r at constant pressure. Similar to the previous circumferentially unstrained case, the maximal value of the radial displacement, obtained at $t_{\text{max}} = 39.32$ [s], only slightly increases to $u_{r\text{max}} = 0.698$ [mm].

The circumferential Cauchy-stress $\sigma_{\theta\theta}$ associated with the axially and circumferentially pre-strained tube is depicted in Figure 4.19 for four representative time-steps $t = \{2, 20, 40, 100\}$ [d]. It becomes apparent that the media still carries the main load which is represented by the significantly higher circumferential Cauchy-stress than compared to the adventitia. In contrast to the circumferentially unstrained tube considered above, however, we observe that the stress particularly at the inner radius of the tube at $t = 40$ [d] is significantly reduced. This is a typical advantageous consequence of the presence of circumferential residual strains.

Again, an ODF-type visualisation for the tensors $\mathbf{A}^{1,2}$ is applied at two Gauss-points—① related to the media and ② to the adventitia—where we observe the alignment of the integration directions with respect to the limiting directions. The included fibre angles of both families of fibres, however, still seem to be approximately the same. An obvious reason is due to the rather similar magnitude of the axial and circumferential stretches. For the particular deformation considered—even though $\lambda_z > \lambda_\theta$ —it turns out that the axial stretches λ_z are only *slightly* higher than the circumferential stretches λ_θ . This disables a pronounced circumferential orientation of the limiting directions in the media and results in an orientation close to $\beta^M \approx 45$ [deg]. As a remedy, one could either reduce (increase) the opening angle in the media (adventitia) even more, or one could apply a non-uniform axial stretch λ_z to be increased (reduced) in the media (adventitia).

To discuss the influence of the residual strains with regard to the limiting directions, we study a rather extreme example of an axially *and* circumferentially pre-stressed tube where the following parameters $R_i^M = 2.135$ [mm], $R_i^A = 3.25$ [mm], $\alpha^M = 60.0$ [deg],

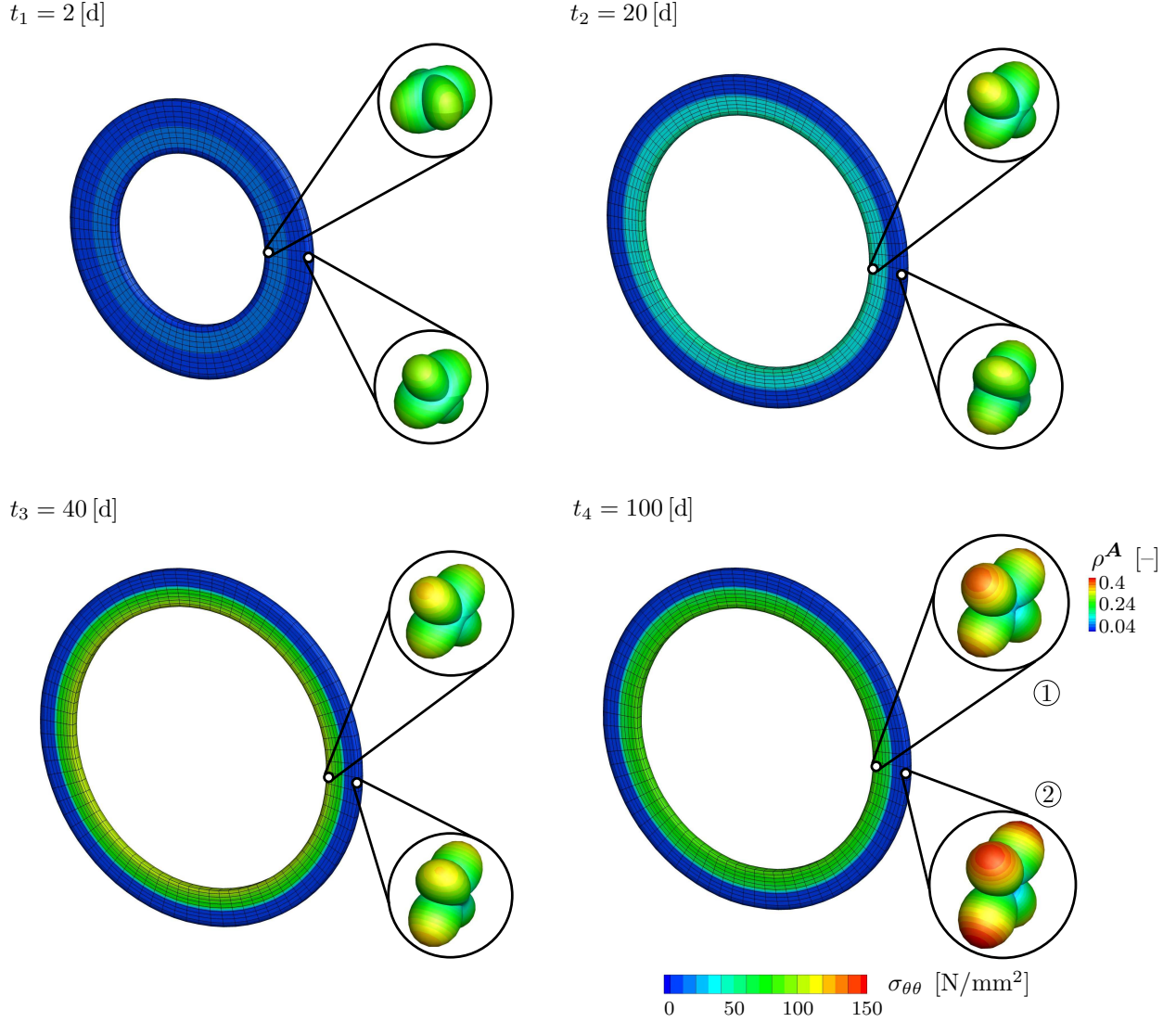


Figure 4.19: Inflation of an axially and circumferentially pre-stressed thick-walled artery-like tube. Contour-plots of the circumferential Cauchy-stress $\sigma_{\theta\theta}$ for representative points in time at $t = \{2, 20, 40, 100\}$ [d] and ODF-type visualisation ρ^A at two different Gauss-points located in the media ① and adventitia ②.

$\alpha^A = 180.0$ [deg] and $\lambda_z = 1.002$ are applied followed by a subsequent, increasingly applied internal pressure. The re-orientation process of the dominant principal strain directions in particular depends on the circumferential pre-stretch. As an example to obtain axially oriented dominant principal strain directions in the media, i.e. $\mathbf{n}_1^{\bar{C}} = \mathbf{e}_z$, it must hold that $\lambda_1^{\bar{C}} = \lambda_z > \lambda_2^{\bar{C}} = \lambda_\theta$. Assuming a constant axial stretch λ_z , this can be ensured by reducing the opening angle α^M of the media. The limiting directions for the media consequently read $\mathbf{l}^{1,2} = \lambda_z \mathbf{e}_\theta \pm \lambda_\theta \mathbf{e}_z$. Taking into account that $\lambda_z > \lambda_\theta$, we conclude that the limiting directions are oriented preferentially towards the

circumferential e_θ -axis. Inverse arguments can be formulated to obtain a preferentially axial orientation of the limiting directions in the adventitia. Basically, this is in line with regard to experimentally obtained preferred fibre angles β^M and β^A where we observe a typical circumferential orientation $0 [\text{deg}] < \beta^M < 45 [\text{deg}]$ for the media and a preferentially axial orientation $45 [\text{deg}] < \beta^A < 90 [\text{deg}]$ for the adventitia. However, even for this rather extreme case, it turns out that the axial stretches λ_z are only *slightly* higher than the circumferential stretches λ_θ . This disables a pronounced circumferential orientation of the limiting directions in the media and rather results in an orientation close to $\beta^M \approx 45 [\text{deg}]$.

At this stage, the simulation results are therefore of mainly qualitative significance, as the calculation of precise quantitative results requires further information on the experimental data such as, for example, integral load-displacement curves and local measurements of fibre distributions. Moreover, it seems attractive to identify further directions of alignment, e.g. based on the methods established in Chapter 2.

5 A microsphere model for the simulation of growth effects

This chapter presents an energy-driven anisotropic microstructural growth formulation for hard biological tissues. The formulation and results presented are based on the ideas outlined in the recent work by Waffenschmidt et al. [283] and Waffenschmidt and Menzel [281]. Similar to Chapter 4, the constitutive model proposed in the following is based on the microsphere concept which allows a straightforward extension of one-dimensional constitutive models to an anisotropic three-dimensional formulation. By creating an anisotropic representation through the integration of one-dimensional constitutive equations over the unit sphere, cf. Bažant and Oh [32], the microsphere approach is extremely versatile and flexible to incorporate inelasticity at small or large strains as, for instance, applied to collagenous tissues in Chapter 4.

In the present chapter, we model growth effects in bone within the framework of open system thermodynamics, as discussed by Kuhl and Steinmann [171]. In this regard, we apply an enhanced balance of mass which models bone adaptation by its density evolution driven by the local strain energy level. We adopt the well-established model by Harrigan and Hamilton [119] and extend this formulation to energy-driven evolution of directional densities which—from the algorithmic point of view—take the interpretation as internal variables. These directional densities are referred to the integration direction of the microsphere and, as an advantage of the model at hand, enable the computation and visualisation of higher-order tensorial density moments which provide detailed insights into the simulated deformation-induced anisotropic local material properties.

The current chapter is organised as follows: In Section 5.1, we briefly summarise relevant kinematic, kinetic and balance relations for bone growth within open system thermodynamics. Next, in Section 5.2, we discuss the model problem of one-dimensional energy-driven density growth in terms of its constitutive equations, its implementation and an illustrative example. In Section 5.3, we generalise the one-dimensional formulation to a three-dimensional setting using the microsphere concept and study a homogeneous model problem. In Section 5.4, we embed the three-dimensional equations for anisotropic energy-driven density growth into a finite element framework to explore the isotropic density distribution and the anisotropic microstructure in the proximal

tibia. Lastly, in Section 5.5, we investigate four three-dimensional optimisation-related benchmark problems with regard to its structure-improving properties.

5.1 Basic micro-kinematics and balance equations

In view of the material model discussed in the following, we introduce the stretch in the direction of the unit-vector \mathbf{r} , i.e.

$$\bar{\lambda} = \sqrt{\mathbf{r} \cdot \mathbf{C} \cdot \mathbf{r}}. \quad (5.1)$$

Even though bone tissue commonly experiences small strains within the physiological deformation range, we apply a finite strain formulation for the sake of generality. As a special case of large strain, the small strain framework is included. The large strain formulation, however, proves to be natural to include different responses in tension and compression, see also Figure 5.1. Computationally, a large strain formulation comes at almost no extra cost, since the overall set of equations is nonlinear anyway.

Throughout this chapter, we consider growth phenomena that are exclusively related to changes in referential density $\rho_0 = J \rho_t$, which can be described by means of the mass balance equation

$$\dot{\rho}_0 = \nabla_{\mathbf{X}} \cdot \mathbf{R} + R_0, \quad (5.2)$$

with $(\dot{\bullet}) = \partial_t(\bullet)|_{\mathbf{X}}$ denoting the material time derivative. The mass flux \mathbf{R} is assumed to vanish, i.e. $\nabla_{\mathbf{X}} \cdot \mathbf{R} = 0$, such that the mass source R_0 coincides with the rate of referential density $\dot{\rho}_0 = R_0$. For the sake of conceptual simplicity, we do not consider a dead-zone as proposed by, for instance, Weinans et al. [290].

5.2 One-dimensional growth

This section reviews basic aspects of the constitutive relations of density growth, where we restrict ourselves to a one-dimensional setting. The one-dimensional theoretical and computational framework provides the basic model for the anisotropic microsphere-based growth model proposed in Section 5.3. We discuss key aspects of the numerical implementation and investigate specific properties of the underlying constitutive model. We refer to Kuhl and Steinmann [172] and Menzel [197] for details with regard to the underlying constitutive theory, whereas in Jacobs et al. [148], Kuhl et al. [166] and Kuhl and Steinmann [171] additional background information on algorithmic aspects is elaborated further.

5.2.1 Constitutive equations

Following Harrigan and Hamilton [118], we adopt a constitutive relation for the mass source,

$$R_0 := k_\rho^* \left[\left[\frac{\rho_0}{\rho_0^*} \right]^{-m^*} \psi_0 - \psi_0^* \right], \quad (5.3)$$

which, combined with the definition of the mass source $\dot{\rho}_0 = R_0$, yields the evolution of the density as

$$\dot{\rho}_0 = k_\rho^* \left[\left[\frac{\rho_0}{\rho_0^*} \right]^{-m^*} \psi_0 - \psi_0^* \right]. \quad (5.4)$$

Herein, ψ_0 denotes a relative density-scaled strain energy per unit volume, ρ_0^* is the initial density and $\psi_0^* = \text{const}$ takes the representation of an energy-type saturation value for the density evolution. Finally, k_ρ^* characterises the rate of density evolution and m^* is an algorithmic exponent ensuring the stability of the algorithm, see Harrigan and Hamilton [117]. Table 5.1 summarises the essential quantities together with their units, wherein quantities associated with superscript $(\bullet)^*$ denote material parameters.

Using these considerations, we express the strain energy per unit volume ψ_0 as

$$\psi_0 = \left[\frac{\rho_0}{\rho_0^*} \right]^{n^*} \psi_0^e(\bar{\lambda}), \quad (5.5)$$

wherein ψ_0^e is a hyperelastic strain energy function in one-dimensional form and n^* denotes a dimensionless porosity exponent depending on the particular open-pored ground substance, see Harrigan and Hamilton [117]. The Piola-Kirchhoff stress takes the representation

$$S = 2 \frac{\partial \psi_0}{\partial \bar{\lambda}^2} = \left[\frac{\rho_0}{\rho_0^*} \right]^{n^*} S^e \quad \text{with} \quad S^e = \frac{1}{\bar{\lambda}} \frac{\partial \psi_0^e}{\partial \bar{\lambda}}. \quad (5.6)$$

The strain energy ψ_0 as well as the stress S are determined by the density-independent quantities ψ_0^e and $S^e = 2 \partial \psi_0^e / \partial \bar{\lambda}^2$, respectively, and are weighted by a relative density power, $[\rho_0 / \rho_0^*]^{n^*}$, where $m^* > n^*$ in order to ensure numerical stability or rather density saturation, see Harrigan and Hamilton [116].

5.2.2 Implementation

The evolution equation (5.4) represents a nonlinear ordinary differential equation, which, in connection with equation (5.5), reads

$$\dot{\rho}_0 = k_\rho^* \left[\left[\frac{\rho_0}{\rho_0^*} \right]^{n^*-m^*} \psi_0^e - \psi_0^* \right]. \quad (5.7)$$

Table 5.1: Quantities included in constitutive relations (5.3) and (5.4).

| Symbol | Description | Unit |
|------------|-------------------------------------|-------------------------------------|
| R_0 | mass source | $[\text{kg} / \text{m}^3 \text{s}]$ |
| ρ_0 | density | $[\text{kg} / \text{m}^3]$ |
| ρ_0^* | initial density | $[\text{kg} / \text{m}^3]$ |
| ψ_0 | strain energy | $[\text{J} / \text{m}^3]$ |
| ψ_0^* | saturation value | $[\text{J} / \text{m}^3]$ |
| k_ρ^* | density evolution (growth) velocity | $[\text{d} / \text{m}^2]$ |
| n^* | porosity exponent | $[-]$ |
| m^* | algorithmic exponent | $[-]$ |

We apply a numerical integration scheme in order to obtain the density at a current time step. Consequently, we introduce respective intervals in time, $\Delta t = t_{n+1} - t_n \geq 0$, and apply an implicit Euler backward integration scheme,

$$\rho_0 = \rho_{0n} + \Delta t \dot{\rho}_0 \quad \text{with} \quad \rho_0|_{t_0} = \rho_0^*. \quad (5.8)$$

Here and in the following, we omit the subscript index $n + 1$ associated with time t_{n+1} for the sake of readability. The related residual form then reads

$$r_\rho(\rho_0) = \rho_0 - \rho_{0n} - \Delta t \dot{\rho}_0 = 0. \quad (5.9)$$

To solve this non-linear equation we suggest a Newton iteration scheme. We expand equation (5.9) in a Taylor series at ρ_0^k with k denoting the particular Newton iteration step. Neglecting terms of second and higher order, we obtain

$$r_\rho(\rho_0^k) + \left. \frac{\partial r_\rho(\rho_0)}{\partial \rho_0} \right|_{\rho_0^k} [\rho_0 - \rho_0^k] = 0 \quad (5.10)$$

and introduce the increment of the referential density as

$$\Delta \rho_0 = \rho_0^{k+1} - \rho_0^k = - \left[\left. \frac{\partial r_\rho(\rho_0)}{\partial \rho_0} \right|_{\rho_0^k} \right]^{-1} r_\rho(\rho_0^k). \quad (5.11)$$

The remaining task is to now derive the partial derivative of the residual $r_\rho(\rho_0)$ with respect to the density at the current time step ρ_0 , which yields

$$\left. \frac{\partial r_\rho(\rho_0)}{\partial \rho_0} \right|_{\rho_0^k} = 1 - \Delta t \frac{\partial \dot{\rho}_0^k}{\partial \rho_0^k}. \quad (5.12)$$

The derivative of the density evolution with respect to the density itself follows from equation (5.7),

$$\frac{\partial \dot{\rho}_0^k}{\partial \rho_0^k} = [n^* - m^*] \frac{k_\rho^*}{\rho_0^k} \left[\frac{\rho_0^k}{\rho_0^*} \right]^{n^* - m^*} \psi_0^e. \quad (5.13)$$

Table 5.2: Constitutive box for the one-dimensional density-evolution-based growth model. Quantities without subscript n are assumed to be associated with t_{n+1} .

| |
|--|
| <p>0. given deformation in terms of the stretch $\bar{\lambda}$ at time t_{n+1} and history data ρ_{0n} of internal density variables at time t_n</p> <p>1. compute density-independent elastic strain energy $\psi_0^e(\bar{\lambda})$</p> <p>2. perform local Newton iteration</p> <p>(a) compute density residual</p> $r_\rho = \rho_0 - \rho_{0n} - \Delta t k_\rho^* \left[\left[\frac{\rho_0}{\rho_0^*} \right]^{n^* - m^*} \psi_0^e - \psi_0^* \right]$ <p>(b) compute linearisation of residual</p> $\frac{\partial \dot{\rho}_0}{\partial \rho_0} = [n^* - m^*] \frac{k_\rho^*}{\rho_0} \left[\frac{\rho_0}{\rho_0^*} \right]^{n^* - m^*} \psi_0^e$ <p>(c) compute density update</p> $\rho_0 \leftarrow \rho_0 + \left[\Delta t \frac{\partial \dot{\rho}_0}{\partial \rho_0} + 1 \right]^{-1} r_\rho$ <p>(d) check tolerance if $r_\rho < \text{tol}$ go to 3. else go to 2. (a)</p> <p>3. compute density weighted Piola-Kirchhoff stress and tangent operator (one-dimensional case: \mathbb{E} necessary only in case of a stress-driven algorithm)</p> $S = \frac{1}{\bar{\lambda}} \left[\frac{\rho_0}{\rho_0^*} \right]^{n^*} \frac{\partial \psi_0^e}{\partial \bar{\lambda}}$ $\mathbb{E} = \frac{1}{\bar{\lambda}^2} \left[\frac{\rho_0}{\rho_0^*} \right]^{n^*} [\bar{\mathbb{E}}_\lambda + \bar{\mathbb{E}}_{\rho_0}]$ <p>with</p> $\bar{\mathbb{E}}_\lambda = \frac{\partial^2 \psi_0^e}{\partial \lambda \partial \lambda} - \frac{1}{\bar{\lambda}} \frac{\partial \psi_0^e}{\partial \lambda}$ $\bar{\mathbb{E}}_{\rho_0} = \frac{\Delta t n^* k_\rho^*}{\rho_0^*} \left[1 - \Delta t \frac{\partial \dot{\rho}_0}{\partial \rho_0} \right]^{-1} \left[\frac{\rho_0}{\rho_0^*} \right]^{n^* - m^*} \left[\frac{\partial \psi_0^e}{\partial \lambda} \right]^2$ |
|--|

We end up with the algorithmic update of the density

$$\rho_0^{k+1} = \rho_0^k + \Delta \rho_0, \quad (5.14)$$

which must be evaluated iteratively as long as the norm of the residual is larger than a pre-defined tolerance.

In case of a one-dimensional force- or rather stress-driven tension/compression test, which is typically accompanied by an iterative procedure in order to calculate the equilibrium configuration, we determine the algorithmic tangent operator,

$$\mathbf{E} = 2 \frac{dS}{d\bar{\lambda}^2} = \mathbf{E}_{\bar{\lambda}} + \mathbf{E}_{\rho_0}, \quad (5.15)$$

By means of the chain rule, we identify the two contributions as

$$\mathbf{E}_{\bar{\lambda}} = 2 \frac{\partial S}{\partial \bar{\lambda}} \frac{\partial \bar{\lambda}}{\partial \bar{\lambda}^2} \quad \text{and} \quad \mathbf{E}_{\rho_0} = 2 \frac{\partial S}{\partial \rho_0} \frac{\partial \rho_0}{\partial \bar{\lambda}^2}, \quad (5.16)$$

wherein the first term represents the elastic moduli and the second term reflects the dependence of the density evolution equation (5.4) on the deformation via the strain energy function ψ_0 .

The first contribution $\mathbf{E}_{\bar{\lambda}}$ can be determined straightforwardly as the elastic tangent modulus $\mathbf{E}^e = 2 \partial S^e / \partial \bar{\lambda}^2$ weighted by the relative density power, $[\rho_0 / \rho_0^*]^{n^*}$, i.e.

$$\mathbf{E}_{\bar{\lambda}} = \left[\frac{\rho_0}{\rho_0^*} \right]^{n^*} \mathbf{E}^e \quad \text{with} \quad \mathbf{E}^e = \frac{1}{\bar{\lambda}^2} \left[\frac{\partial^2 \psi_0^e}{\partial \bar{\lambda} \partial \bar{\lambda}} - \frac{1}{\bar{\lambda}} \frac{\partial \psi_0^e}{\partial \bar{\lambda}} \right]. \quad (5.17)$$

The density-related contribution \mathbf{E}_{ρ_0} can directly be obtained by the partial derivative of S with respect to ρ_0 as

$$\frac{\partial S}{\partial \rho_0} = \frac{n^*}{\rho_0} \left[\frac{\rho_0}{\rho_0^*} \right]^{n^*} S^e. \quad (5.18)$$

We can compute the second term by means of the derivative of equation (5.9) with respect to $\bar{\lambda}^2$ and solving for $\partial \rho_0 / \partial \bar{\lambda}^2$ which results in

$$\frac{\partial \rho_0}{\partial \bar{\lambda}^2} = \Delta t \left[1 - \Delta t \frac{\partial \dot{\rho}_0}{\partial \rho_0} \right]^{-1} \frac{\partial \dot{\rho}_0}{\partial \bar{\lambda}^2} \quad (5.19)$$

with

$$\frac{\partial \dot{\rho}_0}{\partial \bar{\lambda}^2} = \frac{k_\rho^*}{2} \left[\frac{\rho_0}{\rho_0^*} \right]^{n^*-m^*} S^e. \quad (5.20)$$

In summary, the density-related contribution \mathbf{E}_{ρ_0} of the algorithmic tangent operator takes the representation

$$\mathbf{E}_{\rho_0} = \frac{1}{\bar{\lambda}^2} \left[\frac{\rho_0}{\rho_0^*} \right]^{n^*} \left[\frac{\Delta t n^* k_\rho^*}{\rho_0^*} \left[1 - \Delta t \frac{\partial \dot{\rho}_0}{\partial \rho_0} \right]^{-1} \left[\frac{\rho_0}{\rho_0^*} \right]^{n^*-m^*} \left[\frac{\partial \psi_0^e}{\partial \bar{\lambda}} \right]^2 \right]. \quad (5.21)$$

The algorithm related to the constitutive model is summarised in Table 5.2.

Table 5.3: Set of material parameters used for the calculations, as calibrated by Pang et al. [232].

| Symbol | Description | Value | Unit |
|-------------|-------------------------------------|--------|------------------------|
| λ^* | elastic constant | 2186.0 | [N / mm ²] |
| μ^* | elastic constant | 1458.0 | [N / mm ²] |
| ρ_0^* | initial density | 1.0 | [g / cm ³] |
| ψ_0^* | saturation value | 0.0275 | [N / mm ²] |
| k_ρ^* | density evolution (growth) velocity | 0.4 | [d / cm ²] |
| n^* | porosity exponent | 2.0 | [-] |
| m^* | algorithmic exponent | 3.0 | [-] |

5.2.3 Numerical example

To complete the constitutive model, we specify the particular type of the strain energy and assume a compressible neo-Hookean format,

$$\psi_0^e(\bar{\lambda}) = \frac{\lambda^*}{2} \ln^2(\bar{\lambda}) + \frac{\mu^*}{2} [\bar{\lambda}^2 - 1 - 2 \ln(\bar{\lambda})]. \quad (5.22)$$

Based on this, we evaluate the derivatives of the free energy ψ_0^e with respect to the stretch $\bar{\lambda}$ as

$$\frac{\partial \psi_0^e}{\partial \bar{\lambda}} = \frac{1}{\bar{\lambda}} [\lambda^* \ln(\bar{\lambda}) + \mu^* [\bar{\lambda}^2 - 1]] \quad (5.23)$$

and

$$\frac{\partial^2 \psi_0^e}{\partial \bar{\lambda} \partial \bar{\lambda}} = \frac{1}{\bar{\lambda}} \left[\frac{\lambda^*}{\bar{\lambda}} + 2\mu^* \bar{\lambda} - \frac{\partial \psi_0^e}{\partial \bar{\lambda}} \right]. \quad (5.24)$$

In view of the material parameters, we adopt the values calibrated by Pang et al. [232] for the tibia, as summarised in Table 5.3 and set the time step size to $\Delta t = 1.0$ [d]. The tolerance for the local Newton-scheme is $\text{tol} = 10^{-8}$.

To discuss the constitutive behaviour characteristic for density evolution, we consider a one-dimensional homogeneous tension-compression test. External loading is applied stepwise in terms of the axial force F and a stress-driven formulation is chosen as shown in Figure 5.1(a). We preferably adopt realistic force magnitudes up to [800 N] corresponding to the deformation levels obtained in Section 5.4 later on where we elaborate finite-element-based simulations of a tibia.

Figures 5.1(b–d) show the temporal evolution of strain $\bar{\lambda} - 1$, density ρ_0 and relative density $\bar{\rho}_0 = [\rho_0 - \rho_0^*] / \rho_0^*$. Due to the stepwise application of constant forces and with regard to the resulting strain in Figure 5.1(b), we observe a distinct creep-type behaviour, whereas in Figures 5.1(c, d) the (relative) density saturates in a time-dependent or rather viscous manner towards the so-called biological equilibrium state. The biological

equilibrium state depends on the particular loading conditions and can be understood as the state where the deformations and the density remain constant for a given load, i.e. $\dot{\rho}_0 = 0$ and $\dot{\lambda} = 0$. For the chosen loading conditions, in connection with the chosen material parameters, the density increases monotonically with time from one loading level to the next higher loading level. In general, the density may also decrease at lower loading levels as shown in Figure 5.2(b). We observe that the model naturally captures a different material response under tension and compression—the density evolution calculated for tension and compression does not quite coincide. This effect is caused by the typical tension-compression-asymmetry of the neo-Hookean free energy function which becomes more pronounced with increasing levels of deformation. In order to further emphasise this asymmetry, we could incorporate additional modifications of the strain energy function, e.g. by means of strain-related sign-type contributions, which, however, are not considered here.

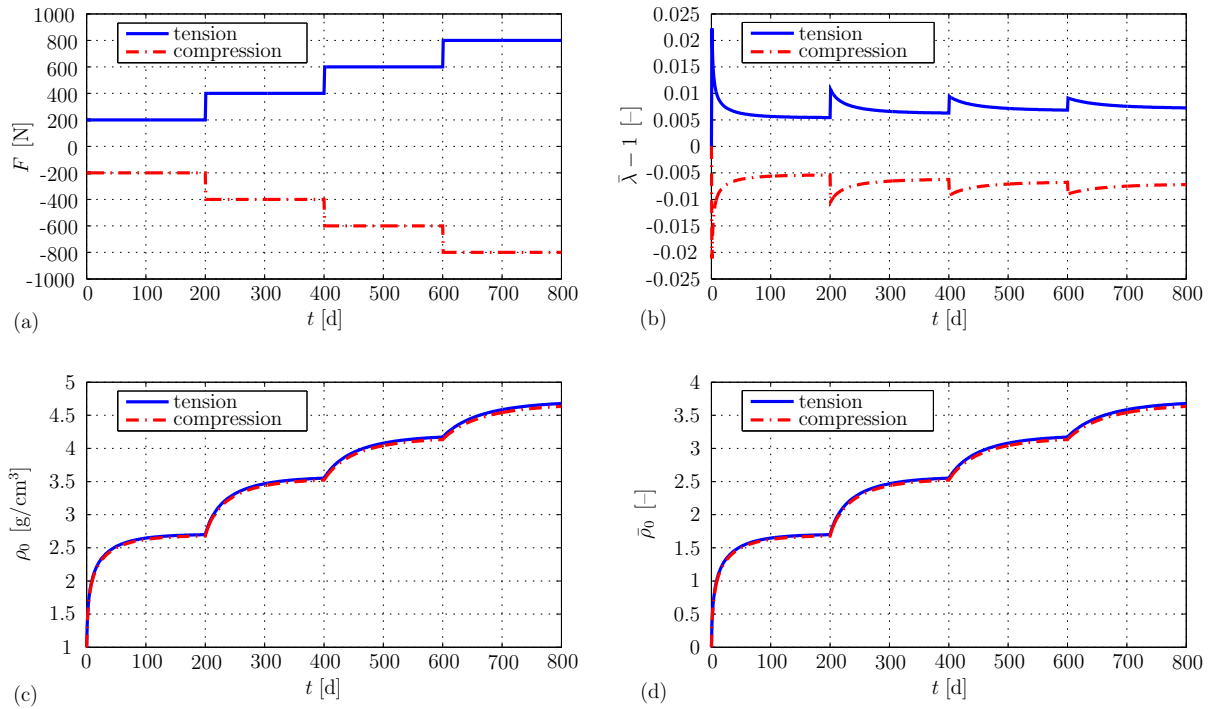


Figure 5.1: Response of the one-dimensional density growth model. (a) Stepwise constant tensile and compressive loading in terms of the axial force F . (b–d) Evolution of strain $\lambda - 1$, density ρ_0 and relative density $\bar{\rho}_0 = [\rho_0 - \rho_0^*]/\rho_0^*$ with respect to time for the material parameters given in Table 5.3.

Furthermore, we investigate the sensitivity of the constitutive response with respect to the material parameters, see Figure 5.2. In order to additionally include resorption effects, we use the loading history displayed in Figure 5.1(a) but reduce the magnitude of the force to $F/10$.

Figure 5.2(a) shows the influence of the initial density ρ_0^* . Even though not directly obvious from evolution equation (5.4), the initial density governs the rate of density

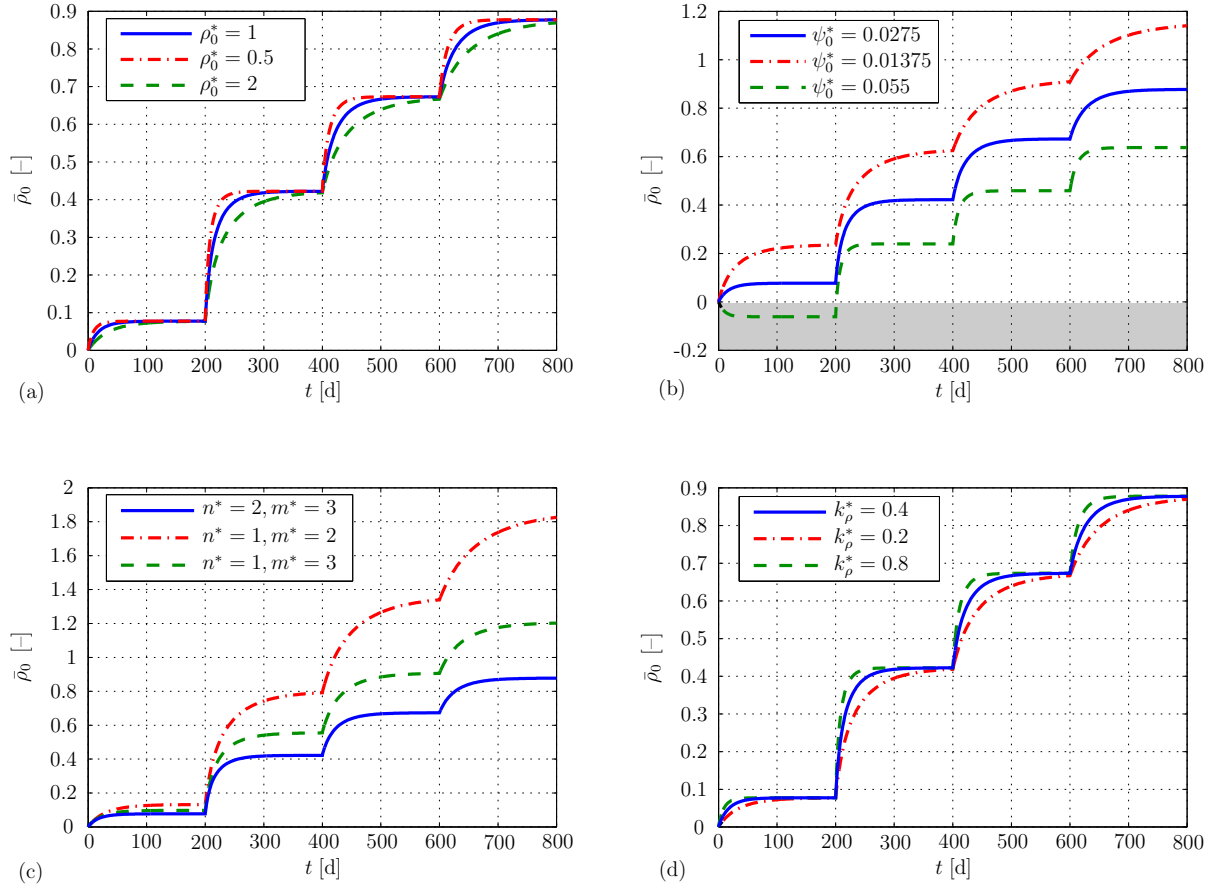


Figure 5.2: Investigation of the sensitivity of the density response $\bar{\rho}_0(t)$ for the loading history depicted in Figure 5.1(a) with an axial force of magnitude $F/10$. The material parameters are modified as compared to the reference material data set given in Table 5.3; modifications: (a) initial density ρ_0 , (b) energy-type saturation value ψ_0^* , (c) algorithmic parameters n^* and m^* , (d) growth velocity k_ρ^* .

evolution—higher initial values of ρ_0^* reduce the growth velocity but result in identical density equilibrium levels. The energy-type saturation or rather target value ψ_0^* essentially influences the level of the density at biological equilibrium. Reducing this parameter leads to a remarkable increase of the density level. However, as indicated above, increasing this parameter—depending on the particular loading level—may cause the material to degrade at lower loading levels as illustrated by the shaded region in Figure 5.2(b). The combination of the algorithmic parameter m^* and the porosity exponent n^* also affects the level and the rate of the density saturation, see Figure 5.2(c). Note, that only the difference $n^* - m^*$ enters the density evolution equation (5.4). However, the curves of the relative density $\bar{\rho}_0$ for the parameter-combinations $n^* = 2, m^* = 3$ and $n^* = 1, m^* = 2$ —so that $n^* - m^* = -1$ in both cases—significantly deviate from one another. This observation is attributed to the present stress-driven loading, cf. equation (5.6), where the porosity exponent n^* enters the definition of the Piola-Kirchhoff stress.

For a strain-driven process, however, these two curves in Figure 5.2(c) would coincide. Finally, k_ρ^* governs the growth velocity as specified in equation (5.4).

5.3 Anisotropic growth – a microsphere approach

This section deals with the extension of the one-dimensional density evolution model, discussed in the previous section, to the three-dimensional macroscopic level by means of the microsphere formulation. One property of the proposed formulation is the inherent direction-dependent response which, in consequence, leads to an anisotropic model of growth by direction-dependent local density evolution. For alternative anisotropic growth models based on macroscopic continuum approaches, we refer to Jacobs et al. [149] and Menzel [197]. Analogous microsphere approaches, including internal variables, are proposed by Göktepe and Miehe [111] and Harrysson et al. [120].

5.3.1 Extension to a three-dimensional formulation

To obtain a fully three-dimensional constitutive model, we now expand the one-dimensional formulation of Section 5.2 using the microsphere concept. Conceptually speaking, the continuum approach is based on a one-dimensional constitutive equation. We extend this one-dimensional constitutive relation to the three-dimensional macroscopic level by means of an integration over the underlying unit-sphere \mathbb{U}^2 . Characteristic for the algorithmic implementation of this approach is a finite number of m unit-vectors \mathbf{r}^i to be considered for the numerical integration over the unit-sphere, by means of which we compute the macroscopic stress tensor and tangent operator.

In the present context of a microsphere model, macroscopic quantities per unit volume are represented by

$$\langle\langle \bullet \rangle\rangle = \frac{1}{4\pi} \int_{\mathbb{U}^2} (\bullet) \, dA, \quad (5.25)$$

which allows us to rewrite the macroscopic strain energy function as

$$\Psi_0 = \langle\langle \psi_0(\bar{\lambda}) \rangle\rangle. \quad (5.26)$$

Herein, ψ_0 denotes the one-dimensional strain energy function introduced in (5.5) and $\bar{\lambda}$ represents the stretch as defined in equation (5.1). Based on this and by analogy with equation (5.6), the macroscopic Piola-Kirchhoff stresses result in

$$\mathbf{S} = 2 \frac{\partial \Psi_0}{\partial \mathbf{C}} = 2 \left\langle \left\langle \frac{\partial \psi_0}{\partial \bar{\lambda}} \frac{\partial \bar{\lambda}}{\partial \mathbf{C}} \right\rangle \right\rangle = \left\langle \left\langle \left[\frac{\rho_0}{\rho_0^*} \right]^{n^*} \mathbf{S}^e \right\rangle \right\rangle \quad (5.27)$$

including the elastic Piola-Kirchhoff stresses

$$\mathbf{S}^e = S^e \mathbf{r} \otimes \mathbf{r} \quad (5.28)$$

weighted by the relative density power $[\rho_0/\rho_0^*]^{n^*}$, where we use relation

$$\frac{\partial \bar{\lambda}}{\partial \mathbf{C}} = \frac{1}{2\bar{\lambda}} \mathbf{r} \otimes \mathbf{r}. \quad (5.29)$$

The application of equation (5.25) to the unit vectors $\mathbf{r} \in \mathbb{U}^2$, and higher order moments thereof, results in constraints such as $\langle \mathbf{r} \rangle = \mathbf{0}$ and $\langle \mathbf{r} \otimes \mathbf{r} \rangle = \frac{1}{3} \mathbf{I}$, see also Appendix B.3.

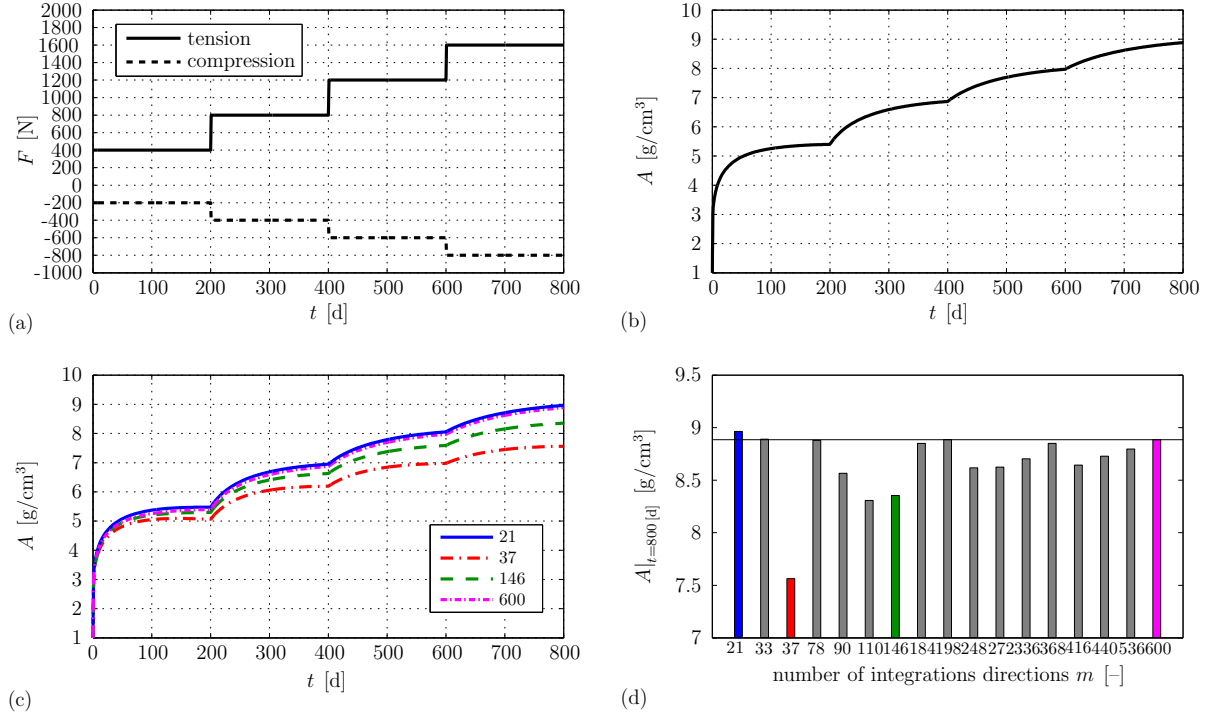


Figure 5.3: Response of the three-dimensional density growth model for a combined homogeneous tension-compression test. (a) Stepwise constant tensile and compressive loading levels in terms of the axial forces F with $F_{\text{tens}} = -2 F_{\text{comp}}$. (b) Evolution of zeroth-order moment A representing the macroscopic density using $m = 21$ integration directions. (c) Comparison of zeroth-order moment A using four different integration schemes. (d) Comparison of the zeroth-order moment $A|_{t=800[d]}$ for 17 different integrations schemes with a maximum number of $m = 600$ integration directions per hemisphere.

5.3.2 Implementation

To integrate the constitutive equations over the unit sphere \mathbb{U}^2 , we adopt m discrete integration direction vectors \mathbf{r}^i and introduce w^i as the related weighting factors. Accordingly, we approximate the continuous representation introduced in equation (5.26) by

$$\langle (\bullet) \rangle = \frac{1}{4\pi} \int_{\mathbb{U}^2} (\bullet) dA \approx \sum_{i=1}^m w^i (\bullet)^i. \quad (5.30)$$

Table 5.4: Constitutive box for the three-dimensional microsphere-based density-growth model. Quantities without subscript n are assumed to be associated with t_{n+1} .

| |
|---|
| <p>0. given deformation in terms of the right Cauchy-Green tensor \mathbf{C} at time t_{n+1} and history data ρ_{0n}^i of internal density variables at time t_n for all m discrete direction vectors $\mathbf{r}^i \in \mathbb{U}^2$</p> <p>1. compute affine micro-stretches for $i = 1, \dots, m$</p> $\bar{\lambda}^i = \sqrt{\mathbf{r}^i \cdot \mathbf{C} \cdot \mathbf{r}^i}$ <p>2. evaluate step 1. and 2. of Table 5.2 using affine micro-stretches, i.e. $\bar{\lambda}^i \equiv \bar{\lambda}$, for $i = 1, \dots, m$</p> <p>3. compute macroscopic Piola-Kirchhoff stresses</p> $\mathbf{S} = \sum_{i=1}^m \frac{1}{\bar{\lambda}^i} \left[\frac{\rho_0^i}{\rho_0^*} \right]^{n^*} \frac{\partial \psi_0^e}{\partial \bar{\lambda}^i} w^i \mathbf{r}^i \otimes \mathbf{r}^i$ <p>4. compute tangent operator</p> $\mathbf{E} = \sum_{i=1}^m \frac{1}{[\bar{\lambda}^i]^2} \left[\frac{\rho_0^i}{\rho_0^*} \right]^{n^*} [\bar{\mathbf{E}}_{\bar{\lambda}}^i + \bar{\mathbf{E}}_{\rho_0}^i] w^i \mathbf{r}^i \otimes \mathbf{r}^i \otimes \mathbf{r}^i \otimes \mathbf{r}^i$ <p>wherein $\bar{\mathbf{E}}_{\bar{\lambda}}^i$ and $\bar{\mathbf{E}}_{\rho_0}^i$ are taken from Table 5.2</p> <p>5. compute zeroth-, second-, and fourth-order density moments A, \mathbf{A} and \mathbf{A} for visualisation purposes, cf. Appendix C.2</p> |
|---|

Several integration schemes over the unit-sphere of different approximation order have been studied in the literature. In this regard, we refer the reader to Figures 5.3(c, d) and the corresponding comments made in Section 5.3.3, where we compare 17 different integration schemes. Apart from this, however, we restrict ourselves to a simple integration scheme based on $m = 21$ integration directions defined on half of the unit-sphere according to Bažant and Oh [32].

We can directly apply the algorithmic update scheme of the one-dimensional growth model described in Section 5.2 to the three-dimensional microsphere formulation. The discrete microsphere approach is based on a one-dimensional constitutive equation defined in terms of the (affine) stretch in every integration direction, i.e.

$$\bar{\lambda}^i = \sqrt{\mathbf{r}^i \cdot \mathbf{C} \cdot \mathbf{r}^i}. \quad (5.31)$$

We adopt the compressible neo-Hooke-type strain energy specified in equation (5.22). Note, that different types of one-dimensional constitutive models can be chosen in the context of modelling biological tissues—for instance the worm-like chain model which provides a sound physical background and, by means of the microsphere model, can straightforwardly be extended to the three-dimensional case; see Chapter 4 or the articles by Kuhl et al. [165], Alastrué et al. [9], and references cited therein. By using equations

(5.27) and (5.28) together with the approximation (5.30), we can express the Piola-Kirchhoff stresses as

$$\mathbf{S} \approx \sum_{i=1}^m \left[\frac{\rho_0^i}{\rho_0^*} \right]^{n^*} S^{ei} w^i \mathbf{r}^i \otimes \mathbf{r}^i, \quad (5.32)$$

with $S^{ei} = \partial_{\bar{\lambda}^i} \psi_0^e(\bar{\lambda}^i) / \bar{\lambda}^i$, cf. equation (5.6).

In view of nonlinear finite-element simulations for example, we apply a Newton scheme to iteratively solve the global system of nonlinear equations. To ensure quadratic convergence of the algorithm, we compute the consistent algorithmic material tangent operator by the total differential of the Piola-Kirchhoff stresses \mathbf{S} with respect to the right Cauchy-Green deformation tensor \mathbf{C} , i.e.

$$\mathbf{E} = 2 \frac{d\mathbf{S}}{d\mathbf{C}} \approx 2 \sum_{i=1}^m \frac{d\mathbf{S}^i}{d\mathbf{C}} = \sum_{i=1}^m \mathbf{E}_{\bar{\lambda}}^i + \mathbf{E}_{\rho_0}^i. \quad (5.33)$$

By means of the chain rule and by analogy to equations (5.15) and (5.16), we identify the two tangent contributions as

$$\mathbf{E}_{\bar{\lambda}}^i = 2 \frac{\partial \mathbf{S}^i}{\partial \mathbf{C}} = 2 \frac{\partial \mathbf{S}^i}{\partial \bar{\lambda}^i} \otimes \frac{\partial \bar{\lambda}^i}{\partial \mathbf{C}} \quad \text{and} \quad \mathbf{E}_{\rho_0}^i = 2 \frac{\partial \mathbf{S}^i}{\partial \rho_0^i} \otimes \frac{\partial \rho_0^i}{\partial \mathbf{C}}, \quad (5.34)$$

which can be determined straightforwardly from the one-dimensional model, cf. equations (5.17, 5.21) and Table 5.2, as

$$\mathbf{E}_{\bar{\lambda}}^i \approx \sum_{i=1}^m \frac{1}{[\bar{\lambda}^i]^2} \left[\frac{\rho_0^i}{\rho_0^*} \right]^{n^*} \bar{\mathbf{E}}_{\bar{\lambda}}^i w^i \mathbf{r}^i \otimes \mathbf{r}^i \otimes \mathbf{r}^i \otimes \mathbf{r}^i \quad (5.35)$$

and

$$\mathbf{E}_{\rho_0}^i \approx \sum_{i=1}^m \frac{1}{[\bar{\lambda}^i]^2} \left[\frac{\rho_0^i}{\rho_0^*} \right]^{n^*} \bar{\mathbf{E}}_{\rho_0}^i w^i \mathbf{r}^i \otimes \mathbf{r}^i \otimes \mathbf{r}^i \otimes \mathbf{r}^i. \quad (5.36)$$

The algorithm related to the constitutive microsphere model is summarised in Table 5.4.

5.3.3 Numerical example

As an illustrative numerical example to emphasise the properties of the computational anisotropic growth model, we now discuss a homogeneous state of three-dimensional deformation. We use the neo-Hookean strain energy function specified in Section 5.2 together with the material parameters summarised in Table 5.3. The time step size Δt is set to 1.0 [d] and the Newton-tolerance is $\text{tol} = 10^{-8}$. We apply stepwise loading by prescribing external tensile and compressive forces, i.e. $\mathbf{F}_1 = F_{\text{tens}} \mathbf{e}_1$ and $\mathbf{F}_2 = F_{\text{comp}} \mathbf{e}_2$

5 A microsphere model for the simulation of growth effects

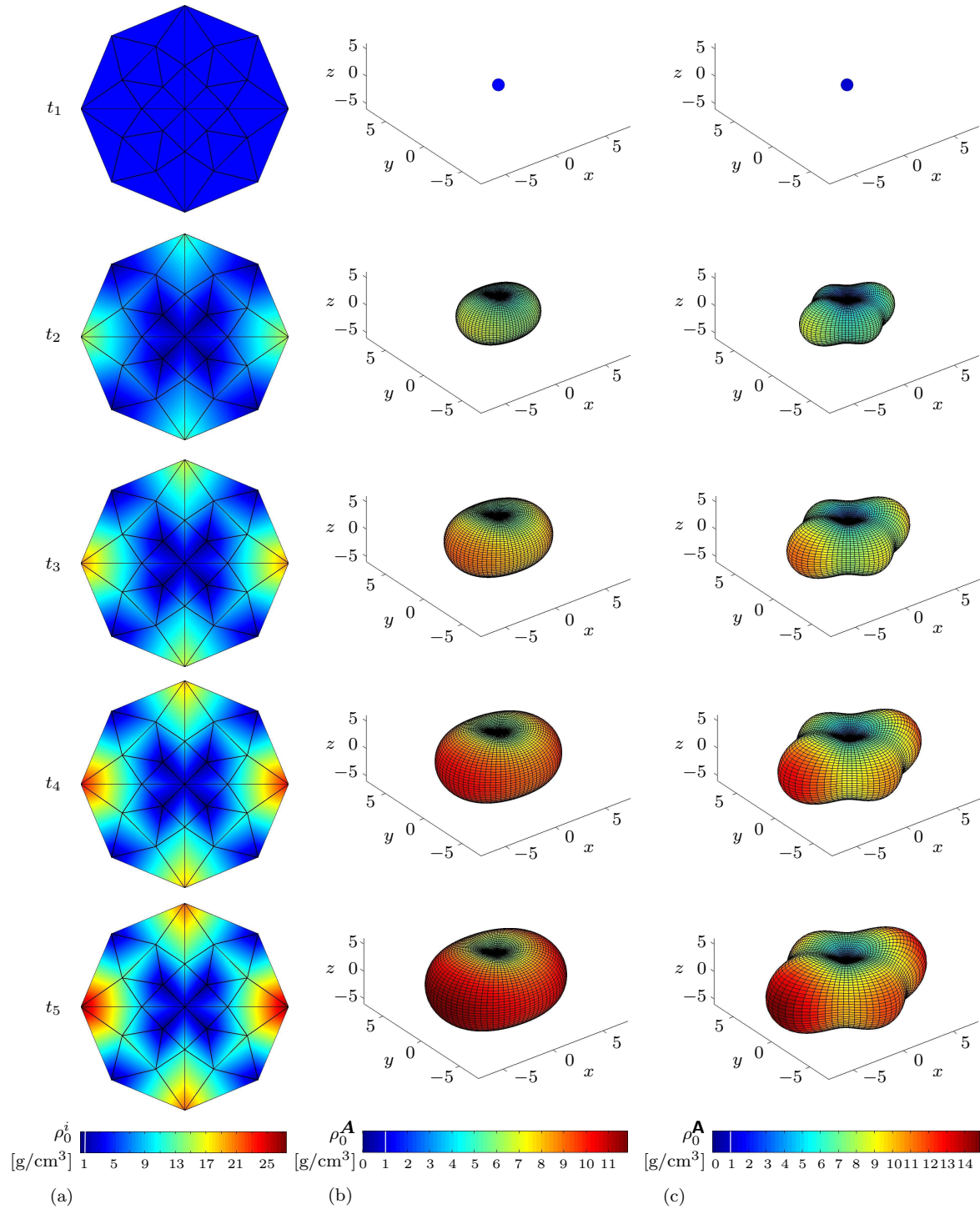


Figure 5.4: Visualisation of anisotropic density evolution with respect to five representative points in time at $t = \{0, 200, 400, 600, 800\}$ [d]. (a) Stereographic pole projection plots visualising the microdensities ρ_0^i and ODF-type surface plots (b) based on second-order density moment \mathbf{A} and (c) based on fourth-order density moment \mathbf{A} . Density-related values larger than one characterise densification whereas values smaller than one represent resorption; $\rho_0^* = 1.0$ [g/cm³].

with $F_{\text{tens}} = -2 F_{\text{comp}}$. The specific loading history is displayed in Figure 5.3(a). Here, we apply a Cartesian frame $\{\mathbf{e}_1, \mathbf{e}_2, \mathbf{e}_3\}$, respectively $\{\mathbf{e}_x, \mathbf{e}_y, \mathbf{e}_z\}$.

Due to the application of the algorithmic microsphere scheme, we obtain m different micro-densities ρ_0^i . In this regard, applying the stereographic pole projection method seems to be the most feasible approach to visualise the micro-densities ρ_0^i directly, cf. Appendix C. As a scalar measure representing the macroscopic density we introduce a density moment of zeroth-order denoted by A , cf. Appendix C.2. Figure 5.3(b) illustrates the evolution of this density-related quantity A . As expected from the response of the one-dimensional model, we observe a characteristic creep-type behaviour saturating in a time-dependent manner towards the biological equilibrium state.

As we will be discussing in the following, material anisotropy evolves for the present model proposed so that the importance and influence of the accuracy of the integration scheme is less pronounced as for the case of non-evolving material anisotropy; see also Chapter 4 and Alastrué et al. [10]. Nevertheless, we perform a sensitivity analysis to study the impact of the number of integration directions for a homogeneous deformation. For the deformation considered, it turns out that the $m = 21$ -point integration scheme yields results comparable to those obtained by generally more accurate higher-order integration schemes; see also Miehe et al. [218], Alastrué et al. [9] or Ehret et al. [91] for more detailed discussion on the influences of the numerical integration schemes over the unit-sphere. In this chapter we take into account three integration schemes reported in Bažant and Oh [32] and 14 integration schemes provided in Heo and Xu [128] where we consider the integration scheme of highest order with $m = 600$ integration directions per hemisphere as a reference solution. For the sake of clarity, only four different integration schemes with $m = \{21, 37, 146, 600\}$ are compared in Figure 5.3(c). We observe that the $m = 21$ -point integration scheme shows good agreement with the reference solution, whereas the $m = 146$ -point and especially the $m = 37$ -point integration schemes show significant deviations compared to the $m = 600$ -reference. More significantly, we evaluate the zeroth-order moment A at $t = 800$ [d] in Figure 5.3(c) and compare 16 different integration schemes to the $m = 600$ -solution which is additionally illustrated by a horizontal reference line. Generally, we observe that a higher number of integration directions does not necessarily lead to more accurate results with respect to the chosen reference solution. Interestingly, the lower-order integration schemes, as, e.g., the $m = 21$ - and especially the $m = 33$ - and $m = 78$ -point integration schemes show excellent agreement with the reference solution for the considered deformation. We will apply the $m = 21$ -point integration scheme for all subsequent simulations.

In order to further study the anisotropic evolution of the density, we use different visualisation techniques which are discussed in more detail in Appendix A. The application of the microsphere scheme offers several beneficial possibilities to illustrate local anisotropic behaviour. We apply stereographic pole projection plots, cf. Appendix C.1, and orientation-distribution-type surface plots, cf. Appendix C.2, which we evaluate at five different points in time, i.e. $t = \{0, 200, 400, 600, 800\}$ [d].

The stereographic pole projection plots in Figure 5.4(a) show the evolution of the individual micro-densities ρ_0^i with the z -direction being perpendicular to the projection plane. The initial isotropic state at $t = 0$ (blue) corresponds to $\rho_0^i = \rho_0^* = 1.0 \forall i = 1, \dots, m$. With progressing deformation, the density distribution changes significantly, resulting in a densification (red) in the main loading directions and a resorption (dark blue) in the unloaded directions. This clearly reflects a direction-dependent or rather anisotropic growth process including texture evolution.

In addition, we visualise the anisotropic density evolution by means of orientation-distribution-function-related quantities in Figure 5.4(b, c), where Figure 5.4(b) displays the second-order density moment \mathbf{A} , which takes the representation of generalising the two-dimensional orientation-distribution-function-type plots by Jacobs et al. [149] to the three-dimensional case. Figure 5.4(c) shows the fourth-order density moment \mathbf{A} , see also Appendix C.2. In both cases, the initial isotropic state (blue) is characterised by a sphere with radius 1.0 since the initial micro-densities $\rho_0^i = \rho_0^* = 1.0 \forall i = 1, \dots, m$. With increasing deformation, shape and size of the orientation-distribution-function-related quantities change significantly. The shape of these higher-order density-related functions characterises the anisotropy evolution while their size represents the growth process itself.

5.4 Numerical example – application to bones

This section covers an application example of the anisotropic density growth formulation as outlined in the previous sections and particularly deals with the simulation of a proximal tibia bone under physiological loading conditions. We refer to Kuhl et al. [166] for a detailed discussion on aspects of finite element implementation, whereas in a recent publication by Pang et al. [232] the same tibia bone structure is investigated in response to gait.

5.4.1 Subject-specific problem – proximal tibia

We now apply the proposed anisotropic growth model to a subject-specific three-dimensional part of a proximal tibia. The three-dimensional tibia model consists of 3190 linear displacement-based tetrahedral finite elements and 893 nodes, see Figure 5.5(a). The respective densities ρ_0^i are stored as internal variables at the finite element integration point level.

We specify the geometry and boundary conditions according to Pang et al. [232], where bone density profiles of a proximal tibia have been studied in response to gait. With regard to the applied Dirichlet boundary conditions, we clamp the displacements at one single node at the bottom of the specimen, i.e. $\mathbf{u} = \mathbf{x} - \mathbf{X} = \mathbf{0}$, whereas all other displacements at the bottom nodes are constrained solely in \mathbf{e}_2 - and \mathbf{e}_3 -direction, i.e. $\mathbf{u} \cdot \mathbf{e}_2 = \mathbf{u} \cdot \mathbf{e}_3 = 0$. Furthermore, we apply Neumann boundary conditions by prescribing two

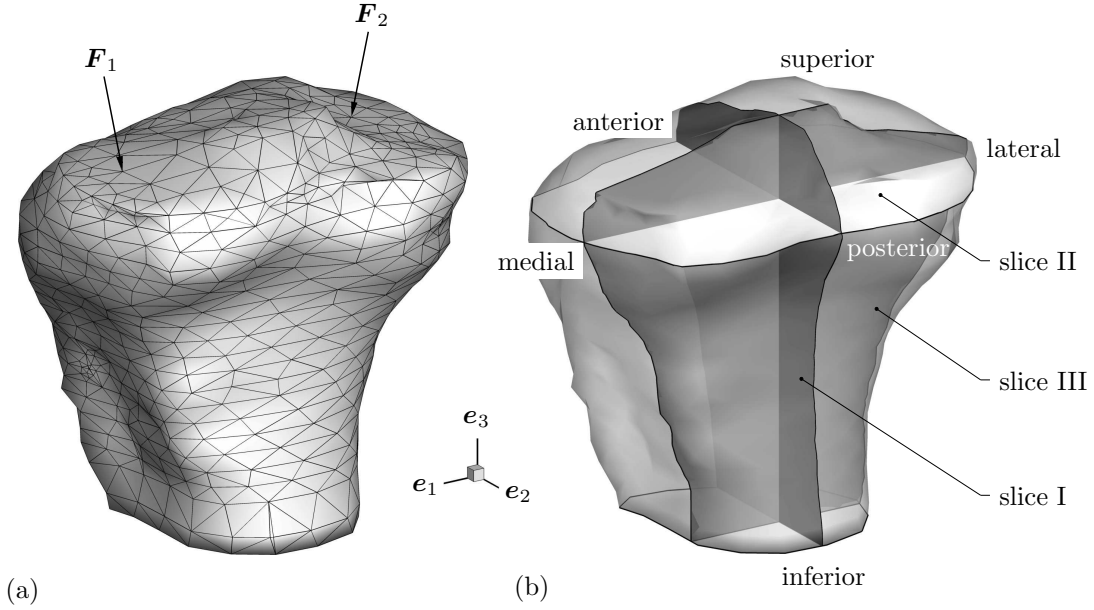


Figure 5.5: Geometry of the upper part of the proximal tibia. (a) Finite element mesh with applied concentrated forces F_1 , F_2 and (b) location of slices I (sagittal slice), II (axial slice) and III (coronal slice) used in Figures 5.8, 5.9 and 5.12.

concentrated forces at two nodes at the top of the specimen, as schematically drawn in Figure 5.5(a). To be specific, $\mathbf{F}_1 = 25.4545 \mathbf{e}_1 - 305.4545 \mathbf{e}_3$ [N] and $\mathbf{F}_2 = -25.4545 \mathbf{e}_1 - 254.5455 \mathbf{e}_3$ [N]; cf. Pang et al. [232]. We apply these external forces by linearly increasing their magnitude within 5.0 [d] and keep \mathbf{F}_1 and \mathbf{F}_2 constant thereafter for 35.0 [d]. In view of the material parameters, we adopt the values summarised in Table 5.3 and the constant time step size of the calculations is $\Delta t = 0.5$ [d].

To analyse the growth process in the proximal tibia under the prescribed loading conditions, we display the evolution of the zeroth-order density moment A at four different points in time, $t = \{10, 20, 30, 40\}$ [d], cf. Figure 5.6. After 10 [d]—the external forces possessing their final maximum magnitudes already after 5 [d]—we observe a remarkable densification of the tibia, in particular in those regions of the bone which are predominantly affected by the loading and thus associated with high levels of strain energy. However, during the subsequent part of the time period considered, the accumulated density does not change significantly in these areas. Instead, as time progresses, the material located at rather non-weight bearing regions—associated with lower strain energy levels—tends to degrade until the biological equilibrium state is reached. At biological equilibrium, the material—as represented by its local densities—is distributed such that the bone provides optimal structural support for forces induced during gait, cf. Pang et al. [232].

Since the growth process is anisotropic, it is reasonable to investigate the evolution of anisotropy by means of representative anisotropy measures. As a scalar-valued quantity we use the difference in maximum and minimum principal values of the second-order

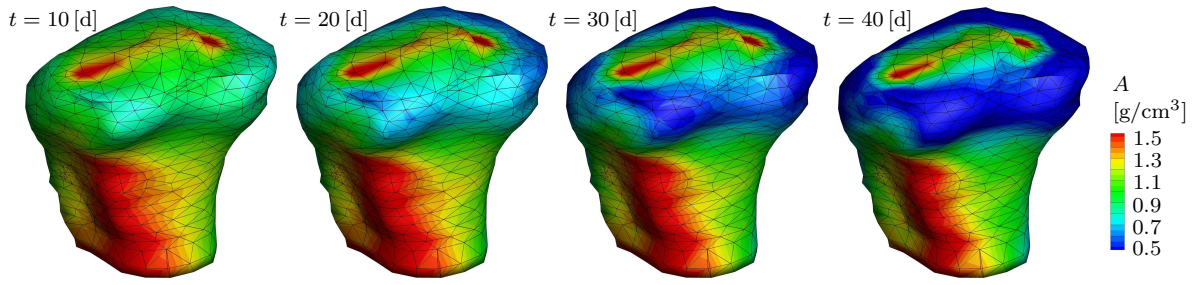


Figure 5.6: Three-dimensional density evolution in the proximal tibia at four different points in time, $t = \{10, 20, 30, 40\}$ [d]. The colour code indicates the evolution of the bone density by means of visualising the zeroth order moment A . As time progresses, from left to right, the bone densifies in areas of high strain energy and degrades in areas of low strain energy until it has approached the biological equilibrium at $t = 40$ [d].

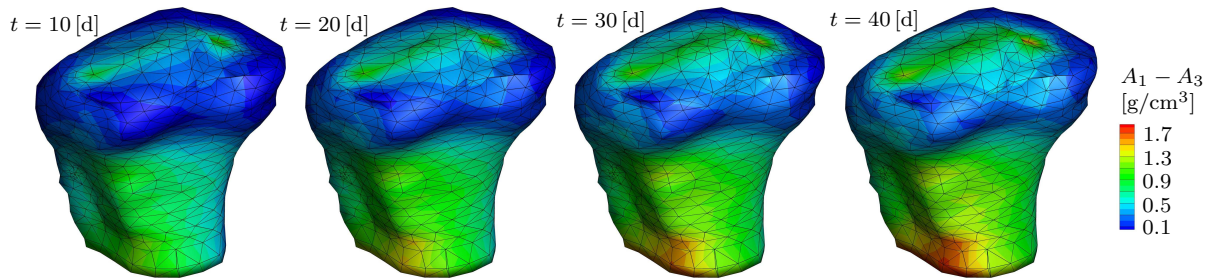


Figure 5.7: Three-dimensional anisotropy evolution in the proximal tibia at four different points in time, $t = \{10, 20, 30, 40\}$ [d]. The colour code indicates the evolution of the anisotropy by means of visualising the difference between the maximum and minimum principal value of \mathbf{A} , i.e. $A_1 - A_3$. As time progresses, from left to right, the anisotropy evolves most significantly in those regions which are predominantly associated with the loading and thus with a high strain energy level.

density moment, $A_1 - A_3$, see Appendix C.2. This anisotropy measure is depicted as a contour plot in Figure 5.7 and referred to four different points in time. The initial isotropic state at $t = 0$ (blue) corresponds to $A_1 - A_3 = 0$. It is clearly seen that the degree of anisotropy changes most significantly in those regions which are predominantly associated with the loading and thus with a high strain energy level. Interestingly, even if the outer upper part of the tibia does not contribute much to the support of the loading, and consequently degenerates with time, the degree of anisotropy also rises in these regions as time progresses.

To investigate the evolution of anisotropy and density in more detail, we now focus on three cross sections or rather slices of the tibia. The first slice I is placed parallel to the $\mathbf{e}_2\text{-}\mathbf{e}_3$ plane and the second slice II is oriented parallel to the $\mathbf{e}_1\text{-}\mathbf{e}_2$ plane, whereas slice III is perpendicular to \mathbf{e}_2 ; see Figure 5.5(b). Within the first two slices, four integration points of particular finite elements are chosen in order to visualise local anisotropic material properties by means of the fourth-order moment \mathbf{A} or rather its corresponding

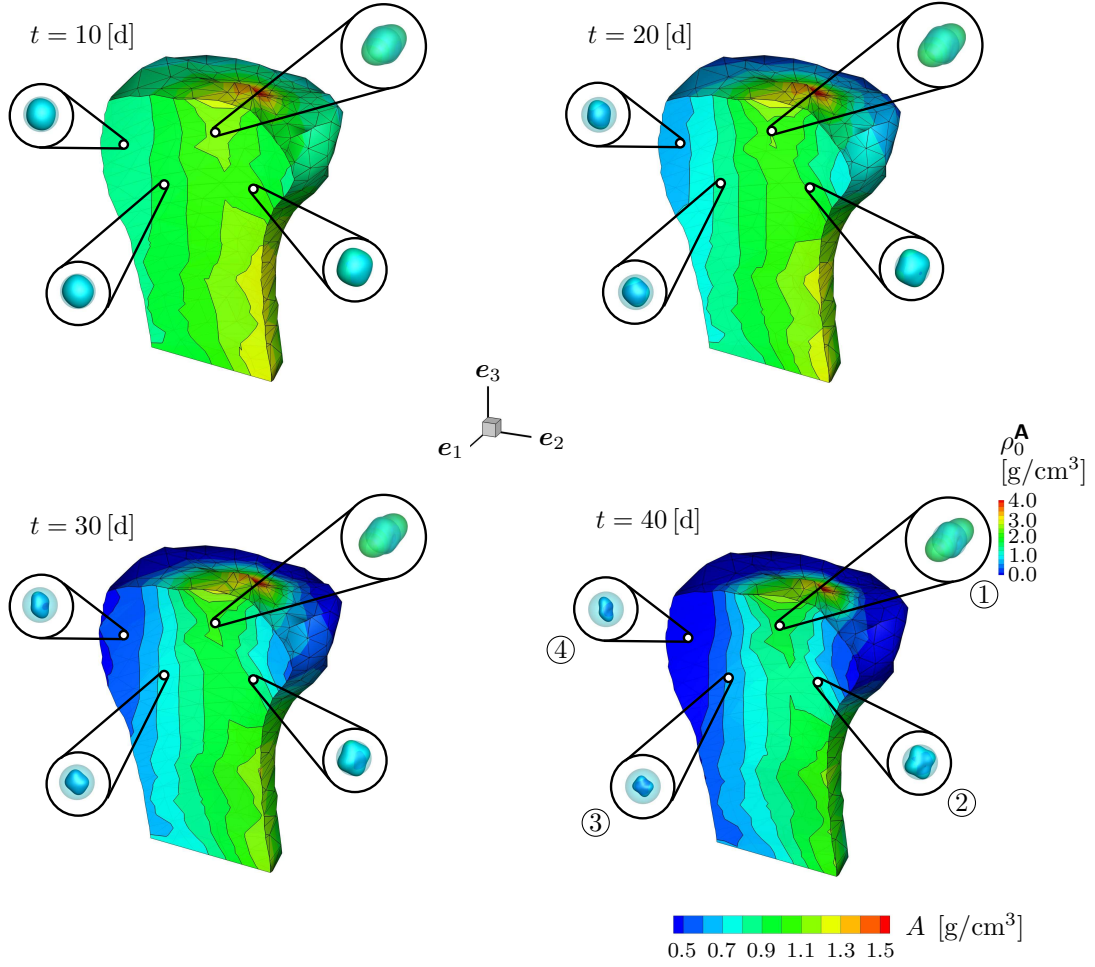


Figure 5.8: Anisotropy evolution in the proximal tibia displayed at four representative integration points located (approximately) in slice I, cf. Figure 5.5(b), and visualised by means of ODFs based on fourth-order density moments \mathbf{A} , whereby the isotropic initial state is plotted additionally as a reference state (shaded sphere). A change in size of the ODF is attributed to densification/resorption; a change in shape of the ODF is attributed to a change of anisotropic material properties. The colour code used for the bone indicates the evolution of the bone density by means of visualising the zeroth-order density moment A .

ODF $\rho_0^{\mathbf{A}}$; see equation (C.9). We also apply the fourth-order compliance tensor \mathbf{C}^e to represent directional Young's modulus surface plots which are based on the ODF $\delta^{-1}\mathbf{C}^e$; see equation (C.11) and Figure C.2(e–f) for the visualisation of three different types of material symmetry.

Figure 5.8 shows the local evolution of anisotropy with respect to time at four different integration points located within slice I. As expected, we observe that ODF ①—located at the top of the bone close to where the load is applied—shows the most significant change in size and shape, which reflects a pronounced growth behaviour accompanied by a considerable change of anisotropic material properties. The other ODFs ②–④ also

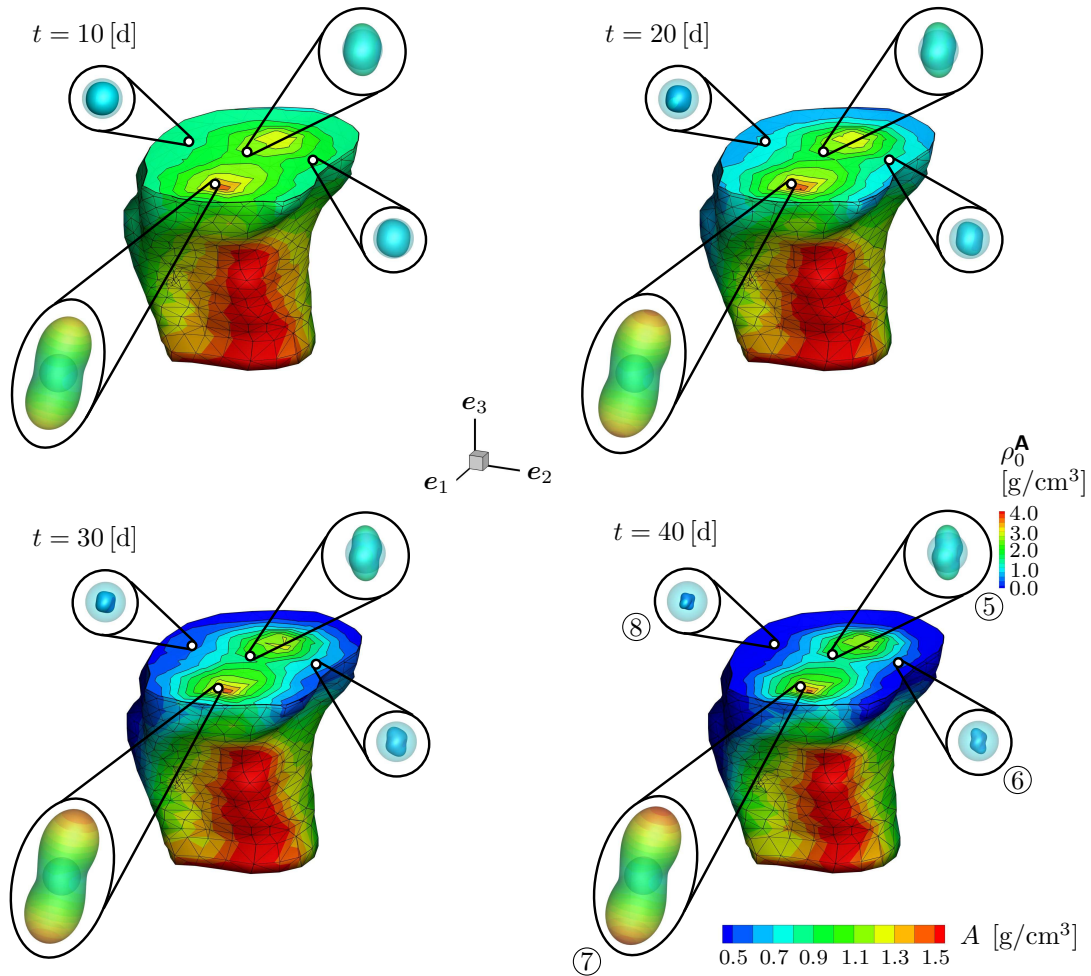


Figure 5.9: Anisotropy evolution in the proximal tibia displayed at four representative integration points located (approximately) in slice II, cf. Figure 5.5(b), and visualised by means of ODFs based on fourth-order density moments \mathbf{A} , whereby the isotropic initial state is plotted additionally as a reference state (shaded sphere). A change in size of the ODF is attributed to densification/resorption; a change in shape of the ODF is attributed to a change of anisotropic material properties. The colour code used for the bone indicates the evolution of the bone density by means of visualising the zeroth-order density moment A .

show anisotropic behaviour or rather texture evolution, since their shape increasingly deviates from their initial spherical distribution which, here and in the following, is indicated by the superimposed transparent sphere. In contrast to ODF ①, however, the ODFs ②–④ shrink which clearly indicates the resorption process of the material located in these points.

By analogy to the considerations above, Figure 5.9 illustrates the local evolution of anisotropy at four other integration points, now located within slice II. In this case, we observe that especially ODF ⑦ shows a very pronounced and elongated shape in combination with a drastic change in size. The distribution of this ODF corresponds

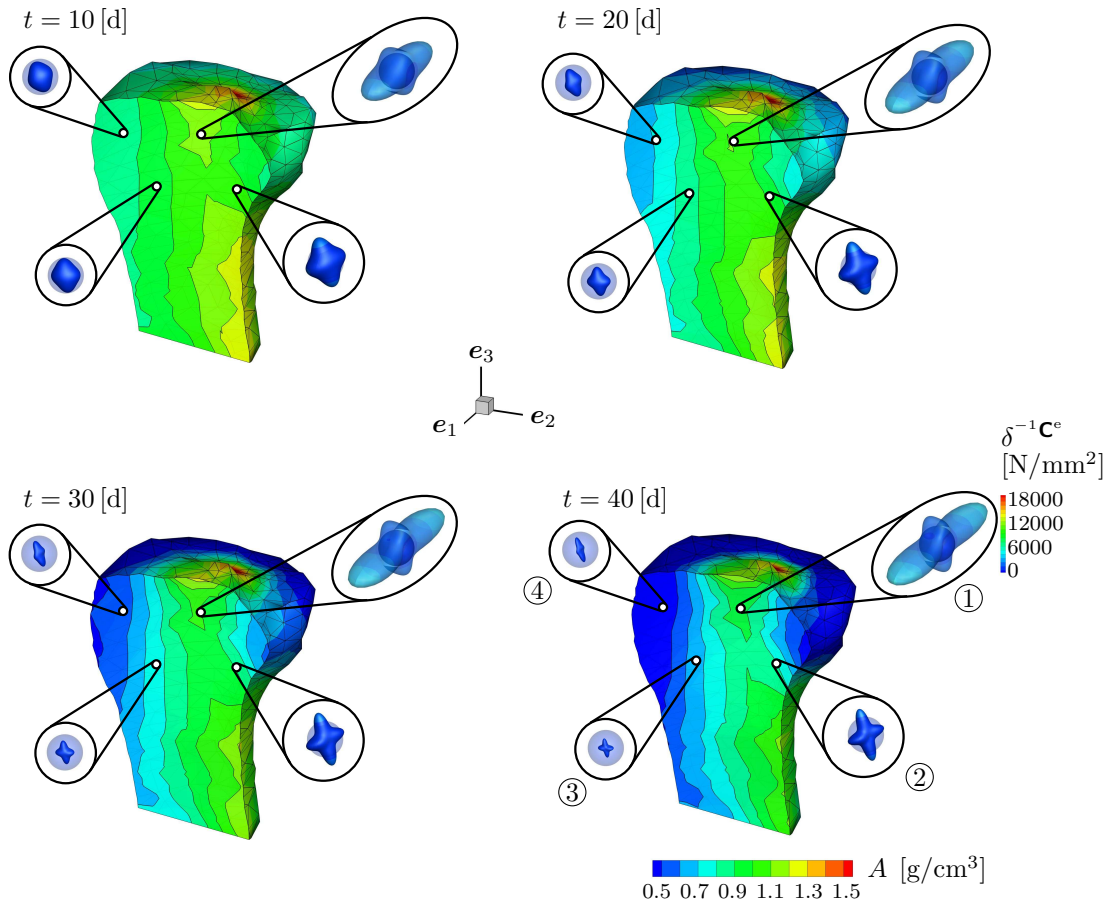


Figure 5.10: Anisotropy evolution in the proximal tibia displayed at four representative integration points located (approximately) in slice I, cf. Figure 5.5(b), and visualised by means of Young’s modulus surface plots, whereby the isotropic initial state is plotted additionally as a reference state (shaded sphere). A change in size of the ODF is attributed to densification/resorption; a change in shape of the ODF is attributed to a change of anisotropic material properties. The colour code used for the bone indicates the evolution of the bone density by means of visualising the zeroth-order density moment A .

to an almost transversely isotropic state. At $t = 10$ [d], when the other ODFs do not show any pronounced changes, ODF ⑦ has almost reached its final state. This effect results from the point, to which ODF ⑦ is referred to, being located in the region close to where the external force \mathbf{F}_1 is applied. The concentric isolines in the contour plots within slice I show these load bearing regions.

To investigate the evolution of the elastic or rather stiffness properties of bone, we additionally apply Young’s modulus surface plots evaluated within the same slices and at the same integration points as introduced and used above. The density-power-weighted elasticity tensor $\mathbf{E}_{\bar{\lambda}}$ in the unloaded initial state at $t = 0$ [d] can be calculated from

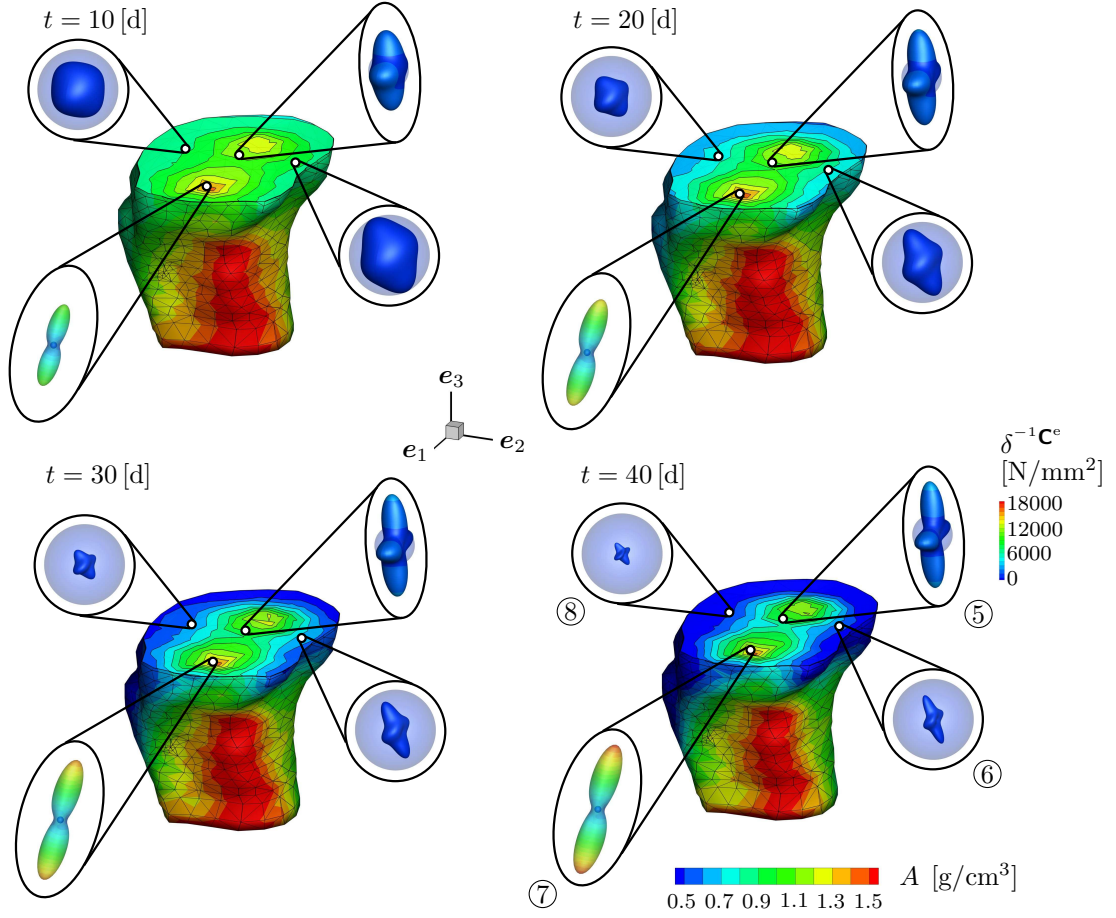


Figure 5.11: Anisotropy evolution in the proximal tibia displayed at four representative integration points located (approximately) in slice II, cf. Figure 5.5(b), and visualised by means of Young's modulus surface plots, whereby the isotropic initial state is plotted additionally as a reference state (shaded sphere, note the different scaling). A change in size of the ODF is attributed to densification/resorption; a change in shape of the ODF is attributed to a change of anisotropic material properties. The colour code used for the bone indicates the evolution of the bone density by means of visualising the zeroth-order density moment A .

equations (5.35) and (B.33). For the specific case of the neo-Hooke-type strain energy and by using equations (5.23) and (5.24) we obtain

$$\mathbf{E}_{\bar{\lambda}}|_{t=0[d]} = \frac{1}{3} [\lambda^* + 2\mu^*] \left[\mathbf{I}_{\text{vol}} + \frac{2}{5} \mathbf{I}_{\text{dev}} \right]. \quad (5.37)$$

Equation (5.37) reflects an initially isotropic, i.e. spherical, distribution of the Young's modulus surface plot with a value of $\delta^{-1}\mathbf{C}^e = 850.33 \text{ [N/mm}^2] \forall \mathbf{r}$; cf. Figures 5.10 and 5.11 where the isotropic reference state is visualised as a shaded sphere. Note, that the microsphere-based tensor $\mathbf{E}_{\bar{\lambda}}|_{t=0[d]}$ does not coincide with the initial elasticity tensor obtained from a standard isotropic neo-Hookean continuum model—in particular the

Table 5.5: Extremal values of directional Young’s moduli $E_{i'}$ in $[\text{N}/\text{mm}^2]$, for $i' = 1, 2, 3$, and relative differences for each ODF, which characterise the respective degree of anisotropy, as given in Figure 5.11.

| ODF | $E_{1'}$ | $E_{2'}$ | $E_{3'}$ | $\frac{E_{2'} - E_{1'}}{E_{1'}}$ | $\frac{E_{2'} - E_{3'}}{E_{3'}}$ | $\frac{E_{1'} - E_{3'}}{E_{3'}}$ |
|-----|----------|----------|----------|----------------------------------|----------------------------------|----------------------------------|
| ⑤ | 1600 | 300 | 2300 | -81% | -86% | -30% |
| ⑥ | 300 | 60 | 550 | -80% | -89% | -45% |
| ⑦ | 1400 | 4000 | 17300 | 186% | -77% | -92% |
| ⑧ | 280 | 50 | 250 | -82% | -80% | 12% |

material parameters λ^* and μ^* do not weight different modes but the sum $\lambda^* + 2\mu^*$ scales both, the volumetric and deviatoric modes.

Figure 5.10 shows the local state of anisotropy, now visualised by means of Young’s modulus surface plots, at the four different integration points located within slice I. As expected from the previous observations, ODF ①—located at the top of the bone close to the loading point—shows the most significant increase in size and change in shape, which reflects a pronounced growth and remodelling behaviour accompanied by a considerable evolution of anisotropic material properties. To give an example, the maximum value of the directional Young’s modulus for ODF ① is $4048 [\text{N}/\text{mm}^2]$. The other ODFs ②–④ also show evolution of material anisotropy but accompanied by a shrinkage in size indicating the resorption process of the material taking place at these material points. For all four integration points, we can identify pronounced orthotropic material properties; see also Figure C.2(f).

By analogy to the considerations above, Figure 5.11 illustrates the local state of anisotropy at the four integration points located within slice II. Similar to ODF ⑦ for $\rho_0^{\mathbf{A}}$ in Figure 5.9, to ODF ⑦ for $\delta^{-1}\mathbf{c}^e$ in Figure 5.11 possesses a very pronounced and elongated shape in combination with a drastic change in size—note the different scaling factors or rather diameters of the respective initial spherical ODFs. The distribution ⑦ corresponds to an almost transversely isotropic state, whereas the other ODFs again exhibit orthotropic behaviour. The maximum value of the directional Young’s modulus for ODF ⑦ is $17300 [\text{N}/\text{mm}^2]$. At this stage, the present study only provides results for a qualitative comparison with experimental data. Experiments reported in the literature for the stiffness properties of the proximal tibia provides data within a range from 20 to $20000 [\text{N}/\text{mm}^2]$; see, e.g., the contribution by Williams and Lewis [296], the study by Goldstein [112] for an extensive summary of data with respect to the anatomic location and function of bone in general and Ashman et al. [18] for the tibial cancellous bone specifically, as well as Rho et al. [248] for a literature survey of methods for determining the elastic modulus of trabecular bone.

To quantitatively/qualitatively compare our simulation with experimental results, we consider specific stiffness values obtained from the Young’s modulus surface plots in Figure 5.10 and compare these to respective stiffness values provided in the experimental study by Ashman et al. [18]. To give a brief summary, Ashman et al. [18] inves-

tigated the anatomical variation of orthotropic elastic moduli of the cancellous bone from three human proximal tibiae using an ultrasonic technique. They found that the material properties are highly heterogeneous, with the axial modulus ranging between 340 [N/mm²] and 3350 [N/mm²]*—*in other words, the measured Young’s moduli depend on the anatomical position. Moreover, the authors showed that the degree of anisotropy of the cancellous bone, determined by the relative differences between three orthogonal moduli, turned out to be more homogeneous than the respective distributions of the Young’s moduli themselves.

Table 5.5 provides extremal values of directional Young’s moduli $E_{i'}$, with the index $i' = 1, 2, 3$ being referred to the related principal directions. For the present study, these are almost aligned with the base system e_i , with $i = 1, 2, 3$, as highlighted in Figure 5.11. Consequently $E_{1'}$ corresponds approximately to the lateral-medial axis, $E_{2'}$ is related to the anterior-posterior axis, and $E_{3'}$ can be referred to the inferior-superior axis. These extremal values are based on the ODFs for $\delta^{-1}c^e$ at the four integrations points ⑤–⑧ located in slice II which are specified and visualised in Figure 5.11. When comparing the simulation results for $E_{i'}$ with the three orthogonal Young’s moduli E_j reported in Ashman et al. [18], we have to notice that E_j are not referred to exactly the same axes as the directional Young’s moduli $E_{i'}$ considered in this chapter. Furthermore, E_1 is referred to the anterior-posterior axis and E_2 reflects the material properties along the lateral-medial axis. Nevertheless, the values for the directional Young’s moduli as summarised in Table 5.5 together with their relative differences characterising the respective degree of anisotropy, are within the same range as those identified by Ashman et al. [18]. ODF ⑦ qualitatively deviates from the experimental results as the simulation predicts, in contrast to the other ODFs discussed, a transversely isotropic distribution. Furthermore, apart from ODF ⑦, the relative differences between $E_{2'}$ and $E_{1'}$, respectively $E_{2'}$ and $E_{3'}$, are nearly constant, even though the respective densities and directional Young’s moduli are rather different. This property is in agreement with the observations made in Ashman et al. [18], i.e. the degree of anisotropy is almost constant within a large range of cancellous bone densities. Note, that the averaged values of relative differences in orthogonal Young’s moduli reported in Ashman et al. [18] are based on three proximal human tibiae using 25 cancellous portions of each specimen. These also arise from different axial cross-sections, whereas we merely consider data at four chosen locations in one axial slice. Moreover, Ashman et al. [18] investigated a different specimen than the one discretised in this chapter.

5.4.2 Three-dimensional density prediction

To quantitatively/qualitatively verify our three-dimensional simulations of the tibia, we adopt the region of interest method—*analogous to Pang et al. [232] and described in, e.g., Hulet et al. [143]*—and evaluate the local bone mineral density (BMD) in fourteen equal-sized regions along the width of a characteristic tibial cross section. In particular, we consider slice III, see Figure 5.5(b), to which we apply a grey-scaled contour plot of the

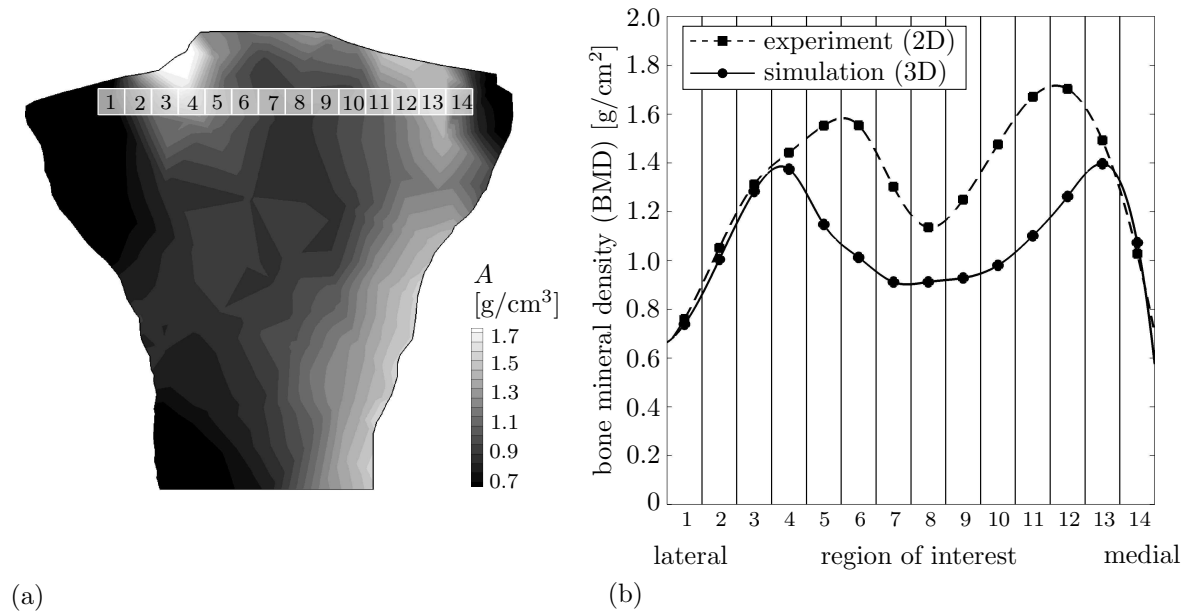


Figure 5.12: Region of interest method to characterize regional density variations in the proximal tibia. (a) The local bone mineral density (BMD) is evaluated in fourteen equal-sized regions along the width of tibial slice III, cf. Figure 5.5(b). (b) Regional variation of bone mineral density in fourteen regions of interest. Squares and dotted lines indicate the experimentally measured bone mineral density extracted from the Dual-Energy X-ray Absorptiometry scan as reported in Pang et al. [232]. Circles and solid lines indicate the computationally predicted bone density extracted from the three-dimensional simulation.

zeroth-order moment A representing the macroscopic density distribution as illustrated in Figure 5.12(a). Based on this, a computationally predicted bone mineral density profile is calculated from gray-scaled bone density profiles by averaging the density values of 2500 pixels within each region of interest and plotted over the width of the slice using a cubic spline data interpolation; see Figure 5.12(b). We compare this computationally predicted BMD-profile to an experimentally measured subject-specific local bone mineral density profile, which was recorded by a Dual-Energy X-ray Absorptiometry (DEXA) scan as reported in Pang et al. [232].

The resulting regional variations of the bone mineral density in the fourteen regions of interest are summarised and compared in Figure 5.12(b). Especially in the lateral regions 1–4 and 13, 14 we observe a good qualitative and quantitative agreement between experimental data and simulation results. Larger deviations are observed in the inner regions where the values of the bone mineral density are underestimated. This is illustrated by an inner region of lower density values in regions 5–12 between the two peak values.

5.4.3 Potential limitations

The observed discrepancies between computationally simulated and experimentally measured BMD-profiles, as shown in the previous subsection, can on the one hand be attributed to the lack of representative experimental data to compare the simulation with. On the other hand, the misfit can also be explained by the following specific properties of the model and discrete boundary value problem considered, see also Pang et al. [232]:

Geometry and mesh The three-dimensional mesh representing the proximal tibia is a generic mesh *not* created on the basis of the subject's own geometry from which the BMD-profile is extracted. As a consequence, neither the chosen cross-section of the tibia, slice III, nor the region of interest might be fully representative for a comparison with the two-dimensional DEXA scan. In this regard, it is also worth noting that DEXA calculates the BMD using *area* measures, instead of providing mass divided by *volume*. In addition, the mesh itself is relatively coarse, especially in the middle region where we observe larger differences between experimentally measured and computationally simulated densities.

Material parameters We assume the same material parameters as calibrated in Pang et al. [232]. However, since we apply a different material model—the microsphere-based neo-Hookean-type model can not be reduced to the macroscopic continuum neo-Hookean model—the material parameters also take a different interpretation. Furthermore, we assume that the bone possesses initially homogeneous and isotropic material properties. However, as also stated in Pang et al. [232], the material properties of the collagen matrix in the subchondral bone are far from being uniform or isotropic in a state which we adopt as the initial configuration. In fact, the outer layer of the tibia consists of cortical bone with a higher density, which does not change in time, while the inner part is composed of the less dense trabecular bone.

Boundary conditions As also discussed in Pang et al. [232], we have simplified the tibiofemoral loading by two representative concentrated forces acting on a single medial and lateral node each. In fact, however, the articular cartilage interface between the femur and tibia can be strained, the representative loading can shift in space and, most importantly, is spread over an area. Furthermore, we neglect forces from muscles, tendons, and the tibiofemoral joint. Lastly, we assume the subchondral bone to be completely isolated, whereas a contact region with the proximal fibula actually affects the *in vivo* loading situation through an elastic interface. Apart from these purely mechanical limitations, other equally important aspects like, e.g., biochemical factors, age, gender, race, or family history are not taken into account.

5.5 Numerical example – application to computational structural design

This section covers illustrative structural-design-related examples based on the anisotropic microsphere growth formulation as summarised in Sections 5.2 and 5.3. Motivated by Borrvall and Petersson [46], we investigate four three-dimensional benchmark-type problems for the design of a structure where we directly adopt the constitutive microsphere-framework for energy-driven anisotropic microstructural growth and density evolution outlined above.

A typical task in solid-mechanics-related engineering lies in the development, improvement and optimisation of structures sustaining mechanical loads—in other words, the maximisation of the structural stiffness and/or minimisation of the effective stress within the structure. In order to consistently treat and solve such structural optimisation problems, different rigorous mathematical formulations have been established. A classic structural optimisation problem consists of a problem-specific objective function, which has to be minimised in consideration of particular constraints with respect to design and state variables. The solution of such problems—if existent at all—is anything but trivial and commonly approximated by means of advanced numerical methods and algorithms for structural optimisation, cf. the extensive review of Bendsøe and Sigmund [40]. A structural optimisation problem is typically solved by using a sequence of convex approximation in conjunction with Lagrangian duality. This approach results in a separable problem that enables an efficient numerical implementation, cf. Bendsøe and Sigmund [40]. For a discussion of such methods of convex approximations and their relations we refer to the textbook by Christensen and Klarbring [67]. Recently, structural optimisation problems have also been solved with a phase-field approach, see Wallin et al. [286] and references cited therein.

In this section we adopt a conceptually different approach for the design of a structure, which is not based on a classic optimisation technique. We adopt the constitutive microsphere-framework for energy-driven anisotropic microstructural growth and density evolution which had originally been proposed for the simulation of isotropic adaptation phenomena in bones; see Sections 5.2 and 5.3.

In view of the material parameters used for the following examples, we adopt the values summarised in Table 5.3 and choose a constant time step size of $\Delta t = 0.5$ [s] for all simulations. Furthermore, the loading magnitude $f = \delta \tau$ is defined in terms of the respective traction magnitude τ multiplied by the stepwise load scaling parameter δ , see Figure 5.13(a). The local densities ρ_0^i , as referred to the underlying discrete integration directions $\mathbf{r}^i \in \mathbb{U}^2$ —with $i = 1, \dots, 21$, cf. Bažant and Oh [32]—are stored as internal variables at the finite element integration point level, with $\rho_0^i|_{t_0} = \rho_0^*$. In consequence, the model becomes path-dependent. Local anisotropic material properties are visualised via equations C.1–C.3 by means of ODF-type representations, as shown in Appendix C.2.

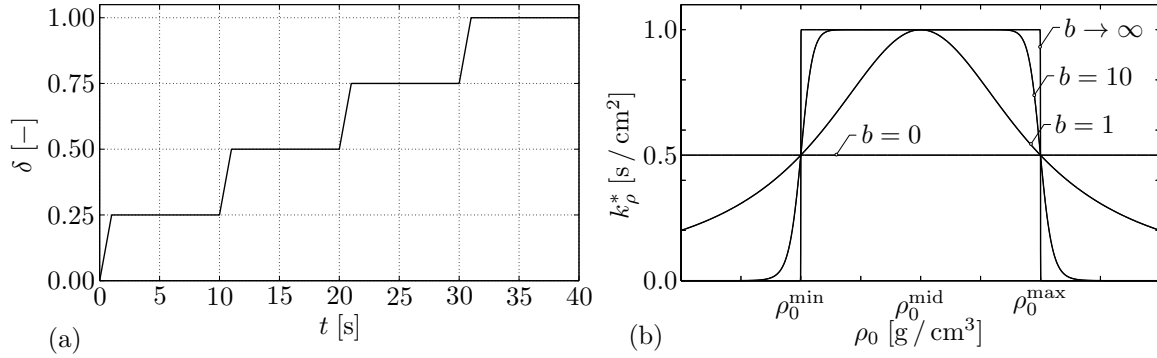


Figure 5.13: (a) Stepwise constant load scaling parameter δ used for the simulations. The magnitude of the respective loading is $f = \delta \tau$, where τ is specified for the respective examples. (b) Generalised bell function as introduced in equation (5.38), plotted for different values of b . For $b = 0$ the original approach without any bounds is restored (here referred to a constant value of $k_\rho^* = 0.5$) whereas for $b \rightarrow \infty$ a sharp lower and upper bound can be included by means of the parameters ρ_0^{\min} and ρ_0^{\max} respectively.

In classic structural optimisation formulations, it is common to prescribe an upper and lower bound for the density. Even if not applied to the subsequent simulations, lower and upper bounds for the density ρ_0 can be straightforwardly incorporated in the present approach, for example by means of replacing the constant growth velocity k_ρ^* by a function in ρ_0 . As one possibility amongst others, a generalised bell function defined as

$$k_\rho^*(\rho_0) = \frac{1}{1 + \left| \frac{\rho_0 - \rho_0^{\text{mid}}}{\rho_0^{\text{max}} - \rho_0^{\text{mid}}} \right|^{2b}} \quad \text{with} \quad \rho_0^{\text{mid}} = \frac{\rho_0^{\text{max}} + \rho_0^{\text{min}}}{2} \quad (5.38)$$

can be introduced, thereby restricting the density to vary between the bounds ρ_0^{\min} and ρ_0^{\max} . The bell function (5.38) is visualised in Figure 5.13(b) for different values of b , where $b \geq 0$ and $\rho_0^{\min} < \rho_0^* < \rho_0^{\max}$.

5.5.1 Cantilever

As a first example we consider a cantilever, see Figure 5.14(a), with $L = 100$ [mm]. Its back side is clamped while a square region of the front is loaded by a shear traction in vertical direction, i.e. $\boldsymbol{\tau} = -\delta \tau \mathbf{e}_2$ with $\tau = 1.6$ [N/mm^2]. The cantilever is discretised with $32 \times 20 \times 6$ linear displacement-based hexahedral elements with 4851 nodes.

The deformation in terms of the vertical displacement $u_2 = \mathbf{u} \cdot \mathbf{e}_2$ recorded at the middle node (\circ) of the white loading region over time is plotted in Figure 5.14(b). Due to the stepwise application of constant shear traction forces, we observe a distinct creep-type adaptation behaviour. The magnitude of the displacement clearly tends to decrease with time for a constant loading level $\boldsymbol{\tau}$, and results from the adaptation process accompanied

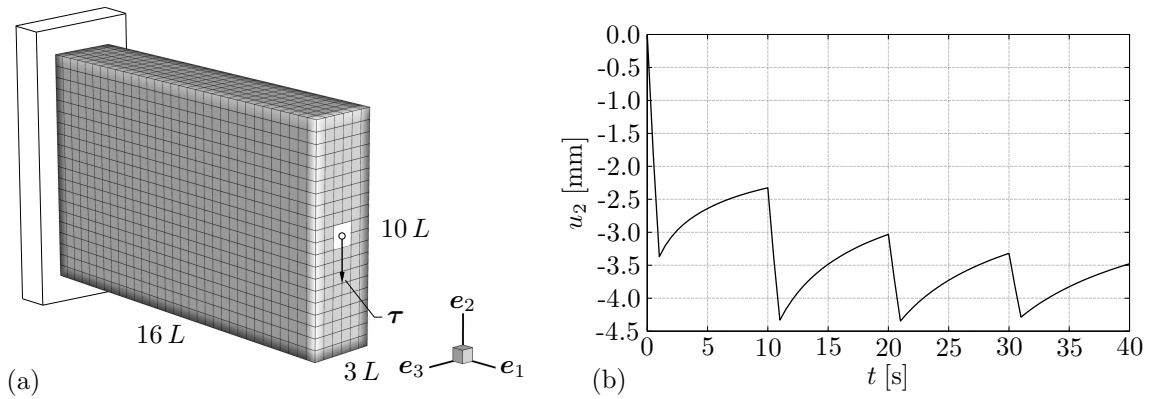


Figure 5.14: (a) Geometry, finite element mesh and boundary conditions of the cantilever. The back side of the beam is clamped while the white region at the front of the beam is exposed to shear traction τ . (b) Evolution of displacement $u_2 = \mathbf{u} \cdot \mathbf{e}_2$ recorded at middle node (\circ) within white region at front side.

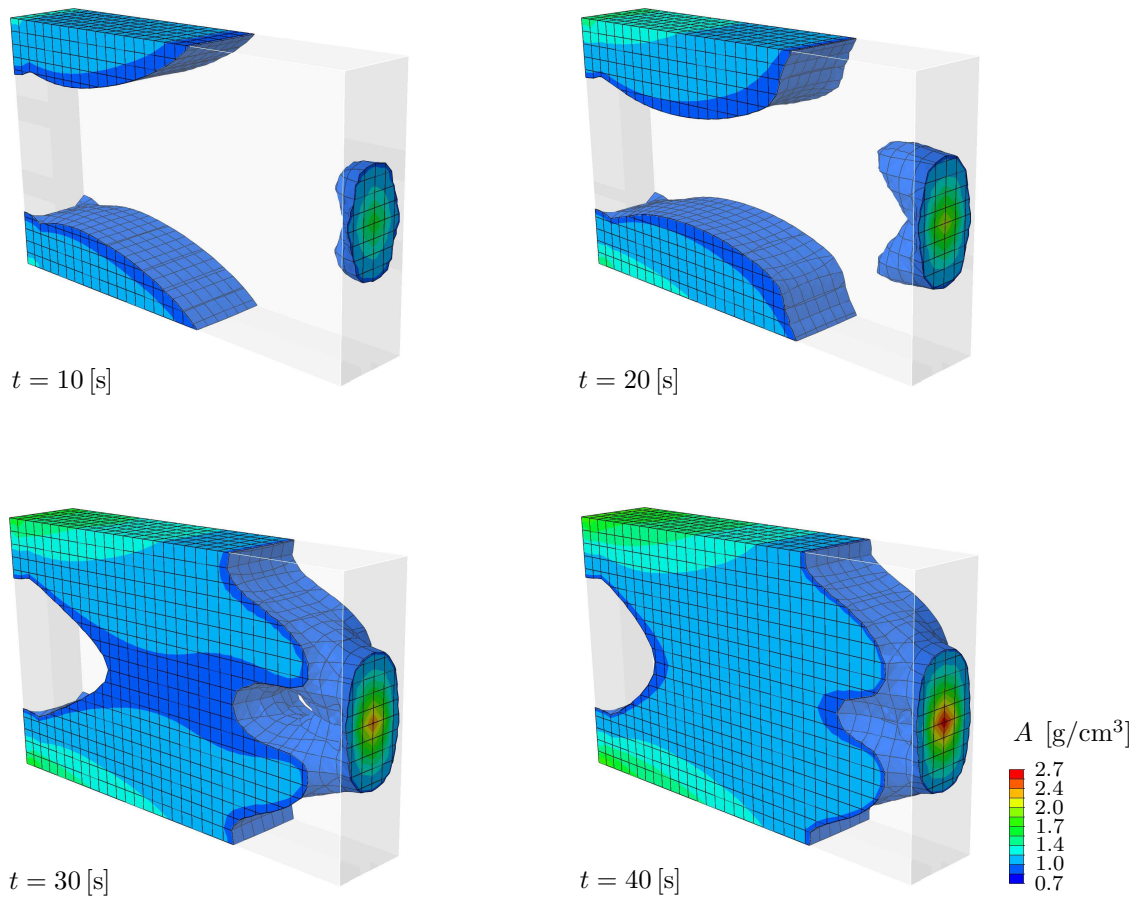


Figure 5.15: Finite element simulation of the cantilever exposed to shear traction, cf. Borrvall and Petersson [46]. Evolution of the zeroth-order density moment A at four different points in time where regions with values of $A < \rho_0^*$ are blanked.

by a change in local density A and corresponds to an increase in stiffness respectively a decrease in compliance. However, we observe that the displacement highlighted tends to saturate towards a characteristic equilibrium state—a state where the deformation and the density remains constant for a given load—but does not fully reach this state for any of the loading levels. To capture this saturation behaviour, one could either increase the time period of the constant loading levels or increase the adaptation velocity k_ρ^* , see Figure 5.2 for a detailed sensitivity-type analysis of the material parameters.

To analyse the growth or rather structural design process in the cantilever under the prescribed loading conditions, we display the evolution of the zeroth-order density moment A at four different points in time, $t = \{10, 20, 30, 40\}$ [s], see Figure 5.15. Here and in the following, degrading regions corresponding to values of $A < \rho_0^*$ are blanked which means that only isosurfaces corresponding to a densification of the material, i.e. $A \geq \rho_0^*$, are visible. However, the blanked degenerated regions still exist and also contribute to the overall load-bearing capacity.

In Figure 5.15, we observe a remarkable densification of the cantilever after 10 [s] particularly in those regions that are predominantly affected by the loading and in consequence associated with high levels of strain energy. For the present problem, these regions are the load-bearing upper and lower flanges of the cantilever as well as the region where the traction is applied. At 40 [s], the expected distribution of the material, i.e. the cantilever provides improved structural support for the applied shear traction, is observed. Compared to the distribution obtained by Borrvall and Petersson [46], we find qualitatively similar results for the cantilever example, even if the reported “I-beam design with varying dimensions of waist and flanges” cannot be reproduced exactly and the blanked degenerated regions still contribute to the overall load-carrying capacity. Moreover, the discretisation in the present study is much coarser—we use only 6 elements over the width of the beam, whereas Borrvall and Petersson [46] use 24 elements.

5.5.2 Crank

As a second example, we consider an L-shaped crank structure with $L = 100$ [mm]. The back side is clamped ($u_1 = u_2 = u_3 = 0$) while a shear traction of $\boldsymbol{\tau} = -\delta\tau\mathbf{e}_3$ with $\tau = 1.5$ [N/mm²] is applied at a small square region at the front of the crank, cf. Figure 5.16(a). The geometry is discretised by 24000 displacement-based hexahedral finite elements resulting in 26901 nodes.

The deformation in terms of the vertical displacement $u_3 = \mathbf{u} \cdot \mathbf{e}_3$ recorded at the middle node (\circ) within the white loading region over time is plotted in Figure 5.16(b). Compared to 5.14(b), a qualitatively similar mechanical response is observed.

Figure 5.17 illustrates the evolution of the zeroth-order density moment A at four different points in time where regions with values of $A < \rho_0^*$ are blanked. Even if we use only 24000 finite elements, the resulting structure is very similar to the results reported by Borrvall and Petersson [46] who applied 256000 elements. The present loading case

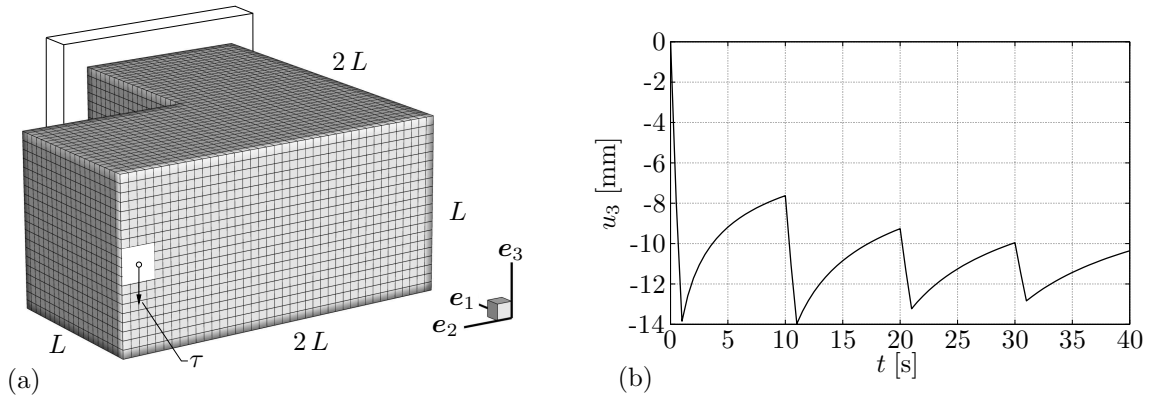


Figure 5.16: (a) Geometry, finite element mesh and boundary conditions of the crank. The back side of the crank is clamped while the white region at the front of the crank is exposed to shear traction τ . (b) Evolution of displacement $u_3 = \mathbf{u} \cdot \mathbf{e}_3$ recorded at middle node (o) within the white region at the front side.

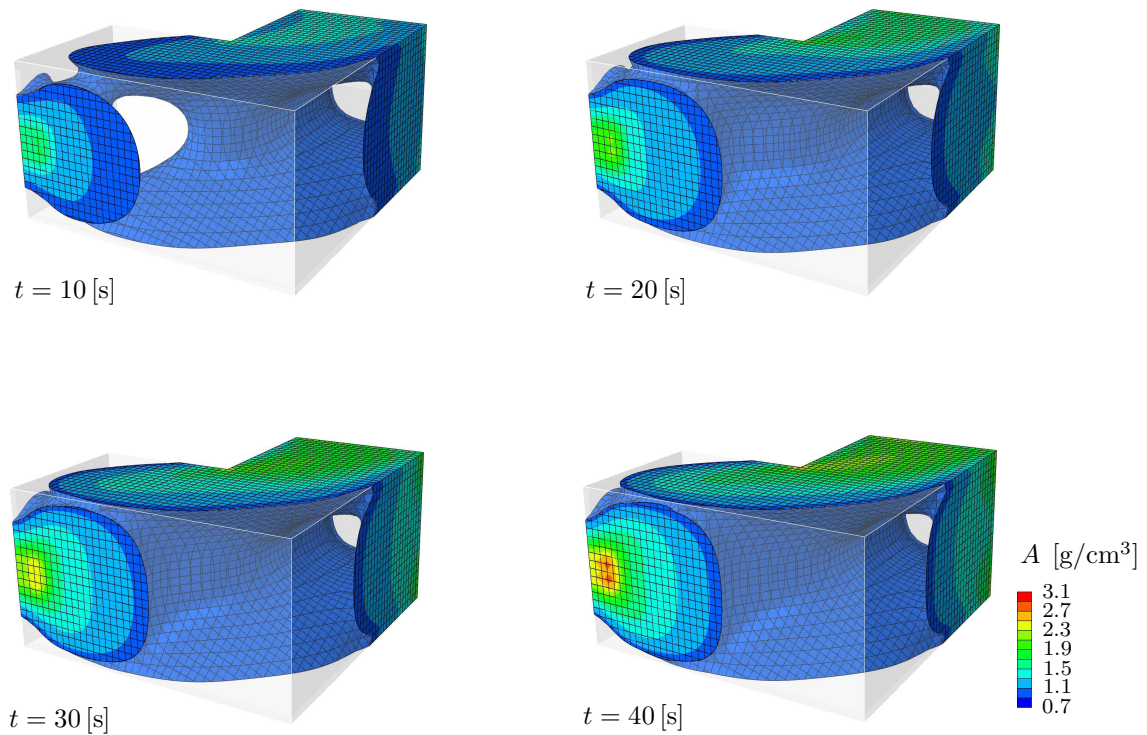


Figure 5.17: Finite element simulation of the crank exposed to shear traction, cf. Borrvall and Petersson [46]. Evolution of the zeroth-order density moment A at four different points in time where regions with values of $A < \rho_0^*$ are blanked.

leads to a combination of bending and torsion: we observe a slanting I-beam character at the outer part of the structure as a result of the bending, while close to the clamped wall the improved shape consists of a tubular section which originates from the torsional loading.

5.5.3 Stool

As a third example, we consider a cube, see Figure 5.18(a), with $L = 100$ [mm]. We apply the loading at the top of the cube by means of a traction in vertical direction, i.e. $\boldsymbol{\tau} = -\delta\tau\mathbf{e}_3$ with $\tau = 5.0$ [N/mm²] and clamp the cube at four square edge regions at the edges. In the work by Borrvall and Petersson [46], however, these regions are supported only in \mathbf{e}_3 -direction with the displacements in \mathbf{e}_1 - and \mathbf{e}_2 -direction being unconstrained. The cube is discretised into $32 \times 32 \times 32$ linear displacement-based hexahedral elements with 35937 nodes.

The evolution of the vertical displacement $u_3 = \mathbf{u} \cdot \mathbf{e}_3$ recorded at the middle node (o) within white region is plotted in Figure 5.18(b).

Figure 5.19 shows the evolution of A at four different points in time where regions with values of $A < \rho_0^*$ are blanked. Similar to Borrvall and Petersson [46], we observe that the resulting structure consists of four legs which somewhat resemble the design of a stool. For the simulations performed in this section, however, the lower parts of the legs of the stool are separated from each other, whereas in Borrvall and Petersson [46] the legs are kept together by a plate on the floor. This effect originates from the specific boundary conditions chosen.

5.5.4 Coathanger

The last example consists of a cross-shaped domain, see Figure 5.20(a) where $L = 100$ [mm], which is discretised into 40000 linear displacement-based hexahedral elements resulting in 44541 nodes. As boundary conditions, we apply shear tractions of $\boldsymbol{\tau} = -\delta\tau\mathbf{e}_3$ with $\tau = 1.0$ [N/mm²] at small square regions at the front and the back side of the specimen while we clamp the displacements at square regions of the lateral parts of the cross.

The vertical displacement $u_3 = \mathbf{u} \cdot \mathbf{e}_3$ recorded at the middle node (o) within the white region over time is displayed in Figure 5.20(b).

Figure 5.21 shows the evolution of A at four different points in time where regions with values of $A < \rho_0^*$ are blanked. Similar to Borrvall and Petersson [46], we observe that the resulting structure resembles the design of a coathanger. It is interesting to see that the evolving improved density distribution consists of a plane surface in the upper middle part of the geometry. There, we observe tensile stresses as well as a plate at the bottom which reaches from the front to the back loading regions and thereby supports compressive stresses.

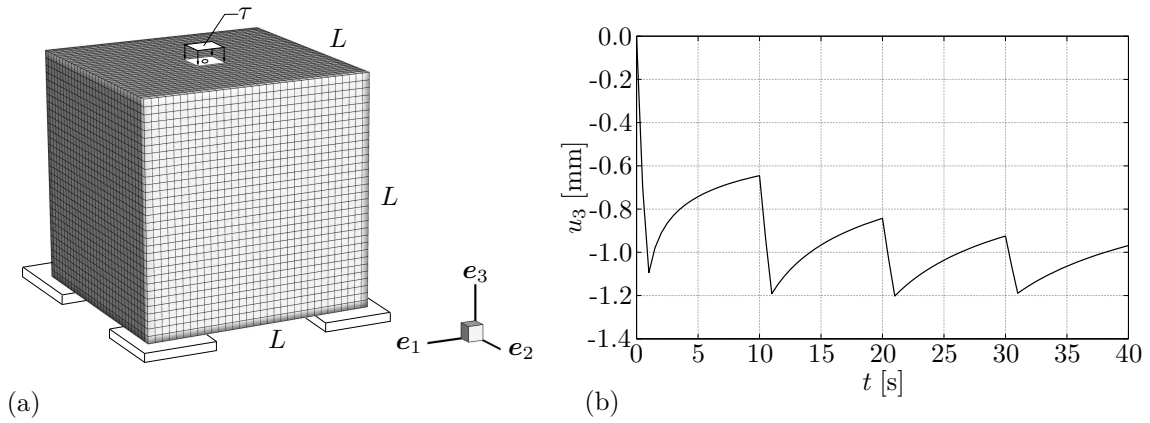


Figure 5.18: (a) Geometry, finite element mesh and boundary conditions of the stool. Four square regions at the bottom edges are clamped while a square region on top of the cube is loaded by means of a traction in vertical direction. (b) Evolution of displacement $u_3 = \mathbf{u} \cdot \mathbf{e}_3$ recorded at middle node (c) within white region at the top side.

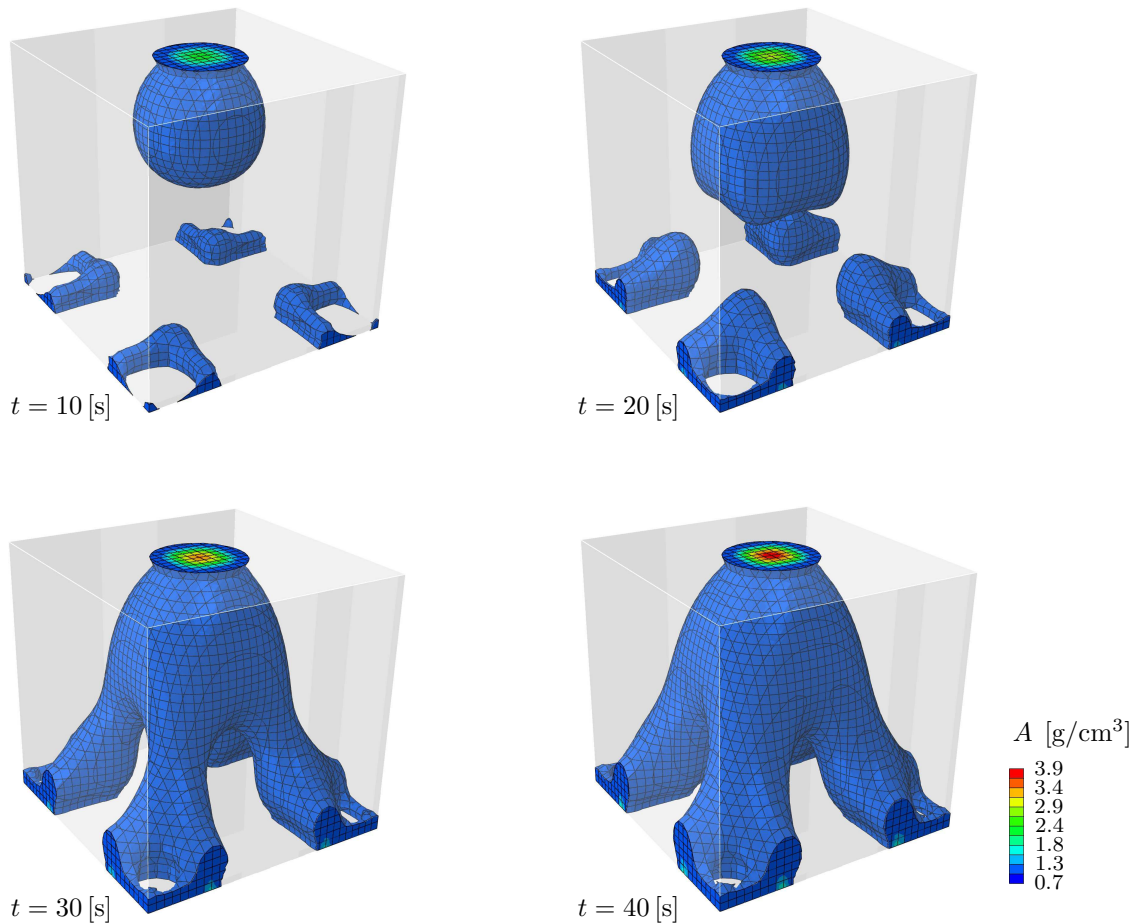


Figure 5.19: Finite element simulation of the stool exposed to traction, cf. Borrvall and Petersson [46]. Evolution of the zeroth-order density moment A at four different points in time where regions with values of $A < \rho_0^*$ are blanked.

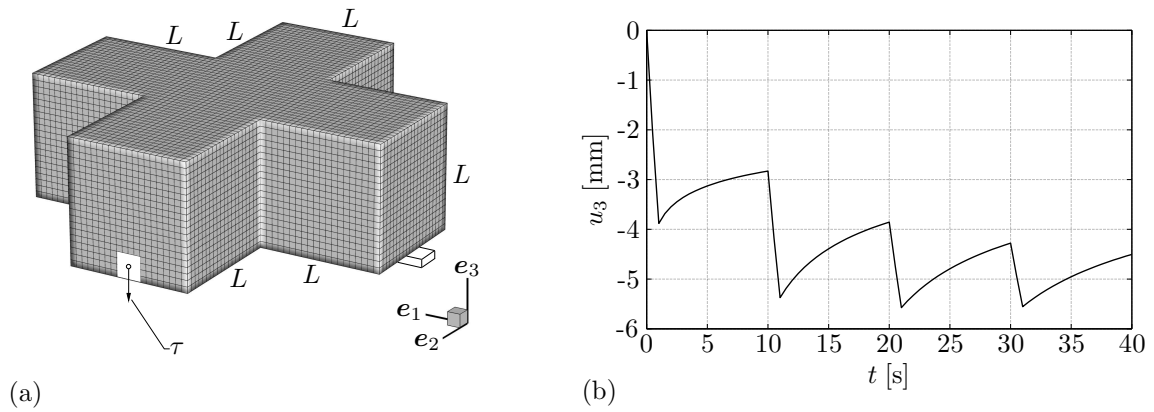


Figure 5.20: (a) Geometry, finite element mesh and boundary conditions of the coathanger. Clamped square regions of the lateral parts of the cross while shear tractions are applied at small square regions at the front and the back of the domain. (b) Evolution of displacement $u_3 = \mathbf{u} \cdot \mathbf{e}_3$ recorded at middle node (o) within white region at the front side.

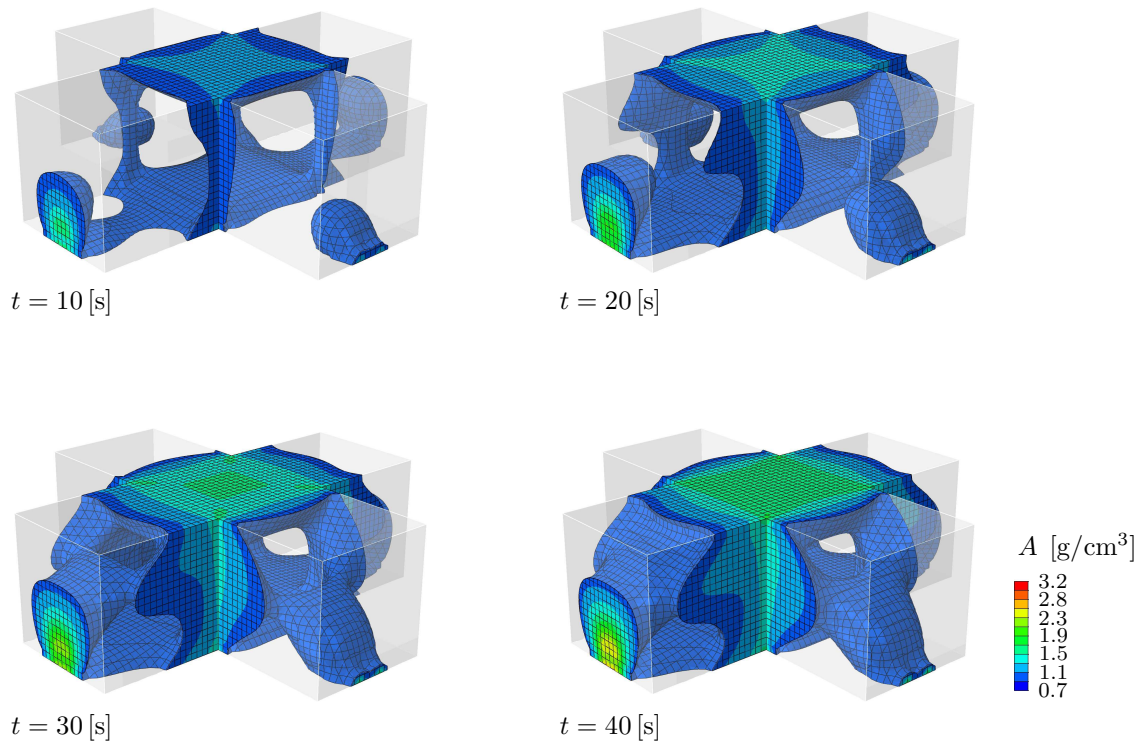


Figure 5.21: Finite element simulation of the coathanger exposed to shear traction, cf. Borrvall and Petersson [46]. Evolution of the zeroth-order density moment A at four different points in time where regions with values of $A < \rho_0^*$ are blanked.

5.5.5 Evolution of anisotropy

Since the growth process modelled in this chapter is anisotropic, we additionally investigate the evolution of anisotropy by means of representative anisotropy measures. As a scalar-valued quantity we use the difference in maximum and minimum principal values of the second-order density moment $\mathbf{A} = A_i \mathbf{n}_i \otimes \mathbf{n}_i$, i.e. $A_1 - A_3$, cf. equation C.2. This anisotropy measure is depicted as a contour plot for all four examples in Figure 5.22 at $t = 40$ [s], where an isotropic state (blue) corresponds to $A_1 - A_3 = 0$. It can clearly be seen that the degree of anisotropy changes most significantly in those regions which are predominantly loaded and thus undergo high strain energy levels.

In order to investigate the evolution of anisotropy in more detail, we now focus on three exemplary integration points so as to visualise local anisotropic material properties by means of the fourth-order moment \mathbf{A} or rather its corresponding ODF-type-function $\rho_0^{\mathbf{A}} = [\mathbf{r} \otimes \mathbf{r}] : \mathbf{A} : [\mathbf{r} \otimes \mathbf{r}]$, cf. equation (C.9).

Figure 5.22(a) shows the local state of anisotropy at three different integration points for the cantilever. As intuitively expected, we see that ODF ① located at the top load-bearing ‘flange’ of the cantilever shows the most significant change in size and shape, which reflects a pronounced growth behaviour accompanied by a considerable change of anisotropic material properties. ODF ③, evaluated near the loading region, also shows moderate anisotropic behaviour or rather texture evolution, since its shape deviates from its initial spherical distribution which, here and in the following, is marked by the superimposed grey-shaded sphere. ODF ②, however, shrinks almost isotropically, i.e. it maintains its spherical shape, which clearly indicates the degradation process of the material located in this point.

By analogy to the considerations above, Figure 5.22(b) illustrates the local state of anisotropy at three different integration points for the crank example. We observe that especially ODF ① shows a very pronounced and elongated shape in combination with a drastic change in size. This distribution corresponds to an almost transversely isotropic state, similar to ODF ① of the cantilever. ODF ②, located near the loading region, shows moderate anisotropic properties, whereas ODF ③ shrinks isotropically which clearly indicates the degradation process of the material located in this point.

Similarly, Figures 5.22(c, d) illustrate the local anisotropy for the stool and the coathanger. In both cases, especially ODFs ① show a very pronounced anisotropic shape in combination with a considerable change in size. ODFs ② and ③ show only moderate anisotropic behaviour.

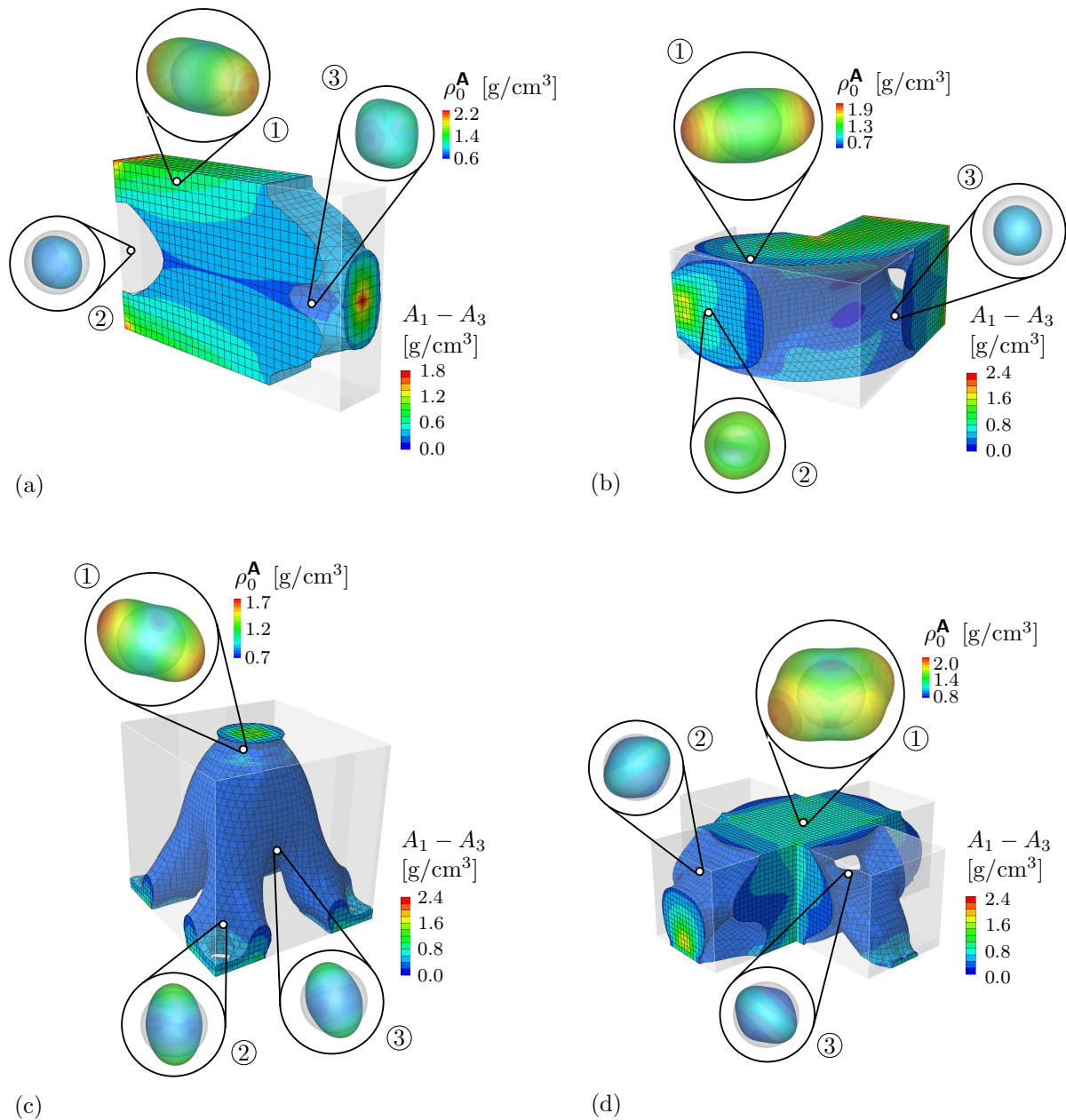


Figure 5.22: Anisotropy evolution for the four examples (a)–(d) at $t = 40$ [s] displayed at representative integration points and visualised by means of ODF-type distributions based on fourth-order density moments \mathbf{A} , whereby the isotropic initial state is plotted additionally as a reference state (grey-shaded sphere). A change in size of the ODF is attributed to densification/degradation; a change in shape of the ODF is attributed to the evolution of anisotropic material properties. The contour plots of the difference between the maximum and minimum principal value of \mathbf{A} , i.e. $A_1 - A_3$, indicates the degree of anisotropy.

6 Concluding remarks

This thesis deals with the constitutive modelling of adaptation and degradation processes for the simulation of the material behaviour of anisotropic soft and hard biological tissues. The modelling is based on the framework of finite deformation continuum mechanics. The constitutive models proposed are based on (in)elastic physical phenomena arising from the micro-mechanical structure of the material.

In **Chapter 2**, we focus on the interaction of mechanical loading levels in arteries with residual stress states and material, respectively structural, properties such as representative fibre orientations. Motivated by the postulate of the stationary total potential energy, a key contribution is to access additional information on preferred material, structural and loading parameters by direct minimisation of the total potential energy with respect to the parameters of interest in the context of the particular boundary value problem at hand. From an energy perspective, these quantities calculated are considered favourable for the design and adaptation of arterial walls. An established constitutive model together with a framework to include states of residual stresses is adopted, whereby the energy-based framework discussed can be transferred to any suitable continuum-mechanics-based constitutive model. The overall level of total potential energy is strongly influenced by the material and structural properties and by the residual stress state. The results can directly be referred to turnover and remodelling phenomena which are related to reorientation processes of the respective fibre families induced by, e.g., mechanical stimuli. To give an example, a stent changes the state of loading in an artery so that a change in fibre orientation may result in an energetically favourable state. Several numerical examples show that the values calculated for, e.g., the axial residual stretch, the opening angle or the fibre angles are in good agreement with physiological values reported in the literature.

Chapter 3 deals with a nonlocal gradient-enhanced continuum damage model within a geometrically non-linear setting for the progressive failure of collagen fibres. As a key aspect, the implicit regularisation of the problem is achieved by enhancement of the local free energy with gradient contributions of the nonlocal damage variable. Equivalence between the local and nonlocal damage field variable is ensured by a penalisation term incorporated within the free energy function. Based on the principle of minimum total potential energy, a coupled system of Euler-Lagrange equations has to be solved in weak

form in order to simulate general boundary value problems. The local elastic constitutive response is represented by a hyperelastic format and is additively composed by an isotropic and an anisotropic part. The inelastic constitutive response is assumed to be governed by a scalar $[1-d]$ -type damage approach, affecting the anisotropic elastic part only. The present gradient-enhanced damage approach proves to be quite robust, even at stages of pronounced softening, and allows the incorporation of practically any suitable *scalar-valued* damage formulation, provided that the damage function decreases faster than the respective stress measure increases with deformation. We consider a couple of three-dimensional numerical examples including isotropic and anisotropic deformation problems subjected to displacement-driven and force-driven loading. The simulation results clearly underline the assumption of a continuous degradation of the fibres contained in an undamaged matrix material. Moreover, the results clearly illustrate the desired regularisation effect and identify the mesh-objectivity by comparing different discretisations. Depending on the particular problem, a significant structural *snap-back*-behaviour is obtained which is enabled by means of using an arc-length solution procedure. Two different finite-element formulations are compared to each other. It transpires that the efficient Q1Q1-elements are able to reproduce the results obtained by the Q2Q1-formulation usually used for gradient-enhanced damage models.

In **Chapter 4**, we propose a remodelling formulation for the deformation-driven evolution of anisotropy. As various soft biological tissues are composed of a ground substrate and fibre assemblies such as collagen, we additively combine an isotropic stress term with stresses related to the contribution of fibres, which generally render the mechanical constitutive law to be anisotropic. The formulation of these fibre contributions is based on a worm-like chain model as generally derived from a sound statistical and micromechanically motivated background. By adopting a computational microsphere-based strategy, this one-dimensional formulation can be applied within a three-dimensional context. Apart from the purely passive response, the biological adaptation of the biological tissues is also incorporated. In this regard, remodelling is understood as a process which renders the internal substructure of the material to adapt to the local loading conditions. For the particular model proposed, we accordingly assume the anisotropic part to the stresses to account for these phenomena. In other words, the referential orientations of the individual fibre contributions depend on the local loading conditions and change in a viscoelastic manner over time. Such an alignment of fibres is often also denoted as reorientation or, from the biological point of view, as turnover. The model established directly combines this remodelling with the computational microsphere approach. To be specific, the respective directions are reoriented which are introduced to perform the numerical integration over the unit-sphere. As a result, the formulation accounts for deformation-induced anisotropy evolution. Without loss of generality, we adopt a distribution of integration directions yielding the initial body to be isotropic. Particular formats of evolution equations for transversely isotropic and orthotropic material behaviour are proposed, which describe the reorientation of a single integration direction. This reorientation process is driven by a representative stretch measure and renders the

related mechanical dissipation term to take a semi-definite quadratic form. The proposed evolution equations result in an alignment of the integration directions with the dominant principal stretch direction for transverse isotropy and with the ‘limiting directions’ for orthotropy so that the biological tissue maximises its load carrying capacity. Saturation effects are, on the one hand, naturally included because the remodelling stops as soon as a direction is aligned with a principal stretch direction. On the other hand, an additional saturation value is introduced to enable further limitation of the maximal degree of anisotropy of the tissue. The numerical examples investigated show the basic algorithmic applicability of the modelling framework and capture fundamental phenomena such as reorientation and remodelling effects observed for soft biological tissues. The formulation established can be applied to the simulation of general boundary value problems and, due to the fact that the initial body has been assumed to be isotropic, can also be used to estimate or rather detect the material’s anisotropic properties under physiological loading conditions.

In **Chapter 5**, we establish a growth model for the energy-driven density-evolution in bone. To model and simulate such anisotropic growth phenomena, we propose a microsphere model which allows to straightforwardly extend one-dimensional constitutive models to an anisotropic three-dimensional formulation. We adopt a well-established one-dimensional model, previously used in the context of three-dimensional but isotropic growth, which includes energy-driven evolution of directional densities. These directional densities are referred to the integration direction of the microsphere and, as an advantage of the model established, enable the computation of higher-order tensorial density moments. Analogous to so-called Young’s moduli plots common in the context of modelling and simulation texture phenomena, the visualisation of such higher-order density moments provides detailed insights into the simulated deformation-induced anisotropic local material properties. Apart from discussing the microsphere-based anisotropic growth model under homogeneous deformations, we investigate the finite element simulation of anisotropic growth in proximal tibia bone. The simulation results capture the densification effects and clearly identify the main load bearing regions. Furthermore, four three-dimensional benchmark-type problems, taken from topology-optimisation-related literature as e.g. Borrvall and Petersson [46], are discussed and the results are compared qualitatively with those obtained by the aforementioned authors. Local anisotropy evolution is visualised by means of orientation-distribution-function-type representations of higher-order density moments.

Future perspectives

The appropriate constitutive modelling of inelastic solid continua in general, and the modelling of biological tissues in particular offers considerable potential for further investigation and future research. In this thesis, we propose different modelling approaches for the constitutive description of adapting and degrading biomaterials. This active field of research is located at the intersection of different scientific disciplines, ranging from physics and mathematics as well as materials and computer sciences to biology and medicine. The ultimate long-term goal is a sophisticated patient-specific real-time prediction of potential risks in surgery and other medical treatments. Even though there seems to be a long way to go, this work aims at making an attempt to contribute towards achieving this goal. As constitutive models a priori can provide only a simplified image of realistic material behaviour, there is always room for improvement. In the following, we emphasise some aspects for possible enhancements and extensions of the models proposed in this work.

Generally, the quantitative, experimental validation is of crucial importance in order to assess the modelling capabilities of the formulations. However, the performance of reliable and suitable experiments is hardly possible in most cases. The simulation of larger boundary value problems and patient-specific mechanobiological structures in connection with the formulation proposed is desirable. This implies the need for 3D image reconstruction capabilities from, e.g., CT-scans, and the related preparation of appropriate finite-element meshes, which is a non-trivial task to achieve for most cases.

To be more specific with regard to the gradient-enhanced continuum damage formulation discussed in **Chapter 3**, it is important to mention that the assumption of an intact matrix and two equally damaging fibre families can provide only a very simplified description of the real (bio)mechanical effects. As a possible extension of the model one could, for instance, apply two independent damage variables for matrix and fibres, as proposed in Calvo et al. [55] for the purely local case, or even three independent damage variables, including matrix-damage and individual damage for each fibre family. In view of a related finite element implementation, however, this would require three individual nonlocal damage fields in the latter case, possibly accompanied by an active-set search in order to identify the currently damaged fibre family of the multi-surface damage problem, see Dimitrijević and Hackl [86] for a regularisation framework for multi-surface damage-plasticity models. Furthermore, an extension to corresponding *tensor-valued* damage approaches, with special emphasis on anisotropic damage formulations, is desirable. With regard to the non-linear elastic material behaviour, we recall that we do not apply a quasi-incompressible neo-Hookean format based on an isochoric-volumetric split, as it is typically done in related articles, see Holzapfel et al. [135] amongst others. From the computational point of view, a mixed or hybrid element formulation should be considered to account for the incompressibility-constraint; see, e.g., the recent work by Welschinger [293], who proposed an appropriate approach to avoid these problems within a gradient-extended continuum formulation, or Ask et al. [19], where an incompressibil-

ity constraint is considered in addition to the underlying coupled problem. In order to avoid numerical inconsistencies such as locking phenomena, an $\bar{\mathbf{F}}$ -approach could also be adopted for the Q1Q1-element with eight integration points. As a further possibility to reduce the CPU-time, one could establish a Q1Q1-element with one integration point and hourglass control of both global field variables. As a long-term goal it is desired to apply the proposed formulation to a more realistic or even patient-specific simulation setting, e.g. with focus on surgical activities such as balloon angioplasty. Furthermore, the comparison and identification of simulated failure and damage properties with related experimental data will be of great interest, especially regarding an appropriate calibration of the gradient parameter c_d for specific boundary value problems; see Mahnken and Kuhl [192]. Moreover, the incorporation of residual stresses for applications based on the gradient-enhanced damage model is of key importance.

In view of the remodelling formulation established in **Chapter 4**, the investigation of different driving forces and a possible combination with macroscopic target stresses constitutes an attractive line of research. The anisotropic stress contributions were based on an affine microsphere model—in future, research on the influence of non-affine isotropic and anisotropic stress terms will also be of interest. Moreover, even though the non-affine stretch part is included in the model, the non-affine tube contribution is neglected at this stage and should be incorporated in future in order to take account of the typical entangled network-like microstructure of soft tissues.

Regarding the anisotropic density-growth formulation proposed in **Chapter 5**, the comparison of simulated local anisotropic material properties with related experimental data will be of great interest in the future. The incorporation of deformation-induced anisotropic adaptation and texture evolution is also of key relevance in view of the modelling and simulation of the interaction of bones with implants as discussed by García et al. [103] and Moreo et al. [220]. Growth phenomena in biological tissues in general effect both changes in density, or rather mass, and changes in volume. One modelling approach to include changes in volume is the so-called multiplicative decomposition of the deformation gradient; see Taber [272] and Kuhl et al. [164] with application of an isotropic multiplicative growth model to the finite-element-simulation of an artery. Such growth models are also established for anisotropic tissues, see Lubarda and Hoger [188], and embedded into iterative finite element formulations to simulate complex boundary value problems; see Menzel [197, 198] and Göktepe et al. [110]. In the future, the anisotropic microsphere model can be combined with the kinematics of multiplicative growth so that additional changes in volume are directly addressed within the constitutive model; see Harrysson et al. [120] where a microsphere model is combined with a multiplicative decomposition of the deformation gradient to simulate the deformation-induced anisotropy evolution in glassy polymers.

A Thin-walled cylindrical tube – membrane approximation

In Section 2.2, we provide the governing kinematics and balance equations of an incompressible cylindrical tube subjected to bending, inflation, extension and torsion. There, the tube is assumed to be *thick-walled*. However, as reported by Ogden [227], the pressure and axial load response of a thick-walled tube is qualitatively very similar to a *thin-walled* tube. For the sake of completeness, we therefore elaborate the underlying equilibrium equations for the thin-walled cylindrical tube, also referred to as *membrane approximation*. These derivations are specifically based on the classic textbook by Ogden [225] and the lecture notes by Ogden [227]. Apart from these references, we refer to the series of papers by Haughton and Ogden [122, 123, 124, 125, 126, 127] for more detailed studies and analyses of thick-walled tubes and their corresponding thin-wall or membrane approximations.

We first rearrange the radial component of the equilibrium equation (2.57) of the underlying boundary value problem, such that

$$\frac{\partial \sigma_{rr}}{\partial r} = \frac{\sigma_{\theta\theta} - \sigma_{rr}}{r}. \quad (\text{A.1})$$

Integration of (A.1) subjected to the boundary conditions (2.58) and (2.59), i.e. $\sigma_{rr} = -p$ on $r = r_i$ and $\sigma_{rr} = 0$ on $r = r_o$, results in the following expression for the pressure p as a function of the inner radius r_i

$$p = \int_{\sigma_{rr}|_{r_i}=-p}^{\sigma_{rr}|_{r_o}=0} d\sigma_{rr} = \int_{r_i}^{r_o} [\sigma_{\theta\theta} - \sigma_{rr}] r^{-1} dr = \int_{r_i}^{r_o} \lambda_{\theta} \partial_{\lambda_{\theta}} \Psi r^{-1} dr. \quad (\text{A.2})$$

In order to obtain the pressure p as a function of the inner circumferential stretch $\lambda_{\theta i}$, we perform a variable substitution $r \rightarrow \lambda_{\theta}$, $r_i \rightarrow \lambda_{\theta i}$ and $r_o \rightarrow \lambda_{\theta o}$, noting that $\lambda_{\theta} = \lambda_{\theta}(r, R(r)) = r/R$ for $k = 1$, see relation (2.34). The remaining task is to express the infinitesimal radius dr in terms of $d\lambda_{\theta}$. For this purpose, we note that

$$\lambda_{\theta i}^2 \lambda_z - 1 = \frac{R^2}{R_i^2} [\lambda_{\theta}^2 \lambda_z - 1] = \frac{R_o^2}{R_i^2} [\lambda_{\theta o}^2 \lambda_z - 1], \quad (\text{A.3})$$

as a consequence of the incompressibility constraint. Using relations $R = r/\lambda_\theta$, $R_i = r_i/\lambda_{\theta_i}$ and $R_o = r_o/\lambda_{\theta_o}$ and solving (A.3) for λ_θ results in

$$\lambda_\theta(r) = \left[\lambda_z - \frac{\lambda_z r_i^2}{r^2} \left[1 - \frac{1}{\lambda_{\theta_i}^2 \lambda_z} \right] \right]^{-1/2}, \quad \lambda_\theta(r) = \left[\lambda_z - \frac{\lambda_z r_o^2}{r^2} \left[1 - \frac{1}{\lambda_{\theta_o}^2 \lambda_z} \right] \right]^{-1/2}, \quad (\text{A.4})$$

where $\lambda_\theta(r = r_i) = \lambda_{\theta_i}$ and $\lambda_\theta(r = r_o) = \lambda_{\theta_o}$. From equations (A.4), we are now able to determine the derivative

$$\frac{d\lambda_\theta}{dr} = -\frac{1}{R} [\lambda_\theta^2 \lambda_z - 1] \quad \text{such that} \quad dr = -R [\lambda_\theta^2 \lambda_z - 1]^{-1} d\lambda_\theta. \quad (\text{A.5})$$

By inserting the infinitesimal radius dr into equation (A.2) and by applying the substitutions $r \rightarrow \lambda_\theta$, $r_i \rightarrow \lambda_{\theta_i}$ and $r_o \rightarrow \lambda_{\theta_o}$, we finally obtain the particular format of the pressure p as a function of the inner circumferential stretch λ_{θ_i} , i.e.

$$p = \int_{\lambda_{\theta_i}}^{\lambda_{\theta_o}} \lambda_\theta \partial_{\lambda_\theta} \Psi \left[-R [\lambda_\theta^2 \lambda_z - 1]^{-1} \right] r^{-1} d\lambda_\theta = \int_{\lambda_{\theta_o}}^{\lambda_{\theta_i}} [\lambda_\theta^2 \lambda_z - 1]^{-1} \partial_{\lambda_\theta} \Psi d\lambda_\theta, \quad (\text{A.6})$$

as originally provided by Ogden [227, eq. (241)]. Similar arguments, not particularised here, lead to the expression of the ‘reduced axial load’ as given in Ogden [227, eq. (244)].

Subsequently, we elaborate the governing equilibrium equations for the *thin-wall* or *membrane approximation* of the cylindrical tube, i.e. $\sigma_{rr} = 0$. Starting with the thin wall approximation, we introduce the kinematic quantities

$$h = \lambda_r H = \frac{H}{\lambda_z \lambda_\theta}, \quad r = \lambda_\theta R, \quad r_i = \lambda_\theta R_i \quad (\text{A.7})$$

as well as the parameter

$$\epsilon = \frac{H}{R_i} = \frac{H}{R} = \frac{h \lambda_z \lambda_\theta^2}{r} \ll 1. \quad (\text{A.8})$$

We observe that the integral expression (A.6) can be approximated by means of the *mean value theorem for integrals* which results in

$$p = \int_{\lambda_{\theta_o}}^{\lambda_{\theta_i}} [\lambda_\theta^2 \lambda_z - 1]^{-1} \partial_{\lambda_\theta} \Psi d\lambda_\theta \approx [\lambda_{\theta_i} - \lambda_{\theta_o}] [\lambda_{\theta_i}^2 \lambda_z - 1]^{-1} \partial_{\lambda_\theta} \Psi. \quad (\text{A.9})$$

Next, the outer circumferential stretch λ_{θ_o} is expressed as a function of the inner circumferential stretch λ_{θ_i} and the small parameter ϵ , i.e. $\lambda_{\theta_o} = \lambda_{\theta_o}(\lambda_{\theta_i}, \epsilon)$, so that

$$\lambda_{\theta_o}(\lambda_{\theta_i}, \epsilon) = \left[\frac{1}{\lambda_z} \left[[\epsilon + 1]^2 [\lambda_{\theta_i} \lambda_z - 1] + 1 \right] \right]^{1/2}. \quad (\text{A.10})$$

We now calculate the Taylor series of $[\lambda_{\theta i} - \lambda_{\theta o}]$ with $\epsilon \rightarrow 0$ which results in

$$[\lambda_{\theta i} - \lambda_{\theta o}](\epsilon) \approx \frac{\lambda_{\theta i}^2 \lambda_z - 1}{\lambda_{\theta i} \lambda_z} \epsilon + \mathcal{O}(\epsilon)^2. \quad (\text{A.11})$$

Within this relation, we use the thin-wall approximation $\lambda_\theta \approx \lambda_{\theta i}$ (replacing $\lambda_{\theta i}$ by λ_θ) and insert this relation into (A.9). This finally yields

$$p = \epsilon [\lambda_\theta \lambda_z]^{-1} \partial_{\lambda_\theta} \Psi, \quad (\text{A.12})$$

which represents the expression originally provided by Holzapfel and Ogden [137, eq. (245)]. Similar arguments lead to the format of the reduced axial load as specified in Holzapfel and Ogden [137, eq. (246)]. Using relations (A.7), we obtain the equilibrium equations of the thin-wall (membrane) approximation of the tube in circumferential and axial direction as

$$\sigma_{\theta\theta} - \frac{r}{h} p = 0, \quad (\text{A.13})$$

$$\sigma_{zz} - \frac{r}{2h} p = 0, \quad (\text{A.14})$$

which represent the renowned ‘Barlow’s formulas’ (known as ‘Kesselformeln’ in German). While the same format of equations is used in Holzapfel and Ogden [137, p. 294], interestingly—and in contrast to the previous procedure—Holzapfel and Gasser [134] and Gasser et al. [107] introduced the inner radius r_i as

$$r_i = r - \frac{h}{2} = \lambda_\theta R - \frac{H}{2 \lambda_z \lambda_\theta} \quad (\text{A.15})$$

instead of using relation (A.7)₃. Consequently, this does not result in the classic format of Barlow’s formula, but in

$$\sigma_{\theta\theta} - \frac{r_i}{h} p = 0, \quad (\text{A.16})$$

$$\sigma_{zz} - \frac{r_i^2}{2hr} p = 0. \quad (\text{A.17})$$

B Comparison of continuum and microsphere-based neo-Hooke models

This section deals with a comparison of continuum and microsphere-based constitutive models. To be specific, the formal equivalence of both formulations is shown by means of a neo-Hooke model. At first, the constitutive equations of a standard macroscopic neo-Hooke model in its decoupled volumetric-isochoric representation is briefly reviewed. A related decoupled microsphere-model is then established and specified for two alternative representations of microsphere-energies of neo-Hookean type. The formal equivalence of the macroscopic and microsphere-models is demonstrated. Finally, we comment on some important computational issues with special regard to the numerical integration over the sphere.

B.1 Decoupled continuum neo-Hooke model

Following the decoupled form according to equation (2.7), a quasi-incompressible isotropic non-linear elastic material is governed by a strain energy function Ψ defined per unit reference volume

$$\Psi(\mathbf{C}) = \Psi_{\text{vol}}(J) + \Psi_{\text{ich}}(\bar{\mathbf{C}}), \quad (\text{B.1})$$

where we define a volumetric energy function, see Doll and Schweizerhof [88] for a detailed discussion on alternative formats, and assume the isochoric contribution to be represented by a common neo-Hookean format, i.e.

$$\Psi_{\text{vol}}(J) = \frac{\kappa}{2} [J - 1]^2, \quad \Psi_{\text{ich}}(\bar{\mathbf{C}}) = \frac{\mu}{2} [\bar{\mathbf{C}} : \mathbf{I} - 3] \quad (\text{B.2})$$

so that the strain energy is a function of the Jacobian J and the isochoric right Cauchy-Green deformation tensor $\bar{\mathbf{C}}$, cf. equation (2.5).

According to equation (2.9), the decoupled expression for the macroscopic Piola-Kirchhoff stress is given by

$$\mathbf{S} = \mathbf{S}_{\text{vol}} + \mathbf{S}_{\text{ich}}. \quad (\text{B.3})$$

On elaborating the partial derivatives in equations (2.10)₂ and (2.11)₂, i.e.

$$p := \frac{\partial \Psi_{\text{vol}}}{\partial J} = \kappa [J - 1], \quad \bar{\mathbf{S}}_{\text{ich}} := 2 \frac{\partial \Psi_{\text{ich}}}{\partial \bar{\mathbf{C}}} = \mu \mathbf{I}, \quad (\text{B.4})$$

we obtain the neo-Hookean-specific volumetric and isochoric stress contributions as

$$\mathbf{S}_{\text{vol}} = \kappa J [J - 1] \mathbf{C}^{-1}, \quad \mathbf{S}_{\text{ich}} = \mu \mathbf{I} : \mathbf{P}, \quad (\text{B.5})$$

cf. equations (2.10)₁ and (2.11)₁.

B.2 Decoupled microsphere-model

According to the microsphere concept and particularly to the article by Carol et al. [60], the macroscopic strain energy $\Psi(\mathbf{C})$ can be expressed by integrating microscopic energy contributions $\psi(J, \bar{\lambda})$ over the surface of the unit sphere \mathbb{U}^2 as

$$\Psi(\mathbf{C}) = \langle \psi(J, \bar{\lambda}) \rangle. \quad (\text{B.6})$$

Here, the microsphere-related strain energy $\psi(J, \bar{\lambda})$ is again assumed to be decoupled in volumetric-isochoric form according to

$$\psi(J, \bar{\lambda}) = \psi_{\text{vol}}(J) + \psi_{\text{ich}}(\bar{\lambda}) \quad (\text{B.7})$$

as a function of the Jacobian J and the affine stretch $\bar{\lambda}$, cf. equation (4.1). Accordingly, by using the standard format of the Piola-Kirchhoff stress tensor (2.8) and by applying the chain rule of differentiation, we obtain

$$\mathbf{S} = \left\langle 2 \frac{\partial \psi}{\partial \mathbf{C}} \right\rangle = \left\langle 2 \frac{\partial \psi_{\text{vol}}}{\partial J} \frac{\partial J}{\partial \mathbf{C}} + 2 \frac{\partial \psi_{\text{ich}}}{\partial \bar{\lambda}^2} \frac{\partial \bar{\lambda}^2}{\partial \mathbf{C}} \right\rangle. \quad (\text{B.8})$$

The partial derivatives of the micro-energies depend essentially on the particular format of the strain energy ψ and are abbreviated as

$$S_{\text{vol}} := p = \frac{\partial \psi_{\text{vol}}}{\partial J}, \quad S_{\text{ich}} := 2 \frac{\partial \psi_{\text{ich}}}{\partial \bar{\lambda}^2} = \frac{1}{\bar{\lambda}} \frac{\partial \psi_{\text{ich}}}{\partial \bar{\lambda}} \quad (\text{B.9})$$

where $\partial J / \partial \mathbf{C} = J \mathbf{C}^{-1} / 2$ and the remaining unknown term $\partial \bar{\lambda}^2 / \partial \mathbf{C}$ can be computed by means of equation (4.1) as

$$\frac{\partial \bar{\lambda}^2}{\partial \mathbf{C}} = \frac{\partial \bar{\lambda}^2}{\partial \mathbf{C}} : \frac{\partial \bar{\mathbf{C}}}{\partial \mathbf{C}} = [\mathbf{r} \otimes \mathbf{r}] : \mathbf{P}, \quad (\text{B.10})$$

in terms of the fourth-order deviatoric projection tensor \mathbf{P} , see Section 2.1.2. Accordingly, the Piola-Kirchhoff stress tensor can be expressed in decoupled form as

$$\mathbf{S} = \mathbf{S}_{\text{vol}} + \mathbf{S}_{\text{ich}} \quad (\text{B.11})$$

with the microsphere-related volumetric and isochoric stress contributions

$$\mathbf{S}_{\text{vol}} = \langle S_{\text{vol}} J \mathbf{C}^{-1} \rangle, \quad \mathbf{S}_{\text{ich}} = \langle S_{\text{ich}} [\mathbf{r} \otimes \mathbf{r}] : \mathbf{P} \rangle. \quad (\text{B.12})$$

B.2.1 Volumetric contribution

The volumetric micro-energy is formulated in accordance to its macroscopic counterpart as

$$\psi_{\text{vol}}(J) = \frac{\kappa}{2} [J - 1]^2. \quad (\text{B.13})$$

It becomes obvious that this volumetric contribution does not depend on the integration direction \mathbf{r} and can consequently be taken out of the integral (B.6). By using closed form expression (B.28), we observe that $\psi_{\text{vol}}(J) = \Psi_{\text{vol}}(J)$ so that (B.13) coincides with the macroscopic format (B.2)₁. Similar arguments hold for the micro-stresses, i.e.

$$S_{\text{vol}} = \kappa [J - 1] \quad (\text{B.14})$$

so that the integrand $S_{\text{vol}} J \mathbf{C}^{-1}$ in equation (B.12)₁ therefore does not depend on the integration direction \mathbf{r} and can be taken out of the integral. When using closed form expression (B.28), we observe that, as $S_{\text{vol}} := p$, the volumetric stress-response of the macroscopic format (B.5)₁ and the microsphere-based version indeed coincide. As a conclusion, it is not necessary to keep the volumetric term within the microsphere framework.

B.2.2 Isochoric neo-Hooke-type contribution

In the following subsections, two formats of isochoric micro-energies ψ_{ich} and related micro-stresses S_{ich} are specified for the case of a one-dimensional neo-Hookean type model and the formal equivalence to the macroscopic neo-Hooke model outlined in Appendix B.1 is demonstrated.

B.2.2.1 Model I – formulation according to Carol et al. [60]

We first adopt the microsphere energy proposed by Carol et al. [60], i.e.

$$\psi_{\text{ich}}(\bar{\lambda}) = \frac{\mu}{2} [3 \bar{\lambda}^2 + 2 \bar{\lambda}^{-3} - 5]. \quad (\text{B.15})$$

where the micro-energy vanishes in the initial undeformed state, i.e. $\psi_{\text{ich}}(\bar{\lambda} = 1) = 0$. By inserting (B.15) into (B.6), decomposing the additive terms from each other and by taking the constant terms out of the integrals, we obtain

$$\Psi_{\text{ich}} = \frac{3\mu}{2} \langle \bar{\lambda}^2 \rangle + \mu \langle \bar{\lambda}^{-3} \rangle - \frac{5\mu}{2} \langle 1 \rangle . \quad (\text{B.16})$$

By using the closed form expressions (B.30), (B.31) and (B.28), we can reproduce the macroscopic format (B.2) as

$$\Psi_{\text{ich}} = \frac{\mu}{2} \bar{\mathbf{C}} : \mathbf{I} + \mu - \frac{5}{2} \mu = \frac{\mu}{2} [\bar{\mathbf{C}} : \mathbf{I} - 3] . \quad (\text{B.17})$$

The micro-stresses can be computed according to (B.9) and (B.15) as

$$\mathbf{S}_{\text{ich}} = 3\mu [1 - \bar{\lambda}^{-5}] , \quad (\text{B.18})$$

where the micro-stress vanishes in the initial undeformed state, i.e. $\mathbf{S}_{\text{ich}}(\bar{\lambda} = 1) = 0$. Inserting equation (B.18) into (B.12)₂ and taking the constant terms out of the integrals, we obtain

$$\mathbf{S}_{\text{ich}} = 3\mu \langle \mathbf{r} \otimes \mathbf{r} \rangle : \mathbf{P} - 3\mu \langle \bar{\lambda}^{-5} \mathbf{r} \otimes \mathbf{r} \rangle : \mathbf{P} . \quad (\text{B.19})$$

By means of the closed form expressions (B.29) and (B.32), this can be simplified to

$$\mathbf{S}_{\text{ich}} = \mu [\mathbf{I} - \bar{\mathbf{C}}^{-1}] : \mathbf{P} . \quad (\text{B.20})$$

It becomes apparent that the second term vanishes since $\bar{\mathbf{C}}^{-1} : \mathbf{P} = \mathbf{0}$. This finally leads to

$$\mathbf{S}_{\text{ich}} = \mu \mathbf{I} : \mathbf{P} , \quad (\text{B.21})$$

which coincides with the macroscopic neo-Hookean format (B.5)₂. Thus, the isochoric stress-response of the macroscopic neo-Hooke model and the proposed microsphere-based version coincide.

B.2.2.2 Model II – alternative formulation

Another possible and simpler format of the microsphere energy not provided in Carol et al. [60] can be formulated as

$$\psi_{\text{ich}}(\bar{\lambda}) = \frac{3\mu}{2} [\bar{\lambda}^2 - 1] , \quad (\text{B.22})$$

where the micro-energy vanishes in the initial undeformed state, i.e. $\psi_{\text{ich}}(\bar{\lambda} = 1) = 0$. By inserting (B.22) into (B.6), decomposing the additive terms from each other and by taking the constant terms out of the integrals, we obtain

$$\Psi_{\text{ich}} = \frac{3\mu}{2} \langle \bar{\lambda}^2 \rangle - \frac{3\mu}{2} \langle 1 \rangle . \quad (\text{B.23})$$

By means of the closed form expressions (B.30) and (B.28), we can reproduce the macroscopic format (B.2) as

$$\Psi_{\text{ich}} = \frac{\mu}{2} \bar{\mathbf{C}} : \mathbf{I} - \frac{3\mu}{2} = \frac{\mu}{2} [\bar{\mathbf{C}} : \mathbf{I} - 3]. \quad (\text{B.24})$$

Consequently, the micro-stresses can be computed according to (B.9) and (B.22) as

$$S_{\text{ich}} = 3\mu. \quad (\text{B.25})$$

It is worth noting that, as opposed to the previous case, the isochoric contribution does not vanish in the initial undeformed state, since $S_{\text{ich}}(\bar{\lambda} = 1) \neq 0$. After inserting equation (B.25) into (B.12)₂, and taking the constant terms out of the integrals, we obtain

$$\mathbf{S}_{\text{ich}} = 3\mu \langle \mathbf{r} \otimes \mathbf{r} \rangle : \mathbf{P}. \quad (\text{B.26})$$

By means of closed form expression (B.29), this can be simplified to

$$\mathbf{S}_{\text{ich}} = \mu \mathbf{I} : \mathbf{P}. \quad (\text{B.27})$$

which coincides with the macroscopic neo-Hookean format (B.5)₂. Thus, the isochoric stress-response of the macroscopic neo-Hooke model and the proposed microsphere-based version coincide.

B.2.2.3 Discussion of both formulations

The isochoric mechanical response of the microsphere-based neo-Hooke models I and II is compared to the continuum neo-Hooke model (B.2)₂ in Figure B.1. A homogeneous isochoric uniaxial tensile deformation is applied, represented by the deformation gradient $\mathbf{F} = \lambda_1 \mathbf{e}_1 \otimes \mathbf{e}_1 + \lambda_1^{-1/2} [\mathbf{e}_2 \otimes \mathbf{e}_2 + \mathbf{e}_3 \otimes \mathbf{e}_3]$. The shear modulus is set to $\mu = 3.0$ [kPa] and we use an $m = 21$ -point integration scheme according to Bažant and Oh [32] for the numerical integration over the unit-sphere. According to the derivations provided in the previous sections, we expect the microsphere-based neo-Hooke models I and II to coincide with the continuum neo-Hooke model.

The isochoric micro-energies ψ_{ich} and micro-stresses S_{ich} are plotted against the affine stretch $\bar{\lambda}$ and depicted in Figures B.1(a, b). It becomes apparent that the micro-responses of both models are completely different. For model I, the micro-energy ψ_{ich} and the micro-stress S_{ich} vanish in the initial undeformed state, i.e. $\psi_{\text{ich}}(\bar{\lambda} = 1) = S_{\text{ich}}(\bar{\lambda} = 1) = 0$, which is to be expected from physical arguments. For the limiting compression case, we observe that $\psi_{\text{ich}}(\bar{\lambda} = 0) \rightarrow \infty$ and $S_{\text{ich}}(\bar{\lambda} = 0) \rightarrow -\infty$ whereas for the infinite tension case, we notice that $\psi_{\text{ich}}(\bar{\lambda} \rightarrow \infty) \rightarrow \infty$ and $S_{\text{ich}}(\bar{\lambda} \rightarrow \infty) \rightarrow 3\mu$. For model II, we also observe that the micro-energy ψ_{ich} vanishes in the initial undeformed state, i.e. $\psi_{\text{ich}}(\bar{\lambda} = 1) = 0$, and tends towards infinity for the limiting tension case, i.e. $\psi_{\text{ich}}(\bar{\lambda} \rightarrow \infty) \rightarrow \infty$. However, in contrast to model I, the micro-stress remains constant,

B Comparison of continuum and microsphere-based neo-Hooke models

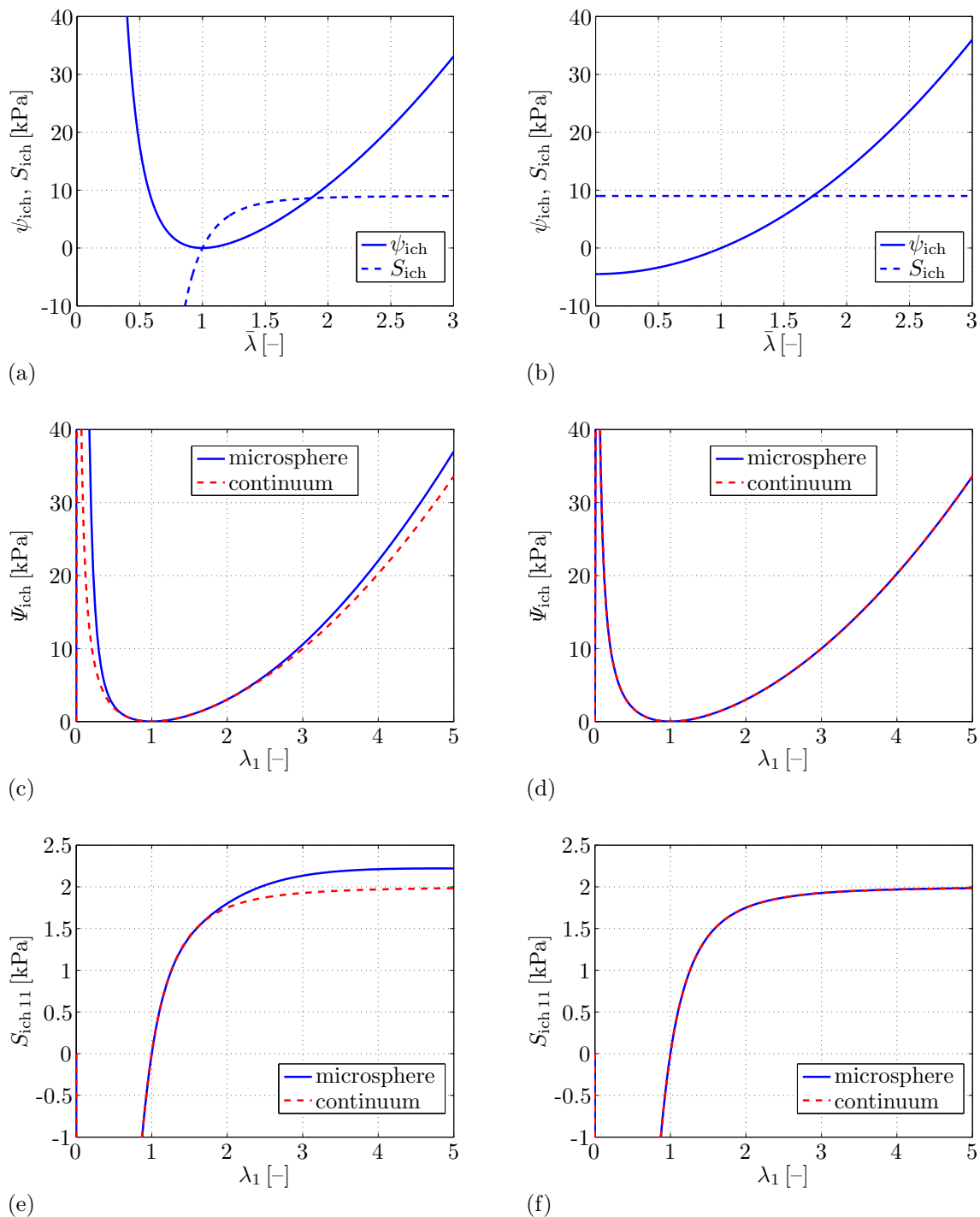


Figure B.1: Isochoric mechanical response of the microsphere-based neo-Hooke models I (left column) and II (right column) using a $m = 21$ -point integration scheme compared to the continuum neo-Hooke model (B.2)₂ for homogeneous isochoric uniaxial tension (shear modulus $\mu = 3.0$ [kPa]). (a, b) Isochoric micro-energy ψ_{ich} and micro-stress S_{ich} plotted against the affine stretch $\bar{\lambda}$. (c, d) Isochoric strain energy Ψ_{ich} and (e, f) isochoric axial Piola-Kirchhoff stress $S_{\text{ich}11}$ plotted against the loading stretch λ_1 .

i.e. $S_{\text{ich}} = 3\mu$, irrespective of the deformation which seems to be abnormal from a physical point of view. Furthermore, we notice that $\psi_{\text{ich}}(\bar{\lambda} = 0) = 3\mu/2 = \text{const}$ for the limiting compression case. Therefore, with regard to a physically sound micro-response, model I turns out to be more favourable than model II.

The macroscopic response in terms of the isochoric strain energy Ψ_{ich} and the axial Piola-Kirchhoff stress $S_{\text{ich}11} = \mathbf{e}_1 \cdot \mathbf{S}_{\text{ich}} \cdot \mathbf{e}_1$ is plotted against loading stretch $\lambda_1 = \mathbf{e}_1 \cdot \mathbf{F} \cdot \mathbf{e}_1$ and is depicted in Figures B.1(c, d) and Figures B.1(e, f), respectively. It becomes apparent that, even though both microsphere models formally coincide with the continuum neo-Hooke formulation as shown in Appendices B.2.2.1 and B.2.2.2, only model II (right column) is able to appropriately reproduce the continuum neo-Hookean response without any noticeable deviations (error in the range of machine precision) even for the comparatively large stretches λ_1 . Model I, however, which corresponds to the format proposed by Carol et al. [60], shows significant deviations in the limiting compression range $\lambda_1 \rightarrow 0$ and, more importantly, in the tension range, especially for $\lambda_1 > 2$. The relative error represented by $\text{err} := |S_{\text{ich}11}^{\text{mic}} - S_{\text{ich}11}|/S_{\text{ich}11}$ at the end of the deformation for $\lambda_1 = 5.0$ using the $m = 21$ -point integration scheme proposed by Bažant and Oh [32] is $\text{err}_{21} = 11.9\%$. This undesired effect is caused by approximation errors during the numerical integration over the unit-sphere. The integrands containing terms like $\bar{\lambda}^k$ with $k < 0$ and k being an odd number, such as $\bar{\lambda}^{-3}$ and $\bar{\lambda}^{-5}$, result in singular integral expressions which cannot be reproduced adequately by the standard (lower order, non-adaptive) $m = 21$ -point cubature rule as applied here. Therefore, with regard to the numerical integration over the sphere and the resulting macroscopic mechanical response, model II behaves more favourable than model I.

The approximation error due to the numerical integration over the unit-sphere can be reduced significantly by using higher order integration schemes. To give an example for model I and the present deformation case, an $m = 248$ -point integration scheme proposed by Heo and Xu [128] reduces the error to $\text{err}_{248} = 0.86\%$. However, as a major disadvantage, higher order integration schemes are generally associated with a higher number of integration directions, thereby increasing (decreasing) the computational cost (efficiency) drastically. As the numerical integration over the sphere has to be evaluated at each Gauss-point of a typical finite element mesh, a restriction of the number of integration directions to, say, $m \leq 100$ is recommended. Otherwise, large-scale computations cannot be accomplished in a reasonable simulation-time.

There is a great deal of literature on integration over the sphere, and associated cubature/integration schemes have been established according to different strategies and investigated especially in the mathematical community, as, for instance, Stroud [270], Lebedev [180], Atkinson [20], Bažant and Oh [32], Lebedev and Laikov [179], Fliege and Maier [98], Heo and Xu [128] and references cited therein. A more detailed quantitative study on integration schemes with regard to the present mechanical application of the microsphere models, however, lies beyond the scope of this section. A systematic investigation of a couple of different integration schemes with special regard to material symmetry conservation properties of affine microsphere models is provided by Ehret

et al. [91] or Alastrué et al. [9] for anisotropic microsphere models; see also Alastrué et al. [10] where integration schemes were adapted to the degree of anisotropy.

B.3 Closed form expressions of surface integrals

Subsequently, we summarise relevant closed form expressions of surface integrals $\langle(\bullet)\rangle = \frac{1}{4\pi} \int_{\mathbb{U}^2} (\bullet) \, dA$ for the integration over the sphere, i.e.

$$\langle 1 \rangle = 1, \quad (\text{B.28})$$

$$\langle \mathbf{r} \otimes \mathbf{r} \rangle = \frac{1}{3} \mathbf{I}, \quad (\text{B.29})$$

$$\langle \bar{\lambda}^2 \rangle = \frac{1}{3} \bar{\mathbf{C}} : \mathbf{I}, \quad (\text{B.30})$$

$$\langle \bar{\lambda}^{-3} \rangle = 1, \quad (\text{B.31})$$

$$\langle \bar{\lambda}^{-5} \mathbf{r} \otimes \mathbf{r} \rangle = \frac{1}{3} \bar{\mathbf{C}}^{-1}, \quad (\text{B.32})$$

$$\langle \mathbf{r} \otimes \mathbf{r} \otimes \mathbf{r} \otimes \mathbf{r} \rangle = \frac{1}{3} \left[\mathbf{I}_{\text{vol}} + \frac{2}{5} \mathbf{I}_{\text{dev}} \right]. \quad (\text{B.33})$$

Even though several other closed form expressions exist, we refrain from listing them in this context due to their negligible relevance for the present work. In this regard, we refer the reader to Lubarda and Krajcinovic [189], Kuhl et al. [174] or Carol et al. [60] amongst others.

C Visualisation of anisotropy

This appendix addresses different techniques used in this thesis in order to visualise anisotropic material properties. To be specific, we make use of stereographic pole projection plots, Appendix C.1, as applied in, for example, Miehe et al. [218] and Alastrué et al. [9]. We also apply two different kinds of orientation-distribution-type surface plots and discuss them in Appendix C.2. The reader is referred to Cazzani and Rovati [65] and Böhlke and Brüggemann [44] for detailed reviews on visualising higher-order tensors and to Menzel et al. [201], where similar representations have been used in the context of fibrous soft biological tissue. A general overview on visualisation techniques for anisotropic material properties and texture evolution is provided in Kocks et al. [159] and references cited therein.

C.1 Stereographic pole projection

By means of the method of stereographic projection, we project scalar quantities—in the context of Chapter 5, for instance, the micro-densities ρ_0^i —related to the vectorial integration directions $\mathbf{r}^i \in \mathbb{U}^2$ onto the equatorial plane by viewing from the south pole; see Figure C.1 for an illustration of the $m = 21$ integration scheme used in this work. In Figure C.1 we emphasise two exemplary integration directions: the intersection of the connecting line between an integration point and the south pole with the equatorial plane is the stereographic projected point sought. The related micro-densities ρ_0^i can be visualised by a contour-plot as shown in Figure 5.4.

C.2 Orientation distribution functions related to higher-order moments

In addition to the method of stereographic projection, we also apply two different orientation distribution function (ODF) type representations. To this end, we introduce

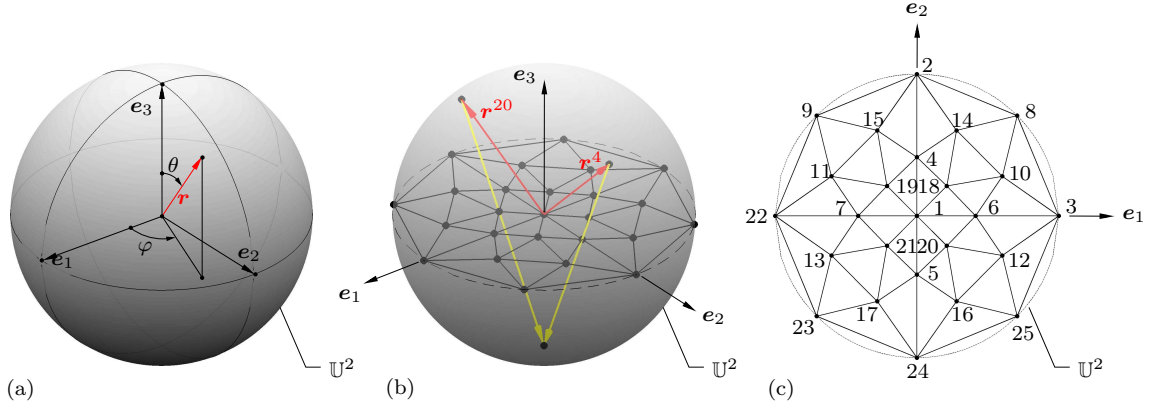


Figure C.1: Stereographic projection: (a) Unit vector \mathbf{r} parameterised by spherical angles φ and θ with respect to a Cartesian base system $\{\mathbf{e}_1, \mathbf{e}_2, \mathbf{e}_3\}$; (b) Graphical illustration of the method of stereographic projection for $m = 21$ integration directions (in the upper half-sphere) by means of two exemplary unit vectors \mathbf{r}^4 and \mathbf{r}^{20} ; (c) Two-dimensional pole projection plot. Points 22–25 are added for visualisation purposes, cf. Miehe et al. [218].

generalised structural tensors or rather higher-order density moments. The scalar moment of zeroth order is introduced as

$$A = \langle \rho_0 \rangle \approx \sum_{i=1}^m \rho_0^i w^i \quad (\text{C.1})$$

and can be interpreted as a measure of the macroscopic density. The moment of second-order reads

$$\mathbf{A} = 3 \langle \rho_0 \mathbf{r} \otimes \mathbf{r} \rangle \approx 3 \sum_{i=1}^m \rho_0^i w^i \mathbf{r}^i \otimes \mathbf{r}^i, \quad (\text{C.2})$$

whereas the moment of fourth order is represented by

$$\mathbf{A} = 5 \langle \rho_0 \mathbf{r} \otimes \mathbf{r} \otimes \mathbf{r} \otimes \mathbf{r} \rangle \approx 5 \sum_{i=1}^m \rho_0^i w^i \mathbf{r}^i \otimes \mathbf{r}^i \otimes \mathbf{r}^i \otimes \mathbf{r}^i. \quad (\text{C.3})$$

Taking identities (B.28), (B.29) and (B.33) in account, we normalise each of these quantities such that an initially isotropic setting at $t = 0$, i.e. $\rho_0^i = \rho_0^*$ results in

$$A|_{t_0} = \rho_0^*, \quad (\text{C.4})$$

$$\mathbf{A}|_{t_0} = \rho_0^* \mathbf{I}, \quad (\text{C.5})$$

$$\mathbf{A}|_{t_0} = \rho_0^* \left[\frac{5}{3} \mathbf{I}_{\text{vol}} + \frac{2}{3} \mathbf{I}_{\text{dev}} \right], \quad (\text{C.6})$$

cf. Bažant and Oh [31] and Lubarda and Krajcinovic [189].

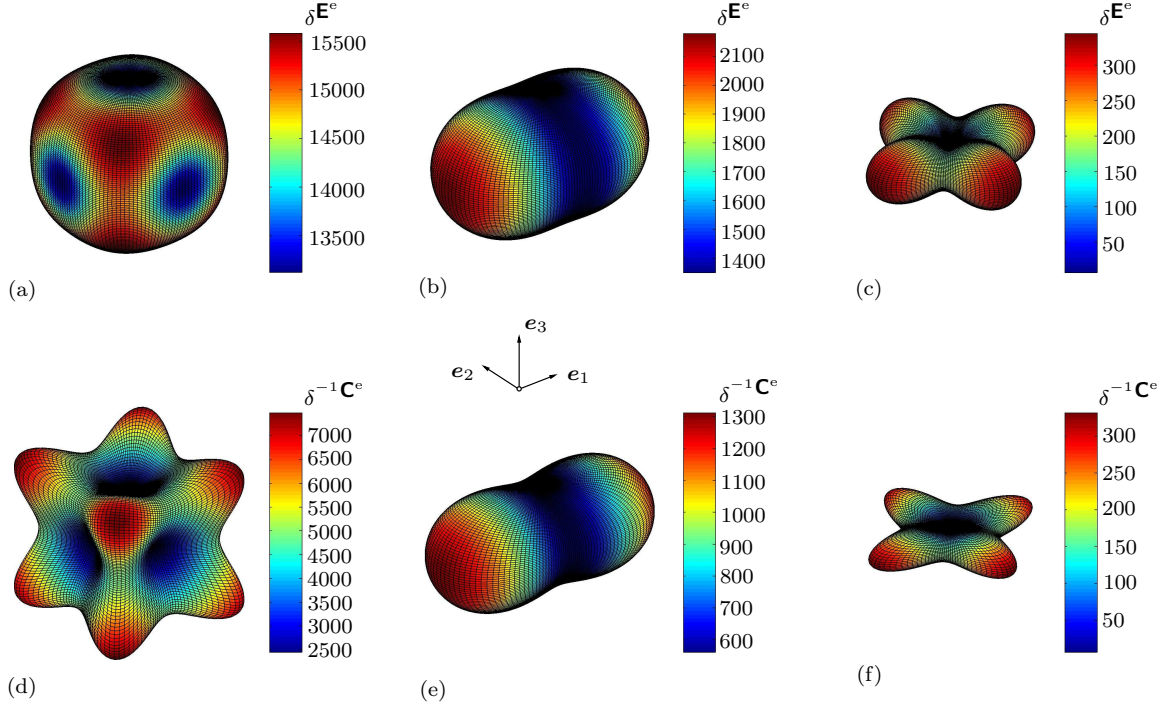


Figure C.2: Visualisation of anisotropy by ODF-type surface plots based on fourth-order elasticity and compliance tensors; upper row (a–c) based on \mathbf{E}^e , lower row (d–f) based on \mathbf{C}^e . Coefficients of \mathbf{E}^e in Voigt notation, superscript v: (a, d) Cubic symmetry with $E_{11}^{e,v} = 13120$, $E_{12}^{e,v} = 11450$, $E_{44}^{e,v} = 2680$, cf. Ma et al. [191]. (b, e) Transverse isotropy with $E_{11}^{e,v} = 2180$, $E_{33}^{e,v} = 1350$, $E_{44}^{e,v} = 375$, $E_{12}^{e,v} = 1010$, $E_{23}^{e,v} = 1000$. (c, f) Orthotropy with $E_{11}^{e,v} = 344.87$, $E_{22}^{e,v} = 344.87$, $E_{33}^{e,v} = 6.92$, $E_{44}^{e,v} = 59.24$, $E_{55}^{e,v} = 30.94$, $E_{66}^{e,v} = 30.94$, $E_{12}^{e,v} = -67.575$, $E_{23}^{e,v} = 0.37$, $E_{13}^{e,v} = 0.37$. Units in $[\text{N}/\text{mm}^2]$.

In order to compute a graphical representation of these higher-order density moments, we parametrise unit vectors $\mathbf{r} \in \mathbb{U}^2$ in terms of spherical coordinates, for example

$$\mathbf{r}(\theta, \varphi) = \sin(\theta) \cos(\varphi) \mathbf{e}_1 + \sin(\theta) \sin(\varphi) \mathbf{e}_2 + \cos(\theta) \mathbf{e}_3. \quad (\text{C.7})$$

This allows the calculation of scalar ODF-type quantities which, for the second-order moment, result in

$$\rho_0^{\mathbf{A}}(\mathbf{A}, \mathbf{r}) = \mathbf{r} \cdot \mathbf{A} \cdot \mathbf{r}, \quad (\text{C.8})$$

cf. Figures 4.2 and 4.4. For the fourth-order moment we similarly introduce

$$\rho_0^{\mathbf{A}}(\mathbf{A}, \mathbf{r}) = [\mathbf{r} \otimes \mathbf{r}] : \mathbf{A} : [\mathbf{r} \otimes \mathbf{r}]. \quad (\text{C.9})$$

Isotropic material properties, in other words $\mathbf{A} \propto \mathbf{I}$ and $\mathbf{A} \propto [\frac{5}{3} \mathbf{I}_{\text{vol}} + \frac{2}{3} \mathbf{I}_{\text{dev}}]$, are represented by purely spherical distributions so that $\rho_0^{\mathbf{A}}$ and $\rho_0^{\mathbf{A}}$ are independent of \mathbf{r} . ODF-type representations of fourth-order tensorial quantities are well-established in the context of so-called Young’s modulus plots; see Kocks et al. [159]. The underlying

fourth-order tensors set to visualise the materials' anisotropy are the elasticity tensor \mathbf{E}^e and the corresponding compliance tensor $\mathbf{C}^e = [\mathbf{E}^e]^{-1}$. By analogy with equation (C.8) we obtain the ODF-type quantities

$$\delta^{\mathbf{E}^e}(\mathbf{E}^e, \mathbf{r}) = [\mathbf{r} \otimes \mathbf{r}] : \mathbf{E}^e : [\mathbf{r} \otimes \mathbf{r}], \quad (\text{C.10})$$

see Figure C.2(a–c), and

$$\delta^{-1\mathbf{C}^e}(\mathbf{C}^e, \mathbf{r}) = [[\mathbf{r} \otimes \mathbf{r}] : \mathbf{C}^e : [\mathbf{r} \otimes \mathbf{r}]]^{-1}, \quad (\text{C.11})$$

see Figure C.2(e–f). Note, that Equation (C.10) represents solely components of the elasticity tensor, whereas Equations (C.11) reflects directional Young's modulus properties; see Cazzani and Rovati [65] and Böhlke and Brüggemann [44] for more background information. In view of the calculation of the compliance tensor as the inverse of the elasticity tensor in Voigt notation, the reader is referred to Nemat-Nasser and Hori [223].

Since higher-order moments include more information on the materials' anisotropic properties with increasing tensorial order, ODF-type plots related to fourth-order moments show a more pronounced anisotropic shape than those related to second-order moments; see Figure 5.4. In view of the moment of second order, we furthermore perform a spectral decomposition,

$$\mathbf{A} = \sum_{j=1}^3 A_j \mathbf{n}_j \otimes \mathbf{n}_j \quad \text{with} \quad \mathbf{n}_i \cdot \mathbf{n}_j = \delta_{ij}, \quad (\text{C.12})$$

to introduce a scalar measure of anisotropy defined by the difference between the largest and smallest principal value of \mathbf{A} , i.e. $A_1 - A_3$; see, e.g., Figures 4.8 and 5.7. In the case of an isotropic or rather spherical distribution, all principal values of \mathbf{A} turn out to coincide so that $A_1 - A_3 = 0$. A spectral decomposition could also be applied to the fourth-order density moment \mathbf{A} , see Kocks et al. [159], but is not applied in this work.

D Implementation of element-formulations via Abaqus subroutine UEL

The non-linear coupled finite-element-formulation outlined in Section 3.3 can be implemented in the commercial finite-element-software Abaqus via so-called *user subroutines*. For a general overview, see the Abaqus Analysis User's Manual [2, ch. 17.1.1]. This section provides a brief review on aspects of implementation in the context of the Abaqus internal user subroutine UEL.

D.1 Vector-matrix-format based on Voigt notation

The finite element approach applied in Section 3.3 is based on the symmetric Cauchy stress tensor $\boldsymbol{\sigma}$ and its work conjugate rate of deformation measure \boldsymbol{d} . This approach is also referred to as 'FE-formulation in current or spatial configuration', cf. Wriggers [299] amongst others. Generally, the particular term refers to the resulting integrals which are calculated over the respective regions of the current configuration. As one alternative, the 'FE-formulation in reference or material configuration' is advocated which is based on the symmetric Piola-Kirchhoff stress tensor \boldsymbol{S} and its work conjugate deformation measure $\dot{\boldsymbol{C}}$. This approach is also referred to as 'total Lagrangian formulation'. Here, the resulting integrals are calculated over the respective regions of the reference configuration. As a third option, the finite element discretisation can also be performed in terms of the unsymmetric Piola stress tensor \boldsymbol{P} and its work conjugate deformation measure $\dot{\boldsymbol{F}}$. It is interesting to note that the linearisation of the latter formulation based on \boldsymbol{P} contains one term only, whereas the linearisation associated with the other two approaches is represented by two terms, namely a material and a geometrical contribution, cf. equation (3.102). In either case, it is important to emphasise that all three formulations are equivalent in view of rendering the same results. For an illustrative overview of different approaches, we refer the reader to the classic textbook by Bathe [25, p. 486].

In the following, we outline an efficient and compact FE-implementation in current or spatial configuration using a common Voigt-notation-based vector-matrix-format.

The vector-matrix-format applied is based on the conventions given in the Abaqus Analysis User's Manual [2, ch. 1.2.2] using a modified Voigt-notation denoted by the superscript v. The second-order Cauchy stress tensor $\boldsymbol{\sigma}$, for instance, can be represented in vector format by

$$\boldsymbol{\sigma}^v = [\sigma_{11} \quad \sigma_{22} \quad \sigma_{33} \quad \sigma_{12} \quad \sigma_{13} \quad \sigma_{23}]^t. \quad (\text{D.1})$$

The fourth-order tangent operator \mathbf{e} transforms to \mathbf{e}^v analogously to $\boldsymbol{\sigma}^v$.

An element-wise arrangement of the nodal field variables, i.e. the placements $\boldsymbol{\varphi}_I$ and the nonlocal damage variable ϕ_K , according to

$$\boldsymbol{\varphi}_e = [\boldsymbol{\varphi}_1 \quad \dots \quad \boldsymbol{\varphi}_{n_{\text{en}}}^t]^t, \quad \boldsymbol{\phi}_e = [\phi_1 \quad \dots \quad \phi_{n_{\text{en}}}^t]^t, \quad (\text{D.2})$$

as well as the introduction of the shape functions N_I^φ , N_K^ϕ in matrix form as

$$\mathbf{N}^\varphi = \begin{bmatrix} N_1^\varphi & 0 & 0 & \dots & N_{n_{\text{en}}}^\varphi & 0 & 0 \\ 0 & N_1^\varphi & 0 & \dots & 0 & N_{n_{\text{en}}}^\varphi & 0 \\ 0 & 0 & N_1^\varphi & \dots & 0 & 0 & N_{n_{\text{en}}}^\varphi \end{bmatrix}, \quad \mathbf{N}^\phi = [N_1^\phi \quad \dots \quad N_{n_{\text{en}}}^\phi] \quad (\text{D.3})$$

enables us to specify the field variables according to relations (3.83) in vector-matrix-notation as

$$\boldsymbol{\varphi}^h = \mathbf{N}^\varphi \cdot \boldsymbol{\varphi}_e, \quad \phi^h = \mathbf{N}^\phi \cdot \boldsymbol{\phi}_e. \quad (\text{D.4})$$

The associated tri-quadratic and tri-linear shape functions N_I^φ and N_I^ϕ , respectively, can be obtained, e.g. from Dhondt [82] or the Abaqus Theory Manual [4, ch. 3.2.4].

Applying a convenient arrangement of the nodal coordinates as

$$\boldsymbol{x}_e = \begin{bmatrix} x_1 & \dots & x_{n_{\text{en}}} \\ y_1 & \dots & y_{n_{\text{en}}} \\ z_1 & \dots & z_{n_{\text{en}}} \end{bmatrix}, \quad \mathbf{X}_e = \begin{bmatrix} X_1 & \dots & X_{n_{\text{en}}} \\ Y_1 & \dots & Y_{n_{\text{en}}} \\ Z_1 & \dots & Z_{n_{\text{en}}} \end{bmatrix}, \quad (\text{D.5})$$

accompanied by an appropriate arrangement of the derivatives of the shape functions, i.e. $\nabla_{\boldsymbol{\xi}} N_I^\varphi$ and $\nabla_{\boldsymbol{\xi}} N_I^\phi$, with respect to the natural coordinates $\boldsymbol{\xi} = (\xi, \eta, \zeta)$ like

$$\boldsymbol{\gamma}^\alpha = \begin{bmatrix} \nabla_\xi N_1^\alpha & \nabla_\eta N_1^\alpha & \nabla_\zeta N_1^\alpha \\ \vdots & \vdots & \vdots \\ \nabla_\xi N_{n_{\text{en}}}^\alpha & \nabla_\eta N_{n_{\text{en}}}^\alpha & \nabla_\zeta N_{n_{\text{en}}}^\alpha \end{bmatrix}, \quad \alpha = \varphi, \phi \quad (\text{D.6})$$

enable us to re-formulate relations (3.87)₂ and (3.88)₂ in terms of the simple expressions

$$\boldsymbol{j}_e = \boldsymbol{x}_e \cdot \boldsymbol{\gamma}^\varphi, \quad \mathbf{J}_e = \mathbf{X}_e \cdot \boldsymbol{\gamma}^\varphi. \quad (\text{D.7})$$

This allows the calculation of the deformation gradient $\mathbf{F}^h = \mathbf{j}_e \cdot \mathbf{J}_e^{-1}$ according to (3.89). Likewise, introducing the spatial gradients of the shape functions $\nabla_x N_I^\varphi$ and $\nabla_x N_I^\phi$ in matrix form as

$$\mathbf{G}^\alpha = \boldsymbol{\gamma}^\alpha \cdot \mathbf{j}_e^{-1} = \begin{bmatrix} \nabla_x N_1^\alpha & \nabla_y N_1^\alpha & \nabla_z N_1^\alpha \\ \vdots & \vdots & \vdots \\ \nabla_x N_{n_{\text{en}}}^\alpha & \nabla_y N_{n_{\text{en}}}^\alpha & \nabla_z N_{n_{\text{en}}}^\alpha \end{bmatrix}, \quad \alpha = \varphi, \phi, \quad (\text{D.8})$$

together with a rearrangement of the spatial gradients of the shape functions as

$$\mathbf{B}^\varphi = \begin{bmatrix} G_{11}^\varphi & 0 & 0 & \dots & G_{n_{\text{en}}1}^\varphi & 0 & 0 \\ 0 & G_{12}^\varphi & 0 & \dots & 0 & G_{n_{\text{en}}2}^\varphi & 0 \\ 0 & 0 & G_{13}^\varphi & \dots & 0 & 0 & G_{n_{\text{en}}3}^\varphi \\ G_{12}^\varphi & G_{11}^\varphi & 0 & \dots & G_{n_{\text{en}}2}^\varphi & G_{n_{\text{en}}1}^\varphi & 0 \\ G_{13}^\varphi & 0 & G_{11}^\varphi & \dots & G_{n_{\text{en}}3}^\varphi & 0 & G_{n_{\text{en}}1}^\varphi \\ 0 & G_{13}^\varphi & G_{12}^\varphi & \dots & 0 & G_{n_{\text{en}}3}^\varphi & G_{n_{\text{en}}2}^\varphi \end{bmatrix}, \quad \mathbf{B}^\phi = \mathbf{G}^{\phi^t} \quad (\text{D.9})$$

enables us to specify the spatial gradient of the field variables according to relations (3.84) in the vector-matrix-notation as

$$\nabla_x \boldsymbol{\varphi}^h = \mathbf{B}^\varphi \cdot \boldsymbol{\varphi}_e, \quad \nabla_x \boldsymbol{\phi}^h = \mathbf{B}^\phi \cdot \boldsymbol{\phi}_e. \quad (\text{D.10})$$

As a result, the internal and external force-vectors on element-level can conveniently be expressed as

$$\mathbf{f}_{\text{int}}^\varphi = \int_{\mathcal{B}_t} \mathbf{B}^{\varphi^t} \cdot \boldsymbol{\sigma}^v \, dv, \quad (\text{D.11})$$

$$\mathbf{f}_{\text{ext}}^\varphi = \int_{\mathcal{B}_t} \mathbf{N}^{\varphi^t} \cdot \bar{\mathbf{b}} \, dv + \int_{\partial \mathcal{B}_t} \mathbf{N}^{\varphi^t} \cdot \bar{\mathbf{t}} \, da, \quad (\text{D.12})$$

$$\mathbf{f}_{\text{int}}^\phi = \int_{\mathcal{B}_t} \mathbf{B}^{\phi^t} \cdot \mathbf{y} \, dv, \quad (\text{D.13})$$

$$\mathbf{f}_{\text{ext}}^\phi = \int_{\mathcal{B}_t} \mathbf{N}^{\phi^t} \cdot \mathbf{y} \, dv, \quad (\text{D.14})$$

while the Jacobians on element-level take the following compact representations

$$\mathbf{K}^{\varphi\varphi} = \int_{\mathcal{B}_t^e} \left[\mathbf{B}^{\varphi^t} \cdot \mathbf{e}^v \cdot \mathbf{B}^\varphi + [\mathbf{G}^\varphi \cdot \boldsymbol{\sigma} \cdot \mathbf{G}^{\varphi^t}] \odot \mathbf{I} \right] dv, \quad (\text{D.15})$$

$$\mathbf{K}^{\varphi\phi} = \int_{\mathcal{B}_t^e} \mathbf{B}^{\varphi^t} \cdot \left[\frac{d\boldsymbol{\sigma}}{d\phi} \right]^v \cdot \mathbf{N}^\phi \, dv, \quad (\text{D.16})$$

$$\mathbf{K}^{\phi\varphi} = \int_{\mathcal{B}_t^e} \mathbf{N}^{\phi^t} \cdot \left[2 \frac{d\mathbf{y}}{d\mathbf{g}} \right]^v \cdot \mathbf{B}^\varphi \, dv, \quad (\text{D.17})$$

$$\mathbf{K}^{\phi\phi} = \int_{\mathcal{B}_t^e} \left[\mathbf{N}^{\phi^t} \left[\frac{d\mathbf{y}}{d\phi} \right]^v \cdot \mathbf{N}^\phi + \mathbf{B}^{\phi^t} \cdot \left[\frac{d\mathbf{y}}{d\nabla_x \phi} \right]^v \cdot \mathbf{B}^\phi \right] dv, \quad (\text{D.18})$$

allowing us to express the geometrical contribution of $\mathbf{K}^{\varphi\varphi}$ conveniently by means of a Kronecker product¹ denoted by the symbol \odot , see Weisstein [292].

D.2 UEL-implementation in Abaqus

Abaqus provides a programming-interface that allows the implementation of element-formulations via the UEL-subroutine, see the Abaqus User Subroutines Reference Manual [5, ch. 1.1.27] or the Abaqus Analysis User's Manual [2, ch. 31.15.1]. The UEL-interface makes it possible to include any element of almost arbitrary complexity such as higher-order elements for coupled problems. A general user element can be used conveniently with the Abaqus-internal solution procedures as, for instance, incremental-iterative Newton-Raphson schemes with adaptive incrementation or arc-length methods such as the modified Riks-algorithm, as discussed in Appendix E. Furthermore, user elements can also be applied in the context of contact problems, even though restricted to the definition of only slave surfaces in such an analysis. As a minor disadvantage, plotting and visualisation of results associated with the application of user elements are not directly supported by the Abaqus Viewer. However, these can be performed by using the subroutines UEXTERNALDB and URDFIL in connection with the Abaqus scripting interface to create binary or ASCII-based output files which, in turn, can be read by the Abaqus Viewer or any other FE-postprocessing software; for details we refer to Section D.5. In the following, we outline particular implementation-issues with regard to the Abaqus user subroutine UEL.

The current estimates of the basic solution variables—placements $\boldsymbol{\varphi}$ and nonlocal damage variable ϕ —at the element-nodes enter the UEL subroutine at the beginning of the iteration and are stored in the vector $\mathbf{U} := \mathbf{d}_e$ which is arranged according to

$$\mathbf{d}_e := [\mathbf{u}_1 \quad \phi_1 \quad \dots \quad \mathbf{u}_{n_{\text{en}}^\varphi} \quad \phi_{n_{\text{en}}^\phi}]^t, \quad (\text{D.20})$$

with the nodal displacements $\mathbf{u}_I = \boldsymbol{\varphi}_I - \mathbf{X}_I$. Furthermore, the referential coordinates \mathbf{X}_e are stored in the array `COORDS` := \mathbf{X}_e and arranged according to the format in (D.5)₂.

¹Let \mathbf{A} be a $m \times n$ matrix, and \mathbf{B} be a $p \times q$ matrix. Their Kronecker product $\mathbf{C} = \mathbf{A} \odot \mathbf{B}$, also called matrix direct product, is defined as $C_{ab} := A_{ij}B_{kl}$ with $a := p[i - 1] + k$ and $b := q[j - 1] + l$ resulting in the $mp \times nq$ matrix

$$\mathbf{A} \odot \mathbf{B} := \begin{bmatrix} A_{11} \mathbf{B} & \cdots & A_{1n} \mathbf{B} \\ \vdots & \ddots & \vdots \\ A_{m1} \mathbf{B} & \cdots & A_{mn} \mathbf{B} \end{bmatrix}. \quad (\text{D.19})$$

The essential quantities to be specified within the UEL-subroutine are the element residual vector **RHS**, the element-based Jacobian or stiffness-matrix **AMATRIX**, and the internal solution-dependent state variables **SVARS**. In summary,

$$\mathbf{RHS}(:, 1) := \mathbf{r}_e, \quad (\text{D.21})$$

$$\mathbf{AMATRIX} := \mathbf{K}_e, \quad (\text{D.22})$$

$$\mathbf{SVARS} := \mathcal{I}_e, \quad (\text{D.23})$$

cf. the system of equations (3.106). It is important to note that, when the classic Newton-Raphson-based solution scheme is used, **RHS** consists of **NRHS=1** column—in contrast to the arc-length method discussed in Appendix F.2 where **NRHS=2**. Definition (D.21) requires that the external force loads $\mathbf{f}_{\text{ext } e}$ must be passed into the UEL by means of distributed load definitions. Coding the subroutine UEL requires the distribution of the loads into consistent equivalent nodal forces and accounting for them in the calculation of the **RHS** array.

D.3 UEL-interface in Abaqus

With regard to the input-file, which basically defines an analysis in Abaqus, a general user-element is introduced by the keyword ***USER ELEMENT**, see the Abaqus Keywords Reference Manual [3], and is fully defined by the sequence

```

*USER ELEMENT, TYPE=Un, NODES=20, ...
... COORDINATES=3, PROPERTIES=n, VARIABLES=n
Data line(s) defining the active degrees of freedom as
DOF1, DOF2, ...
ENOD, DOF1, DOF2, ... , e.g.
1, 2, 3, 11
9, 1, 2, 3
*ELEMENT, TYPE=Un, ELSET=(element-set-label)
Data line(s) defining the connectivity list
*UEL PROPERTY, ELSET=(element-set-label)
Data line(s) specifying material/algorithmic parameters

```

Two parameters, the **TYPE** and the **NODES**, are *required* for a general user-element. The **TYPE**-parameter defines the ‘name’ of the element and is set by the format Un , where $1 \leq n < 10000$ is an integer. In order to use this particular element type, **TYPE=Un** must be assigned to the ***ELEMENT** keyword. The **NODES**-parameter defines the number

of nodes associated with an element of this type which for the present case result in `NODES=20`, cf. Figure 3.3.

Furthermore, several *optional* parameters can be set to define the general user-element. Here, we use the `COORDINATES`, the `PROPERTIES`, and the `VARIABLES`-parameter. Several other parameters exist, but can be omitted for the present problem. The `COORDINATES`-parameter defines the maximum number of coordinates needed in the user subroutine UEL at any node point of the element and is set to 3 representing the three-dimensional Cartesian frame x, y, z . The `PROPERTIES`-parameter specifies the number of material or algorithmic parameters, etc., needed in the user subroutine UEL. Finally, the `VARIABLES`-parameter defines the number of internal variables to be stored within the element and is typically set equal to the number of integration points multiplied by the number of internal variables per integration point.

Subsequently, two data lines define the *active degrees of freedom* (DOFs) associated with the element, cf. Figure 3.3. According to the Abaqus Analysis User's Manual [2, ch. 31.15.1], the active DOFs are generally specified at each node of the element. If the DOFs are identical at all of the element-nodes, the list of DOFs is specified only once, `DOF1` being the first DOF active at the node, `DOF2` the second one, etc. Each time the DOFs at a node change compared to the previous node, a new list of DOFs must be specified, `ENOD` representing the (local) element-node number, wherefrom the new list becomes valid. Thereby, different element-nodes can have different DOFs which is especially beneficial when dealing with coupled field problems as in the present context. The order of DOFs to be maintained for a user element are defined according to the conventions in the Abaqus Analysis User's Manual [2, ch. 1.2.2] and are particularly important for convergence controls in non-linear analyses.

For the applications considered in Chapter 3, nodes 1–8 exhibit displacement and nonlocal damage DOFs. This is defined by the first data line where 1, 2, 3 represent the displacements in x -, y - and z -direction, and where 11 represents the nonlocal damage variable ϕ taking the interpretation of a (scalar) temperature-like quantity. The second data line states that, from node 9 on, only displacement DOFs 1, 2 and 3 are active. This results in an arrangement of the element variables in so far as all of the DOFs at the first node appear first, followed by the DOFs at the second node, etc., see also equation (D.20).

Finally, the values of material or algorithmic parameters associated with the user element are specified by the `*UEL PROPERTY` option. These property values are assigned on an element set basis (`ELSET`) which conveniently enables the use of the same UEL subroutine for user elements with different properties.

D.4 Approximation of Jacobians on element-level

Even though a multitude of algorithms exists for the solution of non-linear systems of equations, in a finite-element-related context, the *classic Newton-Raphson-scheme* is

most frequently applied due to its conceptual simplicity and quadratic rate of convergence close to the solution point. However, in order to guarantee this quadratic convergence behaviour, an *algorithmic* or *consistent linearisation* of the residual function is required. The notion ‘consistent linearisation’ was introduced by Hughes and Pister [141] and represents a linearisation of all quantities related to the non-linear problem. This process involves Jacobians, practically speaking the ‘current tangent’, which—depending on the particular problem—may result in complex analytical expressions which are difficult and time-consuming to derive.

Alternative procedures are proposed in the literature and used for practical applications, such as the *modified Newton-Raphson-scheme* or the *quasi-Newton-scheme* which involve only the ‘initial tangent’ and an ‘approximated inverse of the tangent’, respectively. This reduces the computational cost within a typical iteration-step but, at the same time, increases the number of iterations used, since the convergence rate is no longer quadratic. A detailed summary of different solution methods for non-linear systems of equations, together with an extensive bibliographical references, can be found, e.g., in the textbook by Wriggers [299].

In order to avoid the laborious linearisation process required for the classic Newton-Raphson method, numerical approximation schemes for the determination of Jacobians can be applied. Generally, most of them are based on the concept of (first-order) *forward difference schemes* of the form

$$\frac{\partial f(\mathbf{x})}{\partial x_i} = \frac{f(\mathbf{x} + \epsilon \mathbf{e}_i) - f(\mathbf{x})}{\epsilon} + \mathcal{O}(\epsilon) \quad (\text{D.24})$$

where $\mathbf{x} = x_i \mathbf{e}_i \in \mathbb{R}^n$ and $\epsilon \ll 1$, see Dennis, Jr., and Schnabel [81] amongst others. As a general advantage, this technique is convenient and straightforward to implement. Furthermore, it offers more flexibility, as it can be applied irrespective of the particular problem should a consistent linearisation of function $f(\mathbf{x})$ not (yet) be available. As a disadvantage, this technique results in a—especially for large systems—considerably higher computational cost because function $f(\mathbf{x})$ must be evaluated n -times.

In this section we deal with the numerical approximation of *global Jacobians on element level*, i.e. the approximation of the element-stiffness-matrix, see Table D.1. This approach is particularly useful for test-purposes with regard to single and multi-field problems where the linearisation of the governing balance equations in weak form is not (yet) available, since only the residual vector on element-level is needed. As a major drawback, this procedure results in a very high computational cost, due to the fact that the number of residual-evaluations correlates with the numbers of degrees of freedom per element, i.e. involves n_{edof} additional residual-evaluations. Therefore, this approach turns out to be inappropriate for large coupled three-dimensional problems which may possibly include many degrees of freedom. Nevertheless, it can serve as a ‘debugging-tool’ in order to check whether an analytical representation of the Jacobian on element-level is correct.

Table D.1: Numerical approximation of the Jacobian-matrix on element-level. Quantities without subscript n are assumed to be associated with t_{n+1} .

| |
|--|
| <p>0. given: (pseudo-)vector of element degrees of freedom (edof) \mathbf{d}_e and (pseudo-)vector of internal state variables $\mathcal{I}_{e n}$, both associated with current element e</p> <p>1. calculate residual</p> $\mathbf{r}_e = \mathbf{r}_e(\mathbf{d}_e, \mathcal{I}_{e n})$ <p>2. for $(j) = 1, \dots, n_{\text{edof}}$ compute</p> <p>(a) perturbed element-dofs</p> $\tilde{\mathbf{d}}_e^{(j)} = \mathbf{d}_e^{(j)} + \epsilon \mathbf{e}^{(j)} \quad \text{with unit-vector } \mathbf{e}^{(j)} \in \mathbb{R}^{n_{\text{edof}}}$ <p>(b) perturbed element residual vector</p> $\tilde{\mathbf{r}}_e^{(j)} = \mathbf{r}_e^{(j)}(\tilde{\mathbf{d}}_e^{(j)}, \mathcal{I}_{e n})$ <p>(c) column (j) of numerical element stiffness matrix</p> $\tilde{\mathbf{K}}_e^{i(j)} = \frac{1}{\epsilon} [\tilde{\mathbf{r}}_e^{(j)} - \mathbf{r}_e], \quad \text{for } i = 1, \dots, n_{\text{edof}}$ |
|--|

We establish a forward-difference-based perturbation technique, see Table D.1. Basically, the element-degrees-of-freedom $\mathbf{d}_{e n+1}$ are the primary variables for the perturbation process, where in Table D.1 we omit the subscript index $n + 1$ associated with time t_{n+1} for the sake of readability. This perturbation technique incorporates n_{edof} additional residual computations. As an important aspect, the evaluation of the perturbed residual $\tilde{\mathbf{r}}_e^{(j)}$ is performed assuming ‘frozen’ internal state variables $\mathcal{I}_{e n}$ and, finally, the Jacobian is computed column-wise by a forward-difference. With regard to the perturbation parameter, a value of $\epsilon = 10^{-8}$ turns out to be an appropriate choice for a store up of 16 decimal digits.

D.5 Postprocessing for the UEL-subroutine in Abaqus

As mentioned above, plotting and visualisation of results associated with the application of user elements is not directly supported by the Abaqus Viewer. However, this can be resolved using particular Fortran and C++ subroutines in connection with the Abaqus scripting interface in order to create appropriate binary output files which, in turn, can be read by the Abaqus Viewer. In the following, we briefly outline an Abaqus-internal procedure to create an appropriate output-file which can be read by the Abaqus Viewer.

Applying a general user element in Abaqus, results may be stored in the binary `.fil`-file via, for instance, the input sequence

```
*NODE FILE, NSET=<node-set-label>
U, NT, COORD, CF, RF
```

which defines a request for nodal output data for a prescribed node-set. The second line specifies the identifying ‘keys’ or rather ‘output variable identifiers’ for the variables to be written to the results file. For this case, we store the displacements `U`, temperature-like quantities `NT`—in the present context represented by the nonlocal damage variable ϕ —referential nodal coordinates `COORD`, concentrated forces `CF` and reaction forces `RF`.

The second input sequence

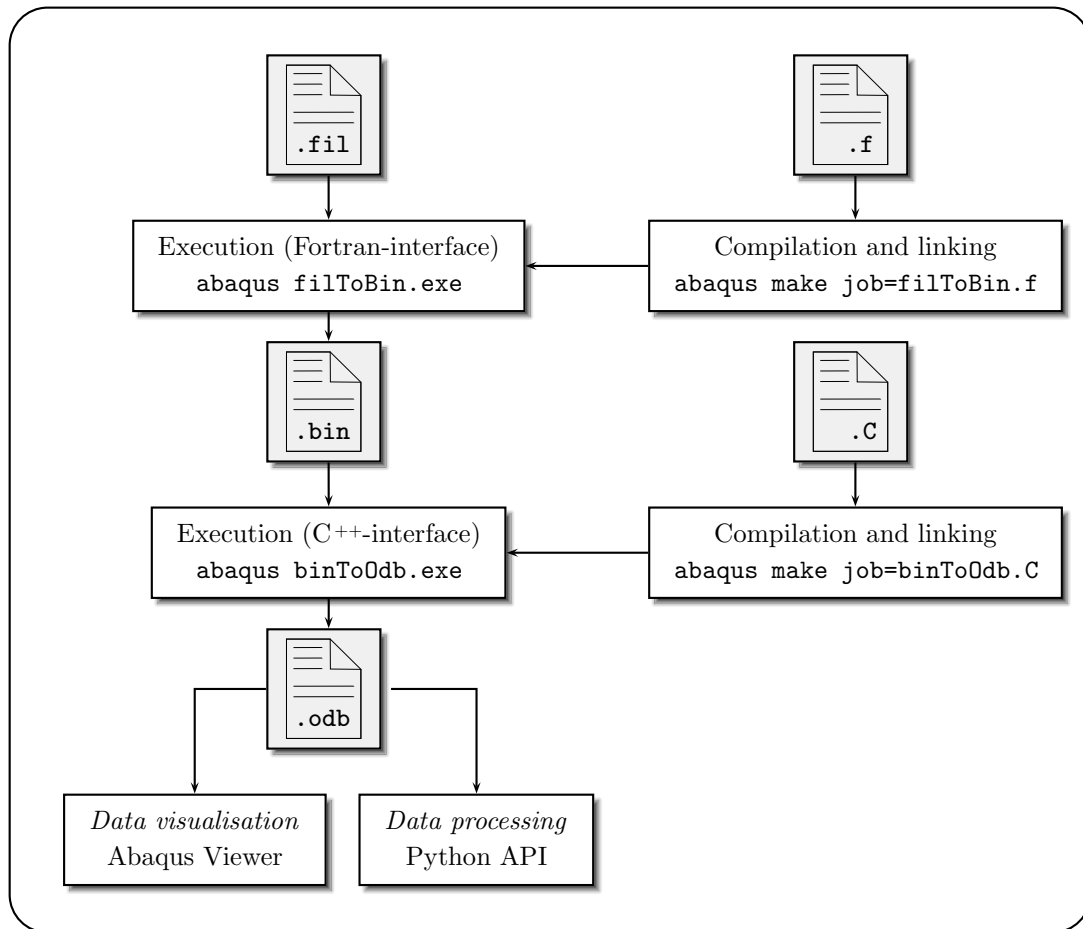
```
*EL FILE, ELSET=<element-set-label>, POSITION=INTEGRATION POINTS
SDV
```

defines a request for element output data at the integration points. For a user defined element, the integration point data can only be stored in the identifier for the solution-dependent state variables `SDV`, making it necessary to prescribe an explicit request for this key.

The Abaqus documentation makes no reference to the binary structure of the `.fil`-file containing the results which, consequently, must be read by means of an Abaqus Fortran-interface by using the subroutines `INITPF`, `DBRNU` and `DBFILE`. To the author’s knowledge, however, there is no Fortran-interface available allowing for the creation of an output database `.odb`-file. Therefore, reading from the `.fil`-file and writing to an `.odb`-file cannot be performed simultaneously. Alternatively, the information can be read from the `.fil`-file and stored in a binary `.bin`-file. The structure of this auxiliary `.bin`-file is defined by the user. Note, that the particular choice of a binary format is by no means mandatory, but turns out to be far more efficient than an ASCII-based format, especially when dealing with large FE-models. Afterwards, the C++-interface can be used to read the information from the `.bin`-file and to create a new `.odb`-file. According to this procedure, it will be possible to visualise the data contained in the final `.odb`-file by means of the Abaqus Viewer and/or to use the Python API to read the output data and analyse the obtained results. A flow-chart of the complete procedure is depicted in Figure D.2. For details on the use of the subroutines `INITPF`, `DBRNU` and `DBFILE` and the use of the C++-interface, we refer the reader to the Abaqus 6.11 Documentation [1].

A typical Fortran-interface used to read the results from the `.fil`-file may not contain a `program`-statement. Instead, the main body of the subroutine is contained within

Table D.2: Flowchart of the postprocessing stage when using a user defined element in Abaqus.



the `ABQmain` subroutine. This subroutine has no input argument and no return values. Similarly, a typical C++-interface used to create a new `.odb`-file may not contain a `main`-function. Instead, the main body of the subroutine is contained within the `ABQmain`-function, where the function's name is case sensitive. It should be noted that, unlike the Fortran-interface, the C++-subroutine allows the use of input arguments for the `main`-function by means of the `argv`-pointer.

Compiling, linking and executing a postprocessing subroutine is a two-step procedure. Let the Fortran-subroutine be referred to as `fromFilToBin.f` and let the C++-subroutine be denoted as `fromBinToOdb.C`. In the first step, compilation and linking of the aforementioned subroutines is achieved by using the `abaqus make` procedure. In the second step, the compilation and linking produces two executable files, i.e. `fromFilToBin.exe` and `fromBinToOdb.exe`. Once the executables have been generated, they may be called by means of the standard `abaqus` command. This procedure is illustrated in Figure D.2.

E Implementation of constitutive models via Abaqus subroutine UMAT

The implementation of constitutive models into an incremental-iterative finite-element framework requires the computation of a stress tensor as well as the corresponding consistent tangent moduli. In the context of the commercial finite-element-software Abaqus, these can be included in the so-called user subroutine UMAT. The particular choice of stress tensor and tangent moduli is prescribed by Abaqus.

E.1 Consistent tangent moduli based on Jaumann stress rates

Starting from the Kirchhoff stress $\boldsymbol{\tau} = \mathbf{P} \cdot \mathbf{F}^t = \mathbf{F} \cdot \mathbf{S} \cdot \mathbf{F}^t$, the related spatial rate-constitutive equations in form of the *Lie derivative of the Kirchhoff stress* read

$$\mathcal{L}_v \boldsymbol{\tau} = \mathbf{F} \cdot \dot{\mathbf{S}} \cdot \mathbf{F}^t = \mathbf{e}^\tau : \mathbf{d}, \quad (\text{E.1})$$

where \mathbf{e}^τ is the spatial elasticity tensor and $\mathbf{d} = \frac{1}{2}[\mathbf{l} + \mathbf{l}^t] = \mathbf{d}^t$ is the symmetric part of the velocity gradient $\mathbf{l} = \dot{\mathbf{F}} \cdot \mathbf{F}^{-1}$ which is commonly denoted as the *rate of deformation tensor*. Equation (E.1) can be formulated in terms of the Jaumann stress rate $\overset{\nabla}{\boldsymbol{\tau}} = \dot{\boldsymbol{\tau}} - \mathbf{w} \cdot \boldsymbol{\tau} - \boldsymbol{\tau} \cdot \mathbf{w}^t$, with the *spin tensor* $\mathbf{w} = \frac{1}{2}[\mathbf{l} - \mathbf{l}^t] = -\mathbf{w}^t$, which results in

$$\begin{aligned} \mathcal{L}_v \boldsymbol{\tau} &= \dot{\boldsymbol{\tau}} - \mathbf{l} \cdot \boldsymbol{\tau} - \boldsymbol{\tau} \cdot \mathbf{l}^t \\ &= \dot{\boldsymbol{\tau}} - [\mathbf{d} + \mathbf{w}] \cdot \boldsymbol{\tau} - \boldsymbol{\tau} \cdot [\mathbf{d} + \mathbf{w}]^t \\ &= \dot{\boldsymbol{\tau}} - \mathbf{w} \cdot \boldsymbol{\tau} + \boldsymbol{\tau} \cdot \mathbf{w} - \mathbf{d} \cdot \boldsymbol{\tau} - \boldsymbol{\tau} \cdot \mathbf{d} \\ &= \overset{\nabla}{\boldsymbol{\tau}} - \mathbf{d} \cdot \boldsymbol{\tau} - \boldsymbol{\tau} \cdot \mathbf{d}, \end{aligned} \quad (\text{E.2})$$

cf. Marsden and Hughes [195] or Miehe [213, 214] amongst others. Relation (E.2) together with (E.1), results in

$$\overset{\nabla}{\boldsymbol{\tau}} = \overset{\nabla}{\mathbf{e}} : \mathbf{d} \quad \text{with} \quad \overset{\nabla}{\mathbf{e}} := \mathbf{e}^\tau + \mathbf{I} \otimes \boldsymbol{\tau} + \boldsymbol{\tau} \otimes \mathbf{I}. \quad (\text{E.3})$$

The corresponding tangent moduli $\tilde{\mathbf{e}} = J^{-1} \overset{\nabla}{\mathbf{e}}$ conjugate to the Cauchy stresses $\boldsymbol{\sigma} = J^{-1} \boldsymbol{\tau}$ read

$$\tilde{\mathbf{e}} := \mathbf{e} + \mathbf{I} \otimes \boldsymbol{\sigma} + \boldsymbol{\sigma} \otimes \mathbf{I}. \quad (\text{E.4})$$

This fourth order tensor does not generally possess minor symmetry, i.e. $\tilde{e}_{ijkl} \neq \tilde{e}_{jikl} \neq \tilde{e}_{ijlk}$, so that only its fully symmetric part

$$\tilde{\mathbf{e}}^{\text{sym}} := \mathbf{e} + \frac{1}{2} [\mathbf{I} \otimes \boldsymbol{\sigma} + \boldsymbol{\sigma} \otimes \mathbf{I} + \mathbf{I} \otimes \boldsymbol{\sigma} + \boldsymbol{\sigma} \otimes \mathbf{I}] \quad (\text{E.5})$$

is taken into account, cf. Stein and Sagar [268].

E.2 UMAT-implementation in Abaqus

Abaqus provides a programming-interface that allows the implementation of general constitutive relations via the user subroutine UMAT, see the Abaqus User Subroutines Reference Manual [5, ch. 1.1.40] or the Abaqus Analysis User's Manual [2, ch. 25.7.1]. A user material can be used along with the robust and versatile Abaqus-internal solution procedures for (quasi-)static and dynamic analyses. Almost any element type can be chosen in connection with complex loading, contact and friction conditions. Furthermore, powerful plotting- and visualisation-capabilities of the results associated with the application of the user material are conveniently supported by Abaqus. In the following, we give an outline on particular implementation-issues with regard to the Abaqus user subroutine UMAT.

Three essential variables are required to be updated within the UMAT subroutine. In particular, the Cauchy stresses $\text{STRESS} := \boldsymbol{\sigma}$, the internal variables $\text{STATEV} := \boldsymbol{\mathcal{I}}$, and the tangent moduli $\text{DDSDDE} := \tilde{\mathbf{e}}$ enter the UMAT at the beginning of the increment and must be updated in this routine at the end of the increment. Due to the non-standard format of $\text{DDSDDE} := \tilde{\mathbf{e}}$, which is not explicitly given in the Abaqus 6.11 Documentation [1], we briefly review some issues related to the DDSDDE -variable.

According to the Abaqus Theory Manual [4, ch. 1.5.3], the objective stress rates used in Abaqus/Standard in connection with solid continuum elements are based on the *Jaumann objective stress rate* for all built-in and user-defined materials. Accordingly, Stein and Sagar [268] report that *tangent moduli related to the Jaumann rate of Kirchhoff stress* are required to obtain quadratic convergence in the underlying Newton-Raphson-scheme. In this regard, we refer to the Abaqus User Subroutines Reference Manual [5, ch. 1.1.40] and the Abaqus Theory Manual [4, ch. 1.5.3] where the format of the required consistent tangent moduli $\text{DDSDDE} := \tilde{\mathbf{e}}$ is specified for *total-form constitutive relations* through the Jaumann stress rate $\overset{\nabla}{\boldsymbol{\tau}} = \dot{\boldsymbol{\tau}} - \boldsymbol{w} \cdot \boldsymbol{\tau} - \boldsymbol{\tau} \cdot \boldsymbol{w}^t$.

The tangent moduli as given in equations (E.4) and (E.5), respectively, essentially reflect the consistent format required for DDSDDE , i.e. $\text{DDSDDE} := \tilde{\mathbf{e}}$. Practically, the non-symmetric format (E.4) can be used, since—unless the unsymmetric equation solution

capability for the user-defined material is invoked—Abaqus automatically uses only the symmetric part of DDSDDDE.

E.3 UMAT-interface in Abaqus

With regard to the input-file, a user-material is introduced by the keyword `*USER MATERIAL`, see the Abaqus Keywords Reference Manual [3]. The following input lines act as the interface to a UMAT:

```
*MATERIAL, NAME=<name>
*USER MATERIAL, CONSTANTS= $n_{sdv}$ 
  Data line(s) specifying the material parameters
*DEPVAR
   $n_{sdv}$ 
*SOLID SECTION, ELSET=ALLELEM, MATERIAL=<name>
*INITIAL CONDITIONS, TYPE=SOLUTION, USER
```

Here, the `*MATERIAL` keyword specifies the ‘name’ of the user material. This name is used to refer to the user-material in the element property options by means of the `*SOLID SECTION` keyword which assigns the user-material defined by the UMAT and its corresponding properties to a particular element set (`ELSET`) of solid continuum elements. As a crucial point, the `*USER MATERIAL` keyword is required to specify material constants for the UMAT. The `*DEPVAR` keyword is needed only for material models containing internal variables and is necessary for the allocation of space for n_{sdv} internal variables at each integration point. In this regard, the `*INITIAL CONDITIONS, TYPE=SOLUTION, USER` option is used to initialise non-zero internal variables via user subroutine SDVINI.

E.4 Approximation of consistent tangent moduli

In this section, we deal with the numerical approximation of *local Jacobians on constitutive level*, i.e. *numerical approximation of consistent tangent moduli/operators*, see Table E.1. This approach is particularly useful for advanced (in)elastic constitutive relations, especially for test and validation purposes in order to investigate the basic characteristics of the constitutive formulation. Furthermore, it provides a reliable ‘debugging-tool’ in order to check the analytical representation of the tangent moduli.

Without going into theoretical details, and by following similar arguments as in Appendix D.4, we briefly specify a modified version of the forward-difference-based perturbation technique in spatial description provided by Miehe [215], albeit here in terms of

Table E.1: Numerical computation of algorithmic tangent moduli in spatial description. Quantities without subscript n are assumed to be associated with t_{n+1} .

| |
|---|
| <p>0. given: deformation gradient \mathbf{F} and internal variables \mathcal{I}_n</p> <p>1. calculate Cauchy stresses $\boldsymbol{\sigma} = \boldsymbol{\sigma}(\mathbf{F}, \mathcal{I}_n)$</p> <p>2. for $(kl) = (11), (22), (33), (12), (13), (23)$ compute</p> <p style="margin-left: 20px;">(a) perturbed deformation gradient $\tilde{F}_{iJ}^{(kl)} = F_{iJ} + \frac{\epsilon}{2} [\delta_{ik} F_{lJ} + \delta_{il} F_{kJ}]$</p> <p style="margin-left: 20px;">(b) perturbed Cauchy stresses $\tilde{\boldsymbol{\sigma}}^{(kl)} = \boldsymbol{\sigma}(\tilde{\mathbf{F}}^{(kl)}, \mathcal{I}_n)$</p> <p style="margin-left: 20px;">(c) column (kl) of spatial tangent moduli $\mathbf{e}_{ij(kl)} = \frac{1}{\epsilon} \left[\frac{\tilde{J}^{(kl)}}{J} \tilde{\sigma}_{ij}^{(kl)} - \sigma_{ij} \right] - \check{\mathbf{e}}_{ij(kl)}, \text{ for } i, j = 1, 2, 3$ with $\tilde{J}^{(kl)} = \det(\tilde{\mathbf{F}}^{(kl)})$ and $\check{\mathbf{e}}_{ij(kl)} = \frac{1}{2} [\delta_{ik} \sigma_{jl} + \delta_{il} \sigma_{jk} + \sigma_{ik} \delta_{jl} + \sigma_{il} \delta_{jk}]$</p> |
|---|

the Cauchy-stresses $\boldsymbol{\sigma}$, see Table E.1. Basically, the deformation gradient \mathbf{F}_{n+1} is the primary variable for the perturbation process where, in Table E.1, we omit the subscript index $n + 1$ associated with time t_{n+1} for the sake of readability. For the present three-dimensional case, this perturbation technique incorporates six additional stress tensor computations. Analogous to Appendix E.4, the evaluation of the perturbed Cauchy stresses $\tilde{\boldsymbol{\sigma}}^{(kl)}$ is performed assuming ‘frozen’ internal state variables \mathcal{I}_n . Note the additional factor \tilde{J}/J within the column-wise calculation of the spatial tangent moduli, compared to the original work by Miehe [215]. The perturbation parameter ϵ crucially affects the rate of convergence and depends on the machine precision, see Dennis, Jr., and Schnabel [81] or Miehe [215]. In this regard, a value of $\epsilon = 10^{-8}$ turns out to be an optimal choice for a store up of 16 decimal digits.

F Arc-length methods

An incremental-iterative Newton-Raphson-based solution scheme may not be appropriate to obtain a solution for unstable problems. Therefore, arc-length procedures are typically applied and turn out to be advantageous and robust enough to obtain static equilibrium states during unstable stages of the response of a force-driven deformation problem and can conveniently enable post-peak branches of load-displacement curves.

In this section, we briefly summarise some basics of arc-length-controlled solution procedures where we restrict ourselves to uncoupled purely mechanical problems. Moreover, we relate and specify the equations with regard to the arc-length algorithm implemented in Abaqus, emphasise issues of implementation in UEL-subroutines and comment on specific control parameters to be specified by the user.

For a general survey of arc-length methods, we refer to the monographs by Crisfield [78, 79] and references cited therein.

F.1 Basic equations

According to general arc-length schemes, the loading parameter λ_{n+1} at time t_{n+1} , introduced to incrementally increase the load-magnitude, is allowed to vary during the iteration process. The particular value of the loading parameter is governed by a non-linear scalar constraint equation of the form $f(\boldsymbol{\varphi}_{n+1}, \lambda_{n+1}) = 0$ in terms of the current displacements $\boldsymbol{\varphi}_{n+1}$ and the current loading parameter λ_{n+1} . For the sake of clarity, we restrict the following description to uncoupled purely mechanical problems; the extension to coupled problems is straightforward. Consequently, the residual format of the non-linear balance of momentum enhanced by the constraint equation reads

$$\mathbf{r}^\varphi(\boldsymbol{\varphi}, \lambda) = \mathbf{f}_{\text{int}}^\varphi(\boldsymbol{\varphi}) - \lambda \mathbf{f}_{\text{ext}}^\varphi = \mathbf{0}, \quad (\text{F.1})$$

$$f(\boldsymbol{\varphi}, \lambda) = 0, \quad (\text{F.2})$$

where, here and in the following, we often omit the subscript index $n + 1$ associated with time t_{n+1} as well as the dependencies on $\boldsymbol{\varphi}$ and λ for the sake of readability. A Taylor

series expansion around the solution at the current iteration step l —terms of quadratic and higher order being neglected—gives

$$\mathbf{r}_{l+1}^\varphi = \mathbf{r}_l^\varphi + \Delta \mathbf{r}^\varphi = \mathbf{0}, \quad (\text{F.3})$$

$$f_{l+1} = f_l + \Delta f = 0, \quad (\text{F.4})$$

with the increments of the residuals

$$\Delta \mathbf{r}^\varphi = \frac{d\mathbf{r}^\varphi}{d\varphi} \cdot \Delta \varphi + \frac{d\mathbf{r}^\varphi}{d\lambda} \Delta \lambda, \quad (\text{F.5})$$

$$\Delta f = \frac{df}{d\varphi} \cdot \Delta \varphi + \frac{df}{d\lambda} \Delta \lambda. \quad (\text{F.6})$$

Herein, the increments $\Delta \varphi = \varphi_{l+1} - \varphi_l$ and $\Delta \lambda = \lambda_{l+1} - \lambda_l$ represent the difference between the values at iteration-step $l+1$ and l , while the derivatives are abbreviated by

$$\mathbf{K}^{\varphi\varphi} := \frac{d\mathbf{r}^\varphi}{d\varphi}, \quad \mathbf{r}_{,\lambda} := \frac{d\mathbf{r}^\varphi}{d\lambda} = -\mathbf{f}_{\text{ext}}^\varphi, \quad (\text{F.7})$$

$$f_{,\varphi} := \frac{df}{d\varphi}, \quad f_{,\lambda} := \frac{df}{d\lambda}. \quad (\text{F.8})$$

This results in the following linearised system of equations on element level

$$\begin{bmatrix} \mathbf{K}^{\varphi\varphi} & -\mathbf{f}_{\text{ext}}^\varphi \\ f_{,\varphi} & f_{,\lambda} \end{bmatrix} \cdot \begin{bmatrix} \Delta \varphi \\ \Delta \lambda \end{bmatrix} = \begin{bmatrix} \lambda \mathbf{f}_{\text{ext}}^\varphi - \mathbf{f}_{\text{int}}^\varphi \\ -f \end{bmatrix}, \quad (\text{F.9})$$

which is neither symmetric nor banded. According to Batoz and Dhatt [26], the solution of this system of equations can be obtained by means of so-called block-solutions

$$\Delta \varphi_r = \mathbf{K}^{\varphi\varphi-1} \cdot [\lambda \mathbf{f}_{\text{ext}}^\varphi - \mathbf{f}_{\text{int}}^\varphi], \quad (\text{F.10})$$

$$\Delta \varphi_\lambda = \mathbf{K}^{\varphi\varphi-1} \cdot \mathbf{f}_{\text{ext}}^\varphi, \quad (\text{F.11})$$

which enable us to give an explicit representation for the increment of the loading factor

$$\Delta \lambda = -\frac{f + f_{,\varphi} \cdot \Delta \varphi_r}{f_{,\varphi} \cdot \Delta \varphi_\lambda + f_{,\lambda}}. \quad (\text{F.12})$$

Based on this, the increment in placement is calculated as

$$\Delta \varphi = \Delta \varphi_r + \Delta \lambda \Delta \varphi_\lambda \quad (\text{F.13})$$

and the updates of displacements and loading-parameter then read $\varphi_{l+1} = \varphi_l + \Delta \varphi$ and $\lambda_{l+1} = \lambda_l + \Delta \lambda$. Note, that within the predictor step at t_0 , constraint condition (F.4) is not determined. As a remedy, the loading parameter λ_n is increased by 1 providing the placement increment based on the last equilibrium state $\{\varphi_n, \lambda_n\}$ reads as

$$\Delta \varphi_\lambda = \mathbf{K}^{\varphi\varphi-1} \cdot \mathbf{f}_{\text{ext}}^\varphi \quad (\text{F.14})$$

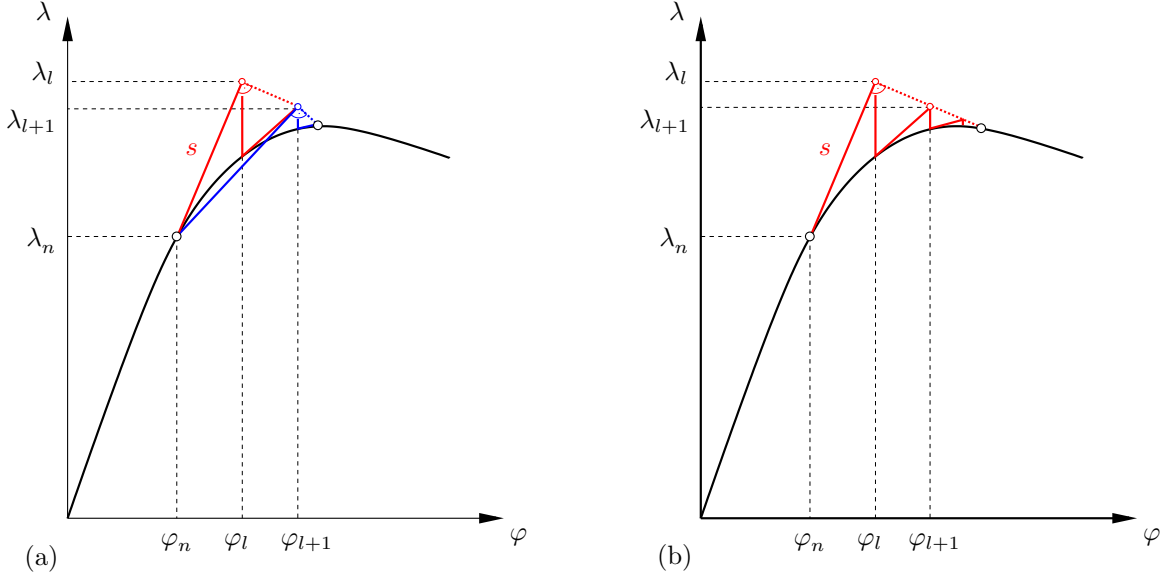


Figure F.1: Illustration of arc-length methods according to Crisfield [78]. (a) Iteration on the current normal plane (Ramm's method), (b) Iteration on the initial normal plane (Riks-Wemper method). Quantities without subscript n are associated with t_{n+1} .

and the distance to the last equilibrium point reads as

$$s_0 = \sqrt{\Delta\varphi_\lambda \cdot \Delta\varphi_\lambda + 1}. \quad (\text{F.15})$$

Comparing the distance s_0 and the prescribed arc-length s , the increments of the loading parameter and the placement can be scaled by $\Delta\lambda = s/s_0$ and $\Delta\varphi = [s/s_0] \Delta\varphi_\lambda$. The updates of the displacements φ_{l+1} and the loading-parameter λ_{l+1} can then be calculated for $l = 0$.

The constraint equation (F.2) remains to be specified. Different solution strategies are suggested in the literature as summarised, for instance, in the monographs by Wagner [285] and Reitingier [247] or in the textbooks by Crisfield [78, 79]. One prominent example is the *iteration on the current normal plane* according to Ramm [244, 245], which in Crisfield [78] is denoted as *Ramm's method*. Following this approach, which is illustrated in Figure F.1(a), the equation

$$f = [\varphi_l - \varphi_n] \cdot [\varphi_{l+1} - \varphi_l] + [\lambda_l - \lambda_n][\lambda_{l+1} - \lambda_l] = 0 \quad (\text{F.16})$$

constrains the solution to the normal plane with respect to the current iteration step. According to equation (F.12), the related increment can be specified as

$$\Delta\lambda = -\frac{[\varphi_l - \varphi_n] \cdot \varphi_r}{[\varphi_l - \varphi_n] \cdot \varphi_\lambda + \lambda_l - \lambda_n}. \quad (\text{F.17})$$

Within this approach, the increment size is limited by moving a given distance along the tangent of the current solution point. Equilibrium is then sought in the plane that passes

through the point thus obtained and that is normal to the same tangent. Moreover, the constraint (F.16) ensures that the iterative change is always normal to the secant change, which causes the equilibrium-search to be normal to the tangent of the previous iteration step, rather than to the tangent at the beginning of the increment. This method can be considered as an extension of the *iteration on the initial normal plane* according to the original work by Riks [249, 250] and Wempner [294] which, following Crisfield [78], is accordingly denoted as *Riks-Wempner method*; see Figure F.1(b) for an illustration.

F.2 Application within general user-elements via Abaqus subroutine UEL

Along with the UEL-subroutine, Abaqus is capable of using self-implemented element-formulations in combination with the Abaqus-internal arc-length procedure, referred to as the *modified Riks algorithm*, see the Abaqus Analysis User's Manual [2, ch. 6.2.4] for general usage aspects. According to the Abaqus Theory Manual [4, ch. 2.3.2], the *modified Riks algorithm* is a version of the aforementioned *iteration on the current normal plane* established by Ramm [244, 245], see also Crisfield [80] or Powell and Simons [242].

In order to be able to use the Abaqus-internal modified Riks algorithm in combination with a UEL-subroutine, we have to meet the following requirements. As described above, the essential quantities to be specified within the UEL-subroutine are the element residual vector `RHS`, the element Jacobian- respectively stiffness-matrix `AMATRX`, and the internal-solution dependent state variables `SVARS`. Regarding `AMATRX` and `SVARS`, no modifications due to the Riks method have to be provided. However, in contrast to the purely Newton-Raphson-based solution scheme, `RHS` now consists of `NRHS=2` columns. The first column `RHS(:,1)` is still associated with the residual vector. The additional second column `RHS(:,2)` contains the increments of external loads of the respective element, also referred to as the *incremental load vector*. In summary,

$$\text{AMATRX} \quad := \mathbf{K}_e^{\varphi\varphi} \tag{F.18}$$

$$\text{RHS}(:,1) \quad := \lambda \mathbf{f}_{\text{ext } e}^{\varphi} - \mathbf{f}_{\text{int } e}^{\varphi} \tag{F.19}$$

$$\text{RHS}(:,2) \quad := \Delta\lambda \mathbf{f}_{\text{ext } e}^{\varphi}, \tag{F.20}$$

cf. the system of equations (F.9). Here, definitions (F.18)–(F.20) require that all (external) force loads $\mathbf{f}_{\text{ext}}^{\varphi}$ must be passed into UEL by means of distributed load definitions so that the force loads are available for the definition of incremental load vectors; the load key `Un` must be used consistently, as discussed in the Abaqus Analysis User's Manual [2, ch. 31.15.1]. The coding in subroutine UEL must distribute the loads into consistent equivalent nodal forces and account for them in the calculation of the `RHS` array, see Appendix G for a consistent incorporation of surface traction forces in a finite-element-setting using Abaqus.

Furthermore, the UEL-subroutine provides the two variables `ADLMAG` and `DDL MAG`, where `ADLMAG` contains the total load magnitudes of the distributed loads at the end of

Table F.1: Control parameters to be used within the input-file accompanied by the keyword `*STATIC`, `RIKS` for the modified Riks method as implemented in Abaqus. The initial load proportionality factor (LPF) is computed as $\Delta\lambda_{\text{in}} = \Delta l_{\text{in}}/l_{\text{period}}$, Abaqus Analysis User's Manual [2, ch. 6.2.4] and Abaqus Keywords Reference Manual [3].

| Symbol | Description |
|---------------------------|--|
| Δl_{in} | initial arc-length increment |
| l_{period} | total arc-length scale factor |
| Δl_{min} | minimum arc-length increment |
| Δl_{max} | maximum arc-length increment |
| λ_{end} | maximum load proportionality factor (LPF) to end increment |
| nod_{mon} | monitored node number |
| dof_{mon} | monitored degree of freedom (DOF) |
| u_{end} | maximum displacement at node and DOF to end increment |

the current increment and where `DDL MAG` represents the increments in the magnitudes of the distributed loads currently active on this element. With regard to relations (F.19) and (F.20), we consequently note that

$$\text{ADLMAG} := \lambda \quad \text{and} \quad \text{DDL MAG} := \Delta\lambda. \quad (\text{F.21})$$

The input-file-setting is identical compared to a conventional modified Riks static analysis without any user-coding, i.e. introduced by `*STATIC`, `RIKS` followed by eight partially optional parameters which are summarised in Table F.1.

G Deformation-dependent loads

The variational form of equilibrium includes the external virtual work (3.25) composed of contributions due to body forces $\bar{\mathbf{b}}$ and surface tractions $\bar{\mathbf{t}}$. This section addresses the incorporation of the latter, i.e. pressure-dependent surface traction forces which are clearly *deformation-dependent*. In this regard, we specify the related equilibrium expression and briefly outline the essential relations for a corresponding finite-element implementation. A detailed discussion on deformation, or rather configuration-dependent loads is provided in the early work of Sewell [257], while their algorithmic treatment and discretisation with regard to finite elements can be found in Schweizerhof and Ramm [256] which forms the basis for related treatises in finite-element textbooks, as, e.g., Bonet and Wood [45] and Wriggers [299] amongst others.

In the following, we restrict ourselves to the important case of *uniform normal pressure* which, for instance, is adopted for the numerical example of the arterial tube in Section 3.4.3.

G.1 Variational form

Let a uniform pressure p act on a surface a characterised by the normal \mathbf{n} . The traction force vector can then be specified as $\bar{\mathbf{t}} = p\mathbf{n}$ and the corresponding variational form is represented by

$$\delta_{\varphi} \Pi_{\text{ext}}^{\text{sur}} = \int_{\partial \mathcal{B}_t} p \delta \varphi \cdot \mathbf{n} \, da, \quad (\text{G.1})$$

where the orientation of the normal \mathbf{n} and the magnitude of the area element da are both displacement-dependent. A convenient parameterisation of the normal and the area element in terms of the surface-coordinates ξ and η can be obtained by means of the tangent vectors $\varphi_{,\xi} := \partial_{\xi} \varphi$ and $\varphi_{,\eta} := \partial_{\eta} \varphi$ as

$$\mathbf{n} = \frac{\varphi_{,\xi} \times \varphi_{,\eta}}{\|\varphi_{,\xi} \times \varphi_{,\eta}\|} \quad \text{and} \quad da = \|\varphi_{,\xi} \times \varphi_{,\eta}\| \, d\xi \, d\eta, \quad (\text{G.2})$$

enabling us to express the relation (G.1) as

$$\delta_{\varphi} \Pi_{\text{ext}}^{\text{sur}} = \int_{\partial \bar{\mathcal{B}}_t} p \delta \varphi \cdot [\varphi_{,\xi} \times \varphi_{,\eta}] d\xi d\eta. \quad (\text{G.3})$$

G.2 Discretisation

The finite element discretisation of (G.3) is performed using isoparametric shape functions N_I^{φ} together with their derivatives with respect to $\boldsymbol{\xi}$ resulting in

$$\varphi \approx \varphi^{\text{h}} = \sum_{I=1}^{n_{\text{sen}}^{\varphi}} N_I^{\varphi}(\boldsymbol{\xi}) \varphi_I, \quad \nabla_{\boldsymbol{\xi}} \varphi \approx \nabla_{\boldsymbol{\xi}} \varphi^{\text{h}} = \sum_{I=1}^{n_{\text{sen}}^{\varphi}} \nabla_{\boldsymbol{\xi}} N_I^{\varphi} \varphi_I, \quad (\text{G.4})$$

where n_{sen}^{φ} is the number of nodes per surface-element. The placements φ are transformed to a quadrilateral reference element with surface-coordinates $\boldsymbol{\xi} := \{\xi, \eta\} \in \partial \bar{\mathcal{B}}$, where $\partial \bar{\mathcal{B}} := \{\boldsymbol{\xi} \in \mathbb{R}^2 | -1 \leq \chi \leq +1; \chi = \xi, \eta\}$ denotes the reference domain. According to (3.93), the element-specific variational form can be expressed by

$$\delta_{\varphi} \Pi_{\text{ext}}^{\text{sur } e} = \sum_{I=1}^{n_{\text{sen}}^{\varphi}} \delta \varphi_I \cdot \mathbf{f}_{\text{sur } I}^{\varphi} \quad \text{with} \quad \mathbf{f}_{\text{sur } I}^{\varphi} = \int_{\partial \bar{\mathcal{B}}} N_I^{\varphi} p \bar{\mathbf{n}} d\xi d\eta \quad (\text{G.5})$$

where $\bar{\mathbf{n}}$ is specified by means of the vector-product in (G.3) as

$$\bar{\mathbf{n}} := \nabla_{\xi} \varphi^{\text{h}} \times \nabla_{\eta} \varphi^{\text{h}} = \begin{bmatrix} \varphi_{2,\xi} \varphi_{3,\eta} - \varphi_{3,\xi} \varphi_{2,\eta} \\ \varphi_{3,\xi} \varphi_{1,\eta} - \varphi_{1,\xi} \varphi_{3,\eta} \\ \varphi_{1,\xi} \varphi_{2,\eta} - \varphi_{2,\xi} \varphi_{1,\eta} \end{bmatrix}. \quad (\text{G.6})$$

For the integration over surfaces in three-dimensional space and resulting properties of equivalent nodal forces for a 20-node hexahedral element, see Dhondt [82, ch. 2.3.4].

G.3 Linearisation

Linearisation is performed following the arguments in Section 3.3.2. The derivative $d\mathbf{r}_I^{\varphi}/d\varphi_J$ exhibits an additional contribution due to the presence of the deformation-dependent term $\mathbf{f}_{\text{sur } I}^{\varphi}$. This results in

$$\mathbf{K}_{IJ}^{\varphi\varphi} = \frac{d\mathbf{r}_I^{\varphi}}{d\varphi_J} = \mathbf{K}_{IJ}^{\varphi\varphi \text{ mat}} + \mathbf{K}_{IJ}^{\varphi\varphi \text{ geo}} - \mathbf{K}_{IJ}^{\varphi\varphi \text{ def}}, \quad (\text{G.7})$$

see equation (3.102). The external force contribution takes the representation

$$\mathbf{K}_{IJ}^{\varphi\varphi \text{ def}} := \int_{\partial \bar{\mathcal{B}}} p N_I^{\varphi} [N_{J,\xi}^{\varphi} \mathbf{N}_{,\eta}^{\varphi} - N_{J,\eta}^{\varphi} \mathbf{N}_{,\xi}^{\varphi}] d\xi d\eta \quad (\text{G.8})$$

in which a skew-symmetric matrix

$$\mathbf{N}_{,\alpha}^{\varphi} = \begin{bmatrix} 0 & \varphi_{3,\alpha} & -\varphi_{2,\alpha} \\ -\varphi_{3,\alpha} & 0 & \varphi_{1,\alpha} \\ \varphi_{2,\alpha} & -\varphi_{1,\alpha} & 0 \end{bmatrix}, \quad \alpha = \xi, \eta \quad (\text{G.9})$$

is introduced, see, e.g., Wriggers [299]. It becomes apparent that the external force contribution $\mathbf{K}_{IJ}^{\varphi\varphi\text{def}}$ and hence the global tangent stiffness matrix \mathbf{K} may become non-symmetric for pressure loading. This means that, generally, no potential can be associated with an arbitrary pressure load. However, special boundary conditions provided, the total assembled stiffness matrix can be symmetric, and a potential consequently exists, see, for instance, Chapter 2 where a double-layered thick-walled cylindrical tube subjected to internal pressure is analysed on the basis of a total potential.

The surface integrals in equations (G.5) and (G.8) are typically evaluated numerically at discrete integration points by means of appropriate quadrature rules, see Zienkiewicz and Taylor [301], Hughes [140] and Bathe [25].

G.4 Implementation via Abaqus subroutine UEL

Along with the UEL-subroutine defining a general user-element, Abaqus is capable of applying *concentrated* point loads or moments without any additional considerations within the UEL-subroutine, see Abaqus Analysis User's Manual [2, ch. 32.4.2]. Furthermore, *distributed* and possibly deformation-dependent loads according to Appendix G.1 can also be defined for a general user-defined element. This, however, requires additional implementation efforts by means of the Abaqus user subroutine UEL.

Following the Abaqus Analysis User's Manual [2, ch. 31.15.1], general distributed loads—in connection with a general user-element—are invoked by the following input-sequence

```
*DLOAD
  (element-set-label), Un, p
```

where the `*DLOAD` keyword is used to attribute the distributed loading to the element-set associated with the load. Furthermore, a load type key `Un` and a reference pressure-type load magnitude `p` must be prescribed. The form of the load type key reads `Un` for uniform loads, where $n := \text{JDLTYP}(1,1)$ denotes an integer and characterises the particular element-face subjected to the load, see Table G.1.

For each active load of type `Un`, the subroutine UEL provides the current magnitude $\text{ADLMAG} := \lambda_{n+1}$ and the current increment in magnitude $\text{DDL MAG} := \Delta\lambda$ of the load, cf. also equation F.21. The coding in subroutine UEL must distribute the loads into

Table G.1: List of element-face-numbers and associated node-numbering corresponding to the hexahedral finite element depicted in Figure 3.3.

| Face no. n | Node no. | | | | | | | |
|--------------|----------|---|---|---|----|----|----|----|
| 1 | 1 | 2 | 3 | 4 | 9 | 10 | 11 | 12 |
| 2 | 5 | 8 | 7 | 6 | 16 | 15 | 14 | 13 |
| 3 | 1 | 5 | 6 | 2 | 17 | 13 | 18 | 9 |
| 4 | 2 | 6 | 7 | 3 | 18 | 14 | 19 | 10 |
| 5 | 3 | 7 | 8 | 4 | 19 | 15 | 20 | 11 |
| 6 | 4 | 8 | 5 | 1 | 20 | 16 | 17 | 12 |

consistent equivalent nodal forces (G.5) and provide their contribution to the Jacobian matrix by means of the load stiffness matrix (G.8).

Due to the possibly non-symmetric global tangent stiffness matrix \mathbf{K} in the case of deformation-dependent loading, a related step definition in Abaqus according to

`*STEP, NLGEOM, INC= n , UNSYMM=YES`

should enable the unsymmetric matrix storage and solution by setting `UNSYMM=YES`. Note, that a non-symmetric equation solution may be four times as expensive as the corresponding symmetric system, see the Abaqus Analysis User's Manual [2, ch. 6.1.1] for details.

Bibliography

- [1] Abaqus 6.11 Documentation, 2011. Dassault Systèmes Simulia Corp.
- [2] Abaqus Analysis User's Manual, 2011. *Abaqus 6.11 Documentation*. Dassault Systèmes Simulia Corp.
- [3] Abaqus Keywords Reference Manual, 2011. *Abaqus 6.11 Documentation*. Dassault Systèmes Simulia Corp.
- [4] Abaqus Theory Manual, 2011. *Abaqus 6.11 Documentation*. Dassault Systèmes Simulia Corp.
- [5] Abaqus User Subroutines Reference Manual, 2011. *Abaqus 6.11 Documentation*. Dassault Systèmes Simulia Corp.
- [6] Abu Al-Rub, R., Voyiadjis, G., 2006. *A finite strain plastic-damage model for high velocity impact using combined viscosity and gradient localization limiters: Part I – theoretical formulation*. International Journal of Damage Mechanics 15, 293–334.
- [7] Aifantis, E., 1992. *On the role of gradients in the localization of deformation and fracture*. International Journal of Engineering Science 30, 1279–1299.
- [8] Aifantis, E., 2011. *On the gradient approach – Relation to Eringen's nonlocal theory*. International Journal of Engineering Science 49, 1367–1377.
- [9] Alastrué, V., Martínez, M., Doblaré, M., Menzel, A., 2009. *Anisotropic micro-sphere-based finite elasticity applied to blood vessel modelling*. Journal of the Mechanics and Physics of Solids 57, 178–203.
- [10] Alastrué, V., Martínez, M.A., Menzel, A., Doblaré, M., 2009. *On the use of non-linear transformations for the evaluation of anisotropic rotationally symmetric directional integrals. Application to the stress analysis in fibred soft tissues*. International Journal for Numerical Methods in Engineering 79, 474–504.
- [11] Alastrué, V., Peña, E., Martínez, M., Doblaré, M., 2007. *Assessing the use of the “Opening Angle Method” to enforce residual stresses in patient-specific arteries*. Annals of Biomedical Engineering 35, 1821–1837.
- [12] Alastrué, V., Rodríguez, J., Calvo, B., Doblaré, M., 2007. *Structural damage models for fibrous biological soft tissues*. International Journal of Solids and Structures 44, 5894–5911.
- [13] Alberts, B., Bray, D., Lewis, J., Raff, M., Roberts, K., Watson, J., 1994. *Molecular Biology of the Cell*. Garland Publishing. 3rd edition.

- [14] Alford, P., Humphrey, J., Taber, L., 2008. *Growth and remodeling in a thick-walled artery model: effects of spatial variations in wall constituents*. Biomechanics and Modeling in Mechanobiology 7, 245–262.
- [15] Almeida, E., Spilker, R., 1998. *Finite element formulations for hyperelastic transversely isotropic biphasic soft tissues*. Computer Methods in Applied Mechanics and Engineering 151, 513–538.
- [16] Ambrosi, D., Ateshian, G., Arruda, E., Cowin, S., Dumais, J., Goriely, A., Holzapfel, G., Humphrey, J., Kemkemer, R., Kuhl, E., Olberding, J., Taber, L., Garikipati, K., 2011. *Perspectives on biological growth and remodeling*. Journal of the Mechanics and Physics of Solids 59, 863–883.
- [17] Arruda, E., Boyce, M., 1993. *A three-dimensional constitutive model for the large stretch behavior of rubber elastic materials*. Journal of the Mechanics and Physics of Solids 41, 389–412.
- [18] Ashman, R., Rho, J., Turner, C., 1989. *Anatomical variation of orthotropic elastic moduli of the proximal human tibia*. Journal of Biomechanics 22, 895–900.
- [19] Ask, A., Denzer, R., Menzel, A., Ristinmaa, M., 2013. *Inverse-motion-based form finding for quasi-incompressible finite electroelasticity*. International Journal for Numerical Methods in Engineering 94, 554–572.
- [20] Atkinson, K., 1982. *Numerical integration on the sphere*. Journal of the Australian Mathematical Society 23, 332–347.
- [21] Baliunas, A., Hurwitz, D., Ryals, A., Karrar, A., Case, J., Block, J., Andriacchi, T., 2002. *Increased knee joint loads during walking are present in subjects with knee osteoarthritis*. Osteoarthritis and Cartilage 10, 573–579.
- [22] Balzani, D., Brinkhues, S., Holzapfel, G., 2012a. *Constitutive framework for the modeling of damage in collagenous soft tissues with application to arterial walls*. Computer Methods in Applied Mechanics and Engineering 213–216, 139–151.
- [23] Balzani, D., Böse, D., Brands, D., Erbel, R., Klawonn, A., Rheinbach, O., Schröder, J., 2012b. *Parallel simulation of patient-specific atherosclerotic arteries for the enhancement of intravascular ultrasound diagnostics*. Engineering Computations 29, 888–906.
- [24] Batdorf, S., Budiansky, B., 1949. *A mathematical theory of plasticity based on the concept of slip*. Technical Note 1871. National Advisory Committee for Aeronautics.
- [25] Bathe, K.J., 1996. *Finite Element Procedures*. Prentice Hall.
- [26] Batoz, J.L., Dhatt, G., 1979. *Incremental displacement algorithms for nonlinear problems*. International Journal for Numerical Methods in Engineering 14, 1262–1267.

-
- [27] Bažant, Z., 1991. *Why continuum damage is nonlocal: Micromechanics arguments*. Journal of Engineering Mechanics 117, 1070–1087.
- [28] Bažant, Z., Di Luzio, G., 2004. *Nonlocal microplane model with strain-softening yield limits*. International Journal of Solids and Structures 41, 7209–7240.
- [29] Bažant, Z., Oh, B., 1983a. *Microplane model for fracture analysis on concrete structures*. Proceedings on the Symposium on the Interaction of Non-Nuclear Munitions with Structures, US Air Force Academy, Colorado Springs, 49–55.
- [30] Bažant, Z., Oh, B., 1983b. *Model of weak planes for progressive fracture of concrete and rock*. Center for Concrete and Geomaterials, Northwestern University, Evanston Report No. 83-2/448m.
- [31] Bažant, Z., Oh, B., 1985. *Microplane model for progressive fracture of concrete and rock*. Journal of Engineering Mechanics 111, 559–582.
- [32] Bažant, Z., Oh, B., 1986. *Efficient numerical integration on the surface of a sphere*. Zeitschrift für angewandte Mathematik und Mechanik 66, 37–49.
- [33] Bažant, Z., Ožbolt, J., 1990. *Nonlocal microplane model for fracture, damage, and size effect in structures*. Journal of Engineering Mechanics 116, 2485–2505.
- [34] Bažant, Z., Prat, P., 1988a. *Microplane model for brittle-plastic material: I. Theory*. Journal of Engineering Mechanics 114, 1672–1688.
- [35] Bažant, Z., Prat, P., 1988b. *Microplane model for brittle-plastic material: II. Verification*. Journal of Engineering Mechanics 114, 1689–1702.
- [36] Bažant, Z., Xiang, Y., Adley, M., Prat, P., Akers, S., 1996a. *Microplane model for concrete: II: Data delocalization and verification*. Journal of Engineering Mechanics 122, 255–262.
- [37] Bažant, Z., Xiang, Y., Prat, P., 1996b. *Microplane model for concrete. I: Stress-strain boundaries and finite strain*. Journal of Engineering Mechanics 122, 245–254.
- [38] Beatty, M., 2004. *An average-stretch full-network model for rubber elasticity*. Journal of Elasticity 70, 65–86.
- [39] Beaupré, G., Orr, T., Carter, D., 1990. *An approach for time-dependent bone modelling and remodelling*. Journal of Orthopaedic Research 8, 651–670.
- [40] Bendsoe, M.P., Sigmund, O., 2003. *Topology Optimization – Theory, Methods and Applications*. Springer.
- [41] Bertsekas, D.P., 1996. *Constrained Optimization and Lagrange Multiplier Methods*. Volume 4 of *Athena Scientific Optimization and Computation Series*. Athena Scientific.
- [42] Bischoff, J., Arruda, E., Grosh, K., 2002. *Finite element simulations of orthotropic hyperelasticity*. Finite Elements in Analysis and Design 38, 983–998.

- [43] Boehler, J. (Ed.), 1987. *Applications of Tensor Functions in Solid Mechanics*. Number 292 in CISM Courses and Lectures, Springer.
- [44] Böhlke, T., Brüggemann, C., 2001. *Graphical representation of the generalized Hooke's law*. *Technische Mechanik* 21, 145–158.
- [45] Bonet, J., Wood, R.D., 2008. *Nonlinear Continuum Mechanics for Finite Element Analysis*. Cambridge University Press.
- [46] Borrvall, T., Petersson, J., 2001. *Large-scale topology optimization in 3D using parallel computing*. *Computer Methods in Applied Mechanics and Engineering* 190, 6201–6229.
- [47] de Borst, R., 1987. *Computation of post-bifurcation and post-failure behavior of strain-softening solids*. *Computers & Structures* 25, 211–224.
- [48] de Borst, R., Pamin, J., 1996. *Some novel developments in finite element procedures for gradient-dependent plasticity*. *International Journal for Numerical Methods in Engineering* 39, 2477–2505.
- [49] Boulanger, P., Hayes, M., 2000. *On finite shear*. *Archive for Rational Mechanics and Analysis* 151, 125–185.
- [50] Boulanger, P., Hayes, M., 2001. *Shear*, in: Fu, Y., Ogden, R. (Eds.), *Nonlinear Elasticity: Theory and Applications*. Cambridge. number 283 in London Mathematical Society Lecture Notes Series, pp. 97–134.
- [51] Boulanger, P., Hayes, M., 2005. *Constructions of unsheared pairs in finite strain*. *International Journal of Non-Linear Mechanics* 40, 289–293.
- [52] Breen, E., 2000. *Mechanical strain increases type I collagen expression in pulmonary fibroblasts in vitro*. *Journal of Applied Physiology* 88, 203–209.
- [53] Brocca, M., Brinson, L., Bažant, Z., 2002. *Three-dimensional constitutive model for shape memory alloys based on microplane model*. *Journal of the Mechanics and Physics of Solids* 50, 1051–1077.
- [54] Calve, S., Dennis, R., Kosnik, P., Baar, K., Grosh, K., Arruda, E., 2004. *Engineering of functional tendon*. *Tissue Engineering* 10, 755–761.
- [55] Calvo, B., Peña, E., Martínez, M., Doblaré, M., 2007. *An uncoupled directional damage model for fibred biological soft tissues. Formulation and computational aspects*. *International Journal for Numerical Methods in Engineering* 69, 2036–2057.
- [56] Caner, F., Carol, I., 2006. *Microplane constitutive model and computational framework for blood vessel tissue*. *Journal of Biomechanical Engineering* 128, 419–427.
- [57] Cardamone, L., Valentín, A., Eberth, J., Humphrey, J., 2009. *Origin of axial pre-stretch and residual stress in arteries*. *Biomechanics and Modeling in Mechanobiology* 8, 431–446.

-
- [58] Carol, I., Bažant, Z.P., 1997. *Damage and plasticity in microplane theory*. International Journal of Solids and Structures 34, 3807–3835.
- [59] Carol, I., Jirásek, M., Bažant, Z., 2001. *A thermodynamically consistent approach to microplane theory. Part I. Free energy and consistent microplane stresses*. International Journal of Solids and Structures 38, 2921–2931.
- [60] Carol, I., Jirásek, M., Bažant, Z., 2004. *A framework for microplane models at large strain, with application to hyperelasticity*. International Journal of Solids and Structures 41, 511–557.
- [61] Carpenter, R., Carter, D., 2010. *Computational simulation of spontaneous bone straightening in growing children*. Biomechanics and Modeling in Mechanobiology 9, 317–328.
- [62] Carter, D., Beaupré, G., 2001. *Skeletal function and form: mechanobiology of skeletal development, aging, and regeneration*. Cambridge University Press.
- [63] Carter, D., Hayes, W., 1977. *Compressive behavior of bone as a 2-phase porous structure*. Journal of Bone and Joint Surgery 59, 954–962.
- [64] Carter, D., Orr, T., Fyhrie, D., 1989. *Relationships between loading history and femoral cancellous bone architecture*. Journal of Biomechanics 22, 231–244.
- [65] Cazzani, A., Rovati, M., 2003. *Extrema of Young's modulus for cubic and transversely isotropic solids*. International Journal of Solids and Structures 40, 1713–1744.
- [66] Chen, M., Zheng, Q.S., Yang, W., 1996. *A micromechanical model of texture induced orthotropy in planar crystalline polymers*. Journal of the Mechanics and Physics of Solids 44, 157–178.
- [67] Christensen, P.W., Klarbring, A., 2009. *An Introduction to Structural Optimization*. Springer.
- [68] Chuong, C., Fung, Y., 1983. *Three-dimensional stress distribution in arteries*. Journal of Biomechanical Engineering 105, 268–274.
- [69] Coelho, P., Fernandes, P., Rodrigues, H., Cardoso, J., Guedes, J., 2009. *Numerical modeling of bone tissue adaptation—A hierarchical approach for bone apparent density and trabecular structure*. Journal of Biomechanics 42, 830–837.
- [70] Coelho, P.G., Fernandes, P.R., Guedes, J.M., Rodrigues, H.C., 2008. *A hierarchical model for concurrent material and topology optimisation of three-dimensional structures*. Structural and Multidisciplinary Optimization 35, 107–115.
- [71] Cowin, S., 1985. *The relationship between the elasticity tensor and the fabric tensor*. Mechanics of Materials 4, 137–147.
- [72] Cowin, S., 2004. *Tissue growth and remodeling*. Annual Review of Biomedical Engineering 6, 77–107.

- [73] Cowin, S., Doty, S., 2007. *Tissue Mechanics*. Springer.
- [74] Cowin, S., Hegedus, D., 1976. *Bone remodelling I: Theory of adaptive elasticity*. Journal of Elasticity 6, 313–326.
- [75] Cowin, S., Humphrey, J. (Eds.), 2000. *Cardiovascular Soft Tissue Mechanics*. Kluwer.
- [76] Cowin, S.C., 1986. *Wolff's law of trabecular architecture at remodeling equilibrium*. Journal of Biomechanical Engineering 108, 83–88.
- [77] Creane, A., Kelly, D., Lally, C., 2012. *Patient Specific Computational Modeling in Cardiovascular Mechanics*, in: Calvo, B., Peña, E. (Eds.), Patient-Specific Computational Modeling. Springer Netherlands. Volume 5 of *Lecture Notes in Computational Vision and Biomechanics*, pp. 61–79.
- [78] Crisfield, M., 1997a. *Non-Linear Finite Element Analysis of Solids and Structures. Volume 1 – Essentials*. Wiley.
- [79] Crisfield, M., 1997b. *Non-Linear Finite Element Analysis of Solids and Structures. Volume 2 – Advanced Topics*. Wiley.
- [80] Crisfield, M.A., 1981. *A fast incremental/iteration solution procedure that handles 'snap-through'*. Computers and Structures 13, 55–62.
- [81] Dennis, Jr., J., Schnabel, R., 1996. *Numerical Methods for Unconstrained Optimization and Nonlinear Equations*. Number 16 in Classics in Applied Mathematics, SIAM.
- [82] Dhondt, G., 2004. *The Finite Element Method for Three-Dimensional Thermo-mechanical Applications*. Wiley.
- [83] DiCarlo, A., Quiligotti, S., 2002. *Growth and balance*. Mechanics Research Communications 29, 449–456.
- [84] Dimitrijević, B., 2010. *On a regularization framework for inelastic material models via gradient enhancement of the free energy function*. Ph.D. Thesis. Fakultät für Bauingenieurwesen, Ruhr-Universität Bochum.
- [85] Dimitrijević, B.J., Hackl, K., 2008. *A method for gradient enhancement of continuum damage models*. Technische Mechanik 28, 43–52.
- [86] Dimitrijević, B.J., Hackl, K., 2011. *A regularization framework for damage-plasticity models via gradient enhancement of the free energy*. International Journal for Numerical Methods in Biomedical Engineering 27, 1199–1210.
- [87] Doblaré, M., García, J., 2002. *Anisotropic bone remodelling model based on a continuum damage-repair theory*. Journal of Biomechanics 35, 1–17.
- [88] Doll, S., Schweizerhof, K., 1999. *On the Development of Volumetric Strain Energy Functions*. Journal of Applied Mechanics 67, 17–21.

-
- [89] Driessen, N.J.B., Wilson, W., Bouten, C.V.C., Baaijens, F.P.T., 2004. *A computational model for collagen fibre remodelling in the arterial wall*. Journal of Theoretical Biology 226, 53–64.
- [90] Eastwood, M., Mudera, V., Mcgrouter, D., Brown, R., 1998. *Effect of precise mechanical loading on fibroblast populated collagen lattices: Morphological changes*. Cell Motility and the Cytoskeleton 40, 13–21.
- [91] Ehret, A.E., Itskov, M., Schmid, H., 2010. *Numerical integration on the sphere and its effect on the material symmetry of constitutive equations – A comparative study*. International Journal for Numerical Methods in Engineering 81, 189–206.
- [92] Epstein, M., Maugin, G., 2000. *Thermomechanics of volumetric growth in uniform bodies*. International Journal of Plasticity 16, 951–978.
- [93] Eringen, A. (Ed.), 1976. *Continuum Physics. Volume IV – Polar and Nonlocal Field Theories*. Academic Press.
- [94] Eringen, A., 2002. *Nonlocal Continuum Field Theories*. Springer.
- [95] Faller, A., Schünke, M., Schünke, G., 2004. *The Human Body – An Introduction to Structure and Function*. Thieme.
- [96] Federico, S., Gasser, T., 2010. *Nonlinear elasticity of biological tissues with statistical fibre orientation*. Journal of the Royal Society Interface 7, 955–966.
- [97] Fernandes, P., Rodrigues, H., Jacobs, C., 1999. *A model of bone adaptation using a global optimisation criterion based on the trajectorial theory of Wolff*. Computer Methods in Biomechanics and Biomedical Engineering 2, 125–138.
- [98] Fliege, J., Maier, U., 1999. *The distribution of points on the sphere and corresponding cubature formulae*. IMA Journal of Numerical Analysis 19, 317–334.
- [99] Flory, P., 1969. *Statistical Mechanics of Chain Molecules*. Wiley.
- [100] Forest, S., 2009. *Micromorphic approach for gradient elasticity, viscoplasticity, and damage*. Journal of Engineering Mechanics 135, 117–131.
- [101] Frémond, M., Nedjar, B., 1996. *Damage, gradient of damage and principle of virtual power*. International Journal of Solids and Structures 33, 1083–1103.
- [102] Fung, Y., 1990. *Biomechanics: Motion, Flow, Stress, and Growth*. Springer.
- [103] García, J.M., Doblaré, M., Cegoñino, J., 2002. *Bone remodelling simulation: a tool for implant design*. Computational Materials Science 25, 100–114.
- [104] García, J.M., Martínez, M.A., Doblaré, M., 2001. *An Anisotropic Internal-External Bone Adaptation Model Based on a Combination of CAO and Continuum Damage Mechanics Technologies*. Computer Methods in Biomechanics and Biomedical Engineering 4, 355–377.
- [105] Garikipati, K., Arruda, E., Grosh, K., Narayanan, H., Calve, S., 2004. *A continuum treatment of growth in biological tissue: the coupling of mass transport and*

- mechanics*. Journal of the Mechanics and Physics of Solids 52, 1595–1625.
- [106] Gasser, T., Holzapfel, G., 2007. *Finite element modeling of balloon angioplasty by considering overstretch of remnant non-diseased tissues in lesions*. Computational Mechanics 40, 47–60.
- [107] Gasser, T., Ogden, R., Holzapfel, G., 2006. *Hyperelastic modelling of arterial layers with distributed collagen fibre orientations*. Journal of the Royal Society Interface 3, 15–35.
- [108] Gent, A., Rivlin, R., 1952. *Experiments on the mechanics of rubber II: the tension, inflation and extension of a tube*. Proceedings of the Physical Society B 65, 487–501.
- [109] Gitman, I., Askes, H., Kuhl, E., Aifantis, E., 2010. *Stress concentrations in fractured compact bone simulated with a special class of anisotropic gradient elasticity*. International Journal of Solids and Structures 47, 1099–1107.
- [110] Göktepe, S., Abilez, O., Kuhl, E., 2010. *A generic approach towards finite growth with examples of athlete’s heart, cardiac dilation, and cardiac wall thickening*. Journal of the Mechanics and Physics of Solids 58, 1661–1680.
- [111] Göktepe, S., Miehe, C., 2005. *A micro-macro approach to rubber-like materials. Part III: The micro-sphere model of anisotropic Mullins-type damage*. Journal of the Mechanics and Physics of Solids 53, 2259–2283.
- [112] Goldstein, S., 1987. *The mechanical properties of trabecular bone: Dependence on anatomic location and function*. Journal of Biomechanics 20, 1055–1061.
- [113] Green, A., Adkins, J., 1970. *Large Elastic Deformations*. Oxford University Press. 2nd edition.
- [114] Guillou, A., Ogden, R., 2006. *Growth in soft biological tissue and residual stress development*, in: Holzapfel, G., Ogden, R. (Eds.), *Mechanics of Biological Tissue*, Springer. pp. 47–62.
- [115] Gurtin, M., Francis, E., 1981. *Simple rate-independent model for damage*. AIAA Journal of Spacecraft 18, 285–288.
- [116] Harrigan, T., Hamilton, J., 1992. *An analytical and numerical study of the stability of bone remodelling theories: dependence on microstructural stimulus*. Journal of Biomechanics 25, 477–488. Corrigendum 26(3):365–366, 1993.
- [117] Harrigan, T., Hamilton, J., 1993a. *Bone strain sensation via transmembrane potential changes in surface osteoblasts: Loading rate and microstructural implications*. Journal of Biomechanics 26, 183–200.
- [118] Harrigan, T., Hamilton, J., 1993b. *Finite element simulation of adaptive bone remodelling: a stability criterion and a time stepping method*. International Journal for Numerical Methods in Engineering 36, 837–854.

-
- [119] Harrigan, T., Hamilton, J., 1994. *Necessary and sufficient conditions for global stability and uniqueness in finite element simulations of adaptive bone remodelling*. International Journal of Solids and Structures 31, 97–107.
- [120] Harrysson, M., Ristinmaa, M., Wallin, M., Menzel, A., 2010. *Framework for deformation induced anisotropy in glassy polymers*. Acta Mechanica 211, 195–213.
- [121] Haughton, D., 2001. *Elastic membranes*, in: Fu, Y., Ogden, R. (Eds.), Nonlinear Elasticity: Theory and Applications. Cambridge. number 283 in London Mathematical Society Lecture Notes Series, pp. 97–134.
- [122] Haughton, D., Ogden, R., 1978a. *On the incremental equations in non-linear elasticity – I. Membrane theory*. Journal of the Mechanics and Physics of Solids 26, 93–110.
- [123] Haughton, D., Ogden, R., 1978b. *On the incremental equations in non-linear elasticity – II. Bifurcation of pressurized spherical shells*. Journal of the Mechanics and Physics of Solids 26, 111–138.
- [124] Haughton, D., Ogden, R., 1979a. *Bifurcation of inflated circular cylinders of elastic material under axial loading – I. Membrane theory for thin-walled tubes*. Journal of the Mechanics and Physics of Solids 27, 179–212.
- [125] Haughton, D., Ogden, R., 1979b. *Bifurcation of inflated circular cylinders of elastic material under axial loading – II. Exact theory for thick-walled tubes*. Journal of the Mechanics and Physics of Solids 27, 489 – 512.
- [126] Haughton, D., Ogden, R., 1980a. *Bifurcation of rotating thick-walled elastic tubes*. Journal of the Mechanics and Physics of Solids 28, 59–74.
- [127] Haughton, D.M., Ogden, R.W., 1980b. *Bifurcation of finitely deformed rotating elastic cylinders*. Quarterly Journal of Mechanics and Applied Mathematics 33, 251–266.
- [128] Heo, S., Xu, Y., 2001. *Constructing fully symmetric cubature formulae for the sphere*. Mathematics of Computation 70, 269–279.
- [129] Himpel, G., Kuhl, E., Menzel, A., Steinmann, P., 2005. *Computational modelling of isotropic multiplicative growth*. Computer Modeling in Engineering and Sciences 8, 119–134.
- [130] Himpel, G., Menzel, A., Kuhl, E., Steinmann, P., 2008. *Time-dependent fibre reorientation of transversely isotropic continua—Finite element formulation and consistent linearization*. International Journal for Numerical Methods in Engineering 73, 1413–1433.
- [131] Hoger, A., 1985. *On the residual stress possible in an elastic body with material symmetry*. Archive for Rational Mechanics and Analysis 88, 271–290.
- [132] Hoger, A., 1986. *On the determination of residual stress in an elastic body*. Journal of Elasticity 16, 303–324.

- [133] Hoger, A., 1993. *The dependence of the elasticity tensor on residual stress*. Journal of Elasticity 33, 145–165.
- [134] Holzapfel, G., Gasser, T., 2001. *A viscoelastic model for fiber-reinforced composites at finite strains: Continuum basis, computational aspects and applications*. Computer Methods in Applied Mechanics and Engineering 190, 4379–4403.
- [135] Holzapfel, G., Gasser, T., Ogden, R., 2000. *A new constitutive framework for arterial wall mechanics and a comparative study of material models*. Journal of Elasticity 61, 1–48.
- [136] Holzapfel, G., Ogden, R. (Eds.), 2003. *Biomechanics of Soft Tissue in Cardiovascular Systems*. Number 441 in CISM Courses and Lectures, Springer.
- [137] Holzapfel, G., Ogden, R. (Eds.), 2009. *Biomechanical Modelling at the Molecular, Cellular and Tissue Levels*. Number 508 in CISM Courses and Lectures, Springer.
- [138] Holzapfel, G., Ogden, R., 2010. *Constitutive modelling of arteries*. Proceedings of the Royal Society A. Mathematical, Physical and Engineering Sciences 466, 1551–1597.
- [139] Holzapfel, G., Stadler, M., Schulze-Bauer, C., 2002. *A layer-specific three-dimensional model for the simulation of balloon angioplasty using magnetic resonance imaging and mechanical testing*. Annals of Biomedical Engineering 30, 753–767.
- [140] Hughes, T., 2000. *The Finite Element Method*. Dover.
- [141] Hughes, T., Pister, K., 1978. *Consistent linearization in mechanics of solids and structures*. Computers & Structures 8, 391–397.
- [142] Huiskes, R., Weinans, H., Grootenboer, H., Dalstra, M., Fudala, B., Slooff, T., 1987. *Adaptive bone-remodeling theory applied to prosthetic-design analysis*. Journal of Biomechanics 20, 1135–1150.
- [143] Hulet, C., Sabatier, J., Souquet, D., Locker, B., Marcelli, C., Vielpeau, C., 2002. *Distribution of bone mineral density at the proximal tibia in knee osteoarthritis*. Calcified Tissue International 71, 315–322.
- [144] Humphrey, J., 2002. *Cardiovascular Solid Mechanics. Cells, Tissues, and Organs*. Springer.
- [145] Humphrey, J., Rajagopal, K., 2002. *A constrained mixture model for growth and remodeling of soft tissues*. Mathematical Models and Methods in Applied Sciences 12, 407–430.
- [146] Hurwitz, D., Sumner, D., Andriacchi, T., Sugar, D., 1998. *Dynamic knee loads during gait predict proximal tibial bone distribution*. Journal of Biomechanics 31, 423–430.
- [147] Imatani, S., Maugin, G.A., 2002. *A constitutive model for material growth and its application to three-dimensional finite element analysis*. Mechanics Research

- Communications 29, 477–483.
- [148] Jacobs, C., Levenston, M., Beaupré, G., Simo, J., Carter, D., 1995. *Numerical instabilities in bone remodeling simulations: The advantages of a node-based finite element approach*. Journal of Biomechanics 28, 449–459.
- [149] Jacobs, C., Simo, J., Beaupré, G., Carter, D., 1997. *Adaptive bone remodeling incorporating simultaneous density and anisotropy considerations*. Journal of Biomechanics 30, 603–613.
- [150] Jirásek, M., 1998. *Nonlocal models for damage and fracture: Comparison of approaches*. International Journal of Solids and Structures 35, 4133–4145.
- [151] Jirásek, M., Bažant, Z., 2001. *Inelastic Analysis of Structures*. John Wiley & Sons.
- [152] Johnson, B., Hoger, A., 1995. *The use of virtual configuration in formulating constitutive equations for residually stressed elastic materials*. Journal of Elasticity 41, 177–215.
- [153] Kachanov, L., 1958. *Time of the rupture process under creep conditions*. Izvestija Akademii Nauk Sojuza Sovetskikh Socialisticeskich Respubliki (SSSR) Otdelenie Techniceskich Nauk (Moskra) 8, 26–31.
- [154] Kachanov, L., 1986. *Introduction to Continuum Damage Mechanics*. Martinus Nijhoff Publishers, Dordrecht, The Netherlands.
- [155] Kadkhodaei, M., Salimi, M., Rajapakse, R., Mahzoon, M., 2007. *Microplane modelling of shape memory alloys*. Physica Scripta 2007, 329.
- [156] Kadkhodaei, M., Salimi, M., Rajapakse, R., Mahzoon, M., 2008. *Modeling of shape memory alloys based on microplane theory*. Journal of Intelligent Material Systems and Structures 19, 541–550.
- [157] Katchalsky, A., Curran, P., 1965. *Nonequilibrium Thermodynamics in Biophysics*. Volume 1 of *Harvard Books in Biophysics*. Harvard University Press.
- [158] Klisch, S., Hoger, A., 2003. *Volumetric growth of thermoelastic materials and mixtures*. Mathematics and Mechanics of Solids 8, 377–402.
- [159] Kocks, U., Tomé, C., Wenk, H.R. (Eds.), 2000. *Texture and Anisotropy – Preferred Orientations in Polycrystals and their Effect on Material Properties*. Cambridge University Press.
- [160] Kouznetsova, V., Geers, M., Brekelmans, W., 2004. *Multi-scale second-order computational homogenization of multi-phase materials: a nested finite element solution strategy*. Computer Methods in Applied Mechanics and Engineering 193, 5525–5550.
- [161] Krajcinovic, D., 1996. *Damage Mechanics*. North-Holland, Amsterdam.
- [162] Krajcinovic, D., Lemaitre, J., 1987. *Continuum Damage Mechanics*. Number 295 in CISM Courses and Lectures, Springer.

- [163] Krstin, N., Nackenhorst, U., Lammering, R., 2000. *Zur konstitutiven Beschreibung des anisotropen beanspruchungsadaptiven Knochenbaus*. Technische Mechanik 20, 31–40.
- [164] Kuhl, E., Maas, R., Himpel, G., Menzel, A., 2007. *Computational modelling of arterial wall growth – Attempts towards a patient specific simulation based on computer tomography*. Biomechanics and Modeling in Mechanobiology 6, 321–331.
- [165] Kuhl, E., Menzel, A., Garikipati, K., 2006. *On the convexity of transversely isotropic chain network models*. Philosophical Magazine 86, 3241–3258.
- [166] Kuhl, E., Menzel, A., Steinmann, P., 2003. *Computational modeling of growth – A critical review, a classification of concepts and two new consistent approaches*. Computational Mechanics 32, 71–88.
- [167] Kuhl, E., Ramm, E., 1999. *Simulation of strain localization with gradient enhanced damage models*. Computational Materials Science 16, 176–185.
- [168] Kuhl, E., Ramm, E., 2000. *Microplane modelling of cohesive frictional materials*. European Journal of Mechanics A/Solids 19, 121–143.
- [169] Kuhl, E., Ramm, E., de Borst, R., 2000a. *An anisotropic gradient damage model for quasi-brittle materials*. Computer Methods in Applied Mechanics and Engineering 183, 87–103.
- [170] Kuhl, E., Ramm, E., Willam, K., 2000b. *Failure analysis of elasto-plastic material models on different levels of observation*. International Journal of Solids and Structures 37, 7259–7280.
- [171] Kuhl, E., Steinmann, P., 2003a. *Mass- and volume specific views on thermodynamics for open systems*. Proceedings of the Royal Society A 459, 2547–2568.
- [172] Kuhl, E., Steinmann, P., 2003b. *Theory and numerics of geometrically non-linear open system mechanics*. International Journal for Numerical Methods in Engineering 58, 1593–1615.
- [173] Kuhl, E., Steinmann, P., 2004. *Material forces in open system mechanics*. Computer Methods in Applied Mechanics and Engineering 193, 2357–2381.
- [174] Kuhl, E., Steinmann, P., Carol, I., 2001. *A thermodynamically consistent approach to microplane theory. Part II. Dissipation and inelastic constitutive modeling*. International Journal of Solids and Structures 38, 2933–2952.
- [175] Kurzhöfer, I., 2007. *Mehrskaligen-Modellierung polykristalliner Ferroelektrika basierend auf diskreten Orientierungsverteilungsfunktionen*. Ph.D. Thesis. Universität Duisburg-Essen, Institut für Mechanik, Bericht Nr. 4.
- [176] Lanir, Y., 1979. *A structural theory for the homogeneous biaxial stress-strain relationships in flat collagenous tissues*. Journal of Biomechanics 12, 423–436.
- [177] Lanir, Y., 1983. *Constitutive equations for fibrous connective tissues*. Journal of Biomechanics 16, 1–12.

-
- [178] Lasry, D., Belytschko, T., 1988. *Localization limiters in transient problems*. International Journal of Solids and Structures 24, 581–597.
- [179] Lebedev, V., Laikov, D., 1999. *A quadrature formula for the sphere of the 131st algebraic order of accuracy*. Doklady Mathematics 59, 477–481.
- [180] Lebedev, V.I., 1976. *Quadratures on a sphere*. Zhurnal Vychislitel'noi Matematiki i Matematicheskoi Fiziki 16, 293–306.
- [181] Lemaitre, J., 1996. *A Course on Damage Mechanics*. Springer. 2nd edition.
- [182] Lemaitre, J., Chaboche, J.L., 1990. *Mechanics of Solid Materials*. Cambridge University Press, Cambridge.
- [183] Leukart, M., Ramm, E., 2003. *A comparison of damage models formulated on different material scales*. Computational Materials Science 28, 749–762.
- [184] Liebe, T., Menzel, A., Steinmann, P., 2003. *Theory and numerics of a thermodynamically consistent framework for geometrically non-linear gradient plasticity*. Int. J. Engng. Sci. 41, 1603–1629.
- [185] Liebe, T., Steinmann, P., 2002. *Two strategies towards geometrically non-linear isotropic gradient damage*. Journal of the Mechanical Behavior of Materials 13, 175–194.
- [186] Liebe, T., Steinmann, P., Benallal, A., 2001. *Theoretical and computational aspects of a thermodynamically consistent framework for geometrically linear gradient damage*. Computer Methods in Applied Mechanics and Engineering 190, 6555–6576.
- [187] Linder, C., Tkachuk, M., Miehe, C., 2011. *A micromechanically motivated diffusion-based transient network model and its incorporation into finite rubber viscoelasticity*. Journal of the Mechanics and Physics of Solids 59, 2134–2156.
- [188] Lubarda, V., Hoger, A., 2002. *On the mechanics of solids with a growing mass*. International Journal of Solids and Structures 39, 4627–4664.
- [189] Lubarda, V., Krajcinovic, D., 1993. *Damage tensors and the crack density distribution*. International Journal of Solids and Structures 30, 2859–2877.
- [190] Luenberger, D., 1984. *Nonlinear Programming*. Addison–Wesley. 2nd edition.
- [191] Ma, D., Friák, M., Neugebauer, J., Raabe, D., Roters, F., 2008. *Multiscale simulation of polycrystal mechanics of textured β -Ti alloys using ab initio and crystal-based finite element methods*. physica status solidi (b) 245, 2642–2648.
- [192] Mahnken, R., Kuhl, E., 1999. *Parameter identification of gradient enhanced damage models with the finite element method*. European Journal of Mechanics - A/Solids 18, 819–835.
- [193] Malvern, L., 1969. *Introduction to the Mechanics of a Continuous Medium*. Prentice-Hall.

- [194] Marquez, J., 2006. *Fourier analysis and automated measurement of cell and fiber angular orientation distributions*. International Journal of Solids and Structures 43, 6413–6423.
- [195] Marsden, J., Hughes, T., 1994. *Mathematical Foundations of Elasticity*. Dover.
- [196] Martins, P., Peña, E., Jorge, R.N., Santos, A., Santos, L., Mascarenhas, T., Calvo, B., 2012. *Mechanical characterization and constitutive modelling of the damage process in rectus sheath*. Journal of the Mechanical Behavior of Biomedical Materials 8, 111–122.
- [197] Menzel, A., 2005. *Modelling of anisotropic growth in biological tissues – A new approach and computational aspects*. Biomechanics and Modeling in Mechanobiology 3, 147–171.
- [198] Menzel, A., 2006. *Anisotropic remodelling of biological tissues*, in: Holzapfel, G., Ogden, R. (Eds.), *Mechanics of Biological Tissue*, Springer. pp. 91–104.
- [199] Menzel, A., 2007. *A fibre reorientation model for orthotropic multiplicative growth – Configurational driving stresses, kinematics-based reorientation, and algorithmic aspects*. Biomechanics and Modeling in Mechanobiology 6, 303–320.
- [200] Menzel, A., Ekh, M., Steinmann, P., Runesson, K., 2002. *Anisotropic damage coupled to plasticity: modelling based on the effective configuration concept*. International Journal for Numerical Methods in Engineering 54, 1409–1430.
- [201] Menzel, A., Harrysson, M., Ristinmaa, M., 2008. *Towards an orientation-distribution-based multi-scale approach for remodelling biological tissues*. Computer Methods in Biomechanics and Biomedical Engineering 11, 505–524.
- [202] Menzel, A., Kuhl, E., 2012. *Frontiers in growth and remodeling*. Mechanics Research Communications 42, 1–14.
- [203] Menzel, A., Steinmann, P., 2001a. *A theoretical and computational framework for anisotropic continuum damage mechanics at large strains*. International Journal of Solids and Structures 38, 9505–9523.
- [204] Menzel, A., Steinmann, P., 2001b. *On the comparison of two strategies to formulate orthotropic hyperelasticity*. Journal of Elasticity 62, 171–201.
- [205] Menzel, A., Steinmann, P., 2003a. *A view on anisotropic finite hyper-elasticity*. Euro. J. Mech. A/Solids 22, 71–87.
- [206] Menzel, A., Steinmann, P., 2003b. *Geometrically nonlinear anisotropic inelasticity based on fictitious configurations: Application to the coupling of continuum damage and multiplicative elasto-plasticity*. International Journal for Numerical Methods in Engineering 56, 2233–2266.
- [207] Menzel, A., Steinmann, P., 2003c. *On the spatial formulation of anisotropic multiplicative elasto-plasticity*. Computer Methods in Applied Mechanics and Engineering 192, 3431–3470.

-
- [208] Menzel, A., Waffenschmidt, T., 2009a. *A microsphere-based remodelling formulation for anisotropic biological tissues*. Philosophical Transactions of the Royal Society A 367, 3499–3523.
- [209] Menzel, A., Waffenschmidt, T., 2009b. *Remodelling of anisotropic soft biological tissues. A computational micro-sphere approach*, in: Oñate, E., Owen, D. (Eds.), X International Conference on Computational Plasticity – COMPLAS X, CIMNE, Barcelona.
- [210] Menzel, A., Waffenschmidt, T., Alastrué, V., 2010. *An anisotropic micro-sphere approach applied to the modelling of soft biological tissues*, in: Kreiss, G., Lötstedt, P., Målqvist, A., Neytcheva, M. (Eds.), Numerical Mathematics and Advanced Applications, Springer. pp. 637–644.
- [211] von Meyer, H., 1867. *Die Architektur der Spongiosa*. Reichert's und Du Bois Reymoid's Archiv für Anatomie und Physiologie 34, 615–628.
- [212] Mühlhaus, H.B., Aifantis, E., 1991. *A variational principle for gradient plasticity*. International Journal of Solids and Structures 28, 845–857.
- [213] Miehe, C., 1994. *Aspects of the formulation and finite element implementation of large strain isotropic elasticity*. International Journal for Numerical Methods in Engineering 37, 1981–2004.
- [214] Miehe, C., 1995. *Discontinuous and continuous damage evolution in Ogden-type large-strain elastic materials*. European Journal of Mechanics A/Solids 14, 697–720.
- [215] Miehe, C., 1996. *Numerical computation of algorithmic (consistent) tangent moduli in large-strain computational inelasticity*. Computer Methods in Applied Mechanics and Engineering 134, 223–240.
- [216] Miehe, C., 2011. *A multi-field incremental variational framework for gradient-extended standard dissipative solids*. Journal of the Mechanics and Physics of Solids 59, 898–923.
- [217] Miehe, C., Göktepe, S., 2005. *A micro-macro approach to rubber-like materials. Part II: The micro-sphere model of rubber viscoelasticity*. Journal of the Mechanics and Physics of Solids 53, 2231–2258.
- [218] Miehe, C., Göktepe, S., Lulei, F., 2004. *A micro-macro approach to rubber-like materials—Part I: the non-affine micro-sphere model of rubber elasticity*. Journal of the Mechanics and Physics of Solids 52, 2617–2660.
- [219] Miehe, C., Koch, A., 2002. *Computational micro-to-macro transitions of discretized microstructures undergoing small strains*. Archive of Applied Mechanics 72, 300–317.
- [220] Moreo, P., Pérez, M., García-Aznar, J., Doblaré, M., 2007. *Modelling the mechanical behaviour of living bony interfaces*. Computer Methods in Applied Mechanics

- and Engineering 196, 3300–3314.
- [221] Nackenhorst, U., Krstin, N., Lammering, R., 2000. *A constitutive law for anisotropic stress adaptive bone remodeling*. Zeitschrift für angewandte Mathematik und Mechanik 80, 399–400.
- [222] Nedjar, B., 2002. *A theoretical and computational setting for a geometrically nonlinear gradient damage modelling framework*. Computational Mechanics 30, 65–80.
- [223] Nemat-Nasser, S., Hori, M., 1993. *Micromechanics: Overall Properties of heterogeneous materials*. Applied Mathematics and Mechanics, Elsevier.
- [224] Noll, W., 1967. *Materially uniform simple bodies with inhomogeneities*. Archive for Rational Mechanics and Analysis 27, 1–32. Errata: W. Noll, R.A. Toupin, and C.C. Wang. *Archive for Rational Mechanics and Analysis*, 31(5):401, 1968.
- [225] Ogden, R., 1997. *Non-Linear Elastic Deformations*. Dover.
- [226] Ogden, R., 2001. *Elements of the theory of finite elasticity*, in: Fu, Y., Ogden, R. (Eds.), *Nonlinear Elasticity: Theory and Applications*. Cambridge. number 283 in London Mathematical Society Lecture Notes Series, pp. 97–134.
- [227] Ogden, R., 2009. *Anisotropy and Nonlinear Elasticity in Arterial Wall Mechanics*, in: Holzapfel, G., Ogden, R. (Eds.), *Biomechanical Modelling at the Molecular, Cellular and Tissue Levels*. Springer. number 441 in CISM Courses and Lectures, pp. 65–108.
- [228] Olsson, T., Stålhand, J., Klarbring, A., 2006. *Modeling initial strain distribution in soft tissues with application to arteries*. Biomechanics and Modeling in Mechanobiology 5, 27–38.
- [229] Ostwald, R., Bartel, T., Menzel, A., 2010. *A computational micro-sphere model applied to the simulation of phase-transformations*. Zeitschrift für angewandte Mathematik und Mechanik 90, 605–622.
- [230] Ostwald, R., Bartel, T., Menzel, A., 2012. *Phase-transformations interacting with plasticity – A micro-sphere model applied to TRIP steel*. Computational Materials Science 64, 12–16.
- [231] Pamin, J., 2005. *Gradient plasticity and damage models: a short comparison*. Computational Materials Science 32, 472–479.
- [232] Pang, H., Shiwalkar, A., Madormo, C., Taylor, R., Andriacchi, T., Kuhl, E., 2012. *Computational modeling of bone density profiles in response to gait: a subject-specific approach*. Biomechanics and Modeling in Mechanobiology 11, 379–390.
- [233] Papenfuss, C., 2000. *Theory of liquid crystals as an example of mesoscopic continuum mechanics*. Computational Materials Science 19, 45–52.
- [234] Peerlings, R.H.J., de Borst, R., Brekelmans, W.A.M., Geers, M.G.D., 1998. *Gradient-enhanced damage modelling of concrete fracture*. Mechanics of Cohesive-frictional Materials 3, 323–342.

- [235] Peerlings, R.H.J., de Borst, R., Brekelmans, W.A.M., de Vree, J.H.P., 1996. *Gradient enhanced damage for quasi-brittle materials*. International Journal for Numerical Methods in Engineering 39, 3391–3403.
- [236] Peña, E., Alastrué, V., Laborda, A., Martínez, M., Doblaré, M., 2010. *A constitutive formulation of vascular tissue mechanics including viscoelasticity and softening behaviour*. Journal of Biomechanics 43, 984–989.
- [237] Pettermann, H., Reiter, T., Rammerstorfer, F., 1997. *Computational simulation of internal bone remodeling*. Archives of Computational Methods in Engineering 4, 295–323.
- [238] Pijaudier-Cabot, G., Bažant, Z., 1987. *Nonlocal damage theory*. Journal of Engineering Mechanics 113, 1512–1533.
- [239] Pipkin, A., Rivlin, R., 1962. *Minimum-weight design for pressure vessels reinforced with inextensible fibres*. ASME Journal of Applied Mechanics WA-151.
- [240] Podio-Guidugli, P., Vergara Caffarelli, G., 1990. *Surface interaction potentials in elasticity*. Archive for Rational Mechanics and Analysis 109, 343–383.
- [241] Polizzotto, C., Borino, G., Fuschi, P., 1998. *A thermodynamically consistent formulation of nonlocal and gradient plasticity*. Mechanics Research Communications 25, 75–82.
- [242] Powell, G., Simons, J., 1981. *Improved iterative strategy for nonlinear structures*. International Journal for Numerical Methods in Engineering 17, 1455–1467.
- [243] Quiligotti, S., 2002. *On bulk growth mechanics of solid-fluid mixtures: kinematics and invariance requirements*. Theoretical and Applied Mechanics 28–29, 277–288.
- [244] Ramm, E., 1981. *Strategies for tracing the nonlinear response near limit points*, in: Wunderlich, W., Stein, E., Bathe, K.J. (Eds.), Nonlinear Finite Element Analysis in Structural Mechanics. Springer Berlin Heidelberg, pp. 63–89.
- [245] Ramm, E., 1982. *The Riks/Wempner approach – an extension of the displacement control method in non-linear analysis*, in: Hinton, E. (Ed.), Non-Linear Computational Mechanics. Pineridge, Swansea, pp. 63–86.
- [246] Reina-Romo, E., Gómez-Benito, M., García-Aznar, J., Domínguez, J., Doblaré, M., 2010. *Growth mixture model of distraction osteogenesis: effect of pre-traction stresses*. Biomechanics and Modeling in Mechanobiology 9, 103–115.
- [247] Reitinger, R., 1994. *Stabilität und Optimierung imperfektionsempfindlicher Tragwerke*. Ph.D. Thesis. Universität Stuttgart, Institut für Baustatik, Bericht-Nr. 17.
- [248] Rho, J.Y., Kuhn-Spearing, L., Zioupos, P., 1998. *Mechanical properties and the hierarchical structure of bone*. Medical Engineering & Physics 20, 92–102.
- [249] Riks, E., 1972. *The application of Newton's method to the problem of elastic stability*. Transactions of the ASME Journal of Applied Mechanics 39, 1060–1066.

- [250] Riks, E., 1979. *An incremental approach to the solution of snapping and buckling problems*. International Journal of Solids and Structures 15, 529–551.
- [251] Rissland, P., Alemu, Y., Einav, S., Ricotta, J., 2009. *Abdominal aortic aneurysm risk of rupture: patient-specific FSI simulations using anisotropic model*. Journal of Biomechanical Engineering 131, 31001.
- [252] Rodrigues, H., Jacobs, C., Guedes, J.M., Bendsø, M.P., 2002. *Global and local material optimization models applied to anisotropic bone adaptation*, in: Pedersen, P., Bendsø, M.P. (Eds.), IUTAM Symposium on Synthesis in Bio Solid Mechanics. Springer Netherlands. Volume 69 of *Solid Mechanics and Its Applications*, pp. 209–220.
- [253] Rogula, D. (Ed.), 1982. *Nonlocal Theory of Material Media*. Number 268 in CISM Courses and Lectures, Springer.
- [254] Sáez, P., Alastrué, V., Peña, E., Doblaré, M., Martínez, M., 2011. *Anisotropic microsphere-based approach to damage in soft fibered tissue*. Biomechanics and Modeling in Mechanobiology 11, 595–608.
- [255] Schriebl, A., Zeindlinger, G., Pierce, D., Regitnig, P., Holzapfel, G., 2012. *Determination of the layer-specific distributed collagen fibre orientations in human thoracic and abdominal aortas and common iliac arteries*. Journal of the Royal Society Interface 9, 1275–1286.
- [256] Schweizerhof, K., Ramm, E., 1984. *Displacement dependent pressure loads in nonlinear finite element analyses*. Computers and Structures 18, 1099–1114.
- [257] Sewell, M., 1967. *On configuration-dependent loading*. Archive for Rational Mechanics and Analysis 23, 327–351.
- [258] Sgarra, C., Vianello, M., 1997. *Rotations which make strain and stress coaxial*. Journal of Elasticity 47, 217–224.
- [259] Šilhavý, M., 1997. *The Mechanics and Thermomechanics of Continuous Media*. Texts and Monographs in Physics, Springer.
- [260] Silver, F., Freeman, J., Seehra, G., 2003. *Collagen self-assembly and the development of tendon mechanical properties*. Journal of Biomechanics 36, 1529–1553.
- [261] Simo, J., 1987. *On a fully three-dimensional finite-strain viscoelastic damage model: Formulation and computational aspects*. Computer Methods in Applied Mechanics and Engineering 60, 153–173.
- [262] Simo, J., Hughes, T., 1998. *Computational Inelasticity*. Volume 7 of *Interdisciplinary Applied Mathematics*. Springer.
- [263] Simone, A., Askes, H., Peerlings, R., Sluys, L., 2003. *Interpolation requirements for implicit gradient-enhanced continuum damage models*. Communications in Numerical Methods in Engineering 19, 563–572.

-
- [264] Spencer, A., 1972. *Deformations of Fibre-Reinforced Materials*. Oxford University Press.
- [265] Spencer, A. (Ed.), 1984. *Continuum Theory of the Mechanics of Fibre-Reinforced Composites*. Number 282 in CISM Courses and Lectures, Springer.
- [266] Spencer, A., Rogers, T., Moss, R., 1974. *An optimal angle of winding for pressurized fibre-reinforced cylinders*. Mechanics Research Communications 1, 27–32.
- [267] Stein, E., de Borst, R., Hughes, T. (Eds.), 2004. *Encyclopedia of Computational Mechanics*. Volume 2, Solids and Structures. Wiley.
- [268] Stein, E., Sagar, G., 2008. *Convergence behavior of 3D finite elements for Neo-Hookean material*. Engineering Computations 25, 220–232.
- [269] Steinmann, P., 1999. *Formulation and computation of geometrically non-linear gradient damage*. International Journal for Numerical Methods in Engineering 46, 757–779.
- [270] Stroud, A., 1971. *Approximate Calculation of Multiple Integrals*. Prentice-Hall, Englewood Cliffs, NJ.
- [271] Svedberg, T., Runesson, K., 1997. *A thermodynamically consistent theory of gradient-regularized plasticity coupled to damage*. International Journal of Plasticity 13, 669–696.
- [272] Taber, L., 1995. *Biomechanics of growth, remodelling, and morphogenesis*. American Society of Mechanical Engineers - Applied Mechanics Reviews 48, 487–545.
- [273] Taylor, G., 1938. *Plastic strain in metals*. Journal of the Institute of Metals 62, 307–324.
- [274] Taylor, R.E., Zheng, C., Jackson, R.P., Doll, J.C., Chen, J.C., Holzbaur, K.R.S., Besier, T., Kuhl, E., 2009. *The phenomenon of twisted growth: humeral torsion in dominant arms of high performance tennis players*. Computer Methods in Biomechanics and Biomedical Engineering 12, 83–93.
- [275] Thylander, S., Menzel, A., Ristinmaa, M., 2012. *An electromechanically coupled micro-sphere framework: application to the finite element analysis of electrostrictive polymers*. Smart Materials and Structures 21, 094008.
- [276] Tkachuk, M., Linder, C., 2012. *The maximal advance path constraint for the homogenization of materials with random network microstructure*. Philosophical Magazine 92, 2779–2808.
- [277] Virga, E., 1994. *Variational Theories for Liquid Crystals*. Volume 8 of *Applied Mathematics and Mathematical Computation*. Chapman & Hall.
- [278] Volokh, K., 2007. *Hyperelasticity with softening for modeling materials failure*. Journal of the Mechanics and Physics of Solids 55, 2237–2264.

- [279] Voyiadjis, G., Abu Al-Rub, R., 2006. *A finite strain plastic-damage model for high velocity impact using combined viscosity and gradient localization limiters: Part II – Numerical Aspects and Simulations*. International Journal of Damage Mechanics 15, 335–373.
- [280] de Vree, J., Brekelmans, W., van Gils, M., 1995. *Comparison of nonlocal approaches in continuum damage mechanics*. Computers & Structures 55, 581–588.
- [281] Waffenschmidt, T., Menzel, A., 2012. *Application of an anisotropic growth and remodelling formulation to computational structural design*. Mechanics Research Communications 42, 77–86.
- [282] Waffenschmidt, T., Menzel, A., 2014. *Extremal states of energy of a double-layered thick-walled tube – Application to residually stressed arteries*. Journal of the Mechanical Behavior of Biomedical Materials 29, 635–654.
- [283] Waffenschmidt, T., Menzel, A., Kuhl, E., 2012. *Anisotropic density growth of bone – a computational micro-sphere approach*. International Journal of Solids and Structures 49, 1928–1946.
- [284] Waffenschmidt, T., Polindara, C., Menzel, A., Blanco, S., 2014. *A gradient-enhanced large-deformation continuum damage model for fibre-reinforced materials*. Computer Methods in Applied Mechanics and Engineering 268, 801–842.
- [285] Wagner, W., 1991. *Zur Behandlung von Stabilitätsproblemen der Elastostatik mit der Methode der Finiten Elemente*. Forschungs- und Seminarberichte aus dem Bereich der Mechanik der Universität Hannover. Bericht-Nr. F 91/1.
- [286] Wallin, M., Ristinmaa, M., Askfelt, H., 2011. *Optimal topologies derived from a phase-field method*. Structural and Multidisciplinary Optimization 45, 171–183.
- [287] Wang, J., Thampatty, B., 2006. *An introductory review of cell mechanobiology*. Biomechanics and Modeling in Mechanobiology 5, 1–16.
- [288] Warren, S., 1995. *Toward a new phenomenological flow rule for orientationally hardening glassy polymers*. Journal of the Mechanics and Physics of Solids 43, 1151–1173.
- [289] Wcisło, B., Pamin, J., Kowalczyk-Gajewska, K., 2013. *Gradient-enhanced damage model for large deformations of elastic-plastic materials*. Archives of Mechanics 65, 407–428.
- [290] Weinans, H., Huiskes, R., Grootenboer, H., 1992. *The behavior of adaptive bone-remodeling simulation models*. Journal of Biomechanics 25, 1425–1441.
- [291] Weisstein, E.W., 2013a. *"Erfi."*. From MathWorld–A Wolfram Web Resource. <http://mathworld.wolfram.com/Erfi.html>.
- [292] Weisstein, E.W., 2013b. *"Kronecker Product."*. From MathWorld–A Wolfram Web Resource. <http://mathworld.wolfram.com/KroneckerProduct.html>.

-
- [293] Welschinger, F., 2011. *A Variational Framework for Gradient-Extended Dissipative Continua. Application to Damage Mechanics, Fracture, and Plasticity*. Ph.D. Thesis. Universität Stuttgart, Institut für Mechanik (Bauwesen), Lehrstuhl I, Bericht Nr.: I-24.
- [294] Wempner, G., 1971. *Discrete approximations related to nonlinear theories of solids*. International Journal of Solids and Structures 7, 1581–1599.
- [295] Weng, S., 1998. *Ein anisotropes Knochenbaummodell und dessen Anwendung*. Technische Mechanik 18, 173–180.
- [296] Williams, J.L., Lewis, J.L., 1982. *Properties and an anisotropic model of cancellous bone from the proximal tibial epiphysis*. Journal of Biomechanical Engineering 104, 50–56.
- [297] Wolff, J., 1870. *Ueber die innere Architectur der Knochen und ihre Bedeutung für die Frage vom Knochenwachstum*. Virchows Archiv für Pathologische Anatomie und Physiologie und für Klinische Medizin 50, 389–453.
- [298] Wolff, J., 1892. *Das Gesetz der Transformation der Knochen*. Hirschwald, Berlin.
- [299] Wriggers, P., 2008. *Nonlinear Finite Element Methods*. Springer.
- [300] Zhang, J., Michalenko, M., Kuhl, E., Ovaert, T., 2010. *Characterization of indentation response and stiffness reduction of bone using a continuum damage model*. Journal of the Mechanical Behavior of Biomedical Materials 3, 189–202.
- [301] Zienkiewicz, O., Taylor, R., 2000. *The Finite Element Method for Solid and Structural Mechanics*. Elsevier.
- [302] Zysset, P., Curnier, A., 1995. *An alternative model for anisotropic elasticity based on fabric tensors*. Mechanics of Materials 21, 243–250. See also Technical Note by S.C. Cowin, *Journal of Biomechanics*, 31:759–762, 1998.

Curriculum Vitae

Personal Data

| | |
|----------------|----------------------|
| Name | Tobias Waffenschmidt |
| Date of Birth | June 21, 1983 |
| Place of Birth | Freudenberg, Germany |
| Marital Status | Single |
| Nationality | German |

School Education

| | |
|-------------------|--|
| 08/1989 – 06/1993 | Primary School, Freudenberg-Büschergrund |
| 08/1993 – 06/2002 | Secondary School, Siegen-Weidenau |

Civilian Service

| | |
|-------------------|---|
| 09/2002 – 06/2003 | Kindergarten for Special Needs Education, Freudenberg-Büschergrund |
|-------------------|---|

University Education

| | |
|-------------------|--|
| 08/2003 – 09/2006 | Undergraduate Studies of Mechanical Engineering (Dual Education System), University of Siegen |
| 10/2006 – 03/2008 | Graduate Studies of Mechanical Engineering, University of Siegen |
| 03/2008 | Academic Degree: Diploma |

Professional Occupation

| | |
|-------------------|--|
| 07/2008 – onwards | Scientific Assistant, Institute of Mechanics, TU Dortmund University |
| 11/2009 – 12/2009 | Visiting Researcher, Group of Structural Mechanics and Material Modelling, University of Zaragoza |